

# Technical Report 15-05

**Thermo-hydro-mechanical  
characterisation and modelling  
of Wyoming granular bentonite**

July 2015

A. Seiphoori

EPFL, Lausanne

**National Cooperative  
for the Disposal of  
Radioactive Waste**

Hardstrasse 73  
CH-5430 Wettingen  
Switzerland  
Tel. +41 56 437 11 11

[www.nagra.ch](http://www.nagra.ch)



# Technical Report 15-05

**Thermo-hydro-mechanical  
characterisation and modelling  
of Wyoming granular bentonite**

July 2015

A. Seiphoori

EPFL, Lausanne

**National Cooperative  
for the Disposal of  
Radioactive Waste**

Hardstrasse 73  
CH-5430 Wettingen  
Switzerland  
Tel. +41 56 437 11 11

[www.nagra.ch](http://www.nagra.ch)

This report was prepared on behalf of Nagra. It refers to the PhD Thesis "Thermo-hydro-mechanical characterisation and modelling of MX-80 granular bentonite" conducted by A. Seiphoori at the Laboratory of Soil Mechanics of Ecole Polytechnique Fédérale de Lausanne (Thèse EPFL, No. 6159). The viewpoints presented and conclusions reached are those of the author and do not necessarily represent those of Nagra.

**ISSN 1015-2636**

"Copyright © 2015 by Nagra, Wettingen (Switzerland) / All rights reserved.

All parts of this work are protected by copyright. Any utilisation outwith the remit of the copyright law is unlawful and liable to prosecution. This applies in particular to translations, storage and processing in electronic systems and programs, microfilms, reproductions, etc."

## Summary

Deep geological repositories are considered to be the most suitable solutions for the disposal of high-level radioactive wastes. In several repository concepts, bentonites are selected as the buffer component of the engineered barrier system to be emplaced between the waste canisters and the host rock. The buffer material involved in the confinement of radioactive waste will be submitted to drastic changes of thermal, hydraulic and mechanical conditions. These conditions may significantly influence the behaviour of the buffer material at both the macroscopic and microscopic levels. Safety assessment of the entire repository requires a detailed understanding of the thermo-hydro-mechanical (THM) evolution of the buffer material under such circumstances.

This research contributes to the investigation of the behaviour of bentonite material in an engineered barrier system for the disposal of radioactive waste in Switzerland. It includes comprehensive experimental characterisations of the behaviour of the material under thermo-hydro-mechanical processes with an insight into the microstructural evolutions. The experimental observations on the behavioural features of the material at the macroscopic and microscopic level provide a sound basis for the development of a water retention model to account for the hydro-mechanical coupling and microstructural evolutions. Therefore, the present report addresses the issue from three main perspectives: (i) macroscopic behaviour, (ii) microstructural evolution and (iii) constitutive/modelling directions.

(i) *Macroscopic behaviour*: a systematic method was used to evaluate the behavioural features of Wyoming granular bentonite under thermo-hydro-mechanical stress paths. After considering a reference grain size distribution, an experimental evaluation of the swelling potential/pressure and the compressibility behaviour of the material was performed. A comprehensive analysis of water retention behaviour was conducted by developing a new technique called the 'Micro-cell' technique, which determines the water retention behaviour with a high resolution by controlling the degree of saturation in the wetting and drying cycles. These initial analyses provided a basis for developing new methodologies for advanced triaxial testing of bentonite materials that experience significant swelling. After developing/calibrating an advanced double-wall triaxial testing system, the thermally-induced strain-stress response of the saturated and unsaturated buffer material and the deviatoric behaviour under a wide range of total suction and confining stresses were evaluated. The effects of the hydraulic gradient and temperature on the hydraulic conductivity of the saturated buffer materials were determined. These experimental activities provided a global picture of the thermo-hydro-mechanical response of the Wyoming granular bentonite under repository-like conditions. The hydro-mechanical response of the granular material influenced by an alternative emplacement technique was assessed within a case study conducted in an underground research laboratory (URL) in Switzerland.

(ii) *Microstructural evolution*: using the microstructural investigation techniques associated with the 'Micro-cell' device, an insight into the fabric evolution of the bentonite material at different hydraulic states along the water retention domain was obtained. Thus, the change in water retention behaviour was linked to the microstructural modifications. The microstructural analysis demonstrated a clear transition from a double-structured (at the compacted state) to a single-structured porosity network (after full saturation) with permanent features that imposed irreversible behaviour in terms of water retention, resulting in an increase in the retention capacity of the material. Analysis of the available information on the hydration of smectite clay at the particle level indicated the evolution of an active porosity within the microstructure, which consequently affects the macroscopic response of the bentonite. Further investigation of the interaction between the microstructure and water retention characteristics was carried out by

analysing the water retention behaviour and microstructural evolution of bentonite and illite materials. This comparison confirmed the existence of an exclusively active (i.e., capillary accessible) porosity within the bentonite microstructure that modified the fabric, particularly when the material approached the full saturation state. The integration of this information from the mutual interaction of the active microstructure and the macroscopic behaviour of bentonite is an important factor in the assessment of the hydro-mechanical response of the buffer material.

(iii) *Constitutive/modelling*: following the experimental characterisation of granular bentonite, a conceptual water retention model was developed to account for the change in the void ratio and the microstructural evolution during the hydration of the bentonite material. The model was based on an elasto-plasticity approach that used a linear anisotropic hardening rule. The model produced the water retention curves for the entire hydraulic domain under a constant void ratio. The scanning behaviour was analysed at a given compaction state by considering the microstructural void ratio at different saturation stages. The developed formulation of the scanning behaviour could be an essential contribution to the constitutive modelling of high-swelling geomaterials.

## Zusammenfassung

Geologische Tiefenlager gelten als sichere Lösung für die Entsorgung hochaktiver Abfälle. Im schweizerischen Lagerkonzept ist zur Verfüllung der Einlagerungsstollen granulares Bentonitmaterial als eine wichtige technische Barrierenkomponente vorgesehen. Das Verfüllmaterial dient dabei zum sicheren Einschluss der radioaktiven Abfälle; nach dem Verschluss des Tiefenlagers ist das Material beträchtlichen Veränderungen der thermischen, hydraulischen und mechanischen Bedingungen ausgesetzt. Solche Veränderungen können die Eigenschaften des Verfüllmaterials sowohl im makroskopischen wie auch im mikroskopischen Betrachtungsmaßstab erheblich beeinflussen. Daher ist ein detailliertes Verständnis der thermo-hydro-mechanischen (THM) Entwicklung des Verfüllmaterials für die Bewertung der Langzeitsicherheit des gesamten Lagersystems unabdingbar.

Die im vorliegenden Bericht dokumentierten Forschungsarbeiten beziehen sich auf das Konzept eines geologischen Tiefenlagers für hochaktive Abfälle in der Schweiz und auf die damit verbundenen technischen Randbedingungen sowie die resultierenden Anforderungen an die Verfüllmaterialien. Die wissenschaftlichen Untersuchungen umfassen die geotechnische Charakterisierung des Bentonitgranulats unter besonderer Berücksichtigung von thermo-hydro-mechanisch gekoppelten Prozessen. Experimente zum Materialverhalten im makroskopischen wie auch mikroskopischen Betrachtungsmaßstab bilden die Grundlage für die Entwicklung eines konzeptuellen Modells zum Wasserretentionsvermögen von granularem Bentonit, welches den mikrostrukturellen Veränderungen entlang verschiedener Sättigungspfade Rechnung trägt. Thematisch ist der Bericht in folgende fachtechnische Aspekte gegliedert: (i) das makroskopische Verhalten, (ii) die mikrostrukturelle Entwicklung und (iii) die modelltechnische Beschreibung des THM-Verhaltens von granularem Bentonit.

(i) *Makroskopisches Verhalten*: Zur Bewertung des Verhaltens von Wyoming Bentonitgranulat unter thermo-hydro-mechanischer Beanspruchung wurde eine systematische Methode verwendet. Unter Berücksichtigung einer Referenzkorngrößenverteilung wurden Experimente zur Charakterisierung des Quellpotenzials / Quelldrucks und des Kompressibilitätsverhaltens des Materials durchgeführt. Das Wasserrückhaltevermögen wurde anhand einer neuen technischen Entwicklung, der sogenannten "micro-cell"-Technik analysiert, welche die Wasserrückhalteigenschaften durch Steuerung des Sättigungsgrads in den Aufsättigungs- und Trocknungszyklen mit einer sehr hohen Genauigkeit bestimmt. Diese initialen Analysen bilden die Grundlage für die Entwicklung neuer Methoden für Triaxial-Tests an erheblich quellendem Bentonitmaterial. Nach der Entwicklung/Kalibrierung eines neuartigen Doppelwand-Triaxial-Testsystems wurde das thermisch induzierte Belastungs-Verformungsverhalten des gesättigten und ungesättigten Verfüllmaterials und insbesondere das deviatorische Verhalten für einen weiten Saugspannungsbereich und unterschiedliche Manteldrücke untersucht. Dadurch kann die Auswirkung des hydraulischen Gradienten und der Temperatur auf die hydraulische Leitfähigkeit des gesättigten Verfüllmaterials bestimmt werden. Diese Experimente ergeben ein umfassendes Bild des thermo-hydro-mechanischen Verhaltens des Wyoming Bentonitgranulats unter standortspezifischen Bedingungen. Darüber hinaus wurde in einer Fallstudie eine alternative Einbringtechnik im Felslabor Grimsel untersucht.

(ii) *Mikrostrukturelle Entwicklung*: Mithilfe von konventionellen mikrostrukturellen Untersuchungsmethoden und einer speziell entwickelten "micro-cell" Apparatur wurde das Verständnis der strukturellen Entwicklung des Bentonitgefüges in Abhängigkeit von Sättigungszustand und Saugspannung erweitert. Dabei wurde der Zusammenhang zwischen der Veränderung des Wasserrückhaltevermögens und den mikrostrukturellen Gefügeänderungen qualitativ und quantitativ untersucht. Die Mikrostrukturanalyse zeigte einen klaren Übergang von einem

Doppelstruktur- (im kompaktierten Zustand) zu einer mono-modalen Porenstruktur (*single porosity* – nach vollständiger Sättigung) mit einem irreversiblen Verhalten in Bezug auf das Wasserrückhaltevermögen (Erhöhung des Wasserretentionsvermögens). Die Analyse der Hydratisierung von reinen Smektit-Proben zeigte die Entwicklung einer aktiven Porosität in der Mikrostruktur an, die somit das makroskopische Verhalten des Bentonits beeinflusst. Weitere Untersuchungen umfassten die Analyse der Wasserrückhaltung und mikrostrukturellen Entwicklung von Wyoming Bentonit-Proben und von Illit-Proben. Dieser Vergleich bestätigte die Existenz einer aktiven (d.h. kapillar zugänglichen) Porosität innerhalb der Bentonit-Mikrostruktur, welche das Gefüge modifiziert, insbesondere wenn das Material eine vollständige Sättigung erreicht hat. Die Kombination dieser Informationen aus der gegenseitigen Wechselwirkung der aktiven Mikrostruktur und dem makroskopischen Verhalten von Bentonit ist ein wichtiger Faktor in der Bewertung des hydro-mechanischen Verhaltens des Verfüllmaterials.

(iii) *Grundlagen / Modellierung*: Nach der experimentellen Charakterisierung des Bentonitgranulats wurde ein konzeptionelles Modell zur Wasserrückhaltung entwickelt, um die Änderung in der Porenzahl und in der mikrostrukturellen Entwicklung während der Aufsättigung von Bentonitmaterial zu berücksichtigen. Das Modell wurde auf Grundlage eines elasto-plastischen Ansatzes entwickelt, der ein lineares, anisotropes Verfestigungsgesetz verwendet. Das Modell erzeugt Wasserrückhaltekurven für den gesamten Sättigungsbereich unter Annahme einer konstanten Porenzahl. Das Hysterese-Verhalten bei einem gegebenen Kompaktierungsgrad wurde unter Berücksichtigung der mikrostrukturellen Porenzahl bei unterschiedlichen Sättigungsstufen analysiert. Die dabei entwickelte Formel kann einen wesentlichen Beitrag zur konstitutiven Modellierung von stark quellenden Geomaterialien liefern.

## Résumé

Le stockage en dépôts géologiques profonds est généralement considéré comme la solution la mieux adaptée au confinement ultime des déchets radioactifs à haute activité. Dans différents concepts de stockage, de la bentonite est retenue comme matériau de la barrière ouvragée mise en place entre les colis de déchets et la roche d'accueil. Ce matériau de confinement des déchets radioactifs sera soumis à de fortes variations des charges thermiques, hydrauliques et mécaniques. Ces variations pourraient avoir un impact significatif sur le comportement microscopique et macroscopique de ce matériau de confinement. Afin d'analyser la sûreté de l'ensemble du dépôt, il est donc nécessaire de posséder une compréhension détaillée de l'évolution thermo-hydro-mécanique (THM) de ce matériau de confinement soumis sous ces conditions.

L'objectif de cette étude a été de caractériser le comportement de la bentonite considérée pour une mise en œuvre dans un système de barrières ouvragées servant au confinement de déchets radioactifs à haute activité en Suisse. Le comportement de la bentonite soumise aux charges THM et en particulier son évolution microstructurale ont été étudiés de manière expérimentale. Les observations expérimentales sur le comportement du matériau aux niveaux macroscopique et microscopique ont permis d'élaborer une loi de comportement microstructural de rétention de l'eau qui intègre le couplage hydromécanique. Ce rapport traite du comportement THM du matériau de confinement selon les trois volets suivants: comportement macroscopique, observations microstructurales et modélisation d'une loi de comportement.

(i) *Le comportement macroscopique*: une méthode systématique a été utilisée pour caractériser le comportement THM couplé de la bentonite granulaire du Wyoming. La déformation due au gonflement, la pression de gonflement et la compressibilité du matériau en ont été déterminées. L'analyse exhaustive de la capacité de rétention d'eau du matériau a été réalisée à l'aide d'une nouvelle technique, dite de la "microcellule", et par laquelle les caractéristiques en rétention d'eau du matériau sont déterminées avec grande précision par des cycles de drainage/imbibition. Ces analyses de base ont permis d'élaborer des méthodologies nouvelles pour en matière d'essais triaxiaux avancés sur bentonites. Après avoir développé/calibré une cellule triaxiale à double paroi, le comportement en contrainte/déformation de la bentonite saturée et non-saturée soumise à des contraintes thermiques, ainsi que son comportement sous charge déviatorique ont été mesurés sur un large spectre de valeurs de succion et de contraintes de confinement. L'impact du gradient hydraulique et de la température sur la conductivité hydraulique de la bentonite saturée ont été déterminés. Ces déterminations expérimentales ont permis l'évaluation du comportement général thermo-hydro-mécanique de la bentonite granulaire du Wyoming, sous conditions similaires à celles du dépôt profond. De plus, au cours d'une étude réalisée au laboratoire de recherche souterrain du Grimsel en Suisse, le comportement hydromécanique de la bentonite granulaire a été évalué, lorsqu'une technique alternative de mise en place par projection des granulés est utilisée.

(ii) *Évolution microstructurale*: les techniques de recherche microstructurale et la méthode dite de la "microcellule" ont permis d'étudier la microstructure de la bentonite aux différents états hydriques décrits par les courbes de rétention d'eau. L'analyse microstructurale a mis en évidence le passage d'une double porosité de l'espace poral (à l'état compacté) à une simple porosité (après saturation complète), entraînant un comportement irréversible en termes de rétention d'eau, et résultant en une capacité de rétention accrue du matériau. L'information disponible sur l'hydratation des smectites explique comment l'évolution d'une porosité active au sein de la microstructure peut affecter le comportement macroscopique de la bentonite. La capacité de rétention d'eau et l'évolution microstructurale de la bentonite ont été comparées à celles des illites, expliquant comment l'évolution microstructurale des argiles actives comme la

bentonite affecte le comportement de rétention de l'eau au niveau macroscopique. Il est donc nécessaire de prendre en compte l'interaction entre la microstructure active et le comportement macroscopique de la bentonite pour en déterminer sa performance hydromécanique.

(iii) *Modélisation d'une loi de comportement*: un modèle conceptuel de rétention d'eau pour la bentonite granulaire du Wyoming a été développé sur la base des observations expérimentales. Il prend en compte l'indice des vides et l'évolution microstructurale en mode d'hydratation de la bentonite. Le modèle est basé sur un comportement élasto-plastique à durcissement anisotrope linéaire. A niveau de compaction donné, le modèle décrit les courbes de rétention d'eau sur l'ensemble du domaine hydrique considéré. Ce modèle constitue une loi de comportement hydromécanique des bentonites granulaires qui applicable pour les stockages souterrains de déchets radioactifs.

## List of Contents

Summary .....	I
Zusammenfassung.....	III
Résumé .....	V
List of Contents.....	VII
List of Tables.....	XI
List of Figures .....	XII
<b>1 Bentonite, buffer and disposal of high level nuclear waste: an introduction.....</b>	<b>1</b>
1.1 General introduction .....	1
1.1.1 Disposal of high level nuclear wastes (HLW).....	1
1.1.2 Evolution of the buffer material .....	3
1.1.2.1 Swelling pressure/potential.....	4
1.1.2.2 Density gradient and compressibility .....	4
1.1.2.3 Water retention and wetting/drying cycling .....	5
1.1.2.4 Fabric and microstructure .....	5
1.1.2.5 Deviatoric and shearing strength .....	5
1.1.2.6 Influence of temperature.....	6
1.1.2.7 Physicochemical and effective stresses .....	6
1.2 THM characterisation and modelling of Wyoming granular bentonite.....	6
1.2.1 Objectives .....	6
1.2.2 Outline of the report .....	7
<b>2 Experimental characterisation of the compressibility, swelling and water retention behaviour of Wyoming granular bentonite.....</b>	<b>9</b>
2.1 Tested material .....	9
2.1.1 Wyoming granular bentonite .....	9
2.1.2 Grain size distribution.....	10
2.1.2.1 Sieve analysis .....	10
2.1.2.2 Hydrometric analysis.....	10
2.1.3 Grain size distribution selected for sample preparation.....	10
2.1.3.1 Effect of static compaction and hydrations on grain size distribution.....	12
2.1.4 Index properties .....	13
2.2 Swelling and compressibility behaviour.....	14
2.2.1 Hydro-mechanical behaviour of compacted swelling clays .....	14
2.2.2 Swelling and compressibility behaviour of Wyoming granular bentonite .....	16
2.2.2.1 Swelling behaviour .....	16

2.2.2.2	One-dimensional volumetric behaviour.....	18
2.3	Water retention behaviour .....	25
2.3.1	Definitions .....	25
2.3.2	Bentonites used as buffer and backfilling materials .....	27
2.3.3	Water retention behaviour of Wyoming granular bentonite .....	29
2.3.3.1	Methodology.....	29
2.3.3.2	Effect of void ratio.....	32
2.3.3.3	Reproducibility of the technique .....	34
2.3.3.4	Retention behaviour in wetting and drying cycles.....	35
2.3.3.5	Effect of confinement on retention behaviour .....	37
2.3.3.6	Effect of granulometry on retention behaviour.....	40
2.3.3.7	Effect of temperature on retention behaviour.....	41
2.4	Summary and conclusions .....	45
<b>3</b>	<b>Experimental characterisation of the microscopic behaviour of Wyoming granular bentonite.....</b>	<b>47</b>
3.1	Fabric and structure of geomaterials.....	47
3.1.1	Crystalline structure of clays .....	48
3.2	Clay mineral – pore water interaction .....	51
3.2.1	Swelling behaviour and diffuse double layer theory .....	53
3.2.2	Influence of temperature on clay – pore water interactions.....	55
3.3	Microstructural observations .....	56
3.3.1	Scanning Electron Microscopy (SEM).....	56
3.3.2	Mercury Intrusion Porosimetry (MIP).....	56
3.3.2.1	Pore size distribution .....	56
3.3.2.2	Measurement principle .....	57
3.3.2.3	Mathematical formulations.....	58
3.3.2.4	Derivation of the retention curve with MIP data .....	60
3.3.2.5	Limitations of the MIP technique .....	61
3.3.3	Microstructure of compacted Wyoming granular bentonite.....	62
3.3.4	Microstructural evolution of Wyoming bentonite during wetting – drying cycles .....	65
3.3.4.1	Microstructural observations .....	66
3.3.4.2	Hydration mechanism and particle subdivision.....	70
3.3.4.3	Microstructural and interlayer void ratio evolutions .....	71
3.3.4.4	Evolution of the intruded micropores in different stress paths.....	73
3.3.5	Confinement and microstructural evolutions.....	73
3.3.6	Focused Ion Beam nanotomography (FIB-nt) technique.....	75
3.3.6.1	Methodology and sample preparation .....	75
3.3.6.2	Results of the FIB-nt technique .....	78

3.3.7	Water retention of active and non-active clays.....	81
3.3.7.1	Water retention and porosity distribution .....	81
3.3.7.2	Microstructural evolutions in wetting and drying cycles.....	83
3.4	Summary and conclusions .....	86
<b>4</b>	<b>A model for water retention behaviour of Wyoming granular bentonite .....</b>	<b>89</b>
4.1	Water retention modelling .....	89
4.2	Water retention features of Wyoming bentonite.....	91
4.2.1	Mathematical formulation .....	94
4.2.2	Model response.....	97
4.2.2.1	Void ratio dependency .....	97
4.2.2.2	Microstructural evolution .....	99
4.3	Summary and conclusions .....	99
<b>5</b>	<b>Thermo-hydro-mechanical characterisation of Wyoming granular bentonite using an advanced triaxial cell system .....</b>	<b>101</b>
5.1	THM triaxial testing in geomaterials.....	101
5.1.1	Backgrounds .....	101
5.1.1.1	Application of suction and temperature.....	102
5.1.1.2	Volume change measurement.....	102
5.2	THM triaxial cell system used in this study .....	103
5.2.1	Calibration procedure .....	106
5.2.1.1	Axial load-deformation calibration.....	106
5.2.1.2	Calibration of the volume change of the sample .....	110
5.3	THM triaxial behaviour of bentonites .....	115
5.4	Triaxial testing on Wyoming granular bentonite.....	117
5.4.1	Sample preparation .....	117
5.4.1.1	Unsaturated conditions .....	117
5.4.1.2	Saturated conditions .....	120
5.4.1.3	Homogenisation during sample preparation.....	121
5.4.2	Triaxial testing procedure at ambient temperature .....	122
5.4.2.1	Unsaturated condition.....	122
5.4.2.2	Saturated condition .....	123
5.4.2.3	Influence of the rubber membrane on the measured deviatoric strength.....	125
5.4.3	Hydraulic conductivity analysis .....	126
5.4.4	Triaxial testing procedure at elevated temperature.....	126
5.5	Experimental results .....	127
5.5.1	Isotropic behaviour .....	127
5.5.2	Deviatoric behaviour at ambient temperature.....	130
5.5.2.1	Visual observation of the tested samples.....	135
5.5.3	Influence of temperature.....	136

5.5.3.1	Influence of temperature on unsaturated volumetric and deviatoric behaviours.....	136
5.5.3.2	Visual observation of the temperature effect on unsaturated samples.....	138
5.5.3.3	Influence of temperature on saturated bentonites .....	139
5.5.4	Hydraulic conductivity of saturated bentonite.....	140
5.6	Summary and conclusions .....	141
<b>6</b>	<b>Assessment of the hydro-mechanical behaviour of shot-clay Wyoming bentonite .....</b>	<b>143</b>
6.1	Shot-clay Wyoming bentonite and technological gaps.....	143
6.2	Tested material .....	144
6.2.1	Sampling procedure .....	144
6.2.2	Index properties .....	145
6.2.3	Microstructural features.....	145
6.3	Experimental programme .....	146
6.3.1	Swelling behaviour .....	147
6.3.2	Water retention behaviour .....	147
6.3.3	Controlled suction hydro-mechanical test .....	148
6.3.3.1	Experimental setup .....	148
6.3.3.2	Hydro-mechanical stress path.....	149
6.4	Test results.....	151
6.4.1	Swelling potential of the as-shot material.....	151
6.4.2	Water Retention behaviour .....	152
6.4.3	Controlled suction hydro-mechanical behaviour.....	153
6.5	Summary and conclusions .....	155
<b>7</b>	<b>Conclusions and perspective .....</b>	<b>159</b>
7.1	Conclusions .....	159
7.2	Outlook for future works .....	160
<b>8</b>	<b>Referenzverzeichnis.....</b>	<b>163</b>
<b>Appendix A</b>	<b>.....</b>	<b>A-1</b>
A.1	List of symbols and abbreviations .....	A-1

## List of Tables

Tab. 2.1:	Grain size distribution (hydrometric analysis, Plötze & Weber 2007).....	10
Tab. 2.2:	Summary of general physical properties of the tested Wyoming granular bentonite. ....	14
Tab. 2.3:	Relative humidity and total suction values resulted from saturated and partly saturated salt solutions.....	42
Tab. 3.1:	Mineralogical composition of Wyoming granular bentonite (Plötze & Weber 2007).....	50
Tab. 3.2:	Summary of general physical properties of the three clays studied in this research.....	50
Tab. 3.3:	Properties of the samples prepared for the FIB analysis (Keller et al. 2014). ....	77
Tab. 5.1:	List of tests performed at ambient temperature ( $T = 24\text{ }^{\circ}\text{C}$ ).....	128
Tab. 5.2:	Compression indices of unsaturated bentonite samples. ....	130
Tab. 5.3:	List of the tests performed at elevated temperature ( $T = 80\text{ }^{\circ}\text{C}$ ). ....	136
Tab. 6.1:	Initial characteristics of the tested specimens in the experimental activities.....	147

## List of Figures

Fig. 1-1:	Example layout of the HLW repository with its main features .....	2
Fig. 1-2:	Schematical sketch of a HLW emplacement room with the compartmentalisation concept adapted from Leupin et al. (2016). .....	3
Fig. 1-3:	Evolution of the bentonite in the emplacement rooms of a HLW repository: .....	4
Fig. 1.3:	Fabric of Wyoming granular bentonite: (a) appearance of granular bentonite at macroscopic scale; photomicrographs of the material at (b) the as compacted state, and (c) after wetting/drying cycles with significant modification of the fabric. ....	5
Fig. 2.1:	Grain size distribution curves of the tested material.....	11
Fig. 2.2:	Different grain size fractions of the granular Wyoming bentonite. ....	11
Fig. 2.3:	Segregation test of the granular material: (a) without fine fractions (smaller than 0.25 mm), and (b) full curve. ....	12
Fig. 2.4:	Apparent grain size distribution of the randomly selected granular samples. ....	12
Fig. 2.5:	Influence of compaction on the apparent grain size distribution of granular bentonite. ....	13
Fig. 2.6:	Influence of wetting/drying cycle on the apparent grain size distribution of granular bentonite. ....	13
Fig. 2.7	Effect of temperature on the evolution of the swelling pressure with time for compacted FEBEX bentonite samples at a dry density of 1.5 Mg/m <sup>3</sup> (Villar et al. 2010). ....	15
Fig. 2.8	Influence of temperature on the compressibility and the yield stress of bentonite materials: (a) GMZ01 bentonite (Ye et al. 2012), and (b) Wyoming bentonite (Tang et al. 2008).....	16
Fig. 2.9:	Swelling pressure developed under constant volume conditions at different dry densities for Wyoming granular bentonite. ....	17
Fig. 2.10:	Swelling behaviour of Wyoming granular bentonite: (a) constant volume swelling pressure, and (b) free volume swelling vs. total suction. ....	18
Fig. 2.11:	Compaction behaviour of the granular bentonite in a standard proctor test and the contours of equal suctions.....	19
Fig. 2.12:	(a) Schematic setup for static compaction tests in controlled-strain condition, and (b) influence of the strain rate on compaction behaviour. ....	20
Fig. 2.13:	Effect of total suction/water content on static compaction behaviour of granular bentonite in terms of: (a) e-log $\sigma_v$ , and (b) yield stress $\sigma_y$ based on the results in part (a). ....	20
Fig. 2.14:	Vertical stress required to reach target dry density at different total suction values. ....	21
Fig. 2.15:	Effect of maximum grain size on the compaction behaviour of the granular bentonite: (a) e-log $\sigma_v$ behaviour, and (b) grain size distributions. ....	21
Fig. 2.16:	(a) High pressure oedometric cell for consolidation tests, and (b) maximum swelling pressure attained under constant volume conditions.....	22

Fig. 2.17:	(a) Swelling behaviour of the material saturated under 8 kPa vertical stress followed by consolidation steps under higher stresses, and (b) consolidation behaviour of the material saturated under constant and free volume conditions.....	23
Fig. 2.18:	Consolidation behaviour of different smectite-based materials reported by Marcial et al. (2002). .....	24
Fig. 2.19:	Compression index $C_c$ for Wyoming bentonite in this study and Na-laponite reported by Al-Mukhtar et al. (1999) in unsaturated and saturated conditions. ....	24
Fig. 2.20:	Typical water retention curve of geomaterials. ....	27
Fig. 2.21:	Contour lines of the dry density after dismantling the full-scale Engineered Barrier (EB) experiment at Mont Terri (García-Siñeriz et al. 2008). ....	28
Fig. 2.22:	(a) Micro-cell components, and (b) WP4C dew-point chilled-mirror potentiometer. ....	30
Fig. 2.23:	(a) Preconditioning of different fractions of the Wyoming granular bentonite, and (b) prepared sample by mixing the different fractions.....	31
Fig. 2.24:	(a) Micro-cell components, and (b) compaction of the material inside the cell using an ad-hoc mould.....	31
Fig. 2.25:	Effect of void ratio on the water retention behaviour of Wyoming granular bentonite: (a) water content vs. total suction, and (b) degree of saturation vs. total suction.....	33
Fig. 2.26:	Evolution of degree of saturation with time for the sample inside the Micro-cell. ....	33
Fig. 2.27:	Evolution of air-entry suction values with void ratio and the total suction at which the samples reach fully saturation.....	34
Fig. 2.28:	Repetition of the determination of the retention behaviour for different void ratios. ....	35
Fig. 2.29:	Comparison of water retention curves obtained by suction measurement and suction control techniques. ....	36
Fig. 2.30:	Hysteresis water retention curve of highly compacted Wyoming granular bentonite. ....	37
Fig. 2.31:	Water retention behaviour of highly compacted bentonite in reversible regions. ....	37
Fig. 2.32:	Effect of confinement on the water retention behaviour. ....	39
Fig. 2.33:	Schematic cross section of the interface between unsaturated material and HAE disc in a pressure plate apparatus (Lu & Likos 2004). ....	39
Fig. 2.34:	Retention behaviour of Wyoming bentonite under free volume conditions.....	39
Fig. 2.35:	Total suction, matric suction and osmotic suction terms of compacted Calcigel reported by Arifin & Schanz (2009).....	40
Fig. 2.36:	(a) Apparent grain size distribution of the granular and powder bentonite samples, and (b) comparison of the retention behaviour compacted at the same void ratio ( $e = 0.53$ ).....	41

Fig. 2.37:	Influence of temperature on the retention behaviour of Wyoming granular bentonite using the Micro-cell technique.....	41
Fig. 2.38:	Schematic cross section of the sorption bench (Salager et al. 2010). .....	42
Fig. 2.39:	Evolution of the degree of saturation of the sample inside the Micro-cell in sorption bench at $T = 80\text{ }^{\circ}\text{C}$ .....	43
Fig. 2.40:	Influence of temperature on the retention behaviour of bentonite combining Micro-cell and sorption bench. ....	44
Fig. 2.41:	Influence of temperature on the water retention behaviour of FEBEX bentonite with dry density of $1.65\text{ Mg/m}^3$ (Villar & Lloret 2004). ....	44
Fig. 3.1:	Schematic representation of elementary particle arrangements (Collins & McGown 1974): (a) individual clay lamella or platelet, (b) clay platelet group interaction, and (c) clothed silt or sand particle interaction. ....	48
Fig. 3.2:	Crystal constitution of clay minerals: (a) aluminium octahedral and silicon tetrahedron units, (b) basic unit layers for kaolinite, and (c) smectite or illite. ....	49
Fig. 3.3:	Crystal constitution of 2:1 structure clays: (a) weak bonding between successive layers in smectite clay minerals, and (b) collapse of interlamellar space by the presence of potassium in illite.....	49
Fig. 3.4:	Schematic illustration of the proportions of water in different levels of porosity. ....	52
Fig. 3.5:	Comparison of the consolidation behaviour of bentonite and illite.....	52
Fig. 3.6:	Theoretical relationship for the swelling pressure of Wyoming bentonite with respect to the dry density (Tripathy et al. 2004) and comparison with the experimental data (Bucher & Müller-Vonmoos 1989).....	54
Fig. 3.7:	Influence of temperature on physical properties of water: (a) density, (b) viscosity, (c) surface tension, (d) dielectric constant, and (e) vapour pressure (data from Lide 2004).....	55
Fig. 3.8:	Different microstructural levels in poured and compacted Wyoming granular bentonite. ....	62
Fig. 3.9:	SEM photomicrographs of Wyoming grains with $e = 0.28$ ( $\rho_d = 2.13\text{ Mg/m}^3$ ).....	63
Fig. 3.10:	SEM photomicrographs of Wyoming granular bentonite at as compacted state with $e = 0.53$ ( $\rho_d = 1.80\text{ Mg/m}^3$ ): (a), (b) bentonite grains coated by aggregates composing the assemblages, and (c), (d) bentonite aggregate arranged in inter-assemblage space. ....	64
Fig. 3.11:	(a) Intra-particle (stacks) porosity measured by means of nitrogen adsorption technique (Minon 2009), and (b) expanded smectite particle (stacks) observed by TEM technique (Tessier et al. 1992). ....	65
Fig. 3.12:	Hysteresis water retention curve of highly compacted Wyoming granular bentonite. ....	66
Fig. 3.13:	Microstructural evolutions during different phases of wetting and drying cycles based on the results of the MIP.....	68
Fig. 3.14:	SEM photomicrographs of Wyoming granular bentonite after a wetting/drying cycle corresponding to point G in Fig. 3.13.....	69

Fig. 3.15:	(a), (b) Average inter-particle distance in smectite and number of sheets per particle vs. total suction, and (c) water retention behaviour of highly compacted bentonite under constant volume conditions. ....	71
Fig. 3.16:	Evolution of the microstructural void ratio and nanostructural void ratio with respect to the total suction for compacted bentonite sample. ....	72
Fig. 3.17:	Evolution of the intruded microstructural void ratio $e_m^*$ with water ratio $e_w$ for Wyoming granular bentonite at different states. ....	73
Fig. 3.18:	(a) Effect of confinement on the water retention behaviour of bentonite, (b) interlayer distance evolution with suction decrease, and (c) number of sheets per particle vs. suction decrease and maximum subdivision under free volume conditions. ....	74
Fig. 3.19:	(a) Free volume swelling, and (b) free volume water retention behaviour of the granular bentonite. ....	75
Fig. 3.20:	Sample preparation from vapour wetted bentonite and compaction at a target dry density in a sample holder of the high-pressure freezing instrument (Keller et al. 2014). ....	76
Fig. 3.21:	(a) Wyoming bentonite at $w = 22.6\%$ due to hydration by liquid and vapour phase, (b) FIB cells and the compaction mould, and (c) sealing clamps for the cells. ....	77
Fig. 3.22:	BSE images of Wyoming bentonite samples with different dry densities mentioned in Tab. 3.3 (Keller et al. 2014). ....	78
Fig. 3.23:	BSE images showing the mesh-like framework: (a) along the boundary of non-clayey particle for sample at lower density and total suction ( $\rho_d = 1.23 \text{ Mg/m}^3$ , $\psi = 3.85 \text{ MPa}$ ), and (b) on sample compacted at higher density and total suction ( $\rho_d = 1.46 \text{ Mg/m}^3$ , $\psi = 13.86 \text{ MPa}$ ; Keller et al. 2014). ....	78
Fig. 3.24:	(a) BSE of the material at the frozen stage (i.e. $-125^\circ\text{C}$ ), and (b) SE image showing the sublimated material at room temperature at the same spot of the sample compacted at a dry density of $1.46 \text{ Mg/m}^3$ (Keller et al. 2014). ....	79
Fig. 3.25:	Visualisation and 3D reconstruction of FIB-nt data: (a), (b) for the sample compacted at a dry density of $1.46 \text{ Mg/m}^3$ , and (c), (d) for the sample compacted at a dry density of $1.67 \text{ Mg/m}^3$ (Keller et al. 2014). ....	80
Fig. 3.26:	Possible particle arrangements in the observed honeycomb structure (Keller et al. 2014). ....	80
Fig. 3.27:	Water retention behaviour of Wyoming bentonite, illite and kaolinite using the 'Micro-cell' technique. ....	81
Fig. 3.28:	Water retention behaviour and porosity distribution in the as compacted state for the Wyoming bentonite, illite and kaolinite samples (all compacted at a dry density of $1.80 \text{ Mg/m}^3$ ). ....	82
Fig. 3.29:	Water retention behaviour of highly active Wyoming bentonite and non-active illite clay in constant volume condition compacted at dry density of $1.80 \text{ Mg/m}^3$ in wetting/drying cycles. ....	84
Fig. 3.30:	Microstructural evolution of of highly active Wyoming bentonite and non-active illite at constant volume conditions compacted at a dry density of $1.80 \text{ Mg/m}^3$ . ....	85

Fig. 4.1:	Conceptual representations of the water retention model proposed by Salager et al. (2013): (a) degree of saturation, and (b) water content ( $s_{conv}$ and $w_{conv}$ are the coordinates of the convergence point). .....	90
Fig. 4.2:	Water retention behaviour of Wyoming granular bentonite: (a) water content vs. total suction, and (b) degree of saturation vs. total suction. ....	92
Fig. 4.3 :	(a) Evolution of the air-entry value suction, total suction at saturation and drying yield total suction with void ratio, and (b) evolution of coefficients of compressibility with void ratio. ....	92
Fig. 4.4:	Water retention behaviour in reversible and irreversible hydraulic domains. ....	93
Fig. 4.5:	(a) Evolution of the microstructural void ration with total suction, and (b) evolution of the drying yield total suction with microstructural void ratio. ....	94
Fig. 4.6:	Proposed model for the water retention behaviour of the bentonite material based on the anisotropic hardening behaviour. ....	95
Fig. 4.7:	Representation of the model to take into account the evolution of the drying yield suction with microstructural void ratio. ....	97
Fig. 4.8:	Calibration of the water retention model with experimental results of Wyoming granular bentonite at (a) poured state ( $e = e_0 = 0.83$ ), and (b) compacted state ( $e = 0.53$ ). ....	98
Fig. 4.9:	Simulation of the retention behaviour of Wyoming granular bentonite compacted at $e = 0.66$ corresponding to dry density of $1.65 \text{ Mg/m}^3$ . ....	98
Fig. 4.10:	(a) Calibration of the model for the microstructural parameters, and (b) simulations of the wetting and scanning path B – B' of Wyoming granular bentonite compacted at $e = 0.53$ corresponding to dry density of $1.80 \text{ Mg/m}^3$ . ....	99
Fig. 5.1:	General view of the THM triaxial system and its associated parts. ....	104
Fig. 5.2:	Schematic layout of the double-wall triaxial cell for testing in unsaturated conditions. ....	105
Fig. 5.3:	(a) Experimental setup for application of the axis translation technique, and (b) special cap for the application of the axis translation technique. ....	105
Fig. 5.4:	Initial and final configurations of the cell in a loading step. ....	107
Fig. 5.5:	Free body diagrams at static equilibrium for different components of the inner-cell system. ....	108
Fig. 5.6:	Evaluation of the stress resulted from tubing connections and frictional force in the loading piston. ....	108
Fig. 5.7:	Force-displacement behaviour of the components of the system in axial loading: (a) upper component,(b) lower component and (c) the porous metallic disc. ....	109
Fig. 5.8:	Measured and corrected force – displacement curve of the PVC sample under axial loading. ....	110
Fig. 5.9:	Geometrical evolution of the inner-cell system due to the loading step and deformation of the sample. ....	111
Fig. 5.10:	Calibration test for the sample volume change: (a) sample volume change in the absence of axial displacement, and (b) volume change of the sample at undrained loading conditions. ....	112

Fig. 5.11:	Apparent volume change of the inner-cell with inner-cell pressure. ....	113
Fig. 5.12:	Correlation between the applied temperature and the sample temperature. ....	113
Fig. 5.13:	Evolution of the inner-cell volume with temperature of the sample. ....	114
Fig. 5.14:	THM loading mechanisms on bentonite barriers in high-level radioactive waste deep geological repositories. ....	115
Fig. 5.15:	Free volume swelling and retention behaviour of granular bentonite material: (a) evolution of the void ratio vs. suction, (b) corresponding water retention behaviour, and (c) visual observation of the swelling at different points along the retention curve. ....	119
Fig. 5.16:	Compaction of the swollen granular bentonite material to the target dry density of 1.5 Mg/m <sup>3</sup> . ....	120
Fig. 5.17:	(a) Experimental setup to saturate the bentonite sample under constant volume conditions, (b) swelling pressure developed during the saturation, (c) unsaturated core of the sample after 5 days, and (d) fully saturated sample after 18 days. ....	121
Fig. 5.18:	Samples prepared for unsaturated and saturated triaxial testing.....	122
Fig. 5.19:	(a) Variation of the water content along the height of the unsaturated sample, and (b) variation of the void ratio of the saturated sample along the height. ....	122
Fig. 5.20:	Evolution of the radial and axial swelling stresses during the swelling phase in the triaxial cell. ....	125
Fig. 5.21:	Derivation of the theoretical failure time in drained triaxial tests from the isotropic consolidation behaviour.....	125
Fig. 5.22:	Extension loading behaviour of the rubber membrane (NBR) used in this study.....	126
Fig. 5.23:	Thermo-mechanical stress path at controlled suction or fully saturated triaxial testing conditions (adapted from Cekerevac & Laloui 2004).....	127
Fig. 5.24:	(a) Influence of the total suction on the isotropic behaviour of Wyoming granular bentonite, (b) variation of degree of saturation in unsaturated tests, and (c) corresponding path for unsaturated tests in water retention plane.....	129
Fig. 5.25:	Deviatoric behaviour of Wyoming granular bentonite: (a), (b) influence of confining stress at $\psi = 100$ MPa, and (c), (d) influence of confining stress at $\psi = 50$ MPa.....	131
Fig. 5.26:	Deviatoric behaviour of Wyoming granular bentonite: (a), (b) influence of confining stress at $\psi = 20$ MPa, and (c), (d) influence of confining stress at saturated conditions. ....	133
Fig. 5.27:	Influence of total suction on the deviatoric behaviour of Wyoming granular bentonite. ....	133
Fig. 5.28:	Influence of the suction and mean total stress on the deviatoric stress at failure of Wyoming granular bentonite. ....	134
Fig. 5.29:	Evolution of the yield surface and Critical State Line (CSL) in the hardening plasticity approach: (a) suction hardening, and (b) strain hardening.....	134
Fig. 5.30:	Failure modes under deviatoric loading at different controlled suction tests. ....	135

Fig. 5.31:	Influence of temperature on the controlled suction volumetric strain behaviour of granular bentonite.....	137
Fig. 5.32:	Influence of temperature on the controlled suction deviatoric behaviour of compacted granular bentonite.....	137
Fig. 5.33:	Simultaneous influence of thermal softening and strain hardening on the yield surface.....	138
Fig. 5.34:	Deviatoric failure modes of compacted Wyoming granular bentonite samples under a total suction of $\psi = 20$ MPa and at different temperatures: (a) under $p = 500$ kPa, and (b) under $p = 2000$ kPa. ....	139
Fig. 5.35:	Evolution of thermal volumetric strains of the saturated sample at applied temperatures.....	139
Fig. 5.36:	Influence of temperature on the volumetric strain behaviour of granular bentonite at saturated conditions. ....	140
Fig. 5.37:	Influence of hydraulic gradient and temperature on the hydraulic conductivity. ....	140
Fig. 6.1:	Shot-clay experiment carried out at the GTS.....	144
Fig. 6.2:	Sampling of the shot-clay Wyoming bentonite: (a) installation of the steel sampling tubes on the tunnel wall, (b) shooting of the mixture of water and bentonite into the tubes, and (c) extracted tube containing the sample. ....	145
Fig. 6.3:	Results of the MIP test on a sample of Wyoming shot-clay bentonite: (a) cumulative void ratio, and (b) pore size density function ( <i>PSD</i> ) vs. pore size diameter. ....	146
Fig. 6.4:	Schematic layout of the experimental setup for the controlled hydro-mechanical test. ....	148
Fig. 6.5:	Shot-clay emplaced before different stages of the construction of the engineered barrier systems- ....	150
Fig. 6.6:	Stress path implemented for the investigation of the hydro-mechanical behaviour of the shot-clay Wyoming bentonite.....	151
Fig. 6.7:	Results of the swelling tests: (a) swelling pressure evolution vs. time under constant volume conditions, and (b) swelling heave and water content evolution under free swelling conditions.....	151
Fig. 6.8:	(a) Void ratio vs. suction for drying path in shot-clay Wyoming bentonite material, (b) retention behaviour of shot-clay Wyoming bentonite in terms of water content, and (c) degree of saturation. ....	152
Fig. 6.9:	Variation of the water content and axial strain of the specimen during the different steps of the applied stress path shown in Fig. 6.6. ....	153
Fig. 6.10:	Results of the controlled suction hydro-mechanical test. ....	154
Fig. 6.11:	Observation of the specimen after opening the cell at the end of different steps: (a) drying due to step B – C, (b) wetting due to step D – E, and (c) full saturation due to step E – F.....	154
Fig. 6.12:	Swelling pressure development during the wetting phase: (a) step D – E, and (b) step E – F in Fig. 6.6. ....	155

- Fig. 6.13: Comparison between the results of the MIP test on a sample of shot-clay Wyoming bentonite and a sample of compacted granular Wyoming bentonite. .... 156
- Fig. 6.14: Swelling pressure vs. initial dry density under constant volume conditions for compacted and shot-clay Wyoming bentonite samples. .... 157
- Fig. 6.15: Comparison of the retention behaviour of shot-clay and the compacted Wyoming bentonite compacted at different initial dry densities. .... 157



# **1 Bentonite, buffer and disposal of high level nuclear waste: an introduction**

## **1.1 General introduction**

### **1.1.1 Disposal of high level nuclear wastes (HLW)**

Embedded in the legal mandate by the Federal government, it is Nagra's mission to develop and implement safe geological repositories in Switzerland for all nuclear waste arising from the use of nuclear energy and from medicine, industry and research (Nagra 2009). Two types of geological repositories are foreseen, one for low and intermediate level waste (L/ILW) and one for spent fuel (SF), vitrified high level waste and long-lived ILW (in this report simply termed "HLW"). The Swiss concept of deep geological disposal of HLW is based on a multiple barrier system, consisting of an Engineered Barrier System (EBS) and the geological barriers (Nagra 2002, Leupin et al. 2016). The principal EBS components of the HLW emplacement rooms are (i) the spent fuel assemblies (SF) / glass matrix (vitrified HLW), (ii) the metallic canisters and (iii) the bentonite backfill, which is surrounded by a tight argillaceous host rock formation (Opalinus Clay).

The metallic canister is made of stainless steel or copper, contributing to the long-term safety functions by confinement of the HLW and attenuation of the radionuclide releases. The canister is designed for a lifetime of to 10'000 years and is expected to fail in the long-term due to corrosion processes (Leupin et al. 2016). The bentonite backfill ("buffer") contributes to the confinement of the HLW (long resaturation times, self-sealing capacity in response to mechanical damage) and to the attenuation of releases (diffusion dominated transport processes, retardation of radionuclide transport by sorption and low solubility of radionuclides in porewater). The buffer material must have a swelling potential to homogenise the density variations associated with the emplacement process and to self-seal technological gaps or the voids that may form due to movements imposed by external forces or internal interactions (e.g. Pusch 1994, Gens 2010, Ferrari et al. 2014). The buffer has to provide enough thermal conductivity to account for the dissipation of the heat from the canister in order to limit the near-field temperature (Leupin et al. 2016).

In several repository concepts (e.g. in Sweden, Spain and Switzerland), bentonite and more precisely smectite-based clays, are proposed as the most suitable materials for the buffer. The buffer material should be emplaced at densities in the range of 1.45 – 1.9 Mg/m<sup>3</sup> to ensure that the transport of dissolved species and water takes place upon a diffusion process and not flow (Pusch & Karnland 1996). In the Swiss concept, a Wyoming bentonite is used as a reference material in the form of compacted blocks to sustain the canister and in granular form to fill the upper gaps between the waste container and the host rock. The required emplacement density is < 1.45 Mg/m<sup>3</sup> to prevent any microbial activity in the immediate vicinity of the metallic canisters (Leupin et al. 2016).

The host rock represents the key component of the geological barrier, ensuring the mechanical stability of the backfilled underground structures and controlling the water saturation of the bentonite buffer. Strong attenuation of radionuclide release is facilitated by the low hydraulic conductivity of the rock (diffusion dominated transport), by its sorption capacity and by efficient colloid filtration (e.g. Nagra 2002). In this context, the Excavation Damaged Zone (EDZ) represents a transitional zone between the EBS and the intact host rock, which is characterised by significant irreversible processes (e.g., brittle failure in response to the excavation process) and significant changes in flow and transport properties (Tsang et al. 2005).

In the Swiss disposal programme the Opalinus Clay has been selected as the preferred host rock, constituting an overconsolidated Jurassic claystone. A generic layout of the Swiss concept for a HLW repository is given in Fig. 1-1 (Leupin et al. 2016).

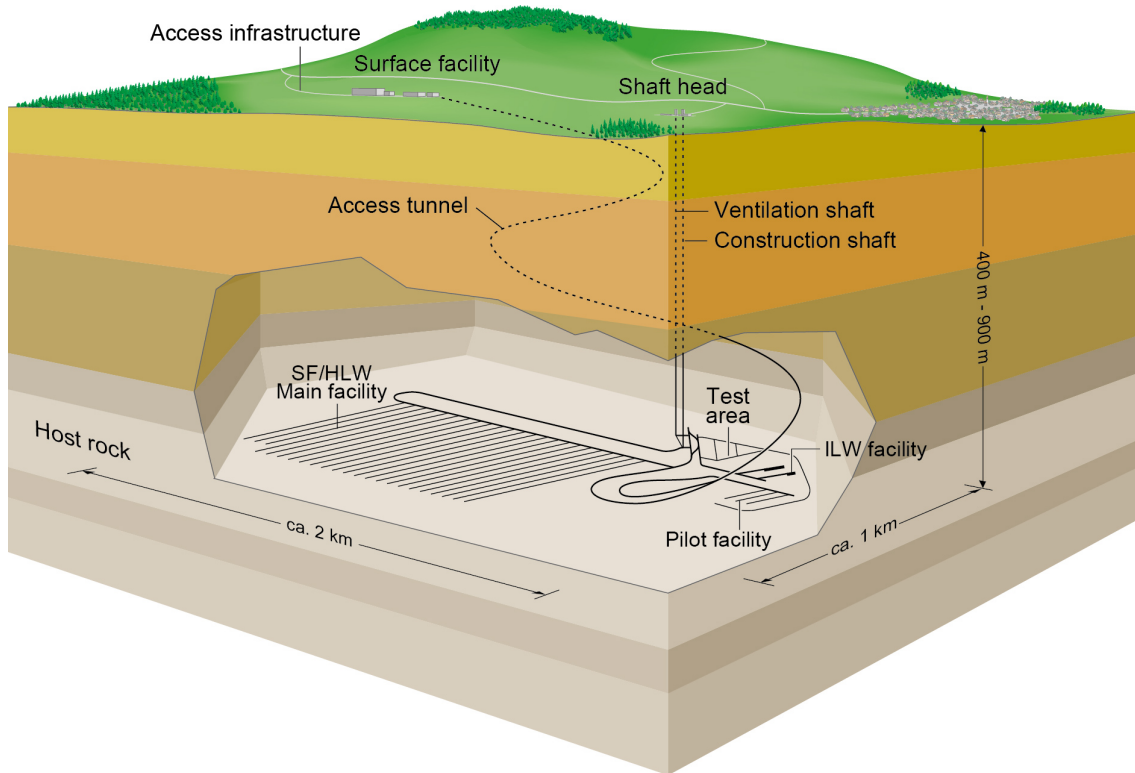


Fig. 1-1: Example layout of the HLW repository with its main features (not drawn to scale):

Main facility (i.e. the emplacement rooms, in which the radioactive waste will be emplaced), pilot facility with representative amounts of the disposed radioactive waste, test area, also called facility for underground geological investigations (FUGI), central area and various types of seals at different locations within the underground tunnel system (after Leupin et al. 2016).

Nagra's current repository concept uses a cementitious liner to support walls of the emplacement rooms and access tunnels, designed to withstand the highest mechanical loads expected to arise during the construction and operational phases (Leupin et al. 2016). To avoid any hydraulic shortcuts along the walls of the SF and HLW emplacement rooms that could arise from the degradation of the liner, and to comply with the principle of compartmentalisation, intermittent sealing sections comprised of granular and preformed bricks of buffer material are emplaced at regular intervals along the rooms, about one for every 10 canisters, to provide a hydraulic barrier. There is no liner where these sealing sections are emplaced, so that bentonite forms a watertight contact directly with the Opalinus Clay. The concept is illustrated in Fig. 1-2.

The stability of the entire repository during its foreseen lifetime has to be analysed where the buffer plays an important role for the mid-term safety of the system (Güven 1990). The buffer material will be subjected to drastic changes in total suction, temperature and mechanical stresses and such thermo-hydro-mechanical (THM) loading has a significant impact on bentonite behaviour.

This study has been the subject of a PhD thesis at EPFL (Lausanne), successfully completed in April 2014 (Seiphooiri 2014). The work was motivated by the challenging task of characterising, understanding and modelling the behaviour of Wyoming granular bentonite used as buffer material in response to coupled THM processes, associated with the disposal of HLW in Switzerland.

The following section describes the demanding subjects associated with the evolution of the bentonite in repository circumstances upon THM loading conditions. These topics establish the main objectives of this thesis.

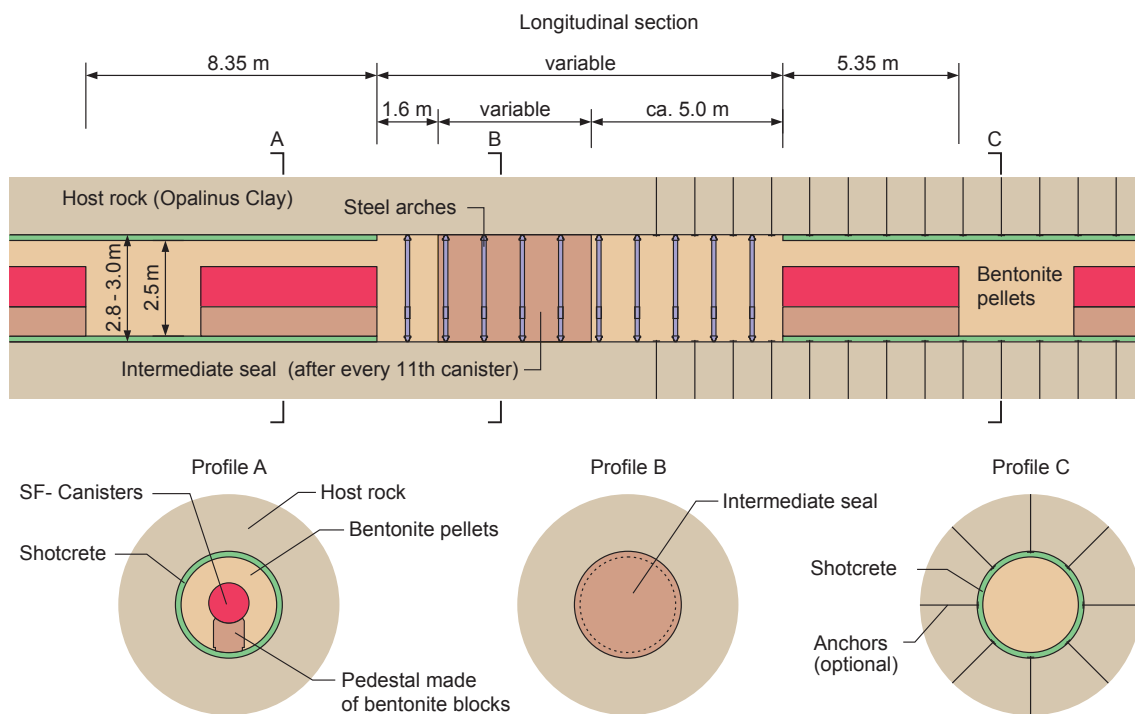


Fig. 1-2: Schematic sketch of a HLW emplacement room with the compartmentalisation concept adapted from Leupin et al. (2016).

Compartmentalisation is provided by a hydraulic barrier at every 11th canister position. This hydraulic barrier is designed to prevent any lateral flow along the emplacement tunnel, which could otherwise occur through degraded cement liners used for stabilising the emplacement tunnel during the construction and operational phase.

### 1.1.2 Evolution of the buffer material

A model of the repository system including the canisters, bentonite and host rock is presented according to the Swiss concept in Fig. 1-3a. Bentonite material in the repository would evolve due to the impact of several factors such as: swelling, local density redistributions, wetting/drying cycles, fabric evolution during hydration/dehydration, deviatoric behaviour and the influence of temperature during the heat emission process. These aspects (illustrated in Fig. 1-3b) are detailed in the following subsections.

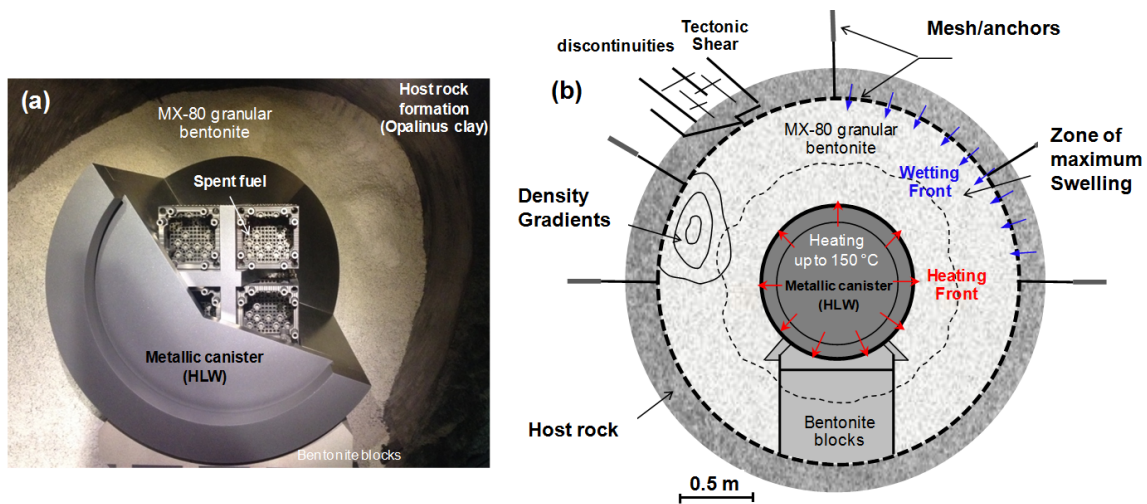


Fig. 1-3: Evolution of the bentonite in the emplacement rooms of a HLW repository:

- (a) Physical model of the Swiss emplacement concept at Mont Terri, Switzerland, and  
 (b) THM phenomena and processes in the HLW near-field (modified from García-Siñeriz et al. 2008).

### 1.1.2.1 Swelling pressure/potential

The emplacement of the bentonite would mostly be at its hygroscopic water content and under a confined condition. The progressive saturation of the buffer upon uptake of water from the host rock would result in the development of swelling pressures. On the other hand, the bentonite could freely swell and fill the technological gaps and other voids formed in the system (Wang et al. 2013, Ferrari et al. 2014). One of the primary tasks of bentonite is to heal such unexpected voids during the construction of the barriers or due to the local loss of the material upon erosion or desiccation cracks in the mid-term. In this regard, evaluation of the swelling potential of the bentonite upon hydration is an important subject.

### 1.1.2.2 Density gradient and compressibility

Although the emplacement of the bentonite would be in the repository under a target dry density, the development of swelling pressure around the surrounding host rock could cause density redistributions within the buffer (e.g. Villar et al. 2005). A zone with the maximum swelling pressure where the wetting would first take place (see Fig. 1-3) could be established that would harden the internal bentonite layers and consequently result in a density gradient in the system. In addition, there would already be a density gradient between the blocks and the adjacent granular bentonite even after the emplacement, since the blocks have higher densities than the emplaced granular bentonite. The influence of such density gradients needs to be well understood in terms of the hydro-mechanical response of the buffer material. Furthermore, due to this internal process upon the hydration of the bentonite at different scales and the tectonically induced stresses, it is important to evaluate the compressibility behaviour of the buffer under saturated and unsaturated conditions.

### 1.1.2.3 Water retention and wetting/drying cycling

Bentonite barriers would be subjected to wetting and drying cycles due to the environmental conditions and the heat generated from the waste canisters. A full analysis of the water retention behaviour of bentonite is required as the key point of the possible hydro-mechanical couplings of the buffer material. An improved understanding of the importance of the void ratio variation, confinement and the wetting/drying cycle on the water retention behaviour of the bentonite is needed to assess the long-term behaviour of the buffer upon the imposed hydro-mechanical conditions.

### 1.1.2.4 Fabric and microstructure

The interaction between the bentonite microstructure and hydration/dehydration at different stages of the hysteresis water retention behaviour must be analysed. The change in fabric could have a significant impact on the macroscopic response of the buffer in terms of water retention and transport behaviours. Although the hydration mechanisms of the smectite minerals and the evolution of interlayer porosity have been already analysed (e.g. Saiyouri et al. 1998, Villar et al. 2007, Nagra 2014), this information has not yet been integrated into the analysis of the water retention of the bentonite subject to wetting-drying cycles. The appearance of the Wyoming granular bentonite material at macroscopic scale is presented in Fig. 1-4a. The photomicrographs describing a significant modification of the fabric after cycles of wetting and drying are also shown in Fig. 1-4b and c. Further analysis is required to investigate how these evolutions of the fabric at the microscale could influence the macroscopic behaviour of the bentonite and its performance as a buffer element. More investigation is also required to analyse the porosity distributions at different density levels that characterise the transport behaviour of the buffer material (e.g. Pusch & Schomburg 1999, Holzer et al. 2010, Keller et al. 2014).

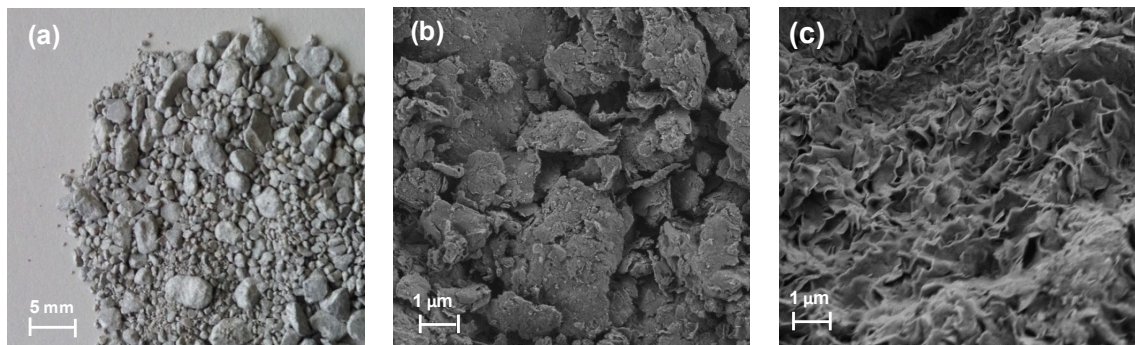


Fig. 1-4: Fabric of Wyoming granular bentonite: (a) appearance of granular bentonite at macroscopic scale; photomicrographs of the material at (b) the as compacted state, and (c) after wetting/drying cycles with significant modification of the fabric.

### 1.1.2.5 Deviatoric and shearing strength

The asymmetric internal hydro-mechanical processes within the bentonite and the tectonically-induced strains resulting from the discontinuities of the external host rock could induce deviatoric loading mechanisms to the buffer material. Tectonic Stresses occur constantly within the earth's crust and induce strains within the local regions containing optimal geological formations. Therefore, understanding the deviatoric failure mechanisms of the bentonite in saturated and unsaturated condition is an important task, particularly where the buffer material

is already confined under high stresses due to internal swelling pressures. However, there is no available information on the deviatoric response of the unsaturated Wyoming bentonite material. One of the reasons could be the shortage of advanced experimental facilities to perform complex hydro-mechanical deviatoric stress paths under wide ranges of total suction and confining stresses. To this end, the shearing response of the buffer needs to be analysed in a systematic procedure involving advanced testing systems, such as triaxial cells, to respond to the need for testing bentonite under repository-like conditions.

#### **1.1.2.6 Influence of temperature**

The temperature in the near-field during heat emission could rise up to 150°C at the canister surface (e.g. De la Fuente 2000, Pusch et al., 2003). The change of mineralogy due to temperature rise could lead to illitisation of the smectite mineral in bentonite material, which can reduce the swelling and water retention capacities of the bentonite. In Leupin et al. (2014) it has been shown that these mineralogical changes are not expected to occur under repository conditions. In terms of macroscopic behaviour, temperature influences the swelling pressure/potential of the buffers and has a significant impact on the hydraulic conductivity of the bentonite. The buffer material would be subjected to heating from the canister and wetting from the host rock, which imposes complex THM stress paths. The level of importance of such thermally-induced behaviours, e.g. plastic strains, should be further evaluated and analysed, preferably in triaxial stress states that provide more realistic stress conditions.

#### **1.1.2.7 Physicochemical and effective stresses**

The effective stress term in bentonite material as the most essential contribution for its constitutive modelling is tightly associated with the stresses originating from the physicochemical activities at a microscopic level (e.g. Sridharan & Rao 1979, Hueckel 1992, Graham et al. 1992). It has also been revealed that the effective stress term is firmly associated with the composition of the pore water (Alonso et al. 2010) particularly for the bentonite, where the main fraction of the pore water is stored through adsorption mechanisms (e.g. Romero & Vaunat 2000). The evolution of the physicochemical stresses and the mutual interactions with the effective stress during different hydro-mechanical actions needs to be further analysed to assess a constitutive framework for the hydro-mechanical analysis of the material.

## **1.2 THM characterisation and modelling of Wyoming granular bentonite**

### **1.2.1 Objectives**

The present report addresses the *THM characterisation and modelling of the behaviour of Wyoming granular bentonite buffer material applied to high-level nuclear waste disposal*. The research was performed in a context dealing with comprehensive experimental characterisations of the macroscopic behaviour of Wyoming granular bentonite under thermo-hydro-mechanical processes. An insight into the microstructure was required in order to interpret the macroscopic observations. This was addressed from both experimental and modelling points of view, leading to the following objectives:

- To provide a comprehensive basis for the hydro-mechanical characterisation and understanding of the behaviour of Wyoming granular bentonite in terms of swelling, compressibility and water retention and to analyse the effects of an emplacement technique on the hydro-mechanical response of the granular bentonite within a practical case study performed at the Grimsel Test Site (GTS, Grimsel URL).

- To provide an insight into the fabric evolution of the bentonite material during the applied hydro-mechanical paths and an analysis of the mutual interactions between the microscopic and macroscopic features.
- To evaluate the thermally-induced strain-stress response of the saturated and unsaturated buffer material and its deviatoric behaviour under a wide range of total suction and confining stresses according to the repository conditions by developing an advanced double-wall triaxial testing system.
- To propose a water retention model to account for the change in the void ratio and the microstructural evolutions during the hydration of the bentonite material as the key points of the hydro-mechanical constitutive modelling.

### 1.2.2 Outline of the report

A systematic approach was used to analyse the THM behavioural features of Wyoming granular bentonite. In particular, the report is presented as follows:

Chapter 2 presents the experimental characterisation of the compressibility, swelling and water retention behaviour of Wyoming granular bentonite. A reference grain size distribution for the granular material is selected and then the hydro-mechanical response of the material is analysed in terms of compressibility behaviour under saturated and unsaturated conditions and swelling capacities. A comprehensive analysis of the water retention behaviour of Wyoming granular bentonite is presented by developing a new technique called '*Micro-cell*'. The influence of the void ratio (dry density), confinement and temperature on the water retention behaviour of the material is studied.

Chapter 3 is devoted to the analysis of the experimental characterisation of the hydro-mechanical behaviour of Wyoming granular bentonite at the microscopic level. The swelling and hydration mechanisms in bentonite material are reviewed with special attention to the microstructural features of active and non-active clays. The behavioural features of the granular bentonite at microscopic scale are investigated in the light of the different microstructural investigation techniques of *Mercury Intrusion Porosimetry* (MIP), *Scanning Electron Microscopy* (SEM) and *Focused Ion Beam nanotomography* (FIB-nt). An insight is presented into the mutual interaction of the microstructural evolution and the macroscopic response in terms of water retention behaviour. The microstructural evolution of compacted Wyoming bentonite and illite clays are associated with the water retention behaviour that provides an interesting picture for the interaction between the microstructure and macroscopic behaviour of active and non-active clays.

Chapter 4 proposes a conceptual model for the water retention curves of Wyoming granular bentonites following the experimental observations on both macroscopic and microscopic behavioural features presented in Chapter 2 and Chapter 3. The model is based on an elasto-plasticity framework that uses a linear anisotropic hardening rule. It is then extended to account for the microstructural evolution during the different hydration phases in a water retention path.

Chapter 5 investigates the thermo-hydro-mechanical analysis of Wyoming granular bentonite by introducing and developing an advanced double-wall triaxial cell. Based on the primary hydro-mechanical analyses presented in Chapter 2, particular sample preparation and testing procedures for saturated and unsaturated conditions are proposed in this chapter. The volumetric and deviatoric behaviour of the material is analysed under a wide range of total suctions, confining stresses and temperatures. This chapter provides a global view of the behaviour of Wyoming granular bentonite subjected to the THM loading states associated with the repository conditions.

Chapter 6 reports the results of an experimental study carried out to characterise the hydro-mechanical behaviour of shot-clay Wyoming bentonite. Shot-claying is considered as an alternative emplacement technique to avoid preferential water and/or gas flow along the walls of the repository tunnel. The expected behaviour of the shot-clay bentonite when subjected to the environmental conditions in the repository was determined. The test results were compared with data on the observed behaviour of compacted Wyoming granular bentonite to assess the effects of the shot-clay emplacement technique on the behaviour of Wyoming granular bentonite.

Chapter 7 finally presents the concluding remarks of the present thesis and proposes a perspective for future studies on the characterisation and modelling of Wyoming bentonite material.

## 2 Experimental characterisation of the compressibility, swelling and water retention behaviour of Wyoming granular bentonite

This chapter is devoted to the experimental characterisation of the compressibility, swelling and water retention behaviour of Wyoming granular bentonite. The outline of this chapter is as follows: first, the description of the tested material in terms of grain size distribution and index properties is presented. The sample preparation procedure for the granular material is introduced considering the maximum grain size limitation for the experimental purposes. The effects of the compaction and hydration on the apparent grain size distribution are analysed. A general sample preparation technique is described and respected for all experiments carried out in this research.

The chapter is continued by analysing the hydro-mechanical behaviour of the granular bentonite in terms of swelling pressure, the saturated and unsaturated compressibility response and finally the water retention behaviour. The state of the art of the hydro-mechanical response of unsaturated geomaterials particularly the bentonite-based clays are integrated in this chapter.

The swelling behaviour under free and confined conditions is evaluated and the influence of the total suction on the compression indices is studied. A comprehensive analysis of the water retention behaviour of the material by developing a new technique called '*Micro-cell*' has been carried out. The influence of the void ratio (dry density), confinement and temperature on the water retention behaviour of the material is evaluated. Considering the particular application of compacted granular bentonite as sealing and buffer material in the vicinity of the waste canisters, a wide range of total suction is considered throughout the water retention and the volumetric behaviour analyses.

### 2.1 Tested material

#### 2.1.1 Wyoming granular bentonite

Wyoming bentonite (and more generally bentonite) refers to a clay material whose major mineralogical component is established by the smectite group. The name comes from its occurrence which is in the Cretaceous Fort Benton unit in Wyoming, USA (Montanez 2002). Smectite mineral is categorised as active clay with high swelling potential. As a result, bentonite is a highly swelling material. Most bentonites are either sodium or calcium-based minerals characterised by the type of exchangeable cations. These cations are adsorbed to the surface of the clay particle during the formation or treatment of the mineral (Pusch & Yong 2006). Further discussions with respect to the mineralogical and microstructural features of smectite clays are given in Chapter 3.

In the context of nuclear waste disposal, sodium bentonite is more widely used due to its high swelling capacity and its very low water hydraulic conductivity. The Wyoming granular bentonite is a Na-smectite-based bentonite planned to be used as buffer material in the Swiss concept for nuclear waste storage (Rometsch et al. 1985, Nagra 2003, Plötze & Weber 2007, Teodori et al. 2011).

In order to fabricate the granular bentonite, Wyoming bentonite is first broken up to a powder state, dried and highly compressed. The compacted bentonite units are produced during a pelletisation process in which the bulk dry density at a water content of 5 – 6 % is increased from 1.17 Mg/m<sup>3</sup> up to 2.10 Mg/m<sup>3</sup>. Then, the big units are broken up and the coarse fractions (grains bigger than 1.5 mm) are rounded by pushing the material through a 100 – 200 m long steel pipe using air pressure. The rounding is carried out to improve the flowability and grain

size distribution (Plötze & Weber 2007). The granular material is delivered to the Laboratory for Soil Mechanics (LMS) under the label 'Mixture E' processed for experimental purposes (Teodori et al. 2011).

## 2.1.2 Grain size distribution

### 2.1.2.1 Sieve analysis

The envelope of the grain size distribution of the material planned to be used in repositories is shown in Fig. 2.1. The discrepancy between the delivered material and the site material is associated with the segregation which occurred during the transportation of the material to the laboratory. The average uniformity coefficient,  $C_U$  of 31.07 and the average curvature number,  $C_c$  of 2.91, have been reported for the site material (Teodori et al. 2011). The minimal emplacement dry density was found to be in the range of 1.47 – 1.49 Mg/m<sup>3</sup> and the maximal emplacement density in the range of 1.68 – 1.70 Mg/m<sup>3</sup>. Possible heterogeneities of the fill dry density and its range were obtained from emplacement trial tests performed in a full-scale tunnel. In additional tests performed prior to the emplacement, the average 'drop' density of the fill was reported as 1.46 Mg/m<sup>3</sup>, with maximum and minimum values of 1.52 and 1.28 Mg/m<sup>3</sup>, respectively. A target dry density of 1.5 Mg/m<sup>3</sup> has been considered in the context of the EB experiment for the final emplacement of the material (Nagra 2003)<sup>1</sup>.

### 2.1.2.2 Hydrometric analysis

Determination of the grain size distribution of the bentonite below 63 µm was reported by Plötze & Weber (2007) through a hydrometric analysis. A sedimentation method according to Stokes' law using 0.01 % calgon solution was carried out on 5 g of the air-dried bentonite and the average results based on 8 repeated tests were reported as seen in Tab. 2.1.

Tab. 2.1: Grain size distribution (hydrometric analysis, Plötze & Weber 2007).

Fraction	> 63 µm	< 20 µm	< 2 µm
Wyoming Bentonite	3.30 %	92.51 %	87.44 %

### 2.1.3 Grain size distribution selected for sample preparation

The reference grain size distribution of the tested material used for sample preparation of different experiments in this research is shown in Fig. 2.1. The maximum grain size of 4 mm was selected for all the experiments due to the limitation considered for the sample dimensions. The granular bentonite with this reference grain size distribution curve was found to have enough pourability under hygroscopic condition ( $T = 22$  °C and  $RH = 34$  %) to reach this target density (1.5 Mg/m<sup>3</sup>) without any compaction.

To prepare a sample at a given void ratio, different grain size fractions of the granular material were mixed according to the reference grain size distribution. The fractions are the dry sieved parts of 4, 2, 1, 0.5, 0.25, 0.125 and 0.064 mm opening (mesh sieves according to DIN 4188) as shown in Fig. 2.2. The granular material then is mixed thoroughly and compacted to the target

<sup>1</sup> In the recent reference concept for the HLW near-field the target dry density of the bentonite buffer should be above 1.45 Mg/m<sup>3</sup> (Leupin et al. 2016)

void ratio (dry density) for the experimental purposes (Fig. 2.2). The curvature coefficient,  $C_c$ , and uniformity coefficient,  $C_u$ , of the tested material are also presented in Fig. 2.1. This granulometry was respected for all experiments including swelling potential, static compaction, oedometric consolidation, water retention and also thermo-hydro-mechanical triaxial experiments (Chapter 5).

The possibility of segregations due to sample preparation was evaluated. The visual observation for the segregation of the granular material can be realised in Fig. 2.3a in the absence of the fine fraction (grains smaller than 0.25 mm), while the material looks more homogeneous for the full range of the grain size fractions (Fig. 2.3b).

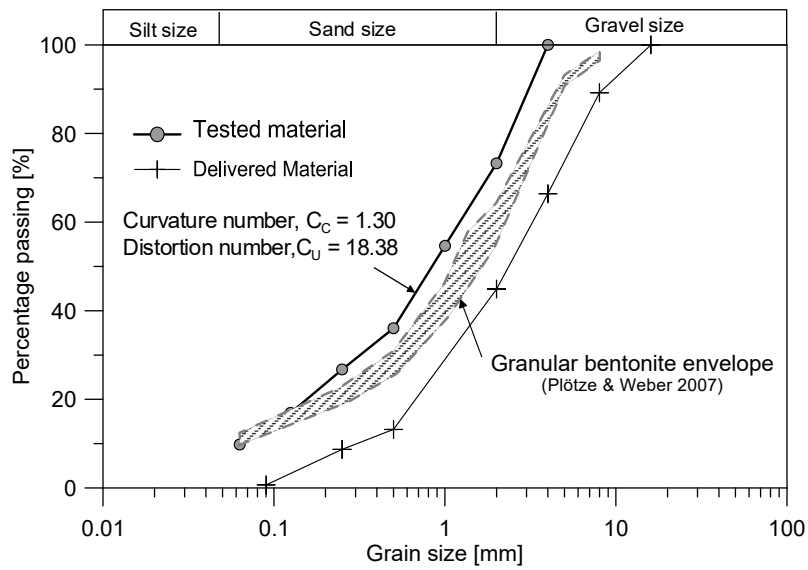


Fig. 2.1: Grain size distribution curves of the tested material.

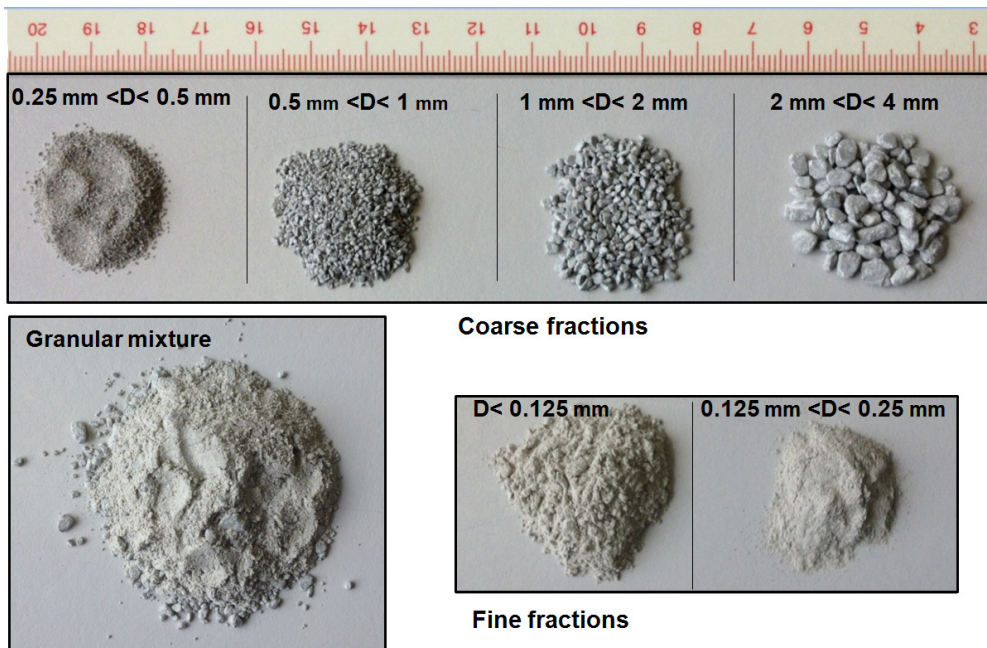


Fig. 2.2: Different grain size fractions of the granular Wyoming bentonite.

In order to check the homogenisation of the samples, random samples from thoroughly mixed granular material were selected and the grain size distribution was analysed. As seen in Fig. 2.4, the grain size distributions were obtained identical to the reference curve that confirms the homogeneity of the material in terms of grain size distribution. An insight into the fabric of the granular material (Chapter 3) shows that bentonite grains (coarse fractions indicated in Fig. 2.2) are coated by the bentonite aggregates (the main part of the fine fractions indicated in Fig. 2.2). The coating of the grains prevents their movement and consequently the segregation of the granular material is minimised.

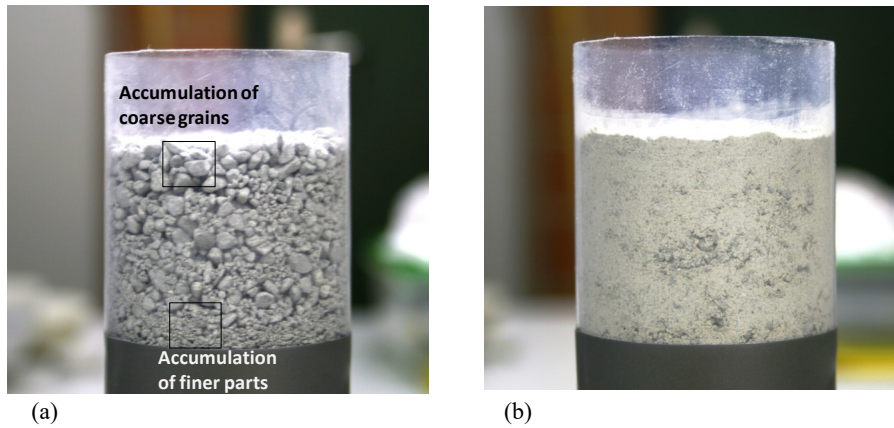


Fig. 2.3: Segregation test of the granular material: (a) without fine fractions (smaller than 0.25 mm), and (b) full curve.

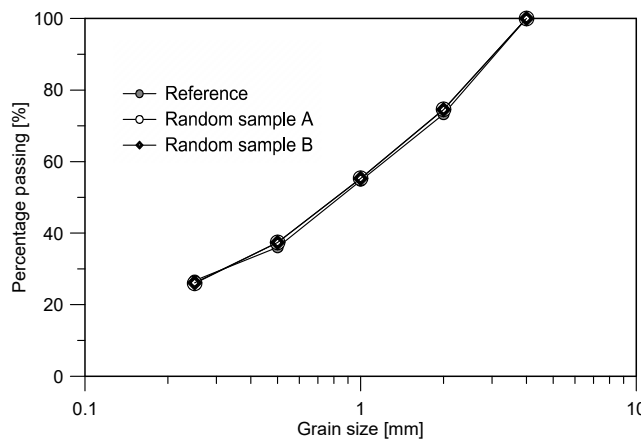


Fig. 2.4: Apparent grain size distribution of the randomly selected granular samples.

### 2.1.3.1 Effect of static compaction and hydrations on grain size distribution

In Fig. 2.5, the influence of compaction on the grain size distribution at hygroscopic condition is analysed using the standard proctor and the static compaction tests. It is seen that the compaction does not have a remarkable influence on the apparent grain size distribution. The effect of hydration was also investigated by applying a wetting/drying cycle on the granular material. The material was first wetted up to a water content of about  $w = 0.40$  in free condition. The hydration of the material was performed up to 0.30 through the vapour phase by placing the

material in a humid chamber ( $RH = 100\%$ ). Further wetting up to  $w = 0.40$  was performed using a pressure plate apparatus (introduced in section 2.4.3.5). The material reached a relative humidity of 98% upon this water content. The sieve analysis then was carried out after the material was air-dried under laboratory conditions ( $T = 22^\circ\text{C}$ ,  $RH = 34\%$ ). This wetting/ drying cycle resulted in the creation of more fine fractions that implies a crushing and splitting process in larger grains as seen in Fig. 2.6.

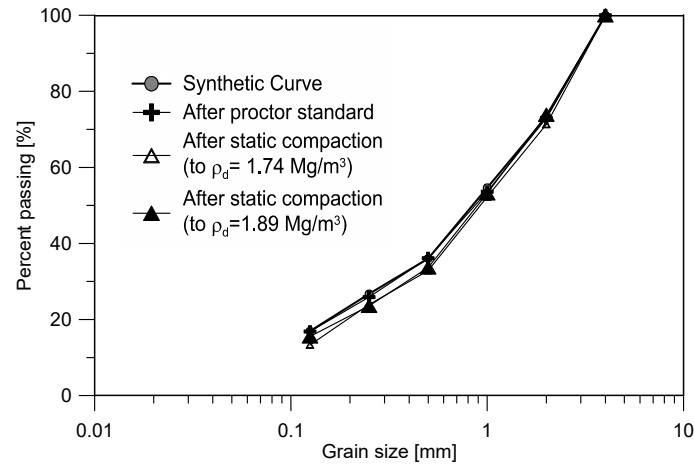


Fig. 2.5: Influence of compaction on the apparent grain size distribution of granular bentonite.

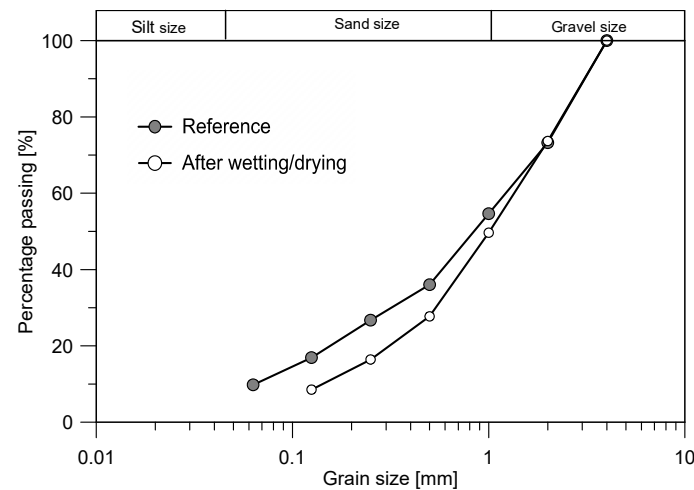


Fig. 2.6: Influence of wetting/drying cycle on the apparent grain size distribution of granular bentonite.

#### 2.1.4 Index properties

The index properties of the granular bentonite were determined in the laboratory. A specific gravity  $G_s = 2.74$  was measured with a pycnometer, using kerdane rather than water (because its non-polarity prevents the development of diffuse double layers). Kerdane is a commercial name of an oil from which aromatics are extracted. It can be substituted with any paraffin oil, like kerosene (Péron et al. 2007). A liquid limit of  $w_l = 420\%$  was measured using the fall cone penetration technique (BSI 1990, Wood 1985). A plastic limit of  $w_p = 65\%$  was determined

according to ASTM D4318. The physical properties of the granular material are summarised in Tab. 2.2. The total suction of 148 MPa was measured under hygroscopic condition using a dew-point chilled-mirror psychrometer (WP4C, Decagon Device, Inc. 2002).

Tab. 2.2: Summary of general physical properties of the tested Wyoming granular bentonite.

Smectite content [%] *	Specific gravity $G_s$	Specific surface area $s$ [ $\text{m}^2/\text{g}$ ] †	Liquid limit $w_l$ [%]	Plastic limit $w_p$ [%]	Hygroscopic water content ( $T = 22\text{ }^\circ\text{C}$ , $RH = 34\%$ ) $w_0$ [%]
85	2.74	523	420	65	5.4

\* Reported by Teodori et al. (2011)

† Plötze & Weber (2007)

## 2.2 Swelling and compressibility behaviour

Bentonite used in the engineered barrier system for the disposal of high-level wastes would be subjected to different hydro-mechanical stress paths. The bentonite material will be emplaced under unsaturated conditions. Since the material will be under confined condition, the saturation from the host rock formation will result in the development of swelling pressures.

The bentonite barrier would be also subjected to the heat generated from the waste canisters. Understanding the hydro-mechanical behaviour of bentonite in terms of swelling, compressibility, water retention behaviour and the influence of temperature on these terms is an essential key point for analysing the long-term performance of the repository system. In the following section, first the general conclusions from the past research carried out on the swelling and compressibility of swelling clays are presented. The reported influence of temperature on the hydro-mechanical behaviour of saturated clays and particularly bentonite materials is presented as well. Then the hydro-mechanical behaviour of Wyoming granular bentonite will be analysed and interpreted in terms of swelling potential and compressibility under oedometric conditions. The water retention behaviour and the influence of temperature on the retention capacity of Wyoming bentonite will be analysed in a separate section.

A comprehensive analysis of the hydro-mechanical triaxial behaviour of compacted bentonites and the influence of temperature will be presented in Chapter 5 using an advanced triaxial testing system.

### 2.2.1 Hydro-mechanical behaviour of compacted swelling clays

The hydro-mechanical behaviour of compacted swelling clays with regard to the swelling capacity and compressibility behaviour at ambient temperature has been studied by various researchers (e.g. Bucher & Mayor 1989, Komine & Ogata 1994, Delage et al. 1998, Al-Mukhtar et al. 1999, Villar 1999, Lloret et al. 2003, Cuisinier & Masrouri 2005, Hoffmann et al. 2007, Villar & Lloret 2008, Nowamooz & Masrouri 2009, Nowamooz et al. 2012).

A common conclusion from these works is that the suction has an important influence on the mechanical properties of the swelling material. The higher the suction, the higher the yield stresses. The compressibility indices of the unsaturated clays exhibit an increase with decreasing suction.

For swelling clays, during a wetting path, swelling behaviour is observed under low stresses and collapse behaviour is registered under high stresses.

In bentonites the swelling pressure upon wetting under constant volume conditions has been reported to increase with dry density in an exponential form (e.g. Komine & Ogata 1994, Villar & Lloret 2008). A slight increase of swelling pressure with a decrease in initial water contents is reported by Villar & Lloret (2008) for compacted bentonites.

The influence of temperature on the mechanical behaviour of saturated clays has been well analysed by various studies (e.g. Campanella & Mitchell 1968, Baldi et al. 1988, Hueckel & Baldi 1990, Kuntiwattanukul et al. 1995, Del Olmo et al. 1996, Delage et al. 2000, Sultan et al. 2002, Cekerevac & Laloui 2004, Hueckel et al. 2009, Cekerevac & Laloui 2010).

In general, it has been reported that the heating may result in the expansion (dilation) of the saturated clays under low stress or high overconsolidation ratios (OCR). Contraction behaviour has been observed under high stress or low OCR. The compressibility indices were found to be independent of the temperature and the yield stress decreases with an increase in temperature. To explain this behaviour, two mechanisms that control the volumetric response of the saturated clays during heating were described by Cui et al. (2000): (1) expansion of soil constituents including solid and liquid and (2) weakening of the mechanical contacts between soil aggregates. The thermal expansion of the material at low stresses is associated with the expansion of the soil constituents and the thermal contraction is related to the mechanical weakening of the contacts at high stresses.

Villar & Lloret (2004) and Villar et al. (2010) investigated the influence of temperature on the hydro-mechanical behaviour of compacted FEBEX bentonites in an oedometric condition. A reduced swelling strain during wetting under constant vertical stress was observed at higher temperatures as well as for the constant volume swelling pressure. The influence of temperature on the constant volume swelling pressure for FEBEX bentonite reported by Villar et al. (2010) is shown in Fig. 2.7. The swelling pressure is decreased by 50 % with an increase in temperature from 30 to 80 °C. Ye et al. (2012) have reported similar trends on the influence of temperature on the swelling pressure of GMZ01 bentonites (75.4 % Na-smectite content). Tang et al. (2008) developed an isotropic cell capable of performing suction and temperature controlled tests. Experiments on compacted Wyoming bentonite under a wide range of total suction, temperature and stress were performed. It was observed that the heating has induced expansion under low pressure and high total suction. At low total suctions and high pressures heating resulted in a contractive behaviour.

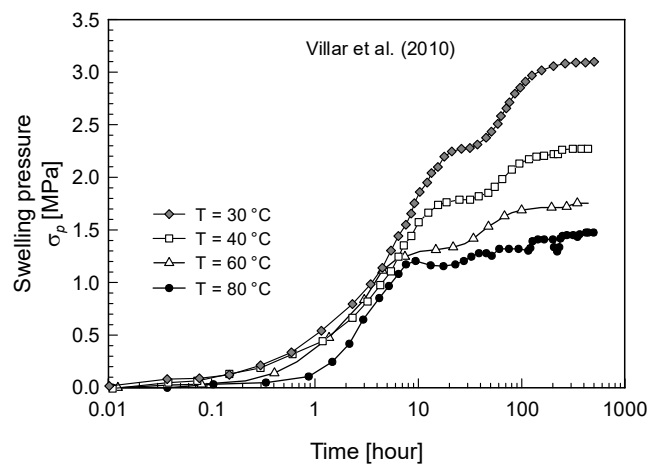


Fig. 2.7 Effect of temperature on the evolution of the swelling pressure with time for compacted FEBEX bentonite samples at a dry density of  $1.5 \text{ Mg/m}^3$  (Villar et al. 2010).

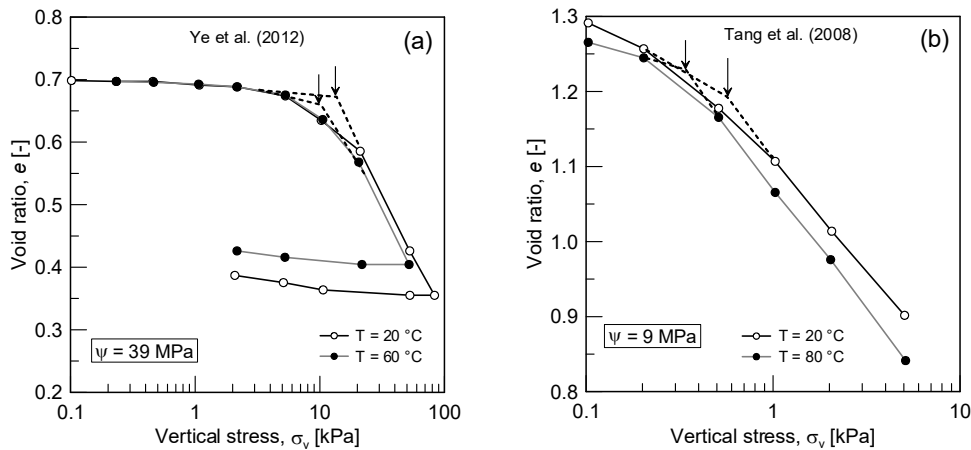


Fig. 2.8 Influence of temperature on the compressibility and the yield stress of bentonite materials: (a) GMZ01 bentonite (Ye et al. 2012), and (b) Wyoming bentonite (Tang et al. 2008).

The overconsolidation ratio and the total suction were found to be the most important parameters that control the thermal volumetric response. The results of the mechanical loadings revealed that a decrease of the total suction resulted in an increase of the compressibility.

The effect of temperature on the compressibility parameters was found to be negligible, while it can induce a slight decrease in the yield stress. Similar results on the influence of temperature on the compressibility parameters were recently reported by Ye et al. (2012). The influence of temperature on the compressibility behaviour and the yield stress of Wyoming and GMZ01 bentonites at two different total suctions of  $\psi = 39$  MPa (Ye et al. 2012) and 9 MPa (Tang et al. 2008) is presented in Fig. 2.8a and b, respectively.

## 2.2.2 Swelling and compressibility behaviour of Wyoming granular bentonite

In this section the hydro-mechanical response of the tested Wyoming bentonite (described in section 2.1) in terms of swelling and one-dimensional compressibility behaviour is presented.

### 2.2.2.1 Swelling behaviour

To evaluate the swelling properties of the granular Wyoming bentonite, constant and free volume swelling tests were performed. The constant volume swelling tests were carried out on samples with 15 mm height and 75 mm diameter. Each sample was prepared with a grain size distribution described in section 2.1.3. For achieving a higher dry density than  $1.5 \text{ Mg/m}^3$ , after emplacement in a rigid steel cell, the granular material was first statically compacted to the target dry density. The material rested on a porous disc connected to a water inlet. The upper part of the sample was in contact with a coarse porous stone and a flushing line was connected to the upper part of the cell. The swelling pressure was measured by installing the cell containing the sample inside a rigid frame to ensure constant volume conditions. A load cell (with an accuracy of 10 kPa with respect to the area of the sample) was placed between the top cap and the frame to measure the swelling pressure. An initial total vertical stress of 80 kPa was applied to ensure a good contact of the various parts of the apparatus. The sample was then inundated with water and the swelling pressure was continuously monitored until it was stabilised. The swelling pressure developed under constant volume conditions with respect to time is presented in Fig. 2.9 for different dry densities. The results of the constant volume swelling

pressure measurement versus dry density are presented in Fig. 2.10a. The obtained results are corresponding with the ones reported by Bucher & Müller-Vonmoos (1989) and Karnland et al. (2008).

A unique trend can be obtained for the constant volume swelling pressure as a function of dry density as follows:

$$\sigma_p = 0.01 e^{3.85\rho_d} \quad \text{Eq. 2.1}$$

where  $\sigma_p$  is the swelling pressure in MPa and  $\rho_d$  is the dry density in  $\text{Mg/m}^3$ . The physical conception behind such a commonly observed behaviour in terms of swelling pressure versus dry density is presented in Chapter 3 where the swelling pressure of the material is associated with the osmotic repulsion within the smectite interlayer pore water. Free swelling tests including the saturated and unsaturated swellings were carried out in order to evaluate the swelling potential in terms of changes in void ratio. The saturated swelling tests were performed by inundating the samples under a surcharge load of 8 kPa and measuring the vertical heave with an LVDT system. A constant pore water pressure of 5 kPa was applied to the sample and the flushing line on the top was opened periodically. This configuration ensured the evacuation of air from the top of the cell during the rising of the wetting front into the sample.

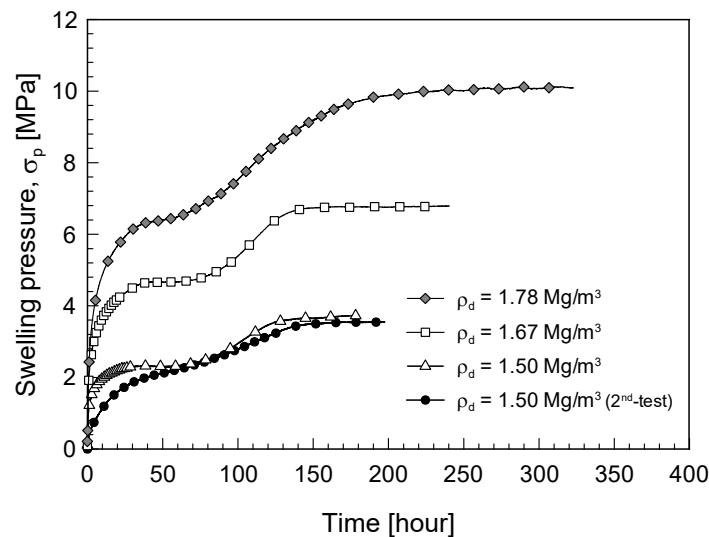


Fig. 2.9: Swelling pressure developed under constant volume conditions at different dry densities for Wyoming granular bentonite.

The unsaturated swelling tests were performed by hydration through the vapour phase. The material was poured inside a cylindrical cell (diameter of 75 mm and varied height up to 100 mm) and then placed in a humid chamber of 100 % relative humidity and under a seating load of 10 kPa for a couple of weeks. The cell was laterally perforated to provide the material to adsorb water through the vapour phase. After reaching certain water contents, the swelling deformation was measured. The total suction of the material at the equalized water content was measured using a WP4C device as well. The results of the free swelling tests in terms of final void ratio at a given suction are depicted in Fig. 2.10b. It is seen that about 40 % of the final swelling happens in the last step when the suction decreases from  $\psi = 3.5 \text{ MPa}$  to saturated conditions.

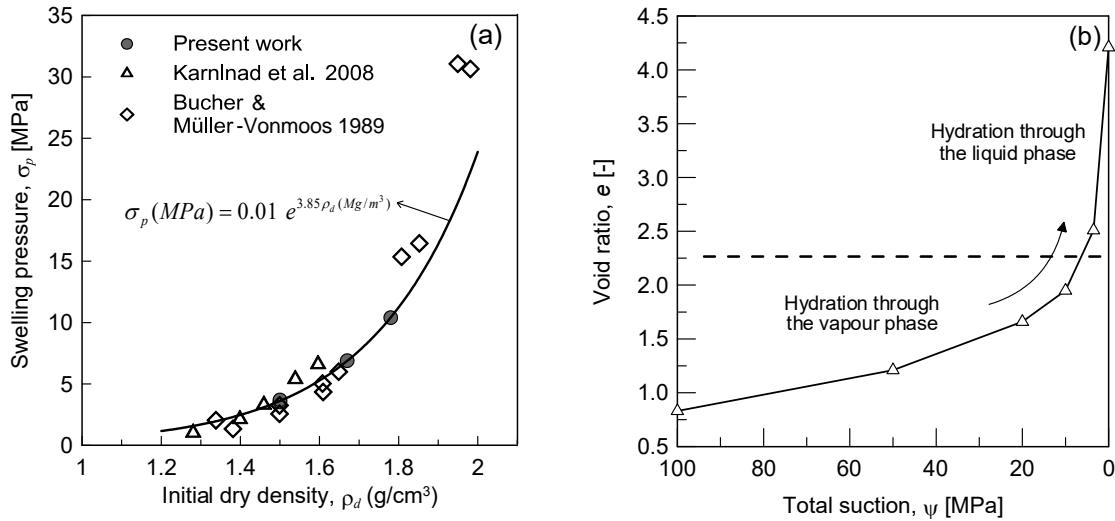


Fig. 2.10: Swelling behaviour of Wyoming granular bentonite: (a) constant volume swelling pressure, and (b) free volume swelling vs. total suction.

**2.2.2.2 One-dimensional volumetric behaviour**

One-dimensional volumetric behaviour of geomaterials is generally determined from laboratory oedometer tests using saturated soil samples. In general, for swelling material, an initial water content of more than the liquid limit for the remoulded soils is selected and followed by oedometric consolidation. However, Wyoming bentonite upon swelling achieves a void ratio of about 11 at the liquid limit ( $w_l = 4.2$ , Tab. 2.2). This evolution of void ratio opposes the practical application of the bentonite as buffer material in nuclear waste repositories where the bentonite remains mainly under confined condition. The following subsections present the effect of water content (and the corresponding total suction) on the compressibility of Wyoming granular bentonite. The standard proctor and static compaction tests are carried out on the material at different total suctions. The consolidation behaviour of samples saturated at constant and free volume conditions are analysed as well.

**a) Standard Proctor test**

The standard proctor test (ASTM D698-07, compaction upon an energy of 600 kN m/m<sup>3</sup>) was performed to obtain the compaction characteristics of the granular material in terms of optimum water content and maximum dry density. Results are presented in Fig. 2.11. The optimum water content of 6.0 % and corresponding maximum dry density of 1.79 Mg/m<sup>3</sup> were obtained by this procedure.

**b) Static compaction test**

In static compaction processes, the material was compacted by a gradually increasing static force. The poured granular material at different total suctions was compacted in a rigid cell and the compaction was achieved by the gradual movement of a piston until reaching a target dry density. The experimental setup for the static compaction test is schematically shown in Fig. 2.12a. The tests were performed in a controlled-strain mode. The cell was designed to have enough isolation to maintain a constant water content of the sample during the loading steps. The poured material at high suction of 100 MPa has an initial dry density of 1.50 Mg/m<sup>3</sup> corresponding to a void ratio of  $e = 0.83$ .

The static compaction tests were conducted at different water contents ( $w$ ) of 0.067, 0.12, 0.18, 0.24, 0.32, corresponding to the total suction ( $\psi$ ) of 100, 50, 20, 10 and 3.5 MPa. The corresponding suctions were measured using a psychrometer.

These tests were performed on samples partially saturated through the vapour phase. For this reason, the material at its hygroscopic water content was stored in a humid chamber to adsorb water through the vapour phase. The samples were continuously weighted until they reached the target water content. The material at a stabilised total suction was then placed in the compaction mould. After that a displacement rate of 0.03 mm/min was applied for the static compaction tests. The rate was proven to be slow enough to prevent the generation of excess pore water in the material. As seen in Fig. 2.12b, the loading was halted at three points during the static compaction test on a sample with a water content of 0.12. After a given waiting time, the loading was resumed. The material followed the main stress path without being affected by the halting time. The results of the static compaction tests at different total suctions are shown in Fig. 2.13a. Since the bentonite material swells upon uptake of water, the initial void ratios at different total suctions are different. The yield stress of the material with respect to the total suction is also depicted in Fig. 2.13b. The static compaction behaviour in terms of variation of the dry density versus water content is presented in Fig. 2.11. The vertical contours present the static compaction path at given water contents. Along these vertical lines, the material approaches the fully saturated state without appreciable change in the total suction.

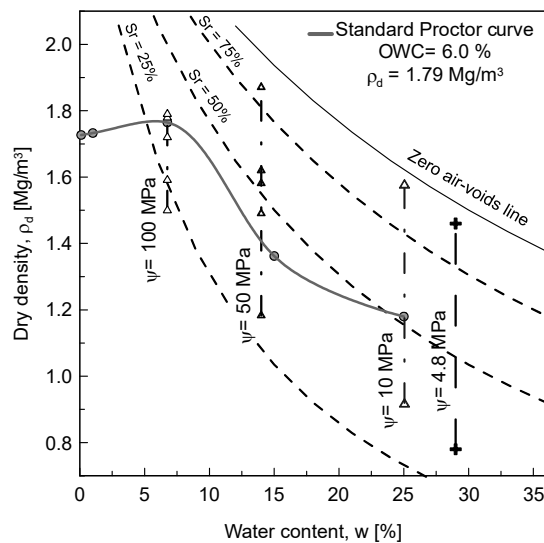


Fig. 2.11: Compaction behaviour of the granular bentonite in a standard proctor test and the contours of equal suctions.

Along the contours of equal suctions, loading mechanism influences mainly the large pores that do not contain free water and the water is stored within the intra-aggregate pores. Consequently, the degree of saturation changes due to the porosity reduction at a constant intra-aggregate water content. Further discussions on the water adsorption mechanisms in bentonite material are presented in Chapter 3.

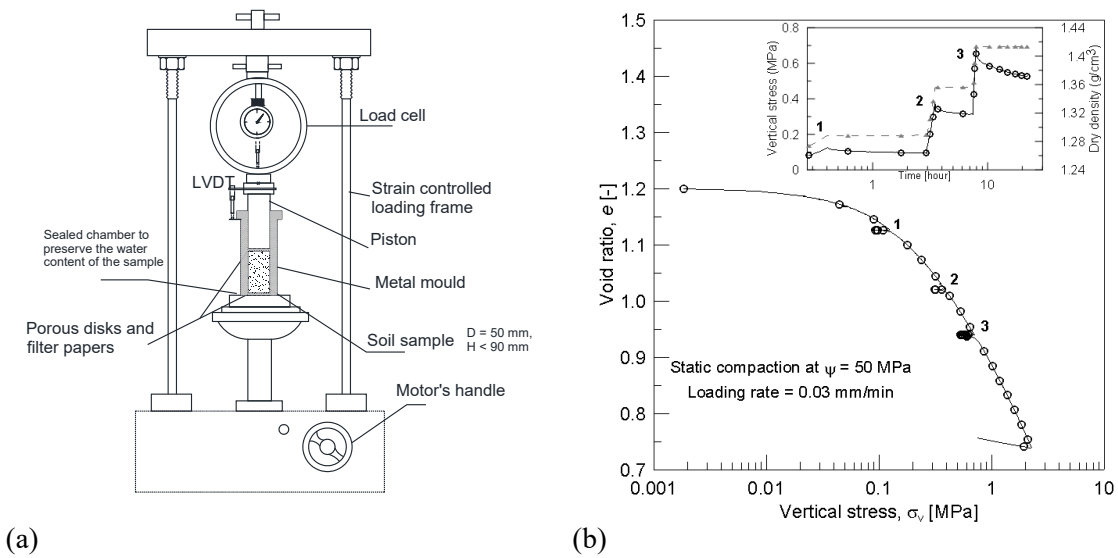


Fig. 2.12: (a) Schematic setup for static compaction tests in controlled-strain condition, and (b) influence of the strain rate on compaction behaviour.

The vertical stresses required to achieve target dry densities at different total suctions are depicted in Fig. 2.14. The experimental data are trended by exponential functions. This graph implies that although the compression index of the granular bentonite increases with decreasing of total suction, the maximum stress required to reach a certain density is higher in the case of the lower suctions. This is due to the work needed to restrain the increase of void ratio due to the swelling deformation of the material.

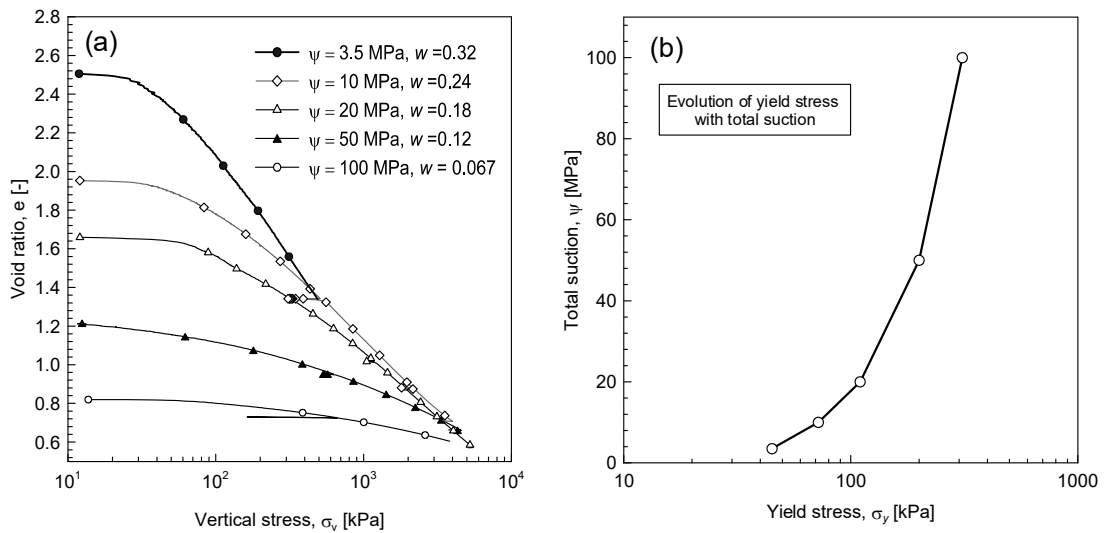


Fig. 2.13: Effect of total suction/water content on static compaction behaviour of granular bentonite in terms of: (a)  $e$ - $\log \sigma_v$ , and (b) yield stress  $\sigma_y$  based on the results in part (a).

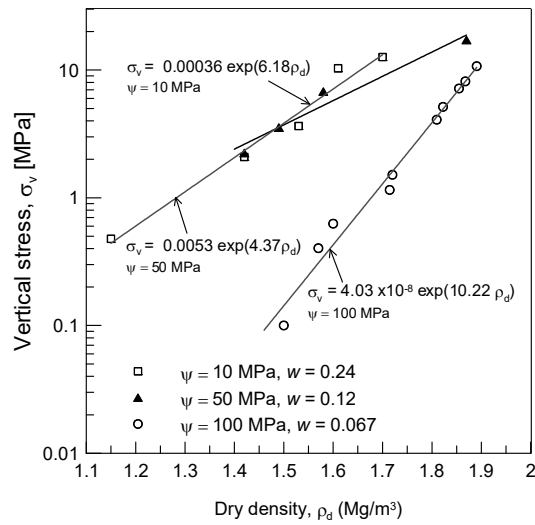


Fig. 2.14: Vertical stress required to reach target dry density at different total suction values.

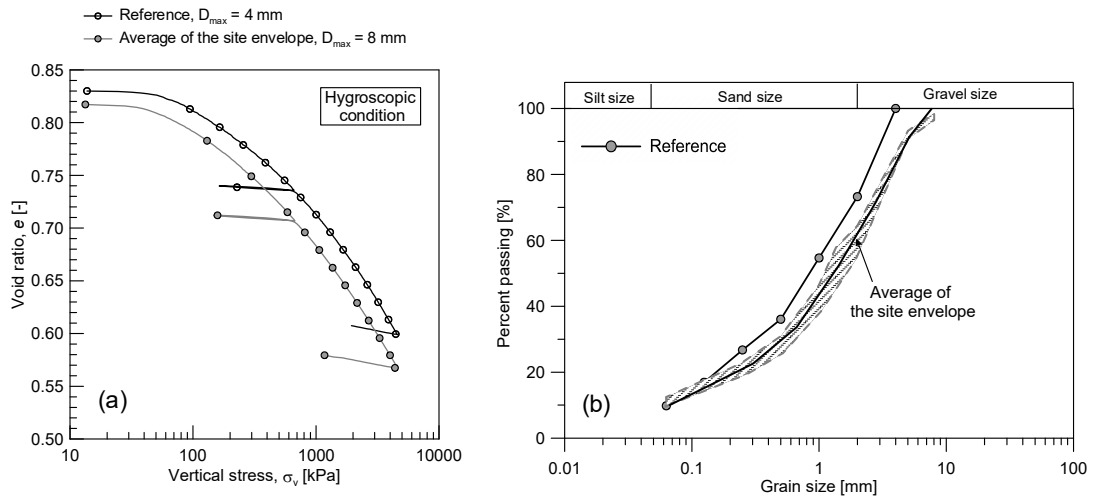


Fig. 2.15: Effect of maximum grain size on the compaction behaviour of the granular bentonite: (a)  $e$ -log  $\sigma_v$  behaviour, and (b) grain size distributions.

The influence of the maximum grain size on the compressibility and the yield behaviour of the granular material is investigated in Fig. 2.15. The static compaction tests were performed on two samples prepared with the reference grain size distribution (tested material) and the average grain size distribution of the material planned to be used in the repositories (Fig. 2.15b). For both cases, the material was under hygroscopic conditions. The effect of the maximum grain size was found negligible in terms of the compressibility and yield stress. This could be associated to the optimized Fuller distribution for both apparent granulometry curves that lead to a homogeneous structure after early stage of the mechanical compaction, more particularly when the grains are mainly coated by the fine fraction as it was shown in Fig. 2.3.

**c) Oedometric consolidation**

A high-pressure oedometer device developed at LMS-EPFL (Salager et al. 2010, Ferrari & Laloui 2012) was used to carry out a consolidation test by applying vertical stresses greater than the constant volume swelling pressure of the granular bentonite. The schematic setup of the high capacity oedometer is shown in Fig. 2.16a. The device holds cylindrical samples with 35 mm diameter and 20 mm height. The sample was prepared under poured conditions at a dry density of  $1.5 \text{ Mg/m}^3$ . The sample was first inundated with distilled water using a pressure/volume controller by applying a water pressure of 10 kPa under constant volume condition. After reaching the maximum swelling pressure (Fig. 2.16b), the saturated material was subjected to vertical stresses greater than the swelling pressure. As seen in Fig. 2.17b, the material follows constant volume conditions upon a saturation phase which resulted in the development of a swelling pressure of about 3 MPa. Then, the loading was applied in two steps up to 16 MPa. The unloading steps were performed in two steps as well. The compression and swelling indices are computed and shown in the graph.

A conventional oedometric cell was also used to perform a consolidation test on an initially saturated sample under 8 kPa of vertical stress. Saturation under this condition resulted in an increase of the void ratio (from  $e = 0.83$  to  $e = 4.26$ ). The corresponding final water content was  $w = 1.55$  which indicated a degree of saturation of 0.99. Then, the vertical stress was increased in the next steps and a given time was considered for the consolidation.

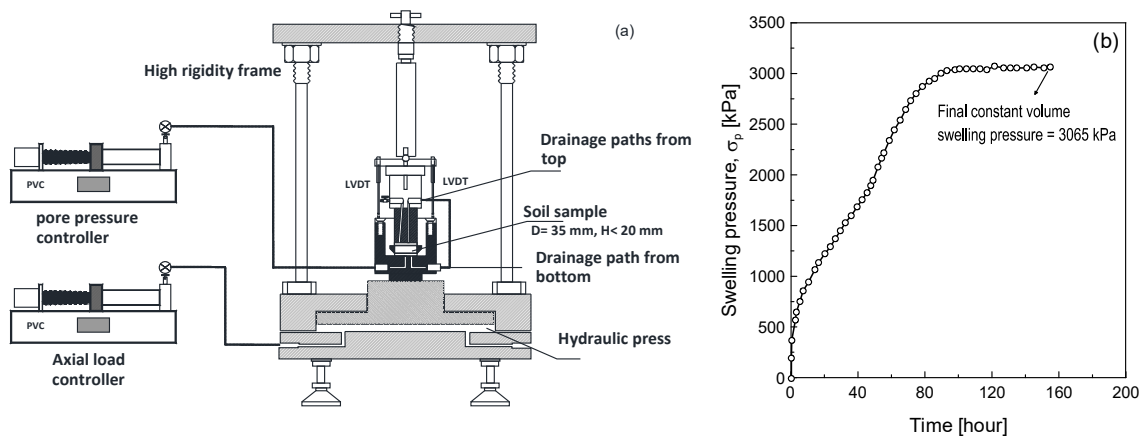


Fig. 2.16: (a) High pressure oedometric cell for consolidation tests, and (b) maximum swelling pressure attained under constant volume conditions.

The evolution of the void ratio during the swelling and consolidation steps with respect to time is shown in Fig. 2.17a. The change of void ratio versus vertical stress is presented in Fig. 2.17b. It can be seen that the material exhibits a normally consolidated condition due to the second step of the vertical loading application. It can be observed that due to the saturation under constant volume conditions, the material is already in a normally consolidated condition when vertical stresses more than the swelling pressure are applied. However, a bilinear behaviour for the normally consolidated state is inferred by analysing the consolidation behaviour of saturated material in both cases.

#### d) Compression index

Based on the oedometric consolidation tests, the compressibility of saturated granular bentonite can be calculated in terms of compression index,  $C_c$ . This parameter is generally defined as the slope of the normally consolidated (NC) line in the  $e$ - $\log \sigma_v$  ( $\sigma_v$  is the total vertical stress) plane through the following equation:

$$C_c = \frac{de}{d(\log \sigma_v)} \quad \text{Eq. 2.2}$$

In addition, a swelling index ( $C_s$ ) can be also defined for the unloading path using Eq. 2.2 for a  $de > 0$ . The computed values are presented in Fig. 2.17b for both curves separately. As seen, there are two different trends in the results of the  $e$ - $\log \sigma_v$ , obtained from the conventional and high capacity oedometer cells. The transition between these two trends (as marked in Fig. 2.17b) is indicated by a dashed line. The normally consolidated state of the compression behaviour in  $e$ - $\log \sigma_v$  plane is supposed to be a straight line for saturated clays and sands. However, here there are two distinct regions according to the applied stresses in a consolidation test. Such behaviour for saturated bentonite material with regards to the range of applied stresses was already reported by some researchers (e.g. Bolt 1956, Marcial et al. 2002, Baille et al. 2010). The results of the compression behaviour of saturated smectite clay materials reported by Marcial et al. (2002) are presented in Fig. 2.18. A bilinear shape was described for such behaviour and two compression indices were defined for each region. For instance, in case of the Na-Ca-Wyoming sample, the compression indices of 5.22 and 0.42 were defined as shown in Fig. 2.18.

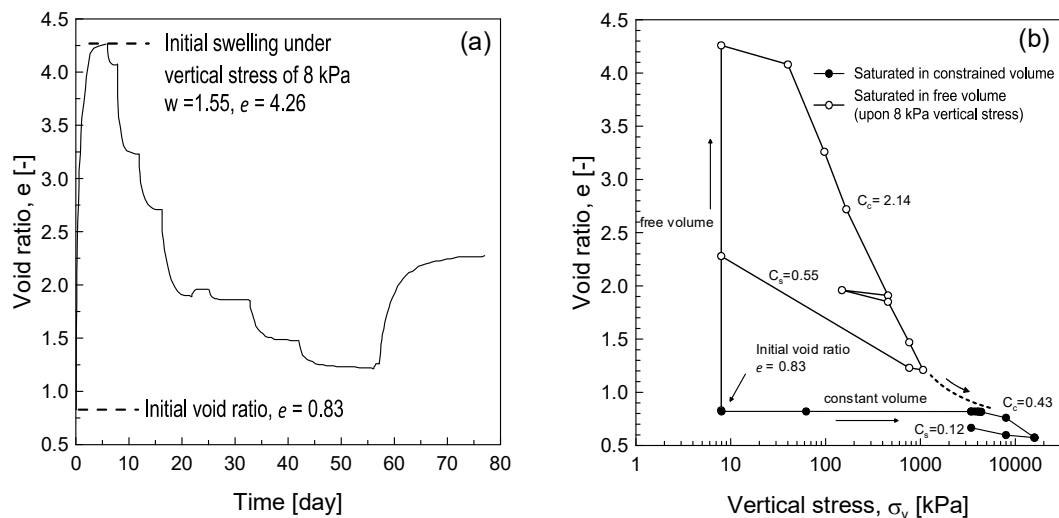


Fig. 2.17: (a) Swelling behaviour of the material saturated under 8 kPa vertical stress followed by consolidation steps under higher stresses, and (b) consolidation behaviour of the material saturated under constant and free volume conditions.

Baille et al. (2010) reported similar trends for the oedometric behaviour of bentonite material from Bavaria (Germany) containing about 60 % smectite clays. The saturated samples were subjected to vertical pressures up to 21 MPa and show two distinctly different values for  $C_c$ . These values were found to decrease from 0.53 to 0.32 with a decrease in void ratio from 1.39 to 0.65.

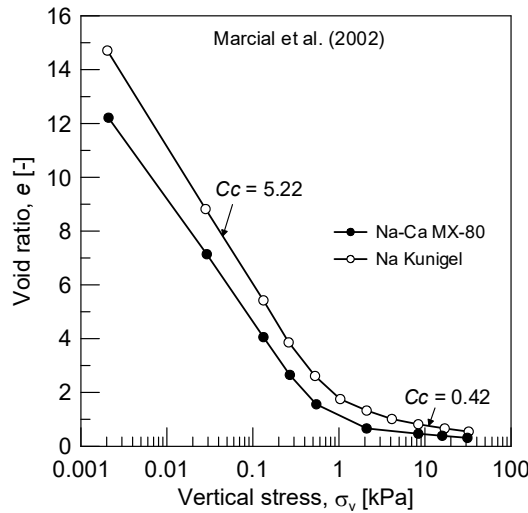


Fig. 2.18: Consolidation behaviour of different smectite-based materials reported by Marcial et al. (2002).

The reason of such behaviour lies in the microstructural features of bentonite material. In lower compression stresses than about 1000 kPa, the change of void ratio is associated with the reduction of the macropores. Upon the initial swelling, the void ratio is increasing due to the swelling and subdivision of the aggregates. Under higher stresses, the macropores are reduced and further change of the void ratio requires expelling adsorbed water from the smectite particles. The former mechanism seems to be initiated for higher stresses than about 1 MPa where the compression index is reduced. The compression indices for unsaturated Wyoming granular bentonite samples subjected to vertical stresses (Fig. 2.13a) were calculated and plotted versus the total suction in Fig. 2.19. The compression index under saturated conditions is also marked in this plot. In addition, the compression indices of saturated and unsaturated Na-laponite reported by Al-Mukhtar et al. (1999) are plotted as well. Na-laponite is a smectite-based synthetic clay with liquid limit of 10.50 and plastic limit of 2.5 (Lambe & Whitman 1979) which is more active than Wyoming bentonite. It is seen that both materials exhibit a similar compressibility behaviour under fully saturated conditions.

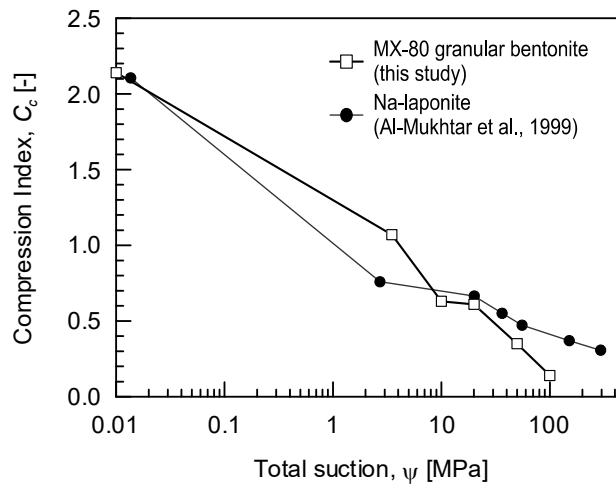


Fig. 2.19: Compression index  $C_c$  for Wyoming bentonite in this study and Na-laponite reported by Al-Mukhtar et al. (1999) in unsaturated and saturated conditions.

## 2.3 Water retention behaviour

Beside the analysis of the compressibility and swelling behaviour, understanding the water retention features of the bentonite is a key point to analyse and predict the hydro-mechanical response of the bentonite. In this section, the general terms to define the water retention behaviour of geomaterials are defined and then the water retention behaviour of bentonite with regard to its particular application in the disposal of radioactive wastes is analysed through a comprehensive experimental study.

### 2.3.1 Definitions

The water retention capacity of geomaterials is often evaluated by seeking the soil water retention curves that relate the liquid phase potential energy (expressed by total suction) to the amount of water retained in the material (in terms of water content or degree of saturation). This water retention behaviour is non-linear, hysteresis and history dependent.

There is an accepted definition for the total suction term corresponding to the free energy of water (Aitchison et al. 1965). The total suction can be also defined as the energy required removing water molecules from a soil matrix by evaporation (Ridley 1993).

This free energy can be measured in terms of partial vapour pressure of the soil pore water. Total suction,  $\psi$ , then is the sum of the matric,  $s$ , and the osmotic suction,  $\pi$ :

$$\psi = s + \pi \quad \text{Eq. 2.3}$$

The matric suction is defined as the difference between the pressure of a wetting and a non-wetting fluid. In the case of the water retention behaviour, the fluids are the air and water. In another definition, matric suction is the measure of the energy required to remove water molecules from the soil matrix without any change in the water state (Ridley 1993). The matric suction is written as:

$$s = u_a - u_w \quad \text{Eq. 2.4}$$

The matric suction is directly linked to the surface tension and the capillary phenomena in partially saturated porous media. Matric suction can be formulated by the Laplace equation:

$$s = u_a - u_w = -\frac{4T \cos \theta_w}{d} \quad \text{Eq. 2.5}$$

Thus, the matric suction is found to be dependent on the pore diameter ( $d$ ), the air – water contact angle ( $\theta_w$ ) and the surface tension ( $T$ ). It is also possible to realise that for contact angles lower than  $90^\circ$  the term on the left side of the equation returns negative values which means that the water is held in tension (with  $u_a$  defined as the atmospheric pressure).

The second term of the free energy can be defined as the osmotic or solute suction. In the particular case of clayey material, the mechanism of osmosis can be analysed from the strong attraction of water molecules by the surface of the clay particles.

Mitchell & Soga (2005) state that the water adsorption mechanisms by dry clays are of several natures, namely: hydrogen bonding, hydration of the exchangeable cations, attraction by osmosis, charged surface dipole attraction and attraction by London dispersion forces and the capillary condensation. The adsorbed water indicates that a clayey material might have water even at a very high total suction and it is not possible to completely dry a sample unless placing

it in an oven for temperatures higher than 100 °C (corresponding to a total suction of 1 GPa). The practical implication of the adsorption mechanism in clayey soils is the consideration of a residual degree of saturation at very high total suction values.

The mechanisms of the water retention in the bentonite material composed of smectite mineral are associated to the hydration of the exchangeable cations and the osmotic mechanism. At the microscopic scale, the attraction by osmosis is due to the negative charge of the clay particles. The two negatively charged clay particles will be in contact through the overlapping diffused double layers. On the other side, due to the concentration of cations in the interlayers, there will be a gradient toward the interlayer for diffusion of the water molecules to equalise the concentration (Tarantino 2010). Thus, hereafter the water retention behaviour of bentonite material will be presented in terms of the total suction ( $\psi$ ).

To define the general terms in water retention curves, a typical water retention curve is presented in Fig. 2.20. The graph exhibits a main wetting path up to the fully saturated state in the plane of  $S_r - \psi$ . The full saturation state here in this study is referred to as the condition where the degree of saturation is equal to 1.0 ( $S_r = 1.0$ ). If the degree of saturation decreases due to a drying attempt, the material follows another path called the main drying. The air-entry value (AEV) is defined as the total suction corresponding to the intersection of the horizontal line at  $S_r = 0.95$  (usually a threshold between 0.95 and 1.0 is selected) with the tangent line to the main drying path. The final state is the residual part where the water is not anymore continuous in the pore space. In capillary soils, such as sand or silt, the water remains at the particle contact at residual state and the soil reaches equilibrium through the vapour phase. For highly plastic clays particularly smectite-based material, for a wide range of the total suction, water remains inside the interlayer pores without creating the water meniscus. For such systems the capillary suction is negligible even at fully saturation under the given void ratio. Thus, the residual state can be defined when the water is hydrating the interlayer cations. At this condition only one water layer is absorbed by the clay particle. Further information and evidences will be presented in Chapter 3 where the microscopic behaviour of the bentonite material is analysed. However, the residual degree of saturation is hereafter defined by the intersection of a horizontal line and the inflection point of the main drying curve at high suction values.

As seen the retention curve has a hysteresis nature. The main wetting and main drying curve encloses a possible hydraulic state for a material (hysteresis domain). Any possible  $S_r - \psi$  curve that scans the hysteresis domain, is therefore referred to as the scanning curve. The behaviour in the scanning region is often assumed as being reversible whereas the water retention curve itself is not reversible through the so-called ink-bottle effect (Tarantino 2010). However, it has to be mentioned that the hysteresis and scanning behaviour of highly swelling clays have not yet been well analysed, particularly for the case of Wyoming bentonite material. In the next section the general challenges in the determination of the water retention behaviour of swelling clays such as bentonite is outlined.

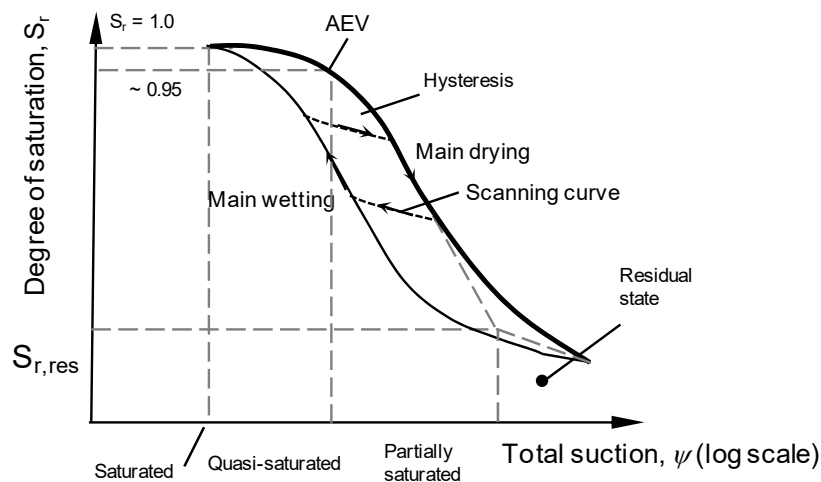


Fig. 2.20: Typical water retention curve of geomaterials.

### 2.3.2 Bentonites used as buffer and backfilling materials

It was mentioned before (Chapter 1) that in the Swiss concept for the disposal of high-level radioactive waste, bentonite will be used in the repository in the form of compacted blocks to sustain the canisters and in granular form around the canisters to fill the space between the waste container and the host rock formation. With respect to the application of bentonites as buffer and backfilling material in such engineered barriers, the following issues have to be considered in the determination of the water retention behaviour:

**Wetting/drying cycles:** bentonite barriers would be subjected to wetting and drying cycles due to the environmental conditions and the heat generated from the waste canisters during the lifetime of the repository. After its emplacement in repositories, at least one cycle of wetting and drying for the buffer material can be anticipated. To the knowledge of the author, there are no available experimental data in the literature on the hysteresis behaviour of the water retention curves of bentonite materials.

**Density gradient:** the granular bentonite is emplaced at a target dry density and will be in confined conditions. However, the development of a density gradient in the system is inevitable. The progressive saturation of the buffer upon uptake of water from the host rock will be followed by the expansion of the bentonite and the consequent filling of technological gaps in the systems. This swelling occurs in the boundaries near the surrounding host rock, where the wetting will first take place. The density gradient may be established with lower densities in the areas where the bentonite can expand and with higher densities in the internal areas where the bentonite is compressed due to the swelling pressure developed in the external parts. For instance, for compacted bentonite blocks emplaced at a target dry density of  $1.6 \text{ Mg/m}^3$ , the final dry density after dismantling the FEBEX in situ test was reported to be in the range of  $1.4 - 1.7 \text{ Mg/m}^3$  (Villar et al. 2005).

In the particular case of the Swiss concept, there is already a density gradient even after the emplacement phase where both compacted bentonite blocks and granular bentonite are presented in the repositories. Contour lines of the dry density in both granular bentonite and compacted blocks after dismantling the full-scale EB experiment at Mont Terri site is shown in Fig. 2.21. The bentonite blocks were emplaced at an initial dry density of  $1.69 \text{ Mg/m}^3$  and the average density of the granular bentonite emplaced by a particular auger machine was

1.36 Mg/m<sup>3</sup> (García-Siñeriz et al. 2008). After saturation of the buffer, lower dry densities in the lower half of the cross section were observed. This observation implies that the upper granular bentonite is compacted due to the swelling of the lower bentonite blocks. However, it should be mentioned that to accelerate the process of saturation of the buffer in this experiment, longitudinal water tubes at different distances from the centre of the tunnel were used to inject water through the buffer (García-Siñeriz et al. 2008). However, the saturation of the buffer in actual repositories will have taken place only from the rock formation front. The saturation direction could influence the redistribution of the dry density within the buffer material.

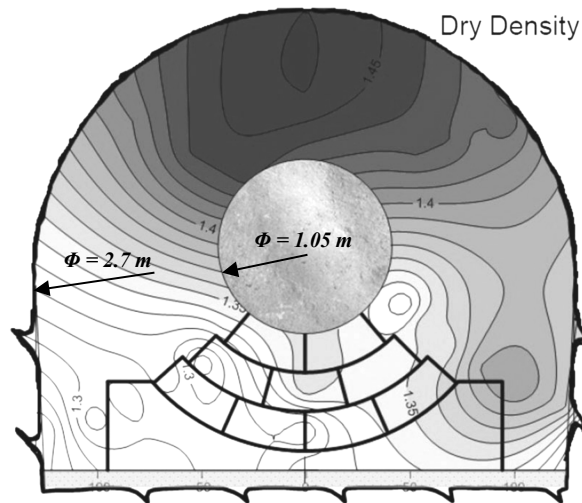


Fig. 2.21: Contour lines of the dry density after dismantling the full-scale Engineered Barrier (EB) experiment at Mont Terri (García-Siñeriz et al. 2008).

**Void ratio dependency:** Because of the existence of a density gradient for the bentonite material in the repositories, variation of the void ratio within the buffer is expected. Villar (2007) has reported an imperceptible influence of void ratio on the water retention curves of FEBEX and Wyoming bentonites for total suctions higher than 10 MPa when presenting the results in terms of water content variation. For the lower suctions, the higher water content was obtained for the less dense samples. The reason of such behaviour can be explained by considering different water retention mechanisms within these materials. Romero & Vaunat (2000) suggested two regions in the water retention domain of compacted moderately swelling clays: the low suction region where the capillary storage mechanism is predominant and the higher suction region where the adsorptive storage mechanism is dominant. The influence of void ratio was found negligible in the latter region. It can be concluded that for instance in the work of Villar (2007), the region for total suctions higher than 10 MPa is associated with the domain that water retention is governed by the adsorption mechanism. In addition, recent studies have also confirmed the influence of the confinement on the water retention behaviour of swelling geomaterials particularly at low suction values (e.g. Al-Mukhtar et al. 1999, Romero & Vaunat 2000, Villar 2007). Although the buffer remains mainly under confined conditions, free swelling can be considered through the technical gaps or any gaps in the external boundaries. As mentioned in Chapter 1, the formation of gaps can be anticipated due to erosion and local loss of bentonite barriers because of phenomena like desiccation cracks. Bentonite material under such circumstance swells and fills up such unexpected gaps in the system. This feature of the bentonite is referred to as the self-healing capacity.

With regard to these considerations, the accurate determination of the water retention curves is undertaken in this section as an essential key point for modelling and predicting the performance of the engineered barriers.

### **2.3.3 Water retention behaviour of Wyoming granular bentonite**

In highly swelling geomaterials such as bentonite, significant volume change happens due to the variation of the water content. Therefore, the water retention behaviour of such material is usually obtained under constant volume conditions (for a given void ratio) and the calculation of the degree of saturation is based on the water exchange (e.g. Lloret et al. 2003, Villar 2007, Romero et al. 2011). In the same direction, in the next section, a detailed description of a new technique for the determination of the water retention curves of Wyoming granular bentonite under a constant void ratio is presented. A comprehensive experimental programme is presented focusing on the influence of the void ratio and confinement on the water retention behaviour, along with an insight into the hysteresis behaviour in wetting – drying paths. The influence of the temperature on the water retention capacity of Wyoming granular bentonite in wetting and drying paths is analysed as well.

#### **2.3.3.1 Methodology**

The experimental methods for analysing the water retention behaviour rely on the measurement or control of the suction in different ranges. Due to high suction values which are needed to obtain appreciable variations of the degree of saturation in bentonites, total suction is often considered to be controlled or measured. Several techniques have been developed to measure the total suction for samples at controlled water contents, such as the filter paper technique (Houston et al. 1994), thermocouple psychrometers (Spanner 1951) and chilled-mirror hygrometers (Gee et al. 1992). Total suction control techniques are mainly based on the control of relative humidity and temperature of a closed system in which the material is enclosed; in this way, the soil liquid phase potential is applied by migration of water molecules in the vapour phase from a reference system of a certain potential to the soil matrix, until equilibrium is satisfied (Romero 2001).

In each of the above-mentioned methods, the water content corresponding to the measured (or controlled) suction is recorded to produce points along the water retention curve. The obtained retention path describes either a wetting or drying curve depending on the initial suction value and the imposed suction variation.

In this research, an improved methodology called 'Micro-cell' for the determination of the water retention behaviour is presented. The Micro-cell is a rigid cell made of brass, which holds samples of 7 mm height and 30 mm in diameter (Fig. 2.22). The cell consists of two parts that merge by the means of a thread lid to provide constant volume condition during wetting.

The top and bottom of the cell are perforated to provide the possibility of water exchange in the vapour or liquid form with the surrounding environment. Filters made of a standard ASTM steel mesh number 200 (opening equal to 75  $\mu\text{m}$ ) are placed at the top and bottom of the sample to prevent migration of the fine material particles. The mesh was proved to have a negligible retention capacity that does not influence the measurement of the sample water content.

The measurement of the total suction is conducted using the WP4C (Decagon Device, Inc. 2002) dew-point chilled-mirror psychrometer (Leong et al. 2003, Cardoso et al. 2007, Schanz et al. 2010). The Micro-cell was designed to be adjusted directly into the device by placing it on the tray of the psychrometer drawer (Fig. 2.22b).

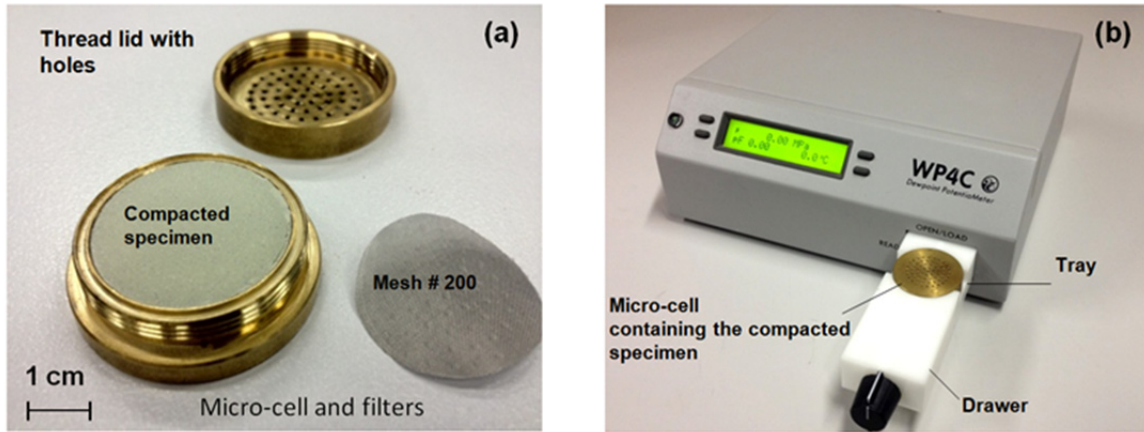


Fig. 2.22: (a) Micro-cell components, and (b) WP4C dew-point chilled-mirror psychrometer.

When WP4C is closed, the relative humidity in the measurement chamber of the device is controlled by the vapour from the sample passing through the holes of the Micro-cell. The relative humidity is then measured by the device reading the dew-point temperature at which condensation happens on the chilled-mirror. The device also controls the temperature of the sample (18 – 40 °C) during the measurement. The total suction ( $\psi$ ) is then calculated according to the psychrometric law:

$$\psi = -\frac{\rho_w RT}{M_w} \ln(RH) \quad \text{Eq. 2.6}$$

where  $R$  is the universal gas constant (i.e. 8.3143 J/mol K),  $\rho_w$  is the water density,  $M_w$  is the molecular mass of water,  $RH$  is the relative humidity and  $T$  is the absolute temperature of the sample. The Micro-cell was first tested using various saturated salt solutions of known water potentials and the corresponding suction values were read with the WP4C; this allowed verifying that the cell is not altering the measurement of the total suction. In the proposed methodology, samples are prepared by pouring and/or statically compacting the material (previously conditioned in the desiccators, Fig. 2.23a) at the target dry density and water content directly into the Micro-cell, using an ad-hoc compaction mould (Fig. 2.24b).

The Micro-cell is then closed and the initial total suction is read with the WP4C. A wetting path is then initiated by placing the Micro-cell in a controlled temperature chamber with an imposed relative humidity of 100 %, in order to let the sample absorb water through the vapour phase.

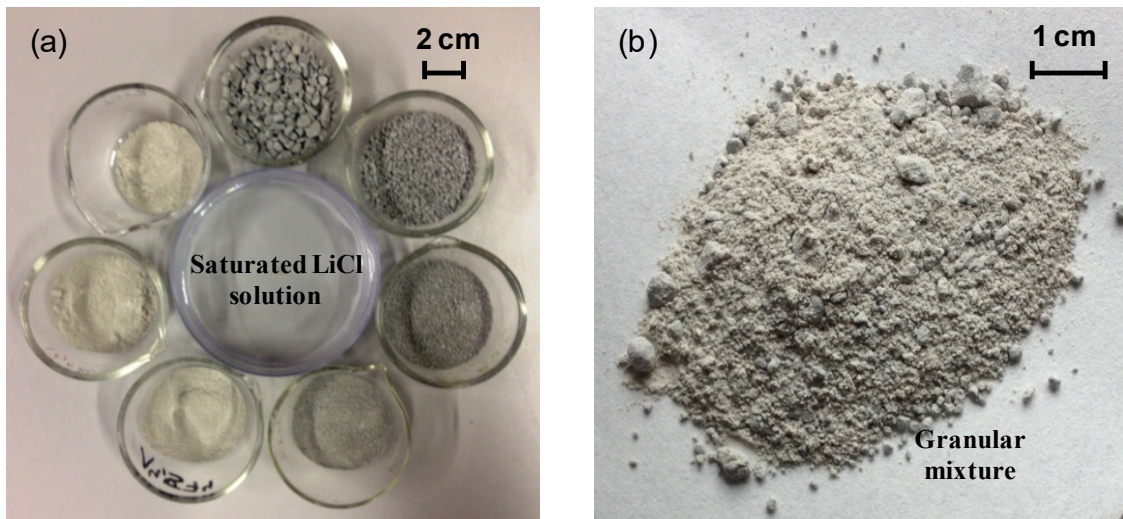


Fig. 2.23: (a) Preconditioning of different fractions of the Wyoming granular bentonite, and (b) prepared sample by mixing the different fractions.

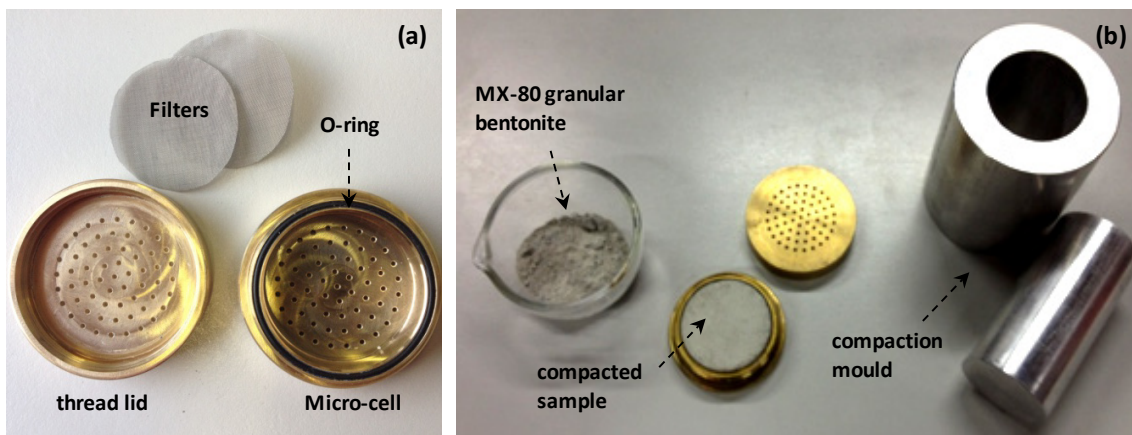


Fig. 2.24: (a) Micro-cell components, and (b) compaction of the material inside the cell using an ad-hoc mould.

The evolution of the water content is monitored by continuous weighting of the Micro-cell using a precision balance. The process is halted once the sample reaches the target water content for the current step; the cell is then sealed and cured for 3 days at a controlled temperature to ensure the homogenisation of water in the sample. The degree of saturation of the sample at step  $i$  as a function of the water content can be calculated through the following expression:

$$S_r^i = S_r^{i-1} + \frac{\rho_s}{\rho_w e} \left( \frac{\Delta M_w^i}{M_s} \right) \quad \text{Eq. 2.7}$$

where  $\Delta M_w^i$  is the incremental water mass transferred in vapour form,  $M_s$  is the dried mass of the sample,  $\rho_s$  is the particle density of the material and  $e$  is the target void ratio at which the sample was compacted. After the curing time, the Micro-cell is inserted in the *WP4C* and the corresponding total suction is read.

The retention curve for the drying path is obtained by air-drying the sample in the Micro-cell at laboratory conditions ( $T = 22\text{ }^{\circ}\text{C}$ ,  $RH = 34\%$ ) in a controlled way. These conditions correspond to an applied suction of 148 MPa (see Eq. 2.6). For applying higher total suctions, samples are placed in a desiccator with a saturated LiCl salt solution (corresponding total suction of 300 MPa). The drying process is monitored by weighting the Micro-cell and it is halted once the target water content is reached; the Micro-cell is then sealed and the total suction is read after a curing time of 3 days. During the drying process, it is possible to compute the degree of saturation while the sample remains in contact with the cell walls. For the tested Wyoming bentonite, preliminary testing allowed to assess the water content values at which the samples lose contact with the cell.

### 2.3.3.2 Effect of void ratio

The apparent grain size distribution of the granular bentonite before compaction is respected as presented in Fig. 2.2. To compact each sample, different grain size fractions were selected and mixed in order to get always the same apparent grain size distribution. A high precision balance (0.001 g) was used to weight different fractions of the material.

Before compaction, the material was stored in a desiccator with a saturated salt solution of LiCl providing a total suction of 300 MPa at  $T = 22\text{ }^{\circ}\text{C}$ . The corresponding water content was in the range of 3.4 – 4.4 %. Samples were prepared directly inside the Micro-cell. The lowest considered dry density was  $1.5\text{ Mg/m}^3$  that corresponds to the dry density obtained by simply pouring the material dried in the desiccator (corresponding void ratio equal to 0.83). Other considered dry densities were obtained by static compaction of the material to the target values of 1.65 and  $1.8\text{ Mg/m}^3$  (corresponding void ratios equal to 0.67 and 0.53, respectively).

The water retention curves of Wyoming granular bentonite at different void ratios are presented in Fig. 2.25. The curves have followed a wetting path, from a high total suction (between 100 – 300 MPa); the difference in the starting conditions is justified with the fast absorption of water by the bentonite once the material is taken out from the desiccator for the sample preparation. The wetting was stopped once the sample did not show further absorption of water. The water content and total suction values for which the fully saturated condition is reached depend on the void ratio (Fig. 2.25). In particular the higher the void ratio, the higher is the water content and the lower is the total suction at which saturation occurs. The wetting paths for the three void ratios lay on the same main wetting path (Fig. 2.25).

Fig. 2.26 shows the evolution of the degree of saturation in time for a sample in the Micro-cell prepared at  $e = 0.83$  and  $S_r = 0.70$  and placed inside a chamber with  $RH = 100\%$ . The graph highlights that the material absorbs continuously water through the vapour phase until saturation is reached. For all the tested conditions, the computed degree of saturation at the end of the wetting path was in the range of  $1.00 \pm 0.005$ ; this observation, along with the results in Fig. 2.26, shows that the accuracy of the method following the wetting process and assessing the degree of saturation is very high.

The drying path was run up to a total suction of 200 MPa. In the plane of total suction versus water content, the drying paths align on a unique trend (Fig. 2.25a).

The two well identified main wetting and drying curves delimit all possible hydraulic states for confined Wyoming granular bentonite. The hysteresis behaviour of the water retention curves is well observable, since the degree of saturation reached in drying paths are always higher than those obtained during the main wetting for a given total suction. A detailed discussion with regard to the hysteresis behaviour is given in the next section.

Observing the plane of degree of saturation versus total suction, the air-entry values can be identified; here the air-entry value is taken as the total suction value at which a degree of saturation equal to 0.95 is reached; the evolution with void ratio is depicted in Fig. 2.27. The curves on this plane are depicted until the point at which the lateral contact of the sample is lost; this point, for each compaction void ratio, is obtained from complementary tests performed on samples that followed the same hydraulic paths and for which the Micro-cells were opened after each equalisation step and inspected by image analysis.

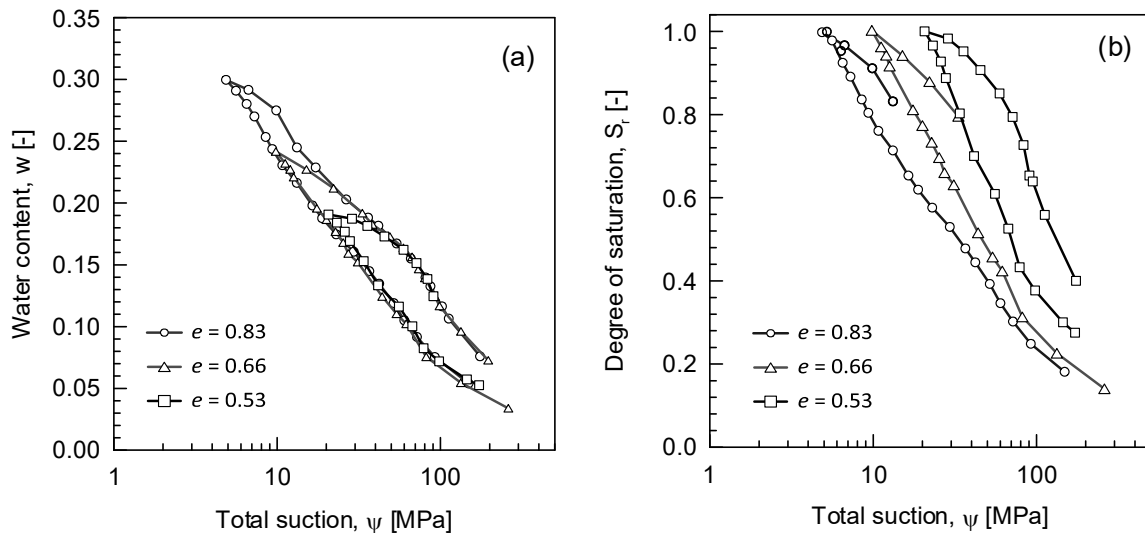


Fig. 2.25: Effect of void ratio on the water retention behaviour of Wyoming granular bentonite: (a) water content vs. total suction, and (b) degree of saturation vs. total suction.

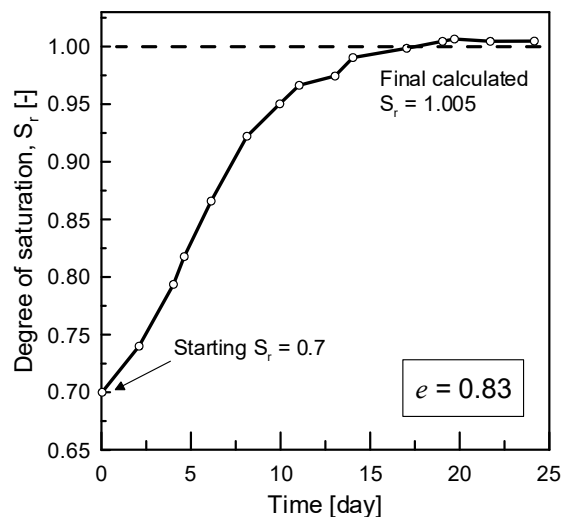


Fig. 2.26: Evolution of degree of saturation with time for the sample inside the Micro-cell.

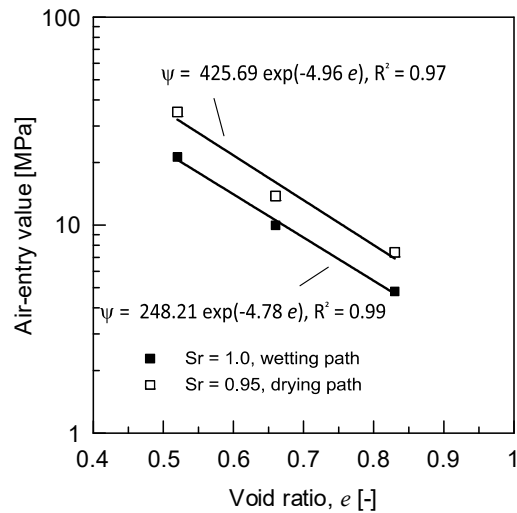


Fig. 2.27: Evolution of air-entry suction values with void ratio and the total suction at which the samples reach fully saturation.

### 2.3.3.3 Reproducibility of the technique

In order to investigate the reproducibility of the obtainable results, the water retention curves at three void ratios ( $e = 0.83$ ,  $0.65$  and  $0.53$ ) were repeated along the wetting path and the results are shown in Fig. 2.28. The obtained curves result in an excellent agreement with the first ones. This circumstance confirms the high resolution and good repeatability of the method.

Dueck (2004) reported data on the retention behaviour of Wyoming in free volume conditions in terms of water content versus relative humidity at controlled temperature. The method consisted in a controlled total suction technique which involves placing several samples in glass jars above the surface of different salt solutions.

Equivalent total suction values have been computed using Eq. 2.6 and the results are reported in Fig. 2.29 along with the retention domain identified by the Micro-cell method. The figure shows that the retention domain embrace well also data obtained in free volume condition; the lack of data on the volumetric behaviour during these suction changes in free volume does not allow a compression in terms of degree of saturation for this data set. In addition, the results of water retention behaviour in a main wetting path on Wyoming bentonite material reported by Delage et al. (2006) and Villar (2007) at a given void ratio are added to this plot. The results are found in the domain determined by Micro-cell in the present study. The Micro-cell method provides a more precise representation of the retention behaviour due to the possibility of including a large number of experimental points along the wetting and drying paths. In the cases of the total suction control techniques, the numbers of data points are limited to the number of salt solutions used to control the relative humidity of the system.

Moreover, the methods based on the suction control technique, involve a slow transfer of water to or from the sample through pure diffusion and the equilibrium is usually obtained after a long time of a couple of months particularly for the main wetting path, while the Micro-cell allowed to obtain each point in a couple of days.

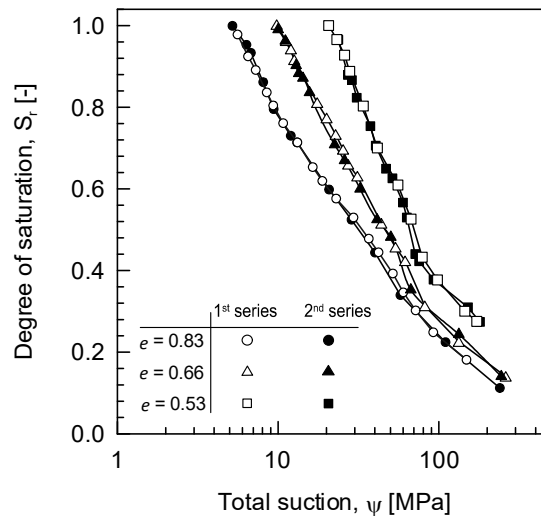


Fig. 2.28: Repetition of the determination of the retention behaviour for different void ratios.

#### 2.3.3.4 Retention behaviour in wetting and drying cycles

It is commonly agreed that for a given void ratio, any possible hydraulic state will be belted in between the main wetting and main drying curves, and the scanning curves describe the transition from a main wetting to a main drying conditions or vice-versa. The wetting/drying cycles are important to be considered when suction cyclic variations are expected in the bentonite used for buffer material in radioactive waste repository barriers. There are no experimental data showing scanning paths for the compacted Wyoming bentonite. For this reason, a series of tests were carried out with the aim of investigating the water retention behaviour in wetting and drying cycles. Tests were performed on samples compacted at  $e = 0.53$  ( $\rho_d = 1.80 \text{ Mg/m}^3$ ). A similar path as showed in Fig. 2.30 was initially followed. The compacted sample was wetted in steps (path A – B – C – D) until full saturation was reached (point D). The main drying was then initiated until a suction value of 95 MPa was reached (path D – E). At this stage, a wetting path (E – F) was imposed reaching again full saturation. Drying was then initiated once more until a suction of 174.5 MPa (point G) and a final wetting was performed until a degree of saturation of 0.95 was reached (point H).

It is observed that the first (D – E) and the second drying path (F – G) are aligned, while after the first wetting (A – D), the material does not follow the initial wetting curve and a new main wetting curve has been created (G' – H).

Before this new main wetting path is reached, scanning curves can be clearly observed (E – E' and G – G'). The results suggest that during the first wetting the material experienced a significant and irreversible modification in the retention behaviour; in particular, after this first saturation, the retention capacity of the material increased in the sense that more water can be stored in the bentonite for a given suction in a wetting path. This observation has a strong impact when the retention behaviour is considered in the design of the engineered barriers. As seen, the full saturation of the material under constant volume conditions resulted in creating a new wetting path for the next hydration cycles.

This phenomenon happened when approaching the first saturation at high degrees where the swelling pressure reached the maximum value. For smectite-based clays, the swelling pressure at a low suction range increases at its highest and in hyperbolic form with a suction decrease (Kassiff & Shalom 1971, Wang et al. 2012). The overall description of the wetting/ drying

episodes is summarised in Fig. 2.31a. In addition, the water retention behaviour on a sample compacted to the same void ratio of 0.53 is plotted in Fig. 2.31b. The results of the previous test were also shown in this plot in grey colour. This water retention test aims at evaluation of the hysteresis response of the material at three different points along the first wetting path. When the material reached degree of saturations of 0.38, 0.62 and 0.88 (points A', B and C), drying paths followed by scanning curves were carried out. As seen, the material exhibits a reversible behaviour in A – A' – A'' path. Then at point B and C corresponding to Fig. 2.31a, a drying and scanning path were performed. The similar behaviour is observed in path B – B' – B and C – C' – C where the material returns to the initial wetting path after drying to B' and C'. As seen the scanning paths are following the initial wetting path.

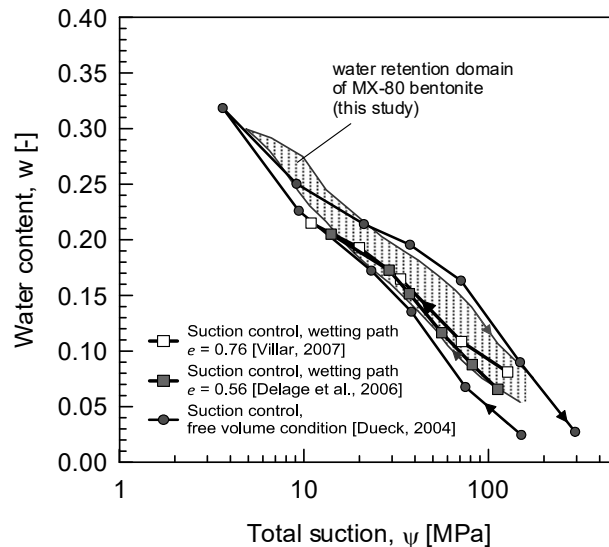


Fig. 2.29: Comparison of water retention curves obtained by suction measurement and suction control techniques.

At point D corresponding to a total suction of  $\psi = 20.6$  MPa, the hydraulic hysteresis followed the creation of a new wetting path. This evolution resulted in a significant increase in the retention capacity that could have a notable remark on the evaluation of the water retention behaviour of buffer at different points of the repository lifetime. This observation could not be explained without an insight into the microstructure of the bentonite material at different stages of the performed hydraulic path. In Chapter 3, the ability of the Micro-cell to provide representative specimens for the microstructural investigation is utilised to perform a systematic analysis of the evolution of the fabric of the material during the wetting and drying cycles.

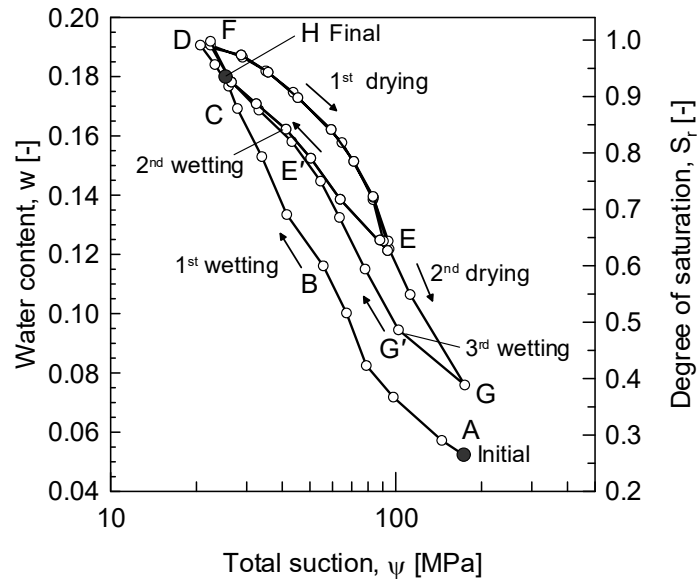


Fig. 2.30: Hysteresis water retention curve of highly compacted Wyoming granular bentonite.

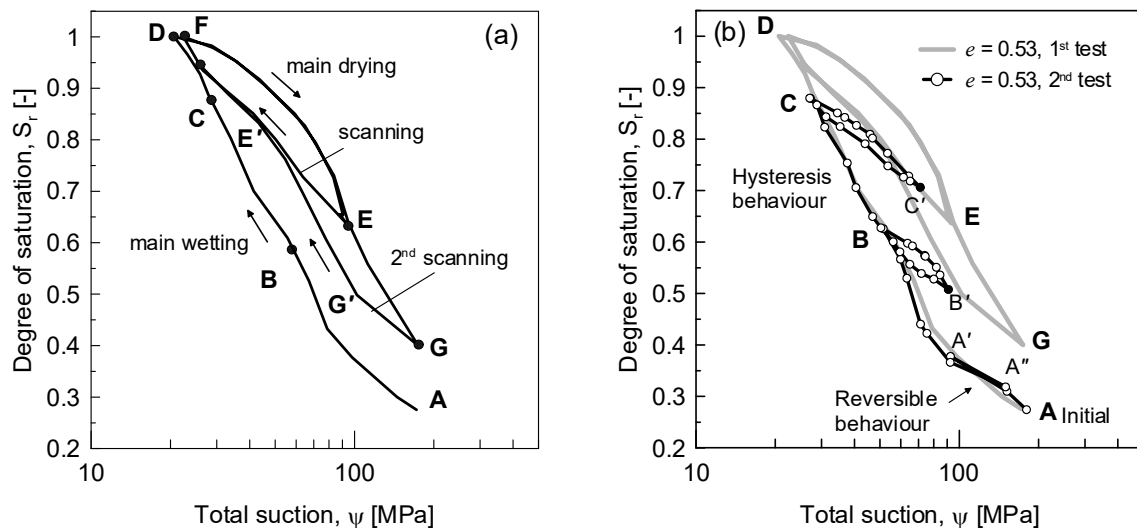


Fig. 2.31: Water retention behaviour of highly compacted bentonite in reversible regions.

### 2.3.3.5 Effect of confinement on retention behaviour

A complementary test to observe the unconfined water retention behaviour of Wyoming bentonite was performed and the results are presented in Fig. 2.32 in terms of water content and total suction. The sample was prepared at an initial void ratio of  $e = 0.83$ . The water retention behaviour of the material in the unconfined condition was determined based on a controlled wetting/drying process and the measurement of the total suction with the psychrometer.

The water retention curves of the material under the confined conditions are also shown in Fig. 2.32. The retention behaviour of the poured specimen at  $e = 0.83$  under confined and unconfined conditions imply that both curves are aligned until the total suction at which the confined specimen reaches the fully saturated state ( $\psi = 4.85$  MPa). At lower suction values, there is a divergence in the confined and unconfined retention behaviour because the unconfined

material is able to adsorb water as suction decreases, while this possibility is hindered for the confined conditions. The water retention curves at void ratios of  $e = 0.66$  and  $e = 0.53$  are also shown in this figure. In case of confined conditions, each sample reached a total suction corresponding to the given void ratio at its fully saturated state.

It is worth mentioning that there is a linear trend in this semi-log plane up to the mentioned point (c) in the region  $ac$  in Fig. 2.32. After point  $c$ , the water retention curve of the unconfined sample diverges in a power trend (region  $c - d$ ). Besides, there is no observable hysteresis behaviour in the retention curve for part  $c - d$ , and it becomes more visible at higher total suctions than 20 MPa. The reason for the lack of hysteresis behaviour in this region will be more analysed in Chapter 3 after introducing the hydration mechanism at the smectite particle levels.

The free volume retention curve after point  $c$  in Fig. 2.32 was obtained using a pressure plate apparatus. The pressure plate apparatus includes a saturated ceramic disc with a known high air-entry (HAE) value. The ceramic disc is usually installed inside a steel vessel pressurised by the air. There are pressure transducers for measuring both the air inside the vessel and the water pressure in the drainage lines beneath the ceramic disc (Richards 1941). The schematic cross section of the pressure plate system including the material and HAE disc is shown in Fig. 2.33. The apparatus works based on the axis translation technique by providing an increase in air pressure equal to the increase in matric suction ( $s = u_a - u_w$ ) at a given water pressure.

The ceramic plate used in this research was designed for an air-entry pressure of 1 MPa. The bentonite samples with known initial water contents were placed on the HAE plate under the applied matric suction. After reaching equilibrium, the water contents of the samples were measured by an oven-drying process. The corresponding measurements were then plotted in Fig. 2.34. It is seen that the results are presented in terms of total suction with the assumption that the capillary mechanism is the major term of the total suction. Accurate evaluation of the total suction term in this region required the knowledge on the osmotic suction term of the bentonite material.

Arifin & Schanz (2009) evaluated the osmotic suction of a Calcigel bentonite (50 – 60 % of Ca-Mg smectite content) by means of the squeezing technique. The technique uses the relationship between electric conductivity and osmotic pressure of a salt solution to calculate the osmotic suction values. The obtained values are presented in Fig. 2.35. The water retention behaviour of Calcigel bentonite with respect to different suction terms is shown in this figure. Total and matric suctions were obtained using the non-contact and contact filter paper methods, respectively. The filter paper method for measuring matric and total suction is described in ASTM D 5298-94 (1994). As observed in Fig. 2.35, a constant osmotic suction value of about 40 kPa was found from the experimental results for water contents higher than 30 %. The osmotic suction term is found negligible with regard to the variation of the total suction versus water content.

It is also observed that the osmotic suction values obtained from the squeezing technique are lower than the values computed from the total suction minus the matric suction. Arifin & Schanz (2009) suggested that the value obtained from total suction minus matric suction using the filter paper method could be associated with the osmotic suction and hydration forces.

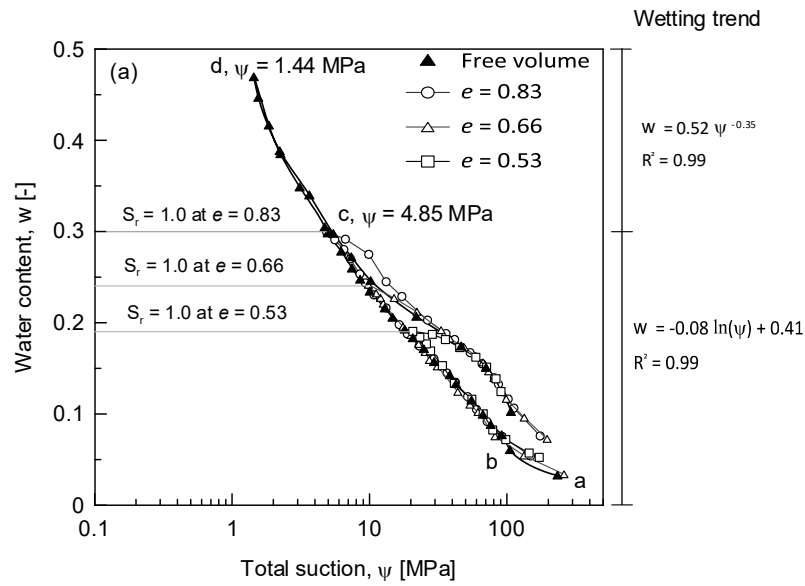


Fig. 2.32: Effect of confinement on the water retention behaviour.

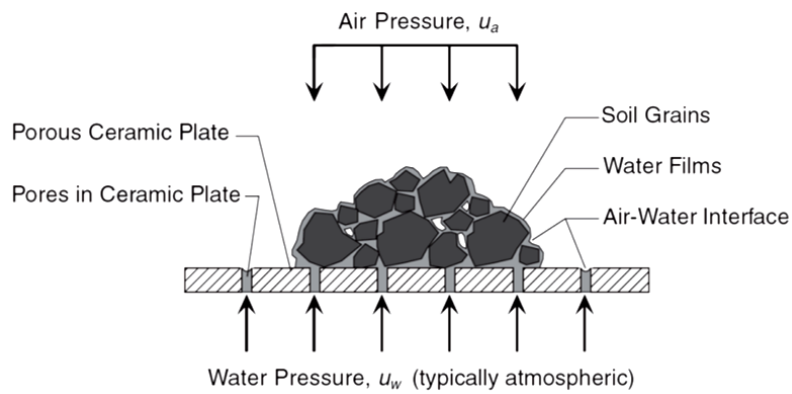


Fig. 2.33: Schematic cross section of the interface between unsaturated material and HAE disc in a pressure plate apparatus (Lu & Likos 2004).

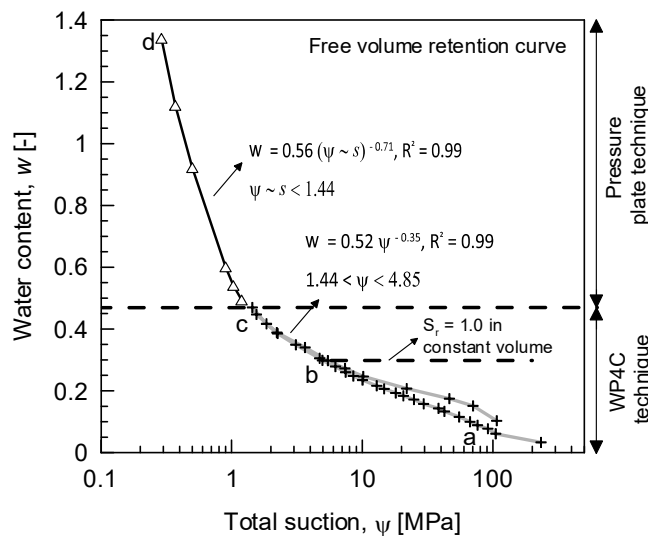


Fig. 2.34: Retention behaviour of Wyoming bentonite under free volume conditions.

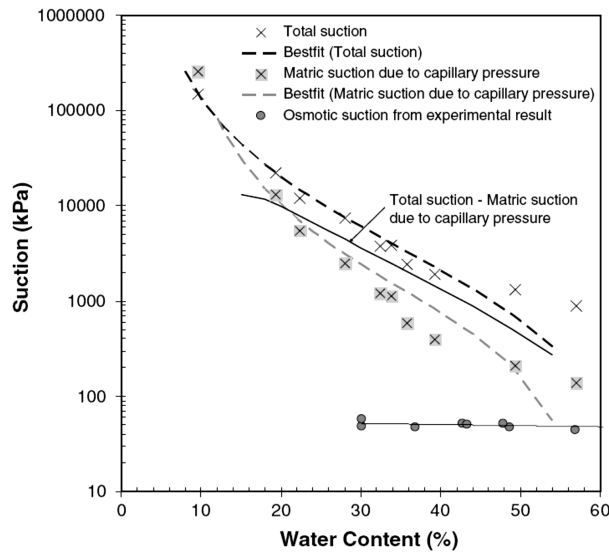


Fig. 2.35: Total suction, matric suction and osmotic suction terms of compacted Calcigel reported by Arifin & Schanz (2009).

### 2.3.3.6 Effect of granulometry on retention behaviour

As it was mentioned in Chapter 1, in the Swiss concept for a repository for spent fuel and high-level waste, the canisters containing the waste are supported on the bentonite blocks, with the space around the canisters subsequently filled up by granular bentonite. Bentonite blocks are usually manufactured with a bulk density of  $2.1 \text{ Mg/m}^3$  by compacting bentonite powder with a water content of 8 – 14 % upon a pressure of 100 MPa resulted in dry density varying in the range of  $1.84 - 1.94 \text{ Mg/m}^3$  (Pusch 1992).

However, in the Swiss concept the bentonite blocks are planned to be used under higher water content and lower dry density ( $w = 15 \%$ ,  $\rho_d = 1.72 \text{ Mg/m}^3$ ). These conditions were considered due to the observation of an instability in the bentonite blocks with a water content of  $w = 10.1 \%$  and a dry density of  $\rho_d = 1.87 \text{ Mg/m}^3$  few hours after the emplacement under repository-like conditions. The instability was associated with the cracking and splitting of the blocks upon the relative humidity in the tunnels.

The water retention curve of compacted bentonite powder (grain size smaller than 0.25 mm) was obtained using the Micro-cell. The sample was supposed to present the bentonite block. The grain size distribution of the granular material is plotted along with the powder material. Fig. 2.36b presents the water retention behaviour of Wyoming granular and compacted powder bentonite materials. The influence of the granulometry was found to be negligible, except that the water retention curve of the compacted powder seems smoother in the wetting path. This observation confirms that the as compacted density is the controlling parameter in the water retention behaviour of Wyoming bentonite. The main difference between the fabric of the compacted granular and powder bentonite is the size of the macropores formed during the compaction. It can be expected that the compacted granular materials have bigger macropores with respect to the compacted powder. However, it seems that the size of the macropores is not influencing the retention behaviour. Such interpretation requires informations on the microstructure of the compacted bentonite material. This topic will be analysed in detail through microstructural investigation techniques in Chapter 3. It will be shown that the water retention behaviour of bentonite material at the as compacted state is controlled by the micropores that are not influenced by the grain size distribution or the compaction state.

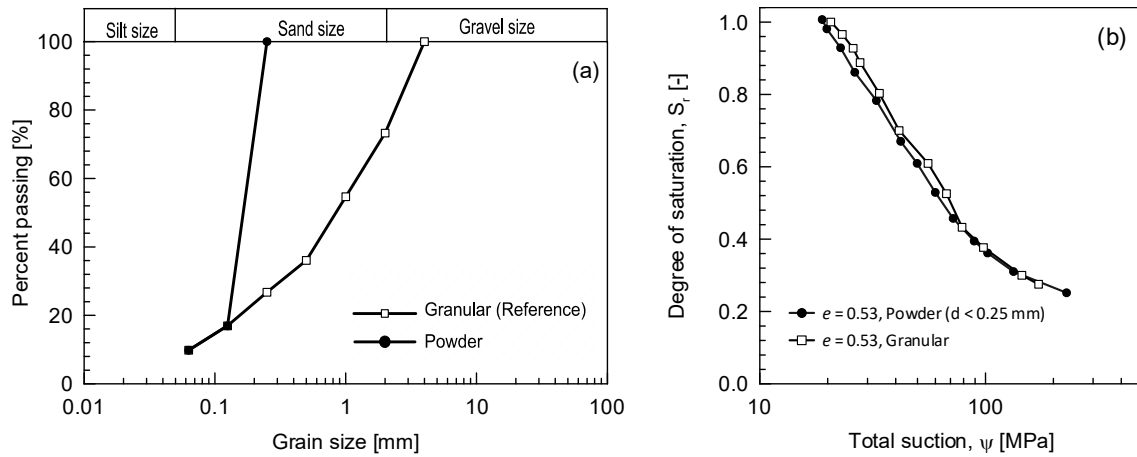


Fig. 2.36: (a) Apparent grain size distribution of the granular and powder bentonite samples, and (b) comparison of the retention behaviour compacted at the same void ratio ( $e = 0.53$ ).

### 2.3.3.7 Effect of temperature on retention behaviour

The influence of temperature can be analysed using Micro-cell up to 40 °C corresponding to the maximum adjustable temperature in the WP4C device. The water retention curves of Wyoming granular bentonite at a void ratio of  $e = 0.83$  were determined for two temperatures of 22° and 40 °C (Fig. 2.37). The influence of temperature in this range was found negligible. The Micro-cell containing the granular bentonite was kept in a controlled temperature humid chamber at 40 °C and after each step of the wetting and drying, the total suction was measured using the WP4C device.

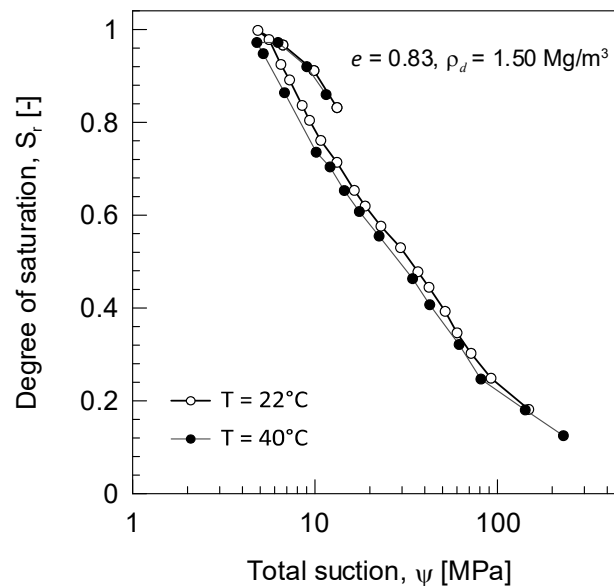


Fig. 2.37: Influence of temperature on the retention behaviour of Wyoming granular bentonite using the Micro-cell technique.

In order to determine the retention curve of the material under higher temperatures, the sorption bench device (Salager et al. 2010) was used. The Micro-cell was used in combination with the sorption bench to apply a constant volume condition to the material during the experiment. Fig. 2.38 describes the general scheme of the sorption bench system (Salager et al. 2010). The system enables testing of several samples at eight different controlled-suction desiccators to impose a certain relative humidity at a given temperature. The relative humidity values were controlled using saturated salt solutions inside the desiccators. The desiccators were immersed into a controlled temperature bath. A precision balance is located on top of the frame allowing continuous weighting of the hanged samples without disturbing the system. Tab. 2.3 lists the different salt solutions used in this study to determine the water retention curve of bentonite at 80 °C.

Tab. 2.3: Relative humidity and total suction values resulted from saturated and partly saturated salt solutions.

	Salt *	Compound	$a$ [%]	$b$ [K]	$RH$ [80 °C]	$\psi$ [80 °C]
1	Lithium Chloride	LiCl	14.53	-75	0.117	349.31
2	Magnesium Chloride	MgCl <sub>2</sub>	29.26	34	0.322	184.77
3	Magnesium Nitrate	Mg(NO <sub>3</sub> ) <sub>2</sub>	25.28	220	0.471	122.70
4	Potassium Iodide	KI	29.35	254	0.603	82.65
5	Sodium Chloride	NaCl	69.2	25	0.743	48.51
6	Potassium Chloride	KCl	49.38	159	0.775	41.66
7	Potassium Sulphate	K <sub>2</sub> SO <sub>4</sub>	86.75	34	0.955	7.48

\* Data from Romero (2001)

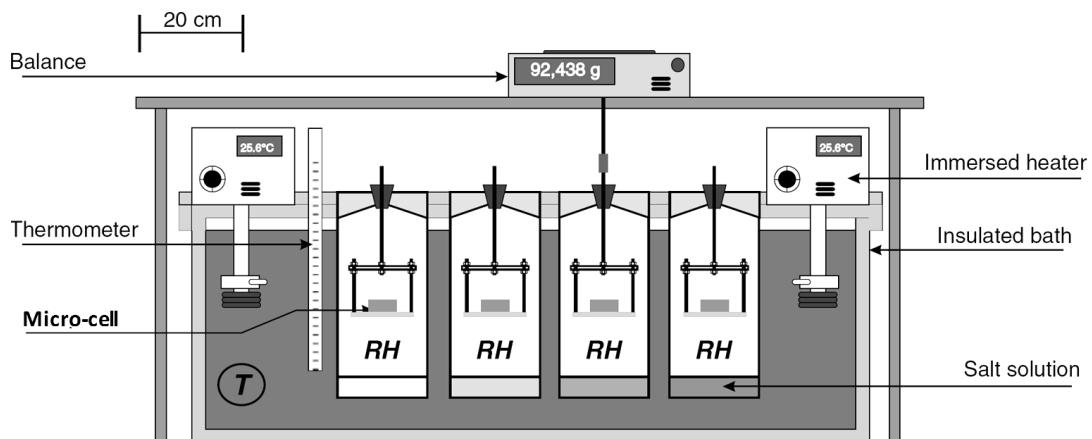


Fig. 2.38: Schematic cross section of the sorption bench (Salager et al. 2010).

The dependency of the relative humidity with temperature,  $T$  (K), is expressed by  $RH = a \exp(b/T)$ , where  $a$  and  $b$  are the parameters mentioned in Tab. 2.3 (Romero 2001). The total suction values were calculated using Eq. 2.6.

In order to determine the water adsorption at this temperature, Micro-cell containing a granular bentonite sample at  $e = 0.83$  was first rested in desiccator number 2 (Tab. 2.3) to tackle a wetting path. After the material reached an equilibrium state, the Micro-cell was moved to the next desiccators with lower suction values as shown in Tab. 2.3.

The evolution of the degree of saturation of the sample with respect to time is depicted in Fig. 2.39. When the material reached the maximum attainable degree of saturation, a drying path was initiated by moving the Micro-cell to desiccators with higher total suctions. The water retention curve obtained at a temperature of  $80\text{ }^{\circ}\text{C}$  is compared with the one at  $22\text{ }^{\circ}\text{C}$  in Fig. 2.40. The results are presented in terms of water content and degree of saturation with respect to the imposed relative humidity at  $80\text{ }^{\circ}\text{C}$ . The results from the Micro-cell are also converted to the relative humidity using Eq. 2.6. Such presentation reveals an important feature of the bentonite material. As discussed in section 2.4.3.1, full saturation was defined when the material reached a degree of saturation of 1.0 and the total suction could reach a value depending on the compaction void ratio. For instance in the case of  $e = 0.83$ , a total suction of 4.85 MPa at  $S_r = 1.0$  was measured which is corresponding to a relative humidity of 96 % (Eq. 2.6). On the other hand, it was shown that even by imposing a relative humidity of 100 % it would not be possible to decrease the total suction (Fig. 2.26). The increase of the water content and consequently decrease in the total suction of the sample were hindered by using the Micro-cell which imposes a constant volume condition. This implies that the total suction of the material is different from the imposed suction at which the material reached the equilibrium in terms of water content. The difference between the applied relative humidity and the corresponding relative humidity from the measured total suction can be referred as a potential for the compacted bentonite material at a given void ratio. Thus, in order to decrease the total suction upon the imposed relative humidity of 100 %, an increase in void ratio should be provided as experimentally presented in Fig. 2.32.

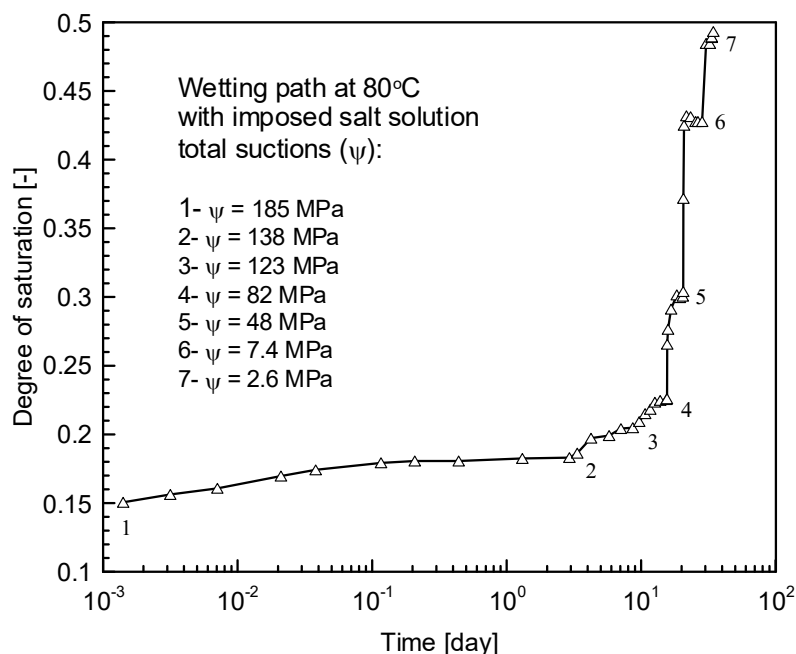


Fig. 2.39: Evolution of the degree of saturation of the sample inside the Micro-cell in sorption bench at  $T = 80\text{ }^{\circ}\text{C}$ .

The implication of this observation criticises the application of the vapour control/transfer technique for the compacted bentonite material. This technique assumes that the total suction of the geomaterial reaches the imposed one after the equilibrium in the transferred mass, while the observations using the Micro-cell question this assumption. In the water retention curve at 80 °C it was assumed that the applied relative humidity is equal to the one of the sample after equilibrium in water content. However, it is believed that the corresponding total suction of the material is lower due to the above discussion.

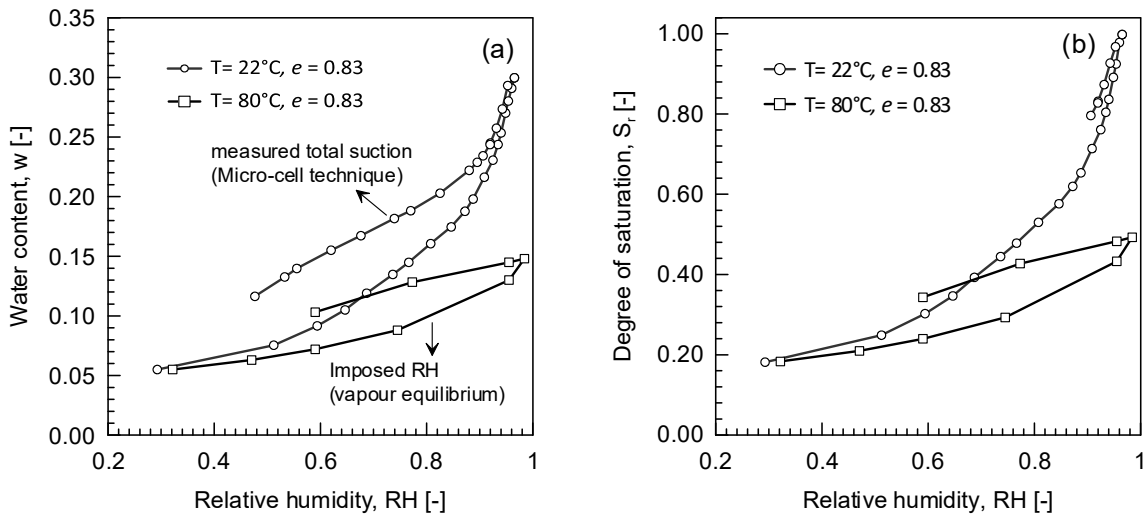


Fig. 2.40: Influence of temperature on the retention behaviour of bentonite combining Micro-cell and sorption bench.

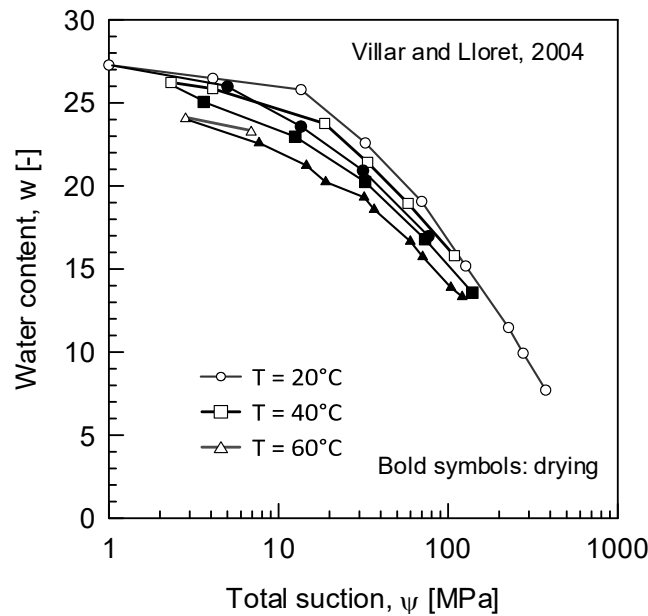


Fig. 2.41: Influence of temperature on the water retention behaviour of FEBEX bentonite with dry density of  $1.65 \text{ Mg/m}^3$  (Villar & Lloret 2004).

In Fig. 2.40b it can be observed that the retention behaviour in terms of degree of saturation was plotted in a whole drying path at 80 °C while this could not be possible for the curve at 22 °C. In fact, the sample can reach a fully saturated state at the lower temperature. Thus, the sample will experience a shrinkage followed by the loss of the lateral contact in the drying path. This does not allow the presentation of the results in terms of degree of saturation for the drying path, but in terms of water content (Fig. 2.40a). For the case of 80 °C, the sample was observed to be still in contact with the cell at the end of the drying path. Therefore, the retention curve can be expressed in terms of degree of saturation as well.

In terms of influence of temperature, the retention capacity of the material decreased by about 49 % of the full saturation obtained at 22 °C. Villar & Lloret (2004) and Villar et al. (2010) presented the water retention behaviour of FEBEX bentonite obtained from a controlled-suction cell at different temperatures (Fig. 2.41). A decrease of the retention capacity is observed due to a temperature increase. It seems that the retention capacity will decrease dramatically when the temperature approaches the boiling point of the water. The influence of temperature on the retention potential of bentonite clays is attributed to the decrease of the hydration capacity of the smectite particles and the osmotic potential (Pusch & Yong 2006).

## 2.4 Summary and conclusions

The following achievements are presented with regard to the content of this chapter from the macroscopic characterisation analysis of the Wyoming granular bentonite:

- The granular bentonite with the proposed apparent grain size distribution has enough pourability to reach the dry density of 1.5 Mg/m<sup>3</sup> without any compaction effort. The material does not exhibit segregation upon this granulometry that provides enough workability and suitability with regard to its particular application as buffer material. This feature is related to the well-graded granulometry and the presence of the fine fractions that coat the bentonite grains.
- The granular bentonite is manufactured and emplaced at its hygroscopic water content ( $w = 5 - 6\%$  at  $RH = 35 - 45\%$ ) with very high total suctions in the range of 100 – 200 MPa. The influence of the compaction stress on the grain size distribution curves at hygroscopic conditions was found to be negligible. However, the bentonite grains show a tendency to exfoliate or break down in smaller aggregates at lower suctions. However, any hydration will have taken place after the emplacement of the granular material under hygroscopic conditions.
- The granular material has a high water activity and swelling potential. A liquid limit of  $w_l = 4.2$  and a high swelling up to a void ratio of  $e = 4.26$  were obtained. A swelling pressure of 3.5 – 4.0 MPa was measured at the lowest dry density.
- Static compaction upon constant water content influences the total void ratio, but not the total suction. Thus, the degree of saturation increases in constant total suction due to a void ratio reduction. Further insight into the microstructural features and the governing water adsorption mechanisms are required to interpret these observations (see Chapter 3). Although the compressibility of the material increases with a suction decrease, a much higher maximum stress is required to assess the target density. This is directly associated to the swelling deformation at lower suctions. The initial saturation of bentonite either under confined or free swelling conditions takes the material to the normally consolidated condition.
- Analysis of the water retention behaviour of granular bentonite using the Micro-cell technique reveals that the water retention curves at different dry densities are aligned in the plane of water content versus total suction. However, the variation of total suction at which

the compacted sample reaches the full saturation state and the air-entry values are an exponential function of the void ratio. Besides, all the possible retention path of compacted bentonite samples were found to be embraced by a hydraulic domain created by the material at the void ratio obtained at poured conditions.

- Water retention behaviour of the compacted granular bentonite indicates an irreversible and permanent change of the wetting path for higher degree of saturations than 90 %. For lower degree of saturations, the initial wetting path remains stable for the wetting – drying cycles. After the fully saturated state, although all drying paths are aligned, a new wetting path is created. This wetting path permanently replaces the first wetting path.
- The influence of the confinement on the retention behaviour revealed a direct relationship between the total suction at which the sample reaches the fully saturated state and the given void ratio. In order to decrease the total suction at saturation, the void ratio should increase. Consequently, the material will absorb water and increase the volume until reaching the new void ratio and the corresponding total suction. The granular material even at the lowest dry density (without compaction) reaches a total suction of 4.85 MPa in the fully saturated state. This total suction is corresponding to a maximum water content of 30 %. Further adsorption of water cannot be obtained under constant volume conditions despite of the tendency of the material to adsorb water.
- The influence of the apparent grain size distribution on the water retention behaviour of Wyoming granular bentonite was found to be negligible. This implies the existence of an adsorption mechanism that is governing the retention behaviour and is not influenced by the apparent grain size distribution.
- The effect of temperature showed that under high temperatures of 80 °C, the retention capacity was decreased by about 50 %. This reduction in retention capacity is attributed to the decrease in osmotic potential and the hydration capacity of the material under higher temperatures.

### 3 Experimental characterisation of the microscopic behaviour of Wyoming granular bentonite

This chapter is dedicated to the experimental characterisation of the hydro-mechanical behaviour of Wyoming granular bentonite at the microscopic scale. The chapter begins with an introduction to the microstructural features of active and non-active clay minerals in terms of crystalline structure and the clay – pore water interaction within the minerals. The concepts behind the swelling mechanisms in active clay minerals and in particular in smectite clay (main component of Wyoming granular bentonite) are presented. The consolidation behaviour of bentonite is compared with non-active clay minerals as kaolinite and illite. The microstructural features of the granular bentonite are presented in the light of different techniques of Mercury Intrusion Porosimetry (MIP), Scanning Electron Microscopy (SEM) and Focused Ion Beam nanotomography (FIB-*nt*). The MIP and SEM analyses were performed in the Laboratory of Construction of Material (LMC) and the Interdisciplinary Centre for Electron Microscopy (CIME) of EPFL. FIB-*nt* was performed at the Centre for Imaging Science and Technology (CIMST) of ETH Zurich. For the last experiment related to FIB-*nt*, the author was involved in the microsample preparation of bentonite material through collaboration with Zurich University of applied Sciences and ETH Zurich.

These techniques are used to observe arrangements at the particle level and to analyse the pore size distribution. The obtained information provides an insight into the microstructure of the material and enables to interpret and correlate the macroscopic hydro-mechanical observations to the microscopic features. The microstructure of the compacted Wyoming granular bentonite during wetting and drying paths is studied using MIP and SEM tests on the representative samples provided by the Micro-cell (see Chapter 2). The FIB-*nt* method is also used to analyse the fabric evolution during uptake of water where the free swelling condition is allowed. Thus, a particular response of Wyoming bentonite in terms of permanent microstructural modification and its influence on the water retention behaviour is well captured in this chapter. To prove this particularity, the microstructure of compacted Wyoming bentonite is compared with illite, a non-active clay mineral, which has a similar crystalline composition as smectite. The experimental observation provides a sound basis for the modelling of the water retention behaviour of compacted bentonite which is the objective of Chapter 4.

#### 3.1 Fabric and structure of geomaterials

Geomaterials are composed of particles arranged in packets or groups. The term fabric or structure is referring to the arrangement of particles, groups and pore spaces in the material. The particle arrangement in different soils includes a variety of forms. Collins & McGown (1974) identified three main groups of fabric elements:

1. Elementary particle arrangements: the single forms of particle interaction at the level of individual clays, silts or sand particles
2. Particles assemblage: units consisting of one or more elementary particle arrangements with defined physical boundaries and specific mechanical function
3. Porosity

Schematic representations of each of the fabric features in the above mentioned classes are shown in Fig. 3.1.

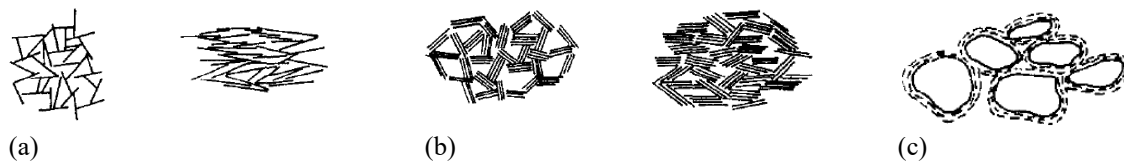


Fig. 3.1: Schematic representation of elementary particle arrangements (Collins & McGown 1974): (a) individual clay lamella or platelet, (b) clay platelet group interaction, and (c) clothed silt or sand particle interaction.

The term stack or particle is a packet of parallel clay platelets. Clay aggregate is basically referred to an arrangement of several stacks. A cluster or assemblage is defined as a group of particles or aggregates into large fabric units. For geomaterials consisting of groups of assemblages, it is common to refer to the inter-assemblage and intra-assemblage porosities. The total void ratio is defined for the whole assemblage. The fabric of geomaterials is generally considered in three levels of scale (Mitchell 1993):

- a) Microfabric: refers to aggregations of particles and the small porosity within them
- b) Minifabric: assemblage of microfabric and the inter-assemblage porosity between them
- c) Macrofabric: this term addresses cracks, fissures, root holes, laminations etc. that refer to the trans-assemblage pores

In this research, the term fabric is referring to levels (a) and (b) and the voids created by fissuration or cracks are not considered. The microfabric is associated with the micropores and minifabric is defined as macropores. In this way, the microstructure here is referred to as the arrangement of the constituent particles and the porosity. The delimiting between these two levels of macro- and micropores is considered based on the microstructural observations and the distribution of the porosity within the material structure.

Wyoming granular bentonite is composed of smectite clay minerals. In order to analyse the particular features of bentonite, it is important to have an insight into the crystalline composition of the smectite. In the following section the microscopic structure of the clay family minerals highlighting the particular features of smectite is presented.

### 3.1.1 Crystalline structure of clays

The smectite or montmorillonite clay mineral is the essential component of Wyoming bentonite. In general, clays are primarily formed of crystalline minerals. The minerals are composed of two basic units of silicon tetrahedrons and aluminium octahedrons (see Fig. 3.2a). These mineral groups are characterised by stacking arrangements of sheets of the basic units. The silicon tetrahedron sheet is referred to as silica sheet and aluminium octahedrons as gibbsite sheet (Mitchell 1993). The simplified views of the silica and gibbsite sheets are commonly used to represent the elements of a basic unit cell of clays (Fig. 3.2b).

There are basically two types of composite layer structures (Reeves et al. 2006) defined as:

- a) Two layer or 1:1 type represented by the kaolinite and serpentine groups characterised as to be composed of one silica and one alumina sheet. The basic unit layers are bounded together by the means of hydrogen bonding (Fig. 3.2b). Thus, water molecules or ions cannot permeate the interlayer between adjacent kaolinite layers and the colloidal properties are associated with the external layers only (Barden & Sides 1970).

- b) Three layer or 2:1 type represented by the illite, smectite, vermiculite and chlorite groups. In the case of illite, the negative charge of the planar surface is balanced by potassium ions. For smectite minerals, the negative charge is balanced by exchangeable cations within the interlayer. In smectite clays, the weak bonding between successive layers results in separation of the layers (Fig. 3.3a), while in illite, the layers are strongly held together by the presence of potassium ions (Fig. 3.3b).

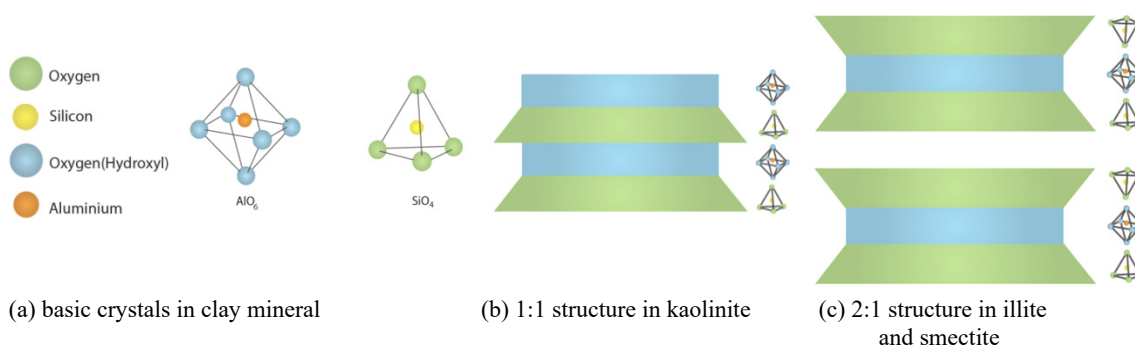


Fig. 3.2: Crystal constitution of clay minerals: (a) aluminium octahedral and silicon tetrahedron units, (b) basic unit layers for kaolinite, and (c) smectite or illite.

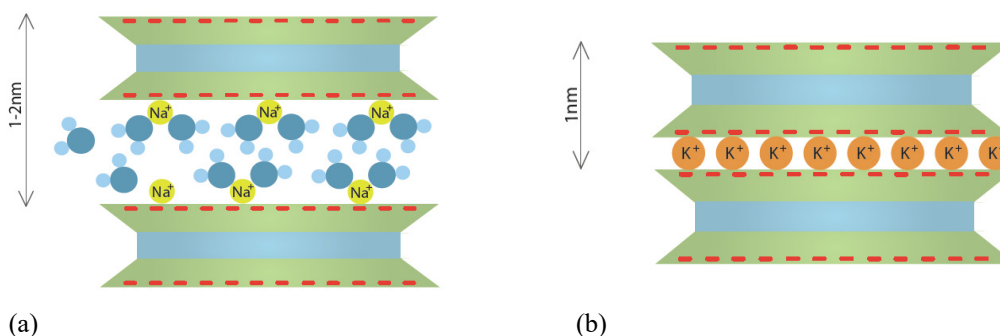


Fig. 3.3: Crystal constitution of 2:1 structure clays: (a) weak bonding between successive layers in smectite clay minerals, and (b) collapse of interlamellar space by the presence of potassium in illite.

Due to isomorphous substitution in the crystal, the clay minerals are negatively charged on the surfaces. This negative charge must be balanced by an extra cation that can be replaced by other cations. Therefore, these cations are called 'exchangeable' cations. The total number of the exchangeable cations is referred to as cation exchange capacity (CEC). It is worth mentioning that for the kaolinite and illite minerals, the exchange capacity originates from the external surfaces of the stacks, while this feature is extended for smectite minerals also within the interlamellar surfaces.

Dispersed systems like clays are known for their high surface area per unit mass. The specific surface relates to the surface area per gram or per cubic centimetre of a dispersed system. Colloidal clay (diameter  $< 0.1 \mu\text{m}$ ) performs 20 times the surface area than the same weight of silt and 1000 times the surface of a very fine sand (Mitchell 1993). The smectite minerals have a very large specific surface. The specific surface excluding the interlayer regions varies between

50 and 120 m<sup>2</sup>/g and the surface of the expanded lattice can rise up to 840 m<sup>2</sup>/g. The lamellae or platelet basically do not exist as single units, but they form stacks which establish clay aggregates (Mitchell 1993).

Wyoming bentonite contains more than 85 % Na-smectite clay. The mineralogical composition of Wyoming granular bentonite reported by Plötze & Weber (2007) is presented in Tab. 3.1. The general characteristics of smectite, illite and kaolinite clay minerals are also listed in Tab. 3.2.

For Wyoming bentonite material studied in this research, a total specific area of 523 m<sup>2</sup>/g and a specific outer surface area of 33.1 m<sup>2</sup>/g were obtained. The total surface was calculated based on the adsorbed water content, and the outer surface area was determined by the nitrogen adsorption technique (Plötze & Weber 2007). The high liquid limit and specific surface area of Wyoming bentonite compared to illite and kaolinite minerals reveal its high water activity. Also, a cation exchange capacity of 74 meq/100 g including 52.4 meq/100 g *Na* (Sodium), 13.2 meq/100 g *Mg* (Magnesium) and 1.4 meq/100 g *K* (Potassium) were measured for the smectite mineral in Wyoming bentonite.

In the next section the mineral – pore water interaction mechanisms for different clay materials are presented highlighting the particular features of smectite clay.

Tab. 3.1: Mineralogical composition of Wyoming granular bentonite (Plötze & Weber 2007).

Wyoming bentonite	Smectite	Muscovite	Quartz	Feldspar	Calcite
Content [%]	84.9	4.8	3.7	5.2	1.3

Tab. 3.2: Summary of general physical properties of the three clays studied in this research.

Clay mineral	Liquid limit $w_l$ [%]	Plastic limit $w_p$ [%]	Specific gravity $G_s$ [-]	Specific surface areas [m <sup>2</sup> /g]
Wyoming	420	65	2.74	523 †
Illite	53	30	2.77	80 – 100 ‡
Kaolinite	45 *	21*	2.65	10 – 20 †

† Plötze & Weber (2007)

‡ Santamarina et al. (2002)

\* Cekerevac (2003)

### 3.2 Clay mineral – pore water interaction

In general, the possible mechanisms for clay mineral-water interaction are known as (Mitchell 1993):

1. *Hydration bonding*: this can easily develop due to the existence of either oxygen or hydroxyl. A hydrogen ion forms a positive end of a dipole which can be attracted to the negative end of an adjacent molecule as a hydrogen bond. This bond is very strong due to the small size of the hydrogen ion.
2. *Hydration of exchangeable cations*: this mechanism becomes more important at lower water contents. Water molecules are attracted to the cations which are already attracted to the negatively charged clay surfaces. The hydration of the interlayer cations causes the interlayer crystalline swelling that characterises the smectite minerals.
3. *Attraction by London dispersion forces*: a sort of loosely Van der Waals attractive forces that could bond water molecules to the clay surfaces.
4. *Osmotic attraction*: the concentration of cations increases as the distance to the clay surface will decrease. Water molecules then will tend to diffuse towards the clay surface due to the electrostatic attraction to equalise the existing concentration. This phenomenon is known as diffuse double layer which is detailed in Section 3.3.1 and referred to as the most important feature of the smectite mineral.

The total potential of pore water is defined as the work per unit quantity to reversibly transport an infinitesimal amount of water from a reservoir at a specific elevation and atmospheric pressure to the point where the pore water exists (Mitchell 1993). The components of the total potential are usually selected as the gravitational, capillary and osmotic (or solute) potentials (Aitchison et al. 1965). The osmotic potential is the osmotic pressure of the pore water and it depends on the composition and capacity of the clay particles to restrain the movements of the adsorbed cations. This potential is negative which means that the water tends to flow in the direction in which the concentration increasing.

In practice, the pore water is generally considered to be a separate phase in soils which has the properties of bulk water. This is more evident in granular material and low plasticity clays like kaolinite (Pusch & Yong 2006). However, in saturated clays, a certain fraction of pore water is in interlamellar space and the rest in the larger void spaces. This fraction depends on the clay mineral type. For a given clay this fraction may vary in different total suction values. In a wide range of high total suction, a major part of pore water remains in interlamellar pores. The physical interaction of pore water and the mineral phase is different for these two water levels and the type of the water – mineral interaction depends on the clay mineral.

In smectite, the hydration water within the interlamellar spaces together with the water in interparticle or inter-stack establishes water that is relatively immobile. Water in the other bigger void spaces has properties similar to bulk water and is relatively mobile (Pusch & Yong 2006). Fig. 3.4 represents the proportion of the immobile water in illite or kaolinite clays compared to smectite clay at the same bulk density. In compacted illite a combination of Van der Waals attractions and the hydration of cations on the outer particle surface are the main retention components.

The two diagrams in Fig. 3.4 represent the respective proportions of pore water. This shows that a majority of pore water in smectite held in the interlamellar spaces. Depending on the distribution of water in these different levels of porosity and the type of the water – mineral interaction, clays have a different macroscopic behaviour.

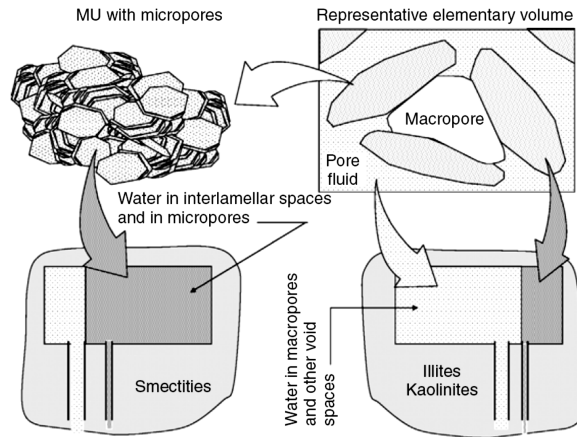


Fig. 3.4: Schematic illustration of the proportions of water in different levels of porosity.

The respective proportions of water from the representative elementary volume on top are shown in the two lower diagrams. MU stands for 'microstructural units' (Pusch & Yong 2006).

Fig. 3.5 presents the consolidation behaviour of Wyoming granular bentonite and illite. In path ABCD the granular bentonite underwent a free swelling from a void ratio of  $e = 0.83$  to  $e = 4.26$  in AB and then it is followed by the consolidation path in BC. The final void ratio, when the load is discharged, is  $e = 2.28$ .

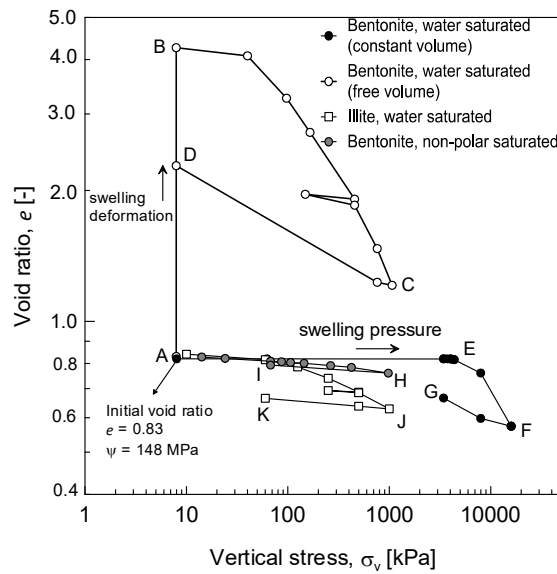


Fig. 3.5: Comparison of the consolidation behaviour of bentonite and illite.

ABCD: stress path of a bentonite sample saturated in free volume condition, AIEFG: stress path of a bentonite sample saturated in constant volume condition, AHJ: stress path of bentonite saturated with non-polar liquid, and AIK the consolidation behaviour of illite saturated with water.

The path AEFG presents the consolidation behaviour of a bentonite sample, which is initially saturated under constant volume conditions. Thus, the material reaches a swelling pressure of 4.3 MPa in AE, and then it is followed by consolidation under up to 16 MPa of vertical stress. Path AH exhibits the consolidation behaviour of granular bentonite initially saturated in non-polar liquid of kerdane. As seen, bentonite exhibits a non-active response with regard to kerdane. This is because the double layer cannot develop for a non-polar liquid like kerdane (more discussion in section 3.3.1).

Finally, path AJK shows the consolidation behaviour of a water saturated illite sample. The hydration of cations in illite does not reflect any swelling deformation in this case. Moreover, the volumetric behaviour of saturated illite is more appreciable than saturated smectite with kerdane. This could be associated with the hydration of illite minerals and the inclusion of water which cannot be established in smectite minerals saturated with kerdane.

In the next section, the concepts of diffuse double layer and the swelling behaviour of smectite minerals are presented.

### 3.2.1 Swelling behaviour and diffuse double layer theory

Swelling or active clay minerals refer to the smectite and vermiculite clays which experience large swelling deformations when saturated with water or polar liquids. The reason of such a behaviour originates from physicochemical forces of diffuse double layers of ions surrounding the clay particles. Ca-smectite can absorb up to three layers of water molecules at a relative humidity of 90 % and in some circumstances at 100 % relative humidity, Na-smectite can absorb more, i.e. up to 4 layers (Saiyouri et al. 1998 and 2004, Villar et al. 2012). This tendency of adsorption of water molecules is due to the difference in ion concentration in solution near the and away from the surfaces of the smectite particles. Thus, there is a trend for cations to diffuse away to attempt an equalisation. On the other hand, the negative electrostatic field generated from the charged surface will prevent such a tendency. This behaviour of ions to diffuse away and the influence of the electrostatic attraction result in ion distribution nearby a clay particle. The negatively charged clay surface and the distributed charge in the adjacent phase are together called *diffuse double layer* (Bolt 1955, van Olphen 1963, Müller-Vonmoos & Kahr 1983).

The Gouy – Chapman diffuse double layer theory (Gouy 1910, Chapman 1913) is the most widely used approach to associate the clay volume change due to the clay particle – water interaction (Bolt 1956, Marcial et al. 2002). In constant volume condition, this tendency results in osmotic repulsion pressure which is referred to as 'swelling pressure' (e.g. Norrish 1954, Barbour & Fredlund 1989).

According to the diffuse double layer theory, the swelling pressure is the difference between the osmotic pressure in the central plane between two clay platelets and the osmotic pressure in the equilibrium solution. In other words, the swelling pressure is the pressure required to keep the clay – water system at the required void ratio when it has access to water or a polar solution.

Although the diffuse double layer is expected to be properly developed at slurry state (Bolt 1956), many researchers have attempted to use the Gouy – Chapman diffuse double layer theory for the determination of the swelling pressure of compacted swelling clays. Madsen & Müller-Vonmoos (1985) reported a good agreement between the theoretical and experimental swelling pressures for an overconsolidated Opalinus Clay material which contains 14 ( $\pm$  4) of illite/smectite mixed layer (Nagra 2002). Komine & Ogata (1996) proposed an equation for the determination of swelling strain and pressure of a highly compacted bentonite. The equation was

developed based on the swelling mechanism for a single platelet. However, for highly compacted bentonite, the double layer thickness is less and the assumptions to develop this equation are not tenable (Tripathy et al. 2004, 2007).

An attempt was done by Tripathy et al. (2004) to evaluate the swelling pressure of several compacted bentonite materials (Wyoming, FEBEX and Montigel). This study revealed that the computed values on the basis of Gouy – Chapman diffuse double layer theory, overestimate the experimental measurements at lower dry densities, while the reverse trend was found at higher dry densities. To improve the theoretical calculation, a relationship between the non-dimensional midplane potential function,  $u$ , and the non-dimensional distance function,  $Kd$ , was established based on the experimental results. It was observed that the difference in  $u$  values (i.e. experimental minus theoretical) increased with an increase in dry densities. The difference in  $u$  values was computed and arithmetically added to the maximum theoretical  $u$  value to obtain the corrected midplane potential. Thus, the swelling pressure equation for Wyoming bentonite was proposed as follows:

$$\sigma_p = 2nkT [\cosh (-7.28 \log_{10} Kd - 2.91) - 1], \nu = 1.14 - 1.50 \tag{Eq. 3.1}$$

where,  $\sigma_p$  is the swelling pressure,  $n$  is the molar concentration of ions in the pore fluid,  $k$  is the Boltzmann's constant,  $T$  is the absolute temperature and  $\nu$  is the valency. As seen in Fig. 3.6a, good agreement was found between the swelling pressures obtained using Eq. 3.1 and the experimental measurements reported by Bucher & Müller-Vonmoos (1989).

Some researchers (Bolt 1956, Sridharan & Jayadeva 1982, Mitchell 1993, Marcial et al. 2002) have, however, pointed out and attributed some differences between experimental data and relationships derived from the diffuse double layer theory. Factors such as partially developed diffuse double layers, difference of the fabric from the concept of parallel plates, surface hydration and electrical attractive forces at particle scale, are the main reasons reported for such discrepancy.

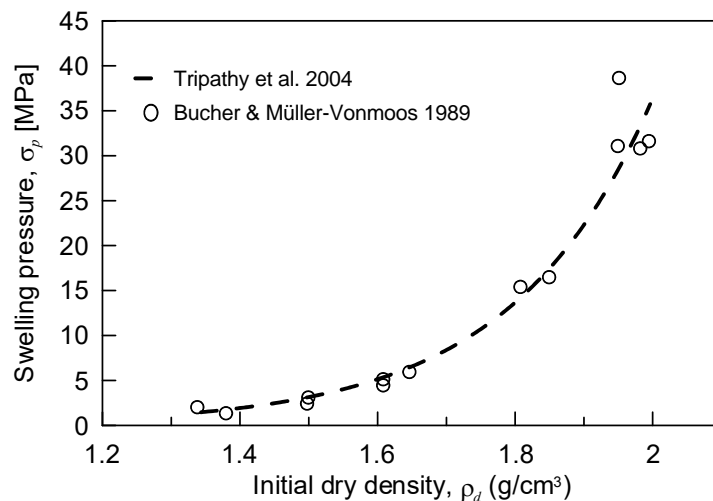


Fig. 3.6: Theoretical relationship for the swelling pressure of Wyoming bentonite with respect to the dry density (Tripathy et al. 2004) and comparison with the experimental data (Bucher & Müller-Vonmoos 1989).

### 3.2.2 Influence of temperature on clay – pore water interactions

In addition to the physical properties of water, temperature can influence the hydration forces (e.g. Pusch et al. 1990), diffuse double layer (e.g. Mitchell 1993), microstructure (e.g. Pusch & Güven 1990, Romero & Li 2005), mineralogy (e.g. De la Fuente et al. 2000, Pusch 2000) and the pore water chemistry (e.g. Arifin 2008).

The influence of temperature on physical properties of water such as density, viscosity, surface tension, dielectric constant and water vapour pressure are plotted in Fig. 3.7. The influence of temperature on the viscosity and consequently the water permeability of bentonite-based clays has been pointed out by some researchers (e.g. Pusch et al. 1990, Villar & Lloret 2004, Villar et al. 2010). On the other hand, the increase of free water (macropore water) due to a transfer of water from the interlayer pores to the macropores was mentioned as another reason of the increased permeability at elevated temperatures (Ma & Hueckel 1993). This tendency could be associated with the influence of temperature on hydration forces within clay and pore water. An increase in temperature would not influence the thickness of diffuse double layer through the decreased dielectric constant term (discussed by Mitchell 1993, Arifin 2008).

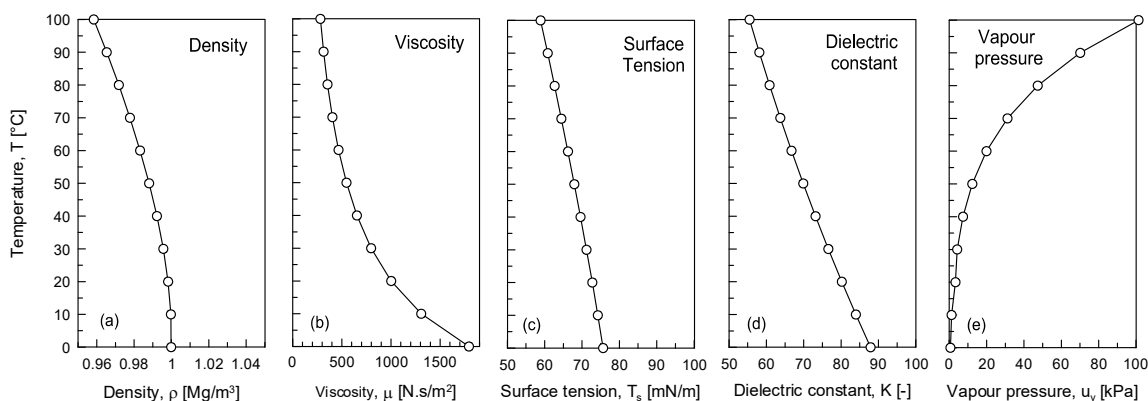


Fig. 3.7: Influence of temperature on physical properties of water: (a) density, (b) viscosity, (c) surface tension, (d) dielectric constant, and (e) vapour pressure (data from Lide 2004).

The temperature could also affect the hydration mechanism at the bentonite particle level. However, there are no evidences for the influence of heating on hydration mechanism of the smectite particles in the literature. The change of mineralogy under high temperatures could be the most important challenge with regard to the application of bentonite in nuclear waste repositories particularly near the canisters. The change of mineralogy could happen due to the illitisation of smectite in the bentonite material. A reorganisation of the crystal lattice of smectite occurs with the replacement of sodium cations by potassium cations. For the occurrence of both processes two main conditions are required: (1) a high activation energy provided by temperatures higher than 60 °C in order to reorganise the lattice and (2) sufficient quantity of available potassium. The general reaction describing this process can be written as (Pusch & Yong 2006):



De la Fuente et al. (2000) reported the illitisation process in bentonite material subjected to high temperature in the range of 120 – 160 °C for a period of more than 180 days. Illitisation would significantly reduce the swelling and water retention capacities of bentonite. In Section 3.4.7.1, the water retention of Wyoming bentonite and illite samples compacted at the same dry

densities will be highlighted. However, this section does not include the influence of induced temperature on the microstructural evolution of Wyoming bentonite material. The osmotic and hydration activities of the smectite mineral have an important impact on the hydro-mechanical response of the bentonite material. Considering these theoretical introductions, hereafter, the microstructural investigation techniques are used to have an insight into the evolutions of the fabric during the different applied hydro-mechanical stress paths.

### **3.3 Microstructural observations**

The microstructure of geomaterials can be detected by several methods depending on the type and scale of the required information. This involves the use of the particle or aggregation scale of less than 100  $\mu\text{m}$ . Microstructural observations help relating the hydro-mechanical response of the material to the observable changes of the fabric. There are different methods for the investigation of the microstructural features namely *Scanning electron microscopy* (SEM), *Environmental Scanning Electron Microscopy* (ESEM), *Transmission Electron Microscopy* (TEM), *X-Ray Diffraction analysis* (XRD), *Focused Ion Beam nanotomography* (FIB-nt), *Mercury Intrusion Porosimetry* (MIP) and *Nitrogen Adsorption Porosimetry* tests. Amongst the above mentioned methods the SEM, FIB-nt and MIP were used to investigate the microstructural evolutions of the Wyoming bentonite in this research. In the following sections, the SEM, MIP and FIB-nt test results are applied to interpret the macroscopic observations of the hydro-mechanical response of the granular Wyoming bentonite.

#### **3.3.1 Scanning Electron Microscopy (SEM)**

The clay microstructure can be evaluated by microscope. Sample preparation is an important aspect in SEM. SEM is a type of electron microscopy that produces photomicrographs of samples by scanning it with focused beams of electrons. The electrons interact with atoms in the material and produce various signals that can be detected. This signal contains information about the material's surface topography and compositions. The electron beam is usually scanned in a raster scan pattern and the position of the beam is combined with the detected signal in order to generate an image. SEM can achieve a resolution of 1 nanometre (Goldstein et al. 2003). SEM and other electron microscopy techniques require the full removal or replacement of the pore liquid. The extraction of the pore fluid should be taken without disturbance of the original soil structure. In this research, freeze drying was used to remove water from bentonite samples. The microscopic observations were carried out using a Carl Zeiss Merlin HR-SEM system. Granular bentonite accordance with the reference granulometry was first compacted to a target void ratio and then specimens were extracted from the centre of the samples and placed on the sample holder for the microscopic observation. Generally, sample preparation is more difficult for compacted granular samples at lower dry densities and water content due to their friability.

#### **3.3.2 Mercury Intrusion Porosimetry (MIP)**

##### **3.3.2.1 Pore size distribution**

Estimation of the pore size and distribution of the porous structure is an important aspect in the study of the soil structure. The deformation behaviour of the porous structure is influenced by pore and particle shape (Mitchell 1993). The number, size and continuity of the porosity structure control storage and the conductivity of fluid through the geomaterials (Olson 1985). Pore size distribution can be evaluated by water adsorption, non-polar liquid desorption,

nitrogen sorption and mercury intrusion porosimetry (Lawrence 1977). In this study MIP tests were used to determine the pore size distribution over a wide range of the porosity in the granular bentonite. Mercury, a non-wetting fluid is intruded into the pore space by increasing the applied pressure. The applied pressure can be related to the pore diameter and a pore size density distribution allowing a quantitative representation of the microstructure can be thus obtained. In the next section, the measurement principle and the mathematical formulations will be presented.

### 3.3.2.2 Measurement principle

During the MIP test a progressive pressure is applied on the non-wetting fluid mercury. Due to the applied pressure, the fluid enters into the dehydrated sample, which is placed in a vacuum chamber. The pressure is applied in subsequent steps intruding first the larger pores and then it is possible to intrude the smaller pores by applying a higher pressure. The pore size distribution can be obtained by relating the applied pressure to the pore size. MIP tests were carried out at the Laboratory of Construction of Materials (LMC) in EPFL using a combined instrument (Pascal 100+400, POROTEC, Thermo Electron Corporations porosimeter device) for measuring the pores in the range of 300  $\mu\text{m}$  to 4 nm attaining a maximum intrusion pressure of 400 MPa. Bulk density ( $\rho$ ) can be calculated from the weight difference of a dilatometer filled with mercury and the dilatometer plus the sample at 100 kPa. The apparent specific solid density ( $\rho_s$ ) can be theoretically calculated by correcting the obtained bulk density with the maximum intruded pore volume at 400 MPa. This measurement is valid upon the assumption of intrusion of all pores within the material. In the case of the existence of non-intruded pores, there is a discrepancy between the estimated densities from MIP tests and the actual ones.

Concerning sample preparation, the sample has first to be dried to eliminate the water presented in the pores, which could prevent mercury intrusion in the pore space. Another exigency related to sample preparation is that the sample has to be small enough to allow high speed freezing, so that a cryptocrystalline structure with no volumetric strain is obtained (Delage 2007). A typical size of 1  $\text{cm}^3$  is usually selected. In order to dehydrate the sample, immersion in liquid nitrogen followed by the sublimation in a vacuum freeze-dryer is considered.

A typical graph of the MIP test is presented in terms of pore size density (*PSD*) function, which is used in the detection of the dominant pore modes of the material and also the cumulative void ratio associated with the intruded porosity within the structure. Aside the *PSD*, the MIP has also been used to attempt the quantitative derivation of the matric suction with respect to the degree of saturation or water content (Romero & Simms 2008). Considering that mercury is a non-wetting fluid, the MIP process can be assumed similar to a drying path in the water retention curve. In this sense, the injection of mercury is equivalent to the ejection of water by the non-wetting front advance of air for the same intruded pore diameter. The matric suction can be associated to the applied pressure and the corresponding degree of saturation can be obtained by considering also the amount of non-intruded pores by mercury. The mathematical expressions to derive this relationship are given in the following section. The use of this derivation should be restricted considering the non-intruded porosity and the dominate retention mechanism (adsorption) at higher total suctions. Thus, the matric – suction relationship should be limited to the range where the suction phenomena is dominated by capillary, thus at lower suction ranges.

### 3.3.2.3 Mathematical formulations

#### Derivation of the pore size density (PSD) function

The mathematical formulation presented in this section is based on the framework proposed by Juang & Holtz (1986) with further development by Montanez (2002).

The relationship that relates pore radius to the applied mercury pressure can be obtained by the Laplace equation which describes the capillary pressure ( $p_{Hg}$ ) sustained across the interface of two fluids:

$$p_{Hg} = -\sigma_{Hg} \cos \theta_{nw} \left( \frac{1}{r_1} + \frac{1}{r_2} \right) \quad \text{Eq. 3.3}$$

where  $\theta_{nw}$  corresponds to the contact angle between vacuum and mercury ( $nw$  for non-wetting fluid) and  $\sigma_{Hg}$  is the interfacial tension of mercury. If the assumption of a cylindrical pore radius is made, the fluid interface is spherical and thus  $r_1 = r_2$ , which leads to Washburn's equation (Washburn 1921):

$$p_{Hg} = -\frac{2\sigma_{Hg} \cos \theta_{nw}}{r} \quad \text{Eq. 3.4}$$

This equation can be further developed replacing the pore radius  $r$  by the pore diameter  $x$ :

$$p_{Hg} = -\frac{4\sigma_{Hg} \cos \theta_{nw}}{x} \quad \text{Eq. 3.5}$$

The main assumption here is based on the ideal cylindrical or parallel infinite plates pore shape and the maintenance of a constant contact angle at equilibrium. This implies that the Washburn equation is only valid for null penetration velocity of mercury. Thus, a quasi-static condition must be reached during the measurement at any step by holding the mercury pressure constant until penetration ceases or falls below a specific rate (Romero et al. 2012).

In the mathematical model, the pores are assumed to be cylindrical. Since real pores are irregular in shape, the model pore diameter  $x$  corresponds to a sort of mean pore diameter. The pore size distribution function is established by determination of the fraction of pore space which has a pore diameter between  $x$  and  $x+dx$ .

If  $f_x(x)$  is assumed to be the pore diameter probability density function, it implies that:

$$\int_0^{\infty} f_x(x) dx = 1 = F_X(x) \quad \text{Eq. 3.6}$$

where  $F_X(x)$  is the complimentary cumulative distribution function and  $f_x(x)dx$  expresses the probability of encountering pore diameters between  $x$  and  $x+dx$ . The volume of pores with a diameter between  $x$  and  $x+dx$  can be defined using a volumetric shape parameter  $s(x)$  which depends on the pore shape model:

$$dV = s(x) f_x(x) dx \quad \text{Eq. 3.7}$$

In regards to Washburn's equation, assuming that the contact angle and the interfacial tension of mercury are constant, leads to:

$$px = cte. \quad \text{Eq. 3.8}$$

And thus by derivation of Eq. 3.8, the following expression is obtained:

$$x dp + p dx = 0 \rightarrow dx = -\frac{x}{p} dp \quad \text{Eq. 3.9}$$

Substituting  $dx$  from Eq. 3.9 in Eq. 3.7 results in:

$$dV = -s(x) f_x(x) \frac{dp}{p} x \quad \text{Eq. 3.10}$$

By introducing the total volume  $V_t$  and the intruded volume  $V$ , that can be obtained through the void ratio of the sample, as a constant and by rearranging the terms in Eq. 3.10, we have:

$$f_x(x) = \frac{p}{xs(x)} \frac{d(V_t - V)}{dp} \quad \text{Eq. 3.11}$$

Introducing a volumetric pore size function  $f_{vx}(x)$  helps elimination of the volumetric shape parameter in Eq. 3.11. This function is defined as:

$$f_{vx}(x) = s(x) f_x(x) \quad \text{Eq. 3.12}$$

By inserting the rearrangement done in Eq. 3.12,  $s(x)$  appears two times in the denominator and can be eliminated. Thus, the following expression is obtained using Eq. 3.11:

$$f_{vx}(x) = \frac{p}{x} \frac{d(V_t - V)}{dp} \quad \text{Eq. 3.13}$$

This expression can be modified by replacing  $dp$  with the use of Eq. 3.9:

$$f_{vx}(x) = -\frac{d(V_t - V)}{dx} \quad \text{Eq. 3.14}$$

This is the expression for the pore size density (*PSD*) function found in the literature. For practical reasons, the *PSD* function can be expressed as a dimensionless term, which leads to:

$$f_{vx}(x) = -\frac{1}{V_t} \left[ \frac{d(V_t - V)}{dx} \right] \quad \text{Eq. 3.15}$$

This equation can be applied to the MIP data through the formation of a relative frequency diagram and by representing the pore diameter  $x$  in a *log* scale. In this case the expression would be:

$$f(\log x_i) = \left[ \frac{\left[ \frac{\Delta(V_t - V)}{V} \right]}{\Delta(\log x)} \right] \quad \text{Eq. 3.16}$$

Since the void ratio of the volume fraction of the intruded mercury can be expressed as:

$$e_{HG} = \frac{V}{V_t} \quad \text{Eq. 3.17}$$

It can also be possible to formulate the expression in Eq. 3.16 as:

$$f(\log x_i) = \frac{\Delta e_{HG}}{\log x} \quad \text{Eq. 3.18}$$

The cumulative complementary distribution of pore size in terms of pore volume can be obtained by integrating the pore size density function  $f_{vx}$  from  $x = 0$  to  $x = \infty$ , giving:

$$F_{px(x)} = \frac{V_t - V}{V} \quad \text{Eq. 3.19}$$

### 3.3.2.4 Derivation of the retention curve with MIP data

The Laplace equation, describing the capillary pressure sustained across the interface of two fluids, in this case the air and water, is formulated as follows:

$$u_a - u_w = \frac{\sigma_w \cos \theta_w}{r} \quad \text{Eq. 3.20}$$

Now, considering that the injection of the non-wetting mercury is equivalent to the ejection of water from the same pore diameter, it is possible to equalise the Laplace equation and the Washburn equation as follows:

$$u_a - u_w = \frac{\sigma_w \cos \theta_w}{\sigma_{Hg} \cos \theta_{mw}} p \quad \text{Eq. 3.21}$$

For mercury (non-wetting), a contact angle ( $\theta_{mw}$ ) ranged between  $139^\circ$  and  $147^\circ$  and an interfacial tension of  $\sigma_m = 0.484 \text{ N/m}^2$  (at  $T = 20 \text{ }^\circ\text{C}$ ) for water (wetting). By inserting those three values in Eq. 3.21, the following expression is obtained:

$$u_a - u_w \approx 0.196 p \quad \text{Eq. 3.22}$$

In which the left side of the equation corresponds to the matric suction. The corresponding degree of saturation hence can be obtained considering the sum of the complementary degree of saturation intruded by mercury,  $S_{rmw}$ , and the equivalent degree of water saturation of the sample,  $S_{rw}$  as follows (Romero et al. 2012):

$$S_{rmw} + S_{rw} = 1 \quad \text{Eq. 3.23}$$

The complementary degree of saturation intruded by mercury can be calculated using the ratio between the void ratio intruded by mercury,  $e_{mw}$ , over the total amount of voids in the sample,  $e$ :

$$S_{rmw} = \frac{e_{mw}}{e} \quad \text{Eq. 3.24}$$

In which the voids intruded by mercury can be obtained by the ratio between the intruded volume and the solid volume:

$$e_{nw} = \frac{V_{nw}}{V_s} \quad \text{Eq. 3.25}$$

In order to estimate the correct degree of saturation, a correction that considers the non-intruded porosity, which can be assimilated to the residual water content  $w_r$ , must be made (Romero et al. 2012):

$$S_{rwcorr} = \frac{w_r}{w_{sat}} S_{rmw} \quad \text{Eq. 3.26}$$

In which  $w_{sat}$  is the water content at fully saturation ( $S_r = 1$ ). The degree of saturation can then be formulated as:

$$S_{rw} = (1 - S_{rmw}) + \frac{w_r}{w_{sat}} S_{rmw} \quad \text{Eq. 3.27}$$

By combination of Eq. 3.24, Eq. 3.25 and Eq. 3.27, the following expression for the complementary degree of saturation can be obtained:

$$S_{rmw} = \left( 1 - \frac{V_{nw}}{eV_s} + \frac{w_r}{w_{sat}} \frac{V_{nw}}{eV_s} \right) \quad \text{Eq. 3.28}$$

### 3.3.2.5 Limitations of the MIP technique

The following main limitations should be considered for the MIP tests when determining the porosity distribution within the materials:

- *Enclosed porosity*: pores are isolated by surrounding solids preventing the intrusion of such pores by mercury (Romero & Simms 2008).
- *Constricted porosity*: pores accessible through smaller ones will not be intruded. The consequence is that the bigger pores will only be detected when the applied pressure is sufficient enough to intrude the smaller pores.
- *Non-intruded porosity*: due to the limited intrusion pressure, pores smaller than a limit size will not be able to be intruded (Delage 2007).
- *Non-detected porosity*: the interlayer distance of smectite platelets (thickness of 9.6 Å) is about 12 Å for 1 layer of water (Saiyouri et al. 1998), while the minimum detectable pore size diameter in the MIP test is about 4 nm. In smectite minerals not all pores are intruded because of these thin intra-particle porosities in the order of nanometres.

In addition to the mentioned limitations, it is worth mentioning that by analysing the intrusion and extrusion cycles, the initial applied pressure is not restored. This evidence leads to the assumption that there is a volume of mercury that is permanently trapped in the sample due to the so called 'throat effect'. The part of porosity that is not affected by the 'throat effect' can be then obtained through a second intrusion that follows the extrusion path. The second cycle is supposed to coincide with the non-constricted or free-porosity (Romero et al. 2012).

Besides, as it was mentioned before, the mathematical model assumes cylindrical pores, while the real pores have irregular shapes. This could also be a limitation for the mathematical derivation of the porosity characteristics.

### 3.3.3 Microstructure of compacted Wyoming granular bentonite

The microstructural features of the as compacted state of Wyoming granular samples were investigated combining MIP analysis and SEM observations (Seiphoori et al. 2014). All specimens for these analyses were prepared at the same water content of 5 %. The apparent grain size distribution of the granular bentonite before compaction is shown in Fig. 2.2. For preparing each specimen, different grain size fractions were selected and mixed in order to get always the same apparent grain size distribution. Specimens were prepared at different void ratios. The highest void ratio which is attainable by simply pouring the material with the selected grain size distribution is 0.83 ( $\rho_d = 1.50 \text{ Mg/m}^3$ ). Specimen with lower void ratios were obtained by static compaction to  $e = 0.66$  ( $\rho_d = 1.65 \text{ Mg/m}^3$ ) and  $e = 0.53$  ( $\rho_d = 1.80 \text{ Mg/m}^3$ ).

In Fig. 3.8, the PSD function of the material in the poured state ( $e = 0.83$ ) and as compacted state ( $e = 0.53$ ) are compared along with the PSD function of a single grain. It is seen that the grain presents a single mode porosity with a modal value  $d = 12 \text{ nm}$ ; the PSD of the single grain would suggest that there is no inter-aggregate porosity within the grains; on the contrary this inter-aggregate porosity was reported by Hoffmann et al. (2007) for bentonite pellets. This difference is well explained considering the difference in production between the pellets and the granular bentonite and in particular the fact that they are both prepared from powder, but the lower water content used for the production of pellets facilitate the formation of aggregates (Pusch 1992). The analysis of Fig. 3.8 would suggest that an indicative pore size diameter of 50 nm can be selected as the maximum intra-grain pore diameter.

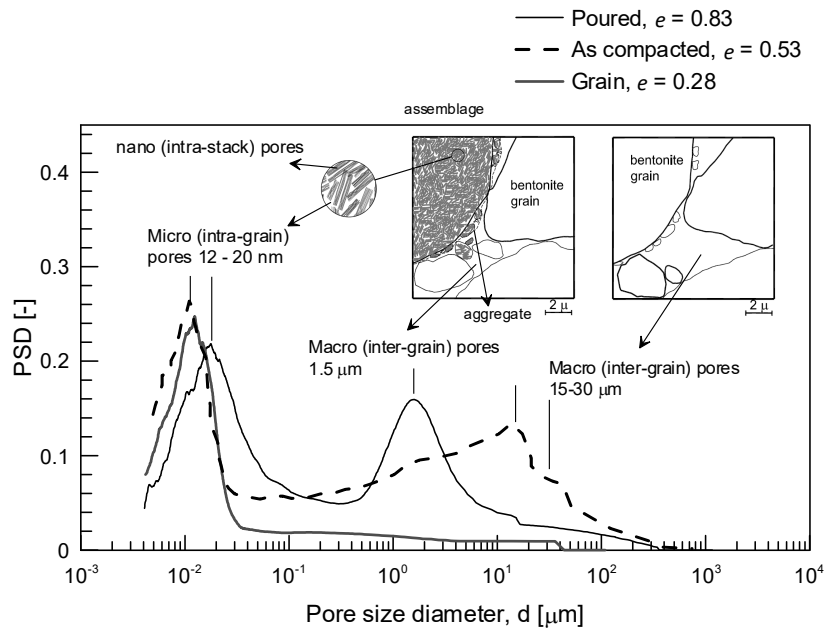


Fig. 3.8: Different microstructural levels in poured and compacted Wyoming granular bentonite.

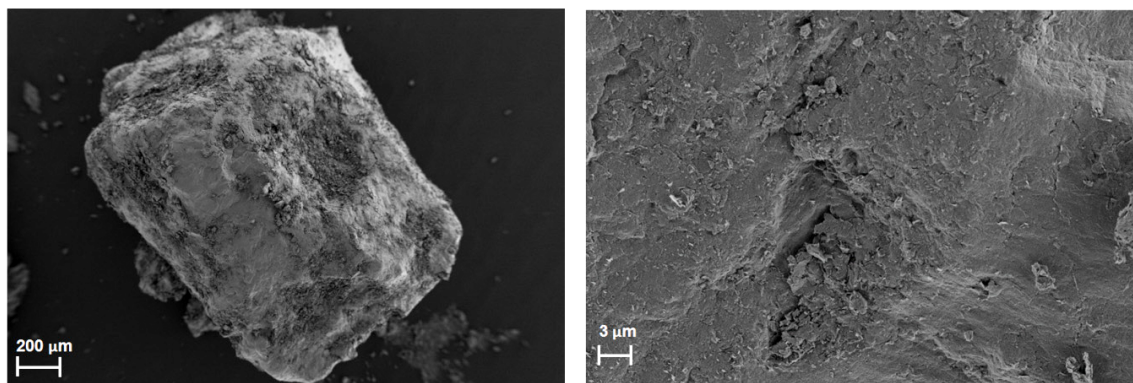


Fig. 3.9: SEM photomicrographs of Wyoming grains with  $e = 0.28$  ( $\rho_d = 2.13 \text{ Mg/m}^3$ ).

A SEM photomicrograph on the surface of an isolated grain is reported in Fig. 3.9 showing a well iso-oriented clay particle arrangement. The poured material exhibits a well distributed pore size dimension; the peak corresponding to the intra-grain porosity is still well visible.

Dominant pores with a mode value in the range of 15 – 30  $\mu\text{m}$  represent inter grain pores; the pores with diameters between the modal value for the intra- and the inter-grain porosity are associated to pores within assemblages created during the specimen preparation and constituted by the finest fraction and the smaller inter grain pores.

The as compacted specimen presented a clear bimodal distribution. Pores with characteristic diameters in the range of 300 nm – 400  $\mu\text{m}$  are clearly detected. The modal value of this family of pores is directly related to the compaction effort, and was measured at  $d = 1.5 \mu\text{m}$  for  $e = 0.53$  (Fig. 3.8) and at  $d = 15 \mu\text{m}$  for  $e = 0.83$ . The modal value for the peak observed for the lower pore dimension is situated at  $d = 20 \text{ nm}$  and the characteristic diameters for these pores are in the range of  $d < 300 \text{ nm}$ . In this range, the compacted granular bentonite shows a wider distribution of pore diameters with respect to the single grain. Interestingly, within this peak, a local maximum can be recognised for the diameter corresponding to the modal value of the grain PSD ( $d = 12 \text{ nm}$ ).

SEM photomicrographs can help to understand the increased range for these pores. Fig. 3.10a and b show an overview of the as compacted material ( $e = 0.53$ ). Grains are well visible as distinct units; they are mostly coated by aggregates composed by the finer clay particles; these aggregates fully occupy the inter-grain space (Fig. 3.10c). Fig. 3.10d exhibits a photomicrograph of the material in another close-up with clear pores of the frequency size of 1.5  $\mu\text{m}$  within the bentonite aggregates. The micropores are here defined as pores between bentonite particles within grain and aggregates. Inter-particle porosity within bentonite aggregates seems to prevail with respect to the inter-particle porosity within the grains (Fig. 3.8).

An indicative value of 300 nm can be assumed to differentiate the microporosity from the macroporosity. This value corresponds well to the diameter suggested by Romero et al. (2011) from the analysis of retention properties of compacted Wyoming bentonite.

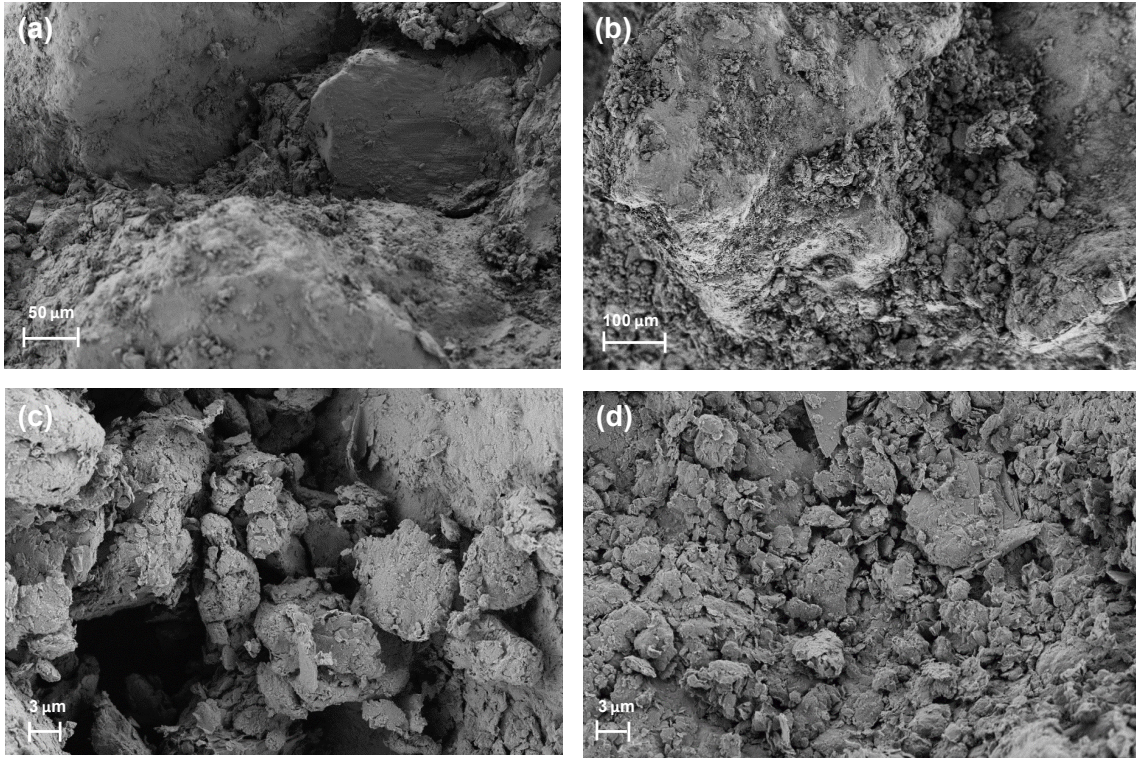


Fig. 3.10: SEM photomicrographs of Wyoming granular bentonite at as compacted state with  $e = 0.53$  ( $\rho_d = 1.80 \text{ Mg/m}^3$ ): (a), (b) bentonite grains coated by aggregates composing the assemblages, and (c), (d) bentonite aggregate arranged in inter-assembly space.

As discussed before, there exists a further level of porosity inferred as intra-particle (or inter-layer) pores which is non-intruded by mercury and not visible in the performed SEM observations either. Characteristics diameters for these pores are strongly dependent on the hydration of the smectite layers and can be in the range of 12.6 to 21.6 Å (Saiyouri et al. 1998).

This level of porosity here is called nano- or intra-particle (stack) pores and schematically is shown in Fig. 3.8. The intra-particle porosity in active clays to which the swelling and osmotic processes are associated, is in the order of 1 – 2 nm (Pusch & Yong 2006) and cannot be intruded and detected by mercury (Delage et al. 2006, Romero 2013). This porosity can, however, be detected by the means of nitrogen adsorption technique (Kaufhold et al. 2013). In this technique the pore-size distributions in the range below 20 nm are obtained by assuming cylindrical pores and applying the Kelvin equation. In this technique, nitrogen is used at  $-196 \text{ }^\circ\text{C}$  as adsorbate, and a vacuum less than  $10^{-5} \text{ mmHg}$  is applied to the samples before. The obtained data are then plotted as nitrogen isotherm and then transformed as cumulative pore volume versus pore size based on the following equation (De Las Cuevas 1997):

$$\ln\left(\frac{u_v}{u_{v,0}}\right) = -\frac{2V_m T_s \cos \beta_w}{rRT} \quad \text{Eq. 3.29}$$

where  $u_v$  and  $u_{v,0}$  are the vapour pressure of the liquid and the saturated vapour pressure, respectively,  $T_s$  is the surface tension,  $V_m$  is the molar volume,  $\beta_w$  is the soil – liquid contact angle,  $T$  is the absolute temperature,  $r$  is the pore radius and  $R$  is the gas constant. Fig. 3.11a depicts the results of the nitrogen adsorption test performed on Wyoming bentonite (Minon

2009). As seen, the intra-stack referred here as nanopores were captured using this technique. The nanopores of the order of about 2 nm measured using this technique seems to prevail the other detectable pores below 10 nm. Fig. 3.11b also depicts a high magnification microphotograph of a saturated smectite particle (stacks) using TEM reported by Tessier et al. (1992). An average interlayer distance of about 1.6 nm has been obtained for the smectite upon this condition.

However, hereafter all pores of the diameter less than 300 nm are considered as micropores except if the nanopores are directly addressed. Thus, the total void ratio is decomposed as  $e = e_m + e_M$ , where  $e_m$  is the microstructural void ratio (micropores volume over solid volume) and  $e_M$  is the macrostructural void ratio (macropores volume over solid volume). As it was stated before, a delimiting diameter of 300 nm is selected for macro- and micropores. In case of decomposition for nanopores, the total void ratio can be decomposed as  $e = e_n + e_m^* + e_M$ , where  $e_n$  is the nanopores volume over solid volume referred to as the non-intruded porosity in MIP tests. Thus,  $e_m^*$  is defined as  $e_m^* = e_m - e_n$  which physically is the microstructural void ratio without the non-intruded void ratio.

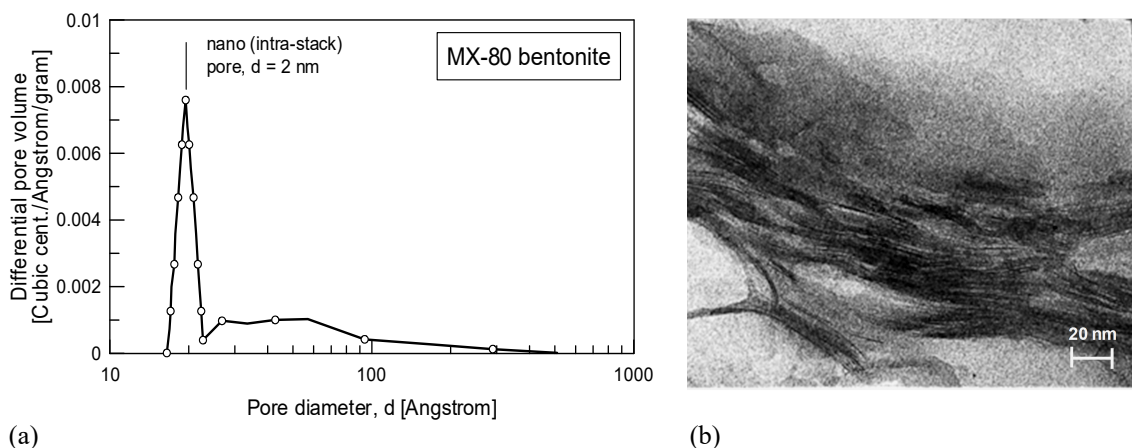


Fig. 3.11: (a) Intra-particle (stacks) porosity measured by means of nitrogen adsorption technique (Minon 2009), and (b) expanded smectite particle (stacks) observed by TEM technique (Tessier et al. 1992).

### 3.3.4 Microstructural evolution of Wyoming bentonite during wetting – drying cycles

As stated in Section 2.3.4, Analysis of the experimental behaviour of the compacted bentonite sample revealed that during the first wetting the material underwent a significant and irreversible change in retention behaviour; in particular, after this first saturation, the retention capacity of the material increased in the sense that more water can be stored in the bentonite for a given suction in a wetting path. This observation could have a strong impact on the retention behaviour of the buffer in the design of engineered barriers.

To study the microstructural features and their evolution along the wetting and drying paths, MIP and SEM tests were performed on specimens at different steps of the retention analysis. Both analyses require dry specimens; to preserve the structural features due to dehydration, freeze-drying was carried out by immersing the Micro-cell containing the specimen directly in

liquid nitrogen (boiling point -196 °C) in order to instantaneously freeze the microstructure and the specimen with subsequent sublimation under applied vacuum (0.06 mbar) to eliminate the frozen pore water at a controlled temperature of -52 °C.

This feature of Micro-cell allows freezing of the structure at a given swelling pressure, reached during the hydraulic path and avoids change of porosity due to stress release upon the opening of the cell; this feature is particularly of interest for fully saturated specimens that may reach very high swelling pressures.

The results are presented in terms of the *PSD* function (Eq. 3.18) and the cumulative void ratio (Eq. 3.19) versus the entrance pore diameter (*d*).

### 3.3.4.1 Microstructural observations

MIP and SEM tests were carried out at different stages of the hydraulic path depicted in Fig. 3.12. Since MIP is a destructive technique, several specimens were prepared at the same initial conditions ( $e = 0.53$ ,  $w_0 = 0.05$ ) and used in this investigation which followed the same wetting and drying history until the conditions were reached for an MIP test.

Fig. 3.13a shows the states during the main wetting path for which MIP tests were performed, while Fig. 3.13b and Fig. 3.13c present the corresponding cumulative void ratio (intruded void ratio by mercury) and the *PSD*, respectively. The as compacted state (A) exhibits a clear bimodal pore size distribution; two peaks with a modal value of approximately 20 nm and 1.5 μm are observed. Pores with a size in the range of 1.5 μm denote the inter-bentonite assemblage pores and they constitute the macropores. For granular bentonite as it was mentioned before, the bentonite grains and the coating aggregates form the bentonite assemblages. The peak at 20 nm is generally observed in compacted granular bentonites and it is associated with intra-grain porosity and intra-aggregates (micropores).

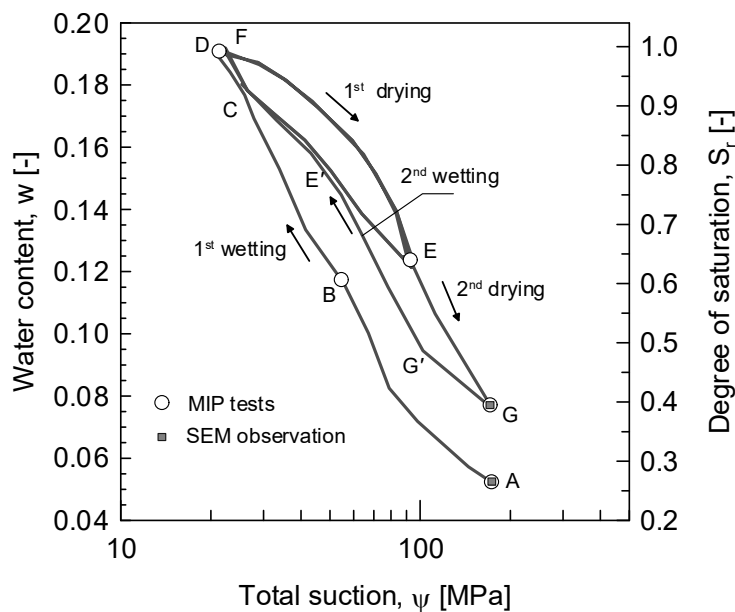


Fig. 3.12: Hysteresis water retention curve of highly compacted Wyoming granular bentonite.

The *PSD* function at point B, where the bentonite specimen has reached the degree of saturation of 0.62, shows a decrease of the macropores volume without change in the modal value with respect to the initial state (point A); micropores do exhibit negligible change.

The cumulative void ratio curve and the *PSD* function of the material under fully saturated conditions (plot D in Fig. 3.13b and Fig. 3.13c) indicate a significant reduction of the macropores due to further hydration of the bentonite assemblages. The micropores' cumulative volume and *PSD* value at the peak were also increased for point D.

The states of the material during the drying path, for which microstructural analyses were carried out, are shown in Fig. 3.13d. Fig. 3.13e and Fig. 3.13f present the cumulative void ratio and the *PSD* functions, respectively. The *PSD* function at point E, when the specimen has reached a degree of saturation of 0.64, exhibits a single porosity distribution similar to the one obtained at full saturation (point D). The cumulative void ratio of point E remains almost identical to the one obtained at point D. This observation indicates a similar structure for the material at points D and E.

Point G (Fig. 3.13d) describes the state at the end of the last drying path after wetting and drying cycles. Fig. 3.13f shows that the material at point G still exhibits a single porosity structure which is analogous to those obtained at points D and E. However, a slight increase in the intruded volume can be appreciated as presented in Fig. 3.13e.

This observation reveals a significant and permanent modification in the bentonite structure with respect to the as compacted state. This structural alteration is perceptible also in SEM analyses.

In Fig. 3.14, SEM photomicrographs of the bentonite sample at point G are presented. As seen in Fig. 3.14a, the bentonite grains are still detectable, while the aggregates have highly expanded when compared to the as compacted state of the material (Fig. 3.10). A further observation at the inter-assemblage space (Fig. 3.14c) shows that the aggregates have been expanded and filled up the macropores and formed a more homogeneous and compacted structure. This structural modification seems to happen when the material approaches a fully saturated state (point D) and remains permanent during the next wetting and drying cycles. This observation is associated to the change of the microstructure due to the inclusion of water molecules in bentonite particles during the hydration. An insight into the water retention behaviour of the material in the first wetting path would help to specify the suction domain at which this structural modification triggers. Available data on the hydration mechanism of the smectite particles are used in the next section to interpret the macroscopic water retention behaviour in the first performed wetting path.

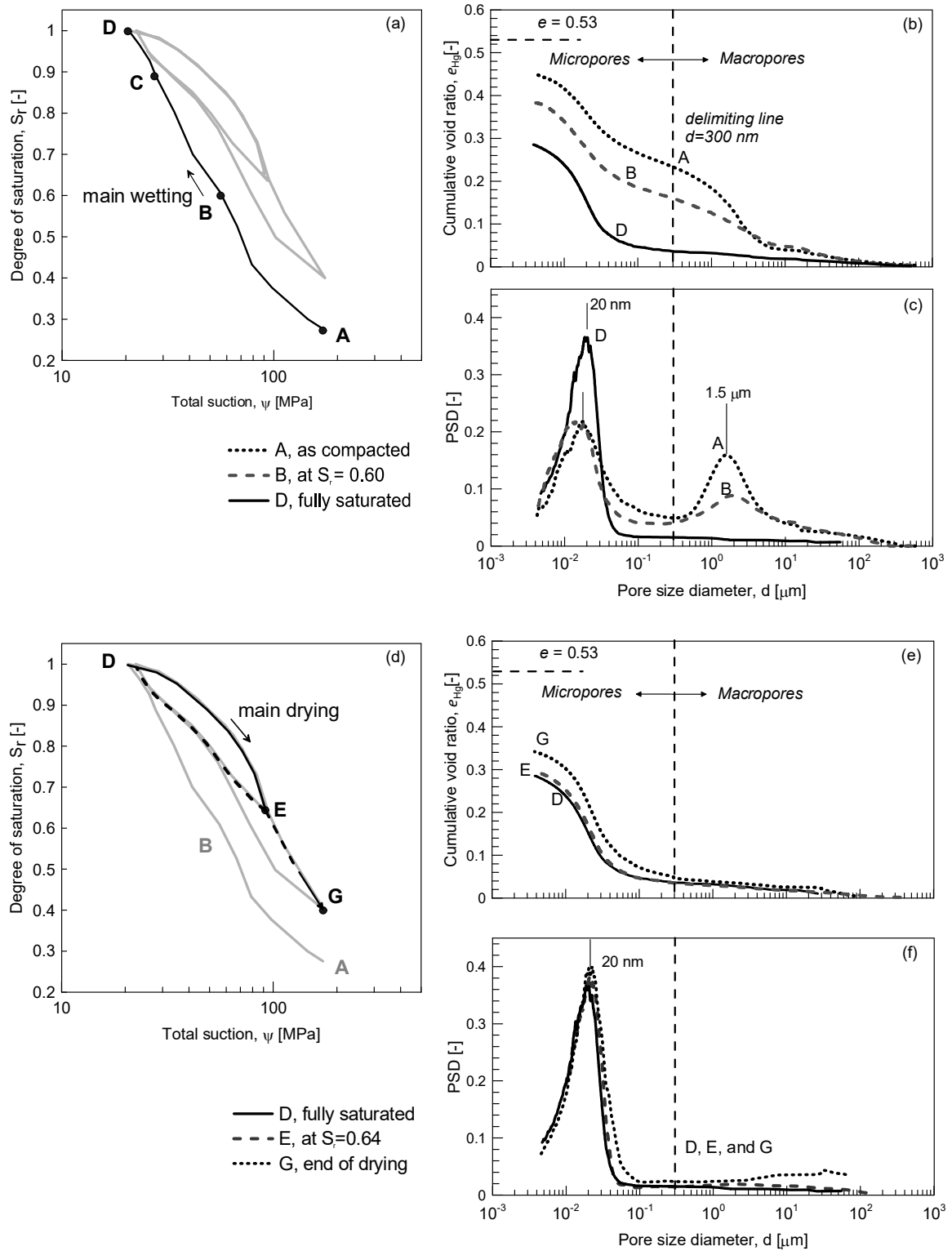


Fig. 3.13: Microstructural evolutions during different phases of wetting and drying cycles based on the results of the MIP.

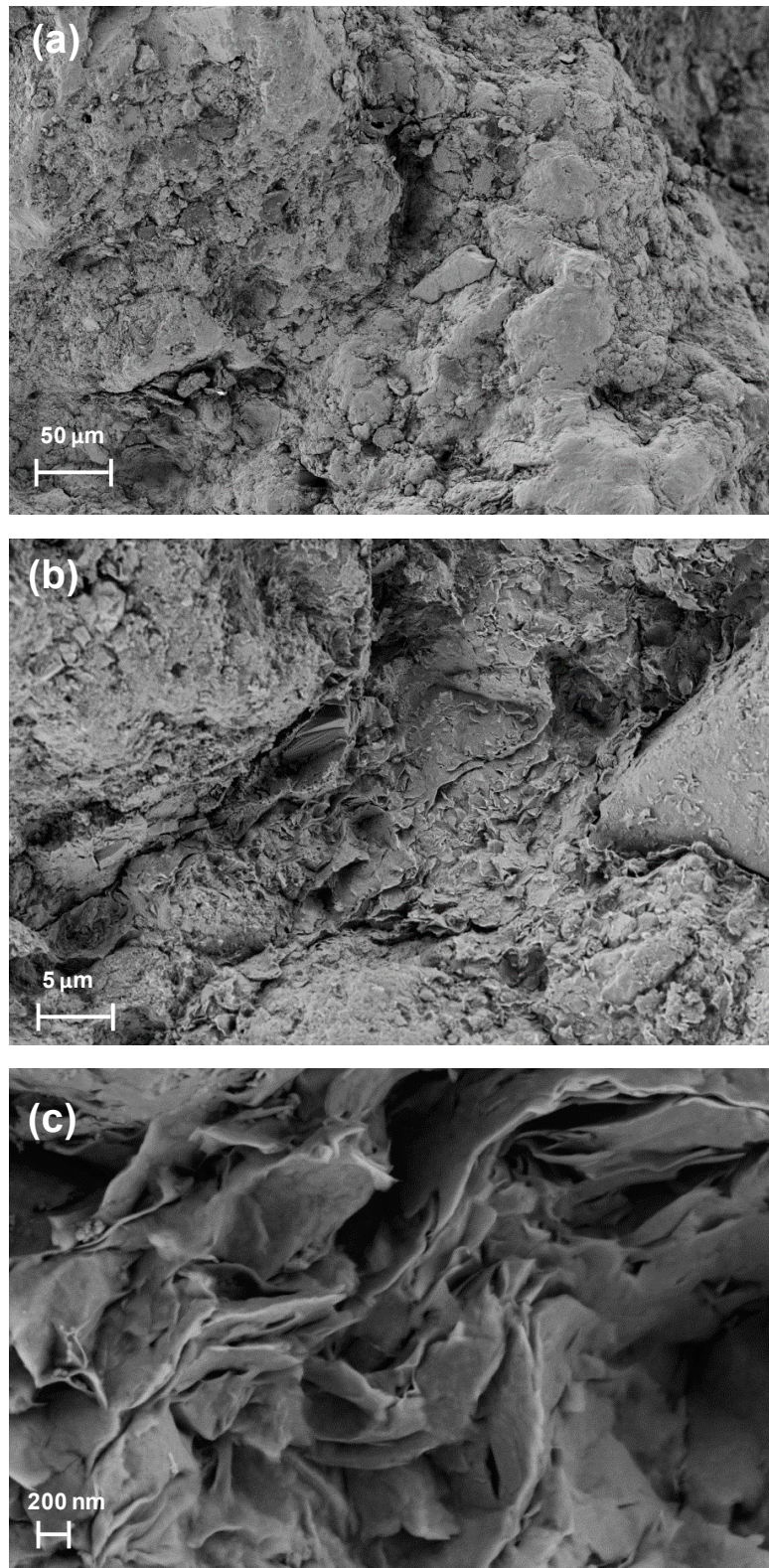


Fig. 3.14: SEM photomicrographs of Wyoming granular bentonite after a wetting/drying cycle corresponding to point G in Fig. 3.13.

### 3.3.4.2 Hydration mechanism and particle subdivision

In smectite minerals, the hydration is governed by the progressive placement of layers of water molecules along the surface of the elementary smectite platelets, initiating from one layer under dry conditions and reaching a maximum of four layers for very low suctions (Saiyouri et al. 1998, Bestel 2014).

Saiyouri et al. (1998), using the X-ray diffraction technique, analysed the hydration mechanism of the smectite particles in compacted Wyoming bentonite, wetted under unconfined conditions. The evolution of the average interlayer distance, the corresponding interlayer water and the number of elementary sheets per smectite particles were described as a function of total suction (Fig. 3.15a and b).

It is seen that the smectite mineral has only one water layer up to about 50 MPa of total suction. The second water layer is absorbed at lower suctions and the third water layer is added at suctions less than 7 MPa. At the same time, the number of layers per particle decreases from some hundreds to 10, when the total suction decreases below 3 MPa.

Bestel (2014) also measured the evolution of the interlayer distance with water content using the neutron diffraction analysis. These results are plotted in Fig. 3.15a in terms of total suction using the water retention curves obtained in this research (Fig. 2.20).

In order to specify the domain at which the hydration mechanism at particle scale could impose structural modifications as discussed in section 3.4.4.1, a water retention test was carried out on a specimen compacted to the same void ratio of  $e = 0.53$  as presented in Fig. 3.15c. The results of the previous test (Fig. 3.12) are also shown in this plot.

This water retention test aims at the evaluation of the hysteresis response of the material at three different points along the first wetting path. When the material reached a degree of saturations of 0.38, 0.62 and 0.88 (points A', B and C), a drying – wetting path was carried out, which resulted in a scanning path.

As seen, the material exhibits a totally reversible retention behaviour in path A – A' – A'' without a hysteresis cycle. The corresponding positions of point A' in Fig. 3.15a and Fig. 3.15b show that the smectite particles have only one layer of water with the maximum number of the sheets per particle. This initial hydration is believed to occur on the mineral surface and around the exchangeable cations ( $\text{Na}^+$  for Wyoming bentonite) in the interlayer space (e.g. Sposito & Prost 1982).

Later at point B, where the material reached a degree of saturation of 0.62, a drying and wetting cycle was performed. It is observed that the scanning curve reaches the initial wetting path by exhibiting hysteresis behaviour in the B – B' – B'' path. The interlayer state of the material at point B shown in Fig. 3.15a and b indicates that the material is near a transition to two layers of water, while the number of sheets per particle is still similar to the as compacted state. The preservation of the main wetting path, despite the reduction in macropores, implies that the water retention behaviour in this suction domain is exclusively controlled by the micropores.

Finally, a drying and wetting path was performed at point C where material reached a degree of saturation of 0.88. As seen, the scanning path again reached the initial wetting path with a hysteresis loop (path C – C' – C''). Fig. 3.15a and b show that the material has adsorbed the second water layer at point C and a subdivision of the smectite particle could happen due to the further hydration. However, the confined configuration here could have prevented the subdivision of the particles during the hydration. It was earlier pointed out that the results of the

hydration mechanism of the particles by Saiyouri et al. (1998) are associated to the hydration in unconfined condition, while the bentonite specimens in the current study is confined using the Micro-cell. Villar et al. (2012) has also reported the influence of the confinement on the inter-layer distance under lower suctions.

Due to further hydration, the material reached a fully saturated state followed by a permanent structural modification and creation of a new wetting path as detailed in Section 3.4.4.1. Another subdivision in the material particles from point C to D can also be appreciated in Fig. 3.15b.

Further subdivision is prevented at point D by applying constant volume conditions, despite the tendency for more hydration. As a result, the total suction remains at 20.6 MPa and the swelling pressure reaches its maximum value. Thus, the material tends to expand and subdivide at the particle level to include more water molecules; even after a fully saturated state.

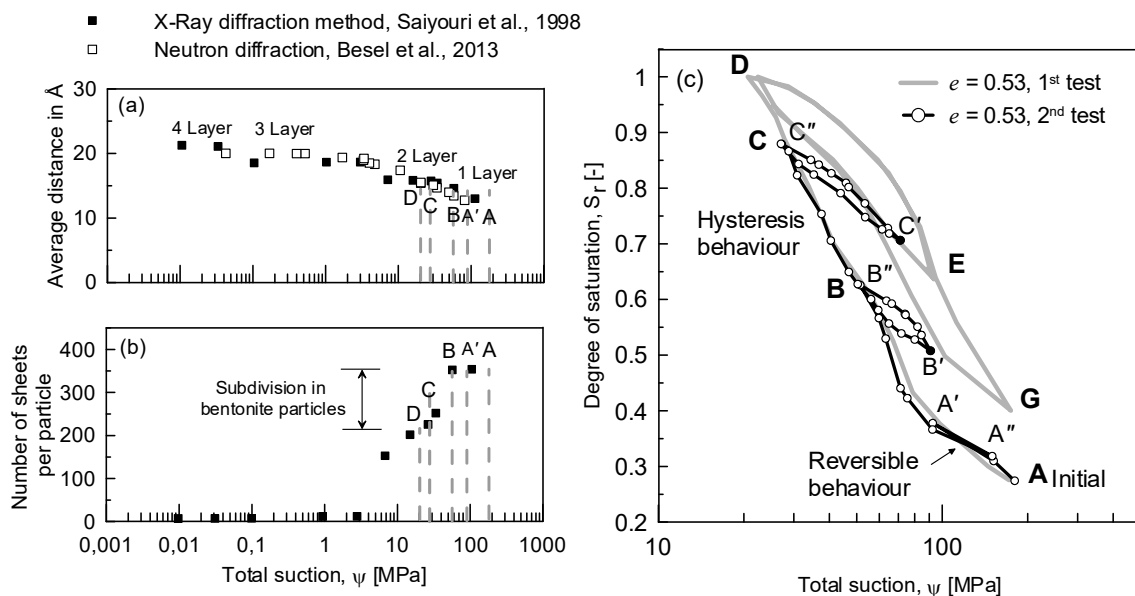


Fig. 3.15: (a), (b) Average inter-particle distance in smectite and number of sheets per particle vs. total suction, and (c) water retention behaviour of highly compacted bentonite under constant volume conditions.

### 3.3.4.3 Microstructural and interlayer void ratio evolutions

As mentioned before, the definition of the micropores from MIP tests was based on assuming a delimiting pore size of 300 nm for separating the micropores from the macropores. The total void ratio is then decomposed as  $e = e_m + e_M$ , where  $e_m$  is the microstructural and  $e_M$  is the macrostructural void ratio. The microstructural void ratio,  $e_m$ , is defined as the micropores volume over solid volume. This section aims at investigating the evolution of this parameter during the hydraulic path applied in section 3.4.4.1.

In Fig. 3.16, the evolution of the microstructural void ratio with respect to the total suction is presented. As seen, the microstructural void ratio is increasing during the wetting from an initial value of 0.3 (corresponding to a degree of saturation of 0.27) to 0.49 at the fully saturated state. Then, after a drying to a degree of saturation of 0.64, there are still no appreciable changes in

the microstructural void ratio. After performing a wetting – drying cycle, the material was dried to a degree of saturation of 0.4, while the microstructural void ratio change remained almost constant. This is another representation of the microstructural modification observed in section 3.4.4.1. Besides, it is possible to introduce a nanostructural void ratio,  $e_n$ , which is defined as the volume of the non-intruded pores to the solid volume and refers to the interlayer pores. Thus, the nanostructural void ratio can be computed from the cumulative void ratio curves in Fig. 3.13 considering the non-intruded part of micropores. This non-intruded part of the micropores describes the interlayer pore system to which the osmotic and swelling phenomena are associated; hence it can be called as the active part of the microstructure.

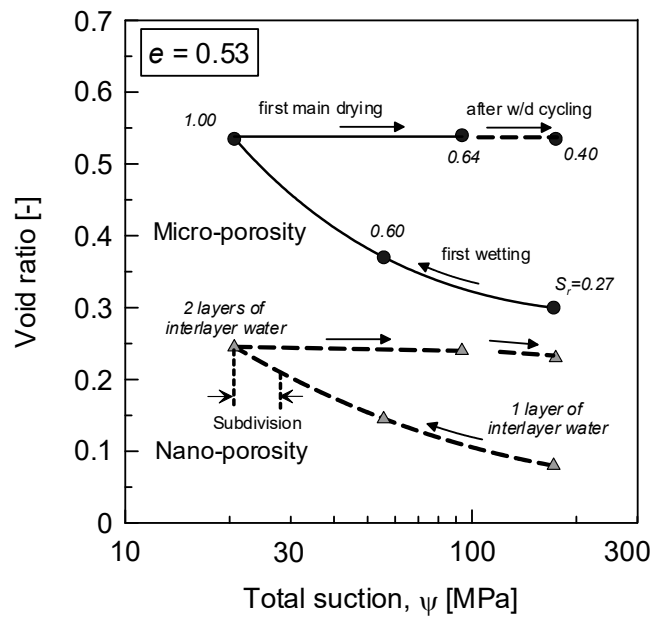


Fig. 3.16: Evolution of the microstructural void ratio and nanostructural void ratio with respect to the total suction for compacted bentonite sample.

Fig. 3.16 presents the evolution of the nanostructural void ratio versus the total suction. The swelling of nanopores indicates the progressive inclusion of the water molecules inside the interlayers when the total suction is decreasing. It also indicates an irreversible change in nano-porosity after the full saturation.

This evolution at the particle level can induce reversible or irreversible changes in micropores depending on the hydration state. Any change of micropores however influences the macroporosity and at a certain level imposes irreversible change in the macroscopic response of the material in terms of water retention behaviour. Thus, the assumption of fully reversible volumetric response at the microstructural level, which is often used to describe the behaviour of double structured clays (e.g. Gens & Alonso 1992, Alonso et al. 1999, Airò Farulla et al. 2010), may not be appropriate for highly active materials.

### 3.3.4.4 Evolution of the intruded micropores in different stress paths

Fig. 3.17, presents the evolution of  $e_m^*$  (defined as the intruded part of the micropores) obtained from the cumulative void ratio plots. The results are plotted versus the water ratio ( $e_w = G_s w$ ). The results of different tests (at given hydraulic and mechanical states) are presented in this plot. In addition to the stress path presented in Fig. 3.12, the MIP results on the bentonite grain, poured granular bentonite, saturated bentonite at  $e = 0.83$ , wetted and dried at the initially poured state, saturated and consolidated at 5 MPa of isotropic total stress are also plotted in this figure. It is seen that the samples that experienced the saturation state have been shifted to a higher stage for parameter  $e_m^*$ , while the samples at the as compacted state and lower degree of saturations were located at a lower stage of  $e_m^*$ .

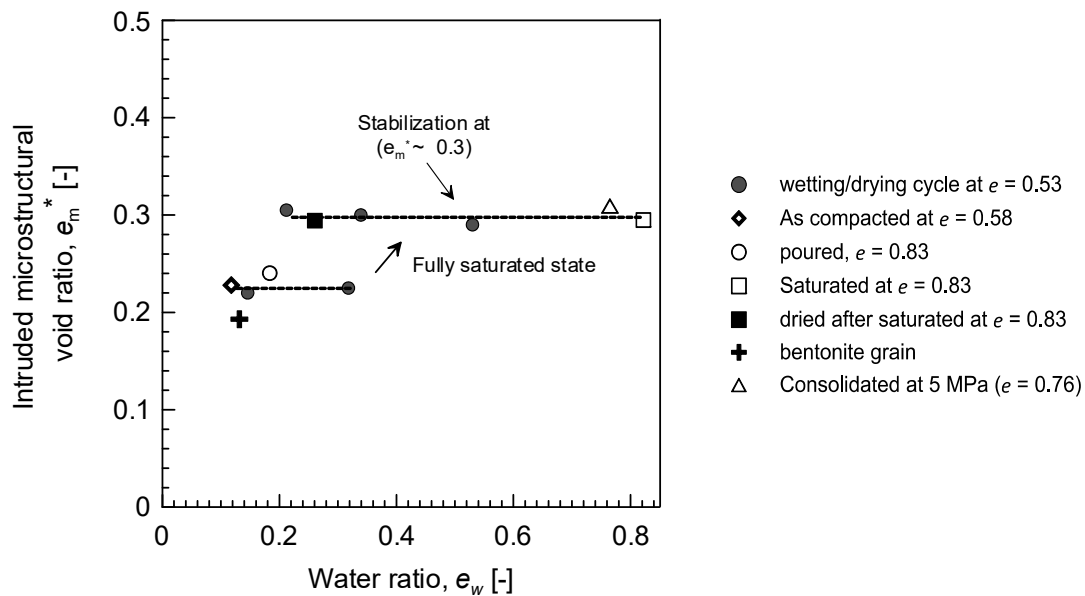


Fig. 3.17: Evolution of the intruded microstructural void ratio  $e_m^*$  with water ratio  $e_w$  for Wyoming granular bentonite at different states.

This observation is associated with the irreversible subdivision of bentonite particles due to the full saturation conditions. It has to be mentioned that the calculation of the nanostructural void ratio,  $e_n = e - e_m$ , is only possible when there is a minimum shrinkage due to the freeze-drying process. As such, the nanostructural void ratio was presented only for the sample compacted at  $e = 0.53$  as seen in Fig. 3.16.

### 3.3.5 Confinement and microstructural evolutions

It was shown in Section 3.4.4 that the water adsorption in bentonite is strongly dependent on the allowed distance between the clay interlayer spaces. The material is tending to adsorb water even after full saturation under a given void ratio. This tendency results in an osmotic repulsion pressure so-called swelling pressure and at the same time the total suction remains at a value corresponding to the void ratio (Fig. 2.19).

A complementary test to observe the unconfined water retention behaviour of Wyoming bentonite was performed and the results are presented in Fig. 3.18a in terms of water content and total suction. The specimen was prepared at the initial void ratio of  $e = 0.83$ . The water retention behaviour of the material at unconfined conditions was determined based on a controlled wetting/drying process and on the measurement of the total suction with the psychrometer.

The water retention curves of the material at confined conditions are also shown in this figure. Focusing on the retention behaviour of the poured specimen at  $e = 0.83$  under confined and unconfined conditions, it is seen that both curves are aligned until the total suction at which the confined specimen reaches the fully saturated state ( $\psi = 4.85$  MPa). At lower suction values, there is a divergence at confined and unconfined retention behaviours, because the unconfined material is able to adsorb water as suction decreases, while for the confined conditions this possibility is hindered.

The corresponding particles' state of the material in Fig. 3.18c shows a significant subdivision from 150 to 12 sheets per particle when the total suction decreases from 6.8 to 2.8 MPa. As seen in Fig. 3.18a, the retention curve under free volume conditions exhibits no hysteresis behaviour in this range where the maximum subdivision has happened.

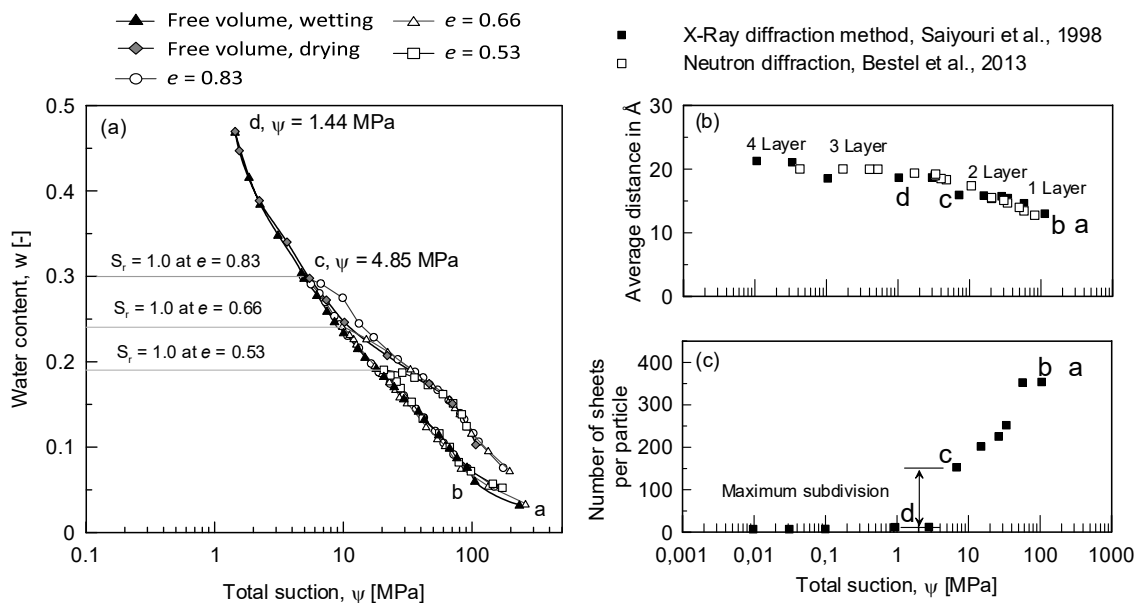


Fig. 3.18: (a) Effect of confinement on the water retention behaviour of bentonite, (b) inter-layer distance evolution with suction decrease, and (c) number of sheets per particle vs. suction decrease and maximum subdivision under free volume conditions.

Practically, due to this subdivision process, material can produce larger pore spaces (expansion of the intra-aggregates and intra-grains) during the hydration and consequently the air-entry suction decreases due to the osmotic potential release. Therefore, one may define the swelling pressure at constant volume conditions as *the attempt of the swelling material to expand and subdivide at the particle scale in order to adsorb more water molecules and consequently decrease the corresponding osmotic potential*. Therefore, the swelling pressure could have a direct correlation to the air-entry suction, and both are a function of the void ratio.

For smectite-based clays, the swelling pressure at a low suction range was found to be increased at its highest and in hyperbolic form with the suction decline (Kassiff & Shalom 1971, Wang et al. 2012) which implies the subdivision at lower suction values. In terms of free swelling behaviour, the maximum change of the swelling deformation was observed at the lower suction range where the maximum subdivision takes place (Fig. 3.19).

On the other side, a maximum water content of 0.3 was found at constant volume retention at which a divergence in constant and free volume retention curves was seen. Villar et al. (2012), using X-ray diffraction analysis, and Bestel (2014), using Neutron diffraction analysis, showed that for smectite minerals in a hydration path, the transition to three layers of water molecules takes place at water contents around 0.3. This water content for Wyoming bentonite corresponds to a total suction of 4.85 MPa. In the next section, the Focused Ion Beam nanotomography (FIB-nt) technique is used to investigate the porosity evolution of bentonite material at a higher water content.

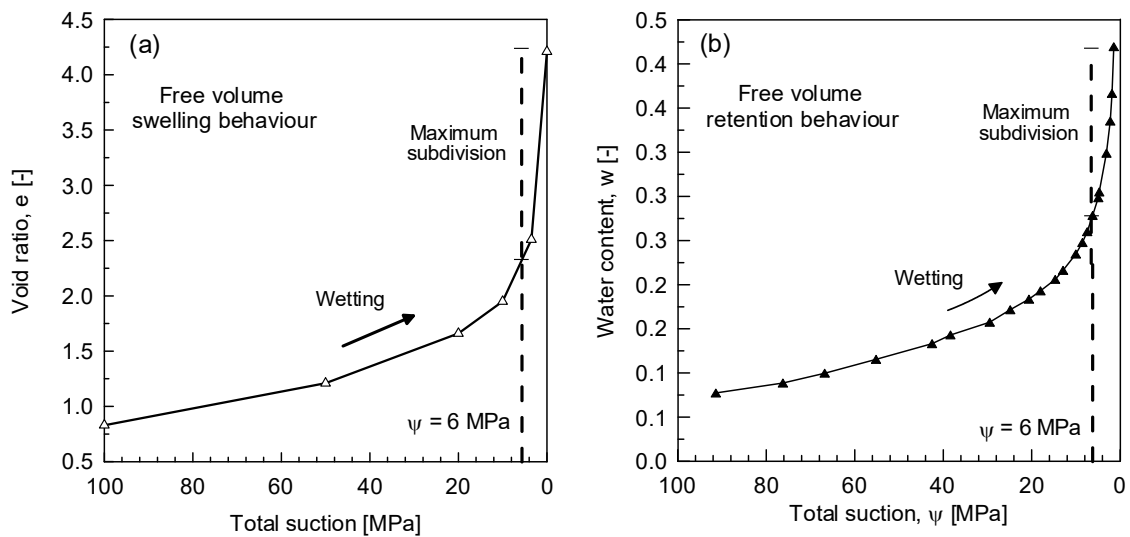


Fig. 3.19: (a) Free volume swelling, and (b) free volume water retention behaviour of the granular bentonite.

### 3.3.6 Focused Ion Beam nanotomography (FIB-nt) technique

#### 3.3.6.1 Methodology and sample preparation

FIB-nt was performed at Centre for Imaging Science and Technology (CIMST) of ETH Zurich. The author was involved in sample preparation and interpretation of the results within the collaboration with Zurich University of Applied Sciences and ETH Zurich (Keller et al. 2014).

The cryo Focused Ion Beam nanotomography (FIB-nt) technique provides a 3D analysis of the pore structure in porous material focusing on the preservation of the fabric during the preparation of samples. The most critical aspect of such cryo fixation techniques is the cooling rate. If the cooling rate is too slow, the formation of ice crystals and phase separation can influence the original bentonite microstructure (Vali & Hesse 1992). To achieve the necessary cooling rates that allow vitrification of the pore water, the sample thickness must be minimised. Therefore, high-pressure freezing is applied to freeze samples with a thickness of 200  $\mu\text{m}$  within milliseconds.

In addition, the approach also avoids mechanical effects due to preparation, or ice crystal formation and phase separation due to conventional freezing. FIB-nt is able to resolve pores with a radius larger than about 10 nm, but it is unable to resolve nanopores or interlayer pores of smectite minerals.

A new procedure is developed in this study for high pressure freezing of compacted bentonite samples. In order to study the pore space evolution as a function of dry density, the hydrated bentonite samples were prepared and compacted directly into the sample holders of the high-pressure freezing instrument. The overview of the method and sample preparation is demonstrated in Fig. 3.21). The tested material was the fraction of Wyoming granular bentonite that passes through a 90 micron sieve. This fraction mainly describes the bentonite aggregates in powder form. Then, the powder was wetted through the vapour phase in a closed chamber during several weeks to reach the target water content. This wetting process was selected to have the maximum homogenisation in terms of water content. Hydration by adding liquid water to the bentonite powder exhibited the formation of larger aggregations which prevented the fabrication of homogenous samples (Fig. 3.21a).

After hydration, a calculated amount of this material was weighed by using a high precision balance (0.0001 g) and subsequently compacted directly in the sample holder for high-pressure freezing. This sample holder consisted of two aluminium half shells, each of which with a recess of 100 microns at a diameter of 5 mm (Fig. 3.21b, c). Three different target densities were assumed and the wetted materials to the target water contents were compacted in the sample holders which construct a cylindrical cell. The properties of the sample holders, wetted material, final dry density of each sample and their corresponding degree of saturations are summarised in Tab. 3.3.

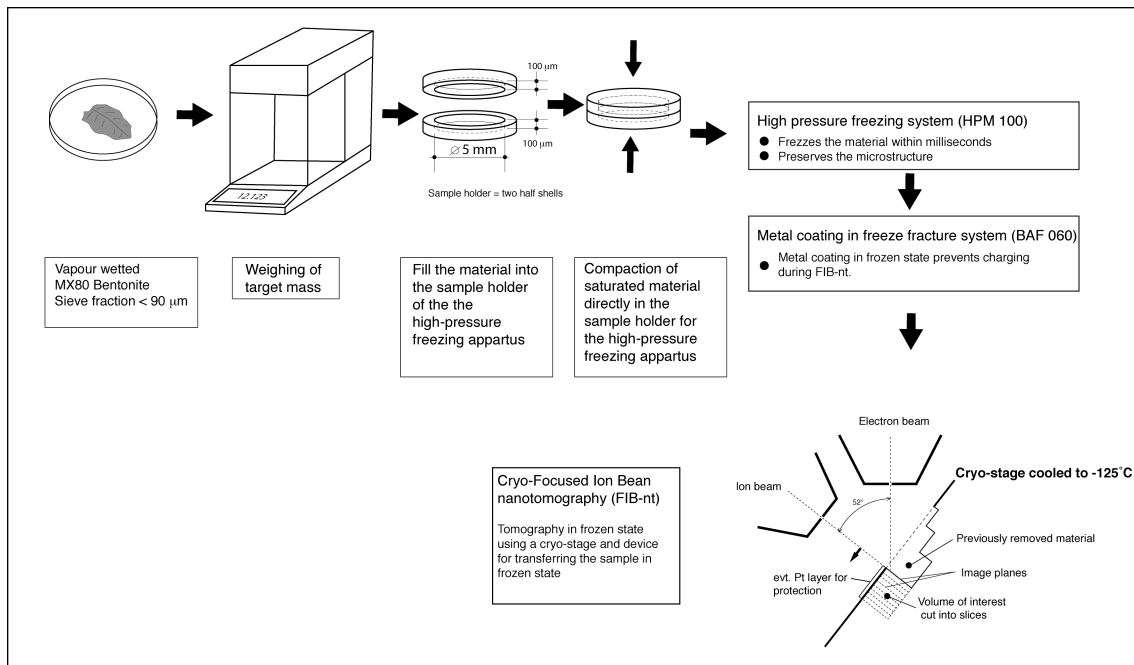


Fig. 3.20: Sample preparation from vapour wetted bentonite and compaction at a target dry density in a sample holder of the high-pressure freezing instrument (Keller et al. 2014).

After compaction, the cells containing the compacted samples were frozen under high pressure (2100 bar) and within milliseconds by using the HPM 100 (Leica) high-pressure freezing system. Freezing at high pressure occurs by the injection of pressurised liquid nitrogen. This treatment prevents the formation of ice crystals and thus preserves the delicate framework of the pore space. By using a freeze fracture system (BAF 060, Baltec) the samples were then coated with metal in frozen state in order to prevent surface charging during FIB-nt. Then, a cryo-transfer device was used to transport the frozen material to a FIB/SEM instrument (Helios Nanolab 600i from FEI) which is equipped with an integrated cryo-stage. In this instrument Focused Ion Beam nanotomography (FIB-nt) was then applied to the material in the frozen state.

FIB-nt was performed with dual beam FIB-SEM instruments, in which the ion and electron beams intersect under an angle of  $52^\circ$  at a focal point on the sample surface. In order to analyse frozen samples, the instrument was equipped with a cryo-stage which allows cooling of the sample down to  $-125^\circ\text{C}$ . Prior to FIB-nt the samples were metal-coated in the freeze-fracturing instrument. The transfer between different instruments (i.e. freeze fracturing instrument to FIB-SEM) of the frozen samples was executed by using a vacuum cryo-transfer system. A detailed description of the technique is given in Keller et al. (2014).

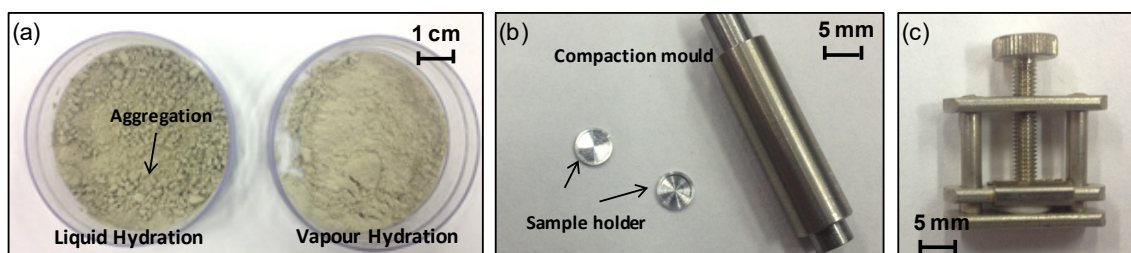


Fig. 3.21: (a) Wyoming bentonite at  $w = 22.6\%$  due to hydration by liquid and vapour phase, (b) FIB cells and the compaction mould, and (c) sealing clamps for the cells.

Tab. 3.3: Properties of the samples prepared for the FIB analysis (Keller et al. 2014).

Sample Name	Holder		Compacted powder		Final sample properties					
	Weight of top cap [g]	Weight of bottom cap [g]	Water content, $w$ [-]	$\psi$ [MPa]	Mass of compacted wet soil + holders [g]	Mass of compacted wet soil [g]	$\rho_d$ [ $\text{Mg}/\text{m}^3$ ]	$\rho_{\text{bulk}}$ [ $\text{Mg}/\text{m}^3$ ]	Porosity, $n$ [-]	Degree of saturation, $S_r$ [-]
7,W,1.3	0.0226	0.0264	0.313	3.85	0.0553	0.0063	1.23	1.62	0.55	0.70
3,W,1.5	0.0226	0.0258	0.226	13.86	0.0554	0.0070	1.46	1.80	0.46	0.71
4,W,1.7	0.0225	0.0254	0.226	13.86	0.0559	0.0080	1.67	2.05	0.39	0.97

### 3.3.6.2 Results of the FIB-nt technique

In order to suppress effects from surface charging, the BSE (Back Scattered Electron) image stacks were only collected. Fig. 3.22 shows three images representing bentonite samples at different dry densities. At a dry density of  $1.67 \text{ Mg/m}^3$  (Fig. 3.22c), the material contains only very few isolated pore objects. However, the presence of macropores is clearly observed in lower dry densities of  $1.23$  and  $1.46 \text{ Mg/m}^3$  in Fig. 3.22a and Fig. 3.22b respectively.

In lower densities, it can be observed that the aggregates in the pore space establish a mesh-like skeleton similar to the honeycomb structure observed in diagenetic smectite. This mesh-like structure composes the clay gel.

Further inspection of the samples at lower densities is presented in Fig. 3.23 showing that the macropore spaces are bridged by delicate clay aggregates. Also, the cells of the mesh-like structure are partly filled with a colloidal material. To a certain extent this material resembles a clay gel observable in clay suspensions (Keller et al. 2014).

Thickness of clay particles forming this framework ranges between  $20$  and  $50 \text{ nm}$ , which suggests that the walls are built by several parallel-oriented clay platelets. The pore radius related to this clay skeleton is in the range of  $10 - 100 \text{ nm}$  indicating the minimum pore size observed in the MIP test which is mentioned here as microspores with a porosity dominated around  $20 \text{ nm}$  (Fig. 3.8).

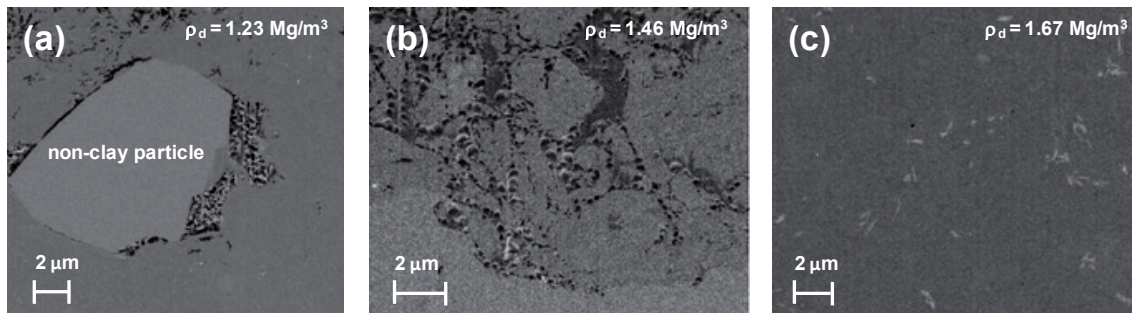


Fig. 3.22: BSE images of Wyoming bentonite samples with different dry densities mentioned in Tab. 3.3 (Keller et al. 2014).

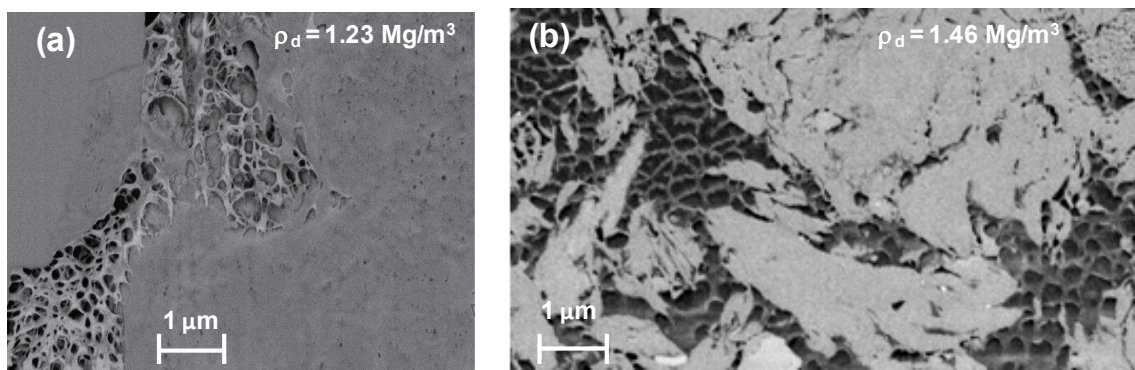


Fig. 3.23: BSE images showing the mesh-like framework: (a) along the boundary of non-clayey particle for sample at lower density and total suction ( $\rho_d = 1.23 \text{ Mg/m}^3$ ,  $\psi = 3.85 \text{ MPa}$ ), and (b) on sample compacted at higher density and total suction ( $\rho_d = 1.46 \text{ Mg/m}^3$ ,  $\psi = 13.86 \text{ MPa}$ ; Keller et al. 2014).

Considering the total suction values that these samples reached, the separation or subdivision of the smectite stacks in the larger pore spaces can be anticipated. The mesh-like structure here can be associated to the expanded clay particles eliminated in higher density and water saturation as seen in Fig. 3.22c.

After imaging in frozen state, the sample was slowly heated under high vacuum in order to sublimate the free water (i.e. amorphous ice) that presumably filled the pore space. Under the high vacuum of about  $10^{-4}$  Pa, sublimation already starts at temperatures higher than  $-110$  °C. Fig. 3.24a shows a BSE image at  $-125$  °C and Fig. 3.24b exhibits an SE image at room temperature of the same spot in the compacted sample at  $1.46$  Mg/m<sup>3</sup>. As seen, the sublimation process did not remove the mesh-like structure. This structure has a lower density with regard to the rest of the material matrix. The arrows in Fig. 3.24b indicate the network of cracks formed during the sublimation process. Such cracks preferentially develop around larger particles and likely formed during the drying of the finer matrix.

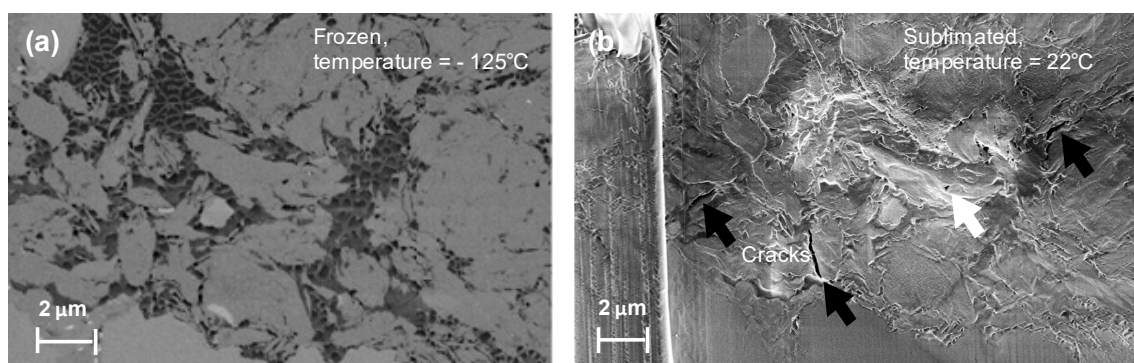


Fig. 3.24: (a) BSE of the material at the frozen stage (i.e.  $-125$  °C), and (b) SE image showing the sublimated material at room temperature at the same spot of the sample compacted at a dry density of  $1.46$  Mg/m<sup>3</sup> (Keller et al. 2014).

A 3D reconstruction image of the pore space, related to dry densities of  $1.46$  and  $1.67$  Mg/m<sup>3</sup> are shown in Fig. 3.25. In Fig. 3.25b, the regions marked with red colour are presenting the pores. In Fig. 3.25d, in addition to pores, the non-smectite impurities are also shown. These particles are associated with the presence of about 15 % of feldspar, muscovite, quartz and calcite (Tab. 3.1).

At higher densities, the sample lacks the mesh-structure and contains a very small fraction of open pores (0.1 % of the volume), while the mesh-like structure provides at least 30 % of the volume for the sample at  $1.46$  Mg/m<sup>3</sup> dry density. The majority of these pores are in the range of 10 – 30 nm for  $1.67$  Mg/m<sup>3</sup> and 10 – 300 nm for the  $1.46$  Mg/m<sup>3</sup> dry density samples.

It was earlier mentioned that the thickness of the walls of the mesh-like structure was in the order of tens nanometres. This would suggest that the walls are built up by more than ten face-to-face arranged smectite layers. Interestingly, the cores or cells of this structure are not filled with free water which indicates a governing adsorption mechanism. BSE images showed that the core fill has a lower density than the surrounding clayey material. This implies that the cores are filled up with a material that is structurally different from the surrounding face-to-face particles.

The lower density might be related to the presence of more water layers between particle layers. In higher densities, the honeycomb or mesh-like structure might have been destroyed during the compaction. This reminds of the process where the granular bentonite grains are fabricated

which results in a highly dense and single porosity structure as discussed in Section 3.4.3. This also indicates that the honeycomb structure (Fig. 3.26) can only be formed at comparatively low densities and inside the larger inter-grain or inter-assembly pore spaces. At higher densities, lack of space prevents the formation and arrangement of the honeycomb structure.

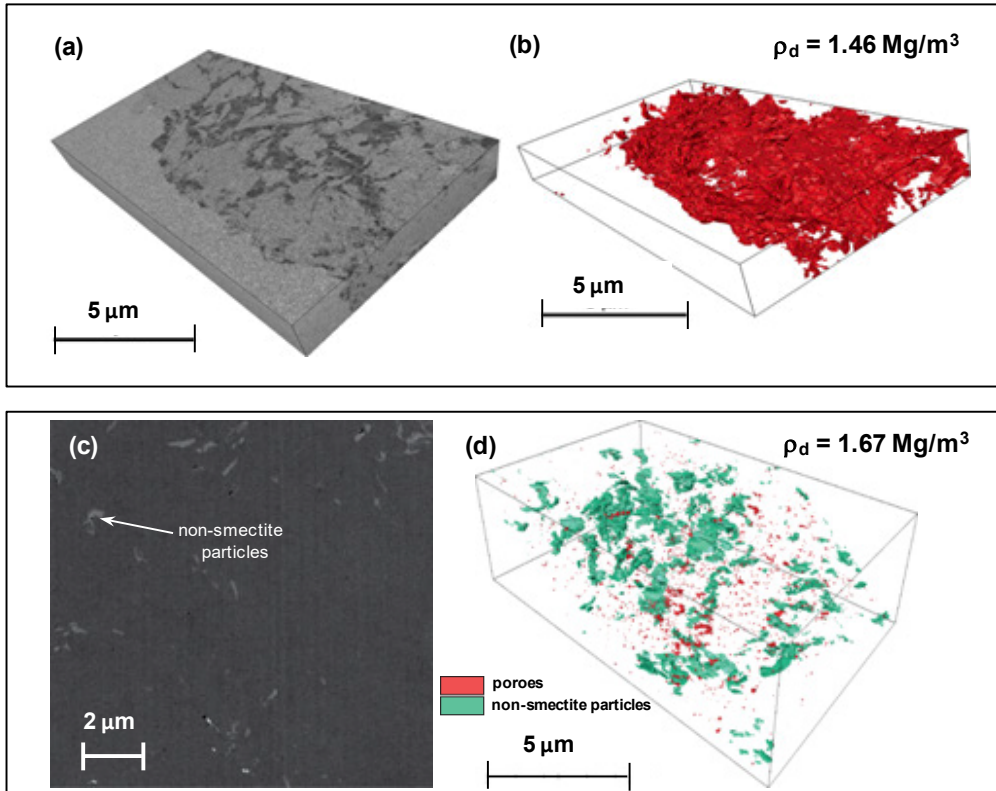


Fig. 3.25: Visualisation and 3D reconstruction of FIB-nt data: (a), (b) for the sample compacted at a dry density of 1.46 Mg/m<sup>3</sup>, and (c), (d) for the sample compacted at a dry density of 1.67 Mg/m<sup>3</sup> (Keller et al. 2014).

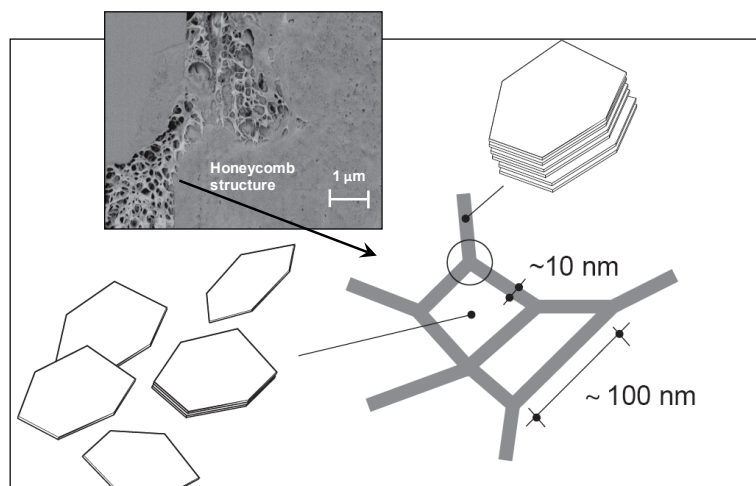


Fig. 3.26: Possible particle arrangements in the observed honeycomb structure (Keller et al. 2014).

### 3.3.7 Water retention of active and non-active clays

#### 3.3.7.1 Water retention and porosity distribution

The retention behaviour of Wyoming bentonite, illite and kaolinite clays are presented in Fig. 3.27. The Micro-cell (Section 2.3.3) was used to determine the water retention curves. The specimens were prepared by compaction of the fine fractions in powder form (fraction size less than 0.25 mm diameter) at the same dry densities of  $1.80 \text{ Mg/m}^3$ .

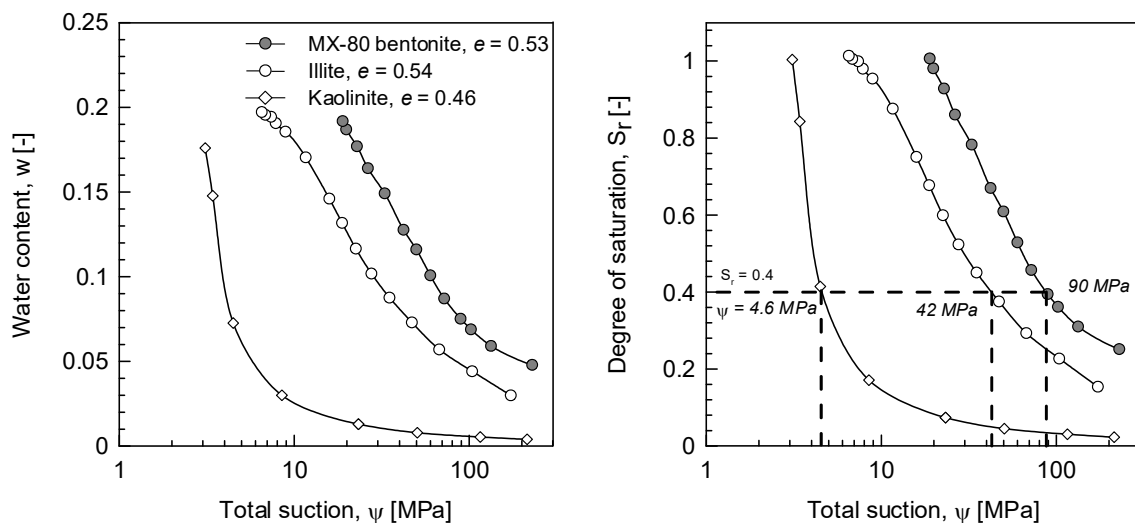


Fig. 3.27: Water retention behaviour of Wyoming bentonite, illite and kaolinite using the 'Micro-cell' technique.

A significant difference between the retention capacities of Wyoming bentonite and other clay minerals can be observed. For instance, at a given degree of saturation of 40 %, total suctions of 4.6, 42 and 90 MPa can be obtained for kaolinite, illite and Wyoming bentonite, respectively. This difference is associated with the different mechanisms that contributed to the water retention behaviour. The reason that the kaolinite mineral has a low retention potential is due to a capillary dominated behaviour within its structure. Kaolinite clays behave in principle as very fine silt or soils consisting of quartz grains (Pusch & Yong 2006). In smectite, the hydration of interlayer cations (Na in case of Wyoming bentonite) and the osmotic potential result in a high water retention capacity (detailed in Section 3.3). Illite mineral behaves in between the other two clay minerals in terms of water retention behaviour.

In this section, the retention behaviour and the evolution of the microstructure of Wyoming bentonite and illite clay are investigated using the Micro-cell and MIP test results.

In Fig. 3.28, the water retention curves and the MIP results in terms of cumulative void ratio and the *PSD* functions are presented. The MIP test for bentonite is obtained for the compacted granular sample. In Chapter 2, it was shown that granulometry does not influence the retention behaviour of the compacted bentonite, but the porosity distribution might be different in the macropore domain.

In Fig. 3.28b, the intruded void ratio of compacted illite and kaolinite samples is in agreement with the total void ratio, which confirms that mercury was able to intrude almost all porosity within kaolinite and illite structures. However, in case of compacted Wyoming bentonite, about 15.7 % of the total porosity could not be intruded by mercury. This porosity was associated to the presence of the interlayer or nanopores in the smectite mineral. As it was mentioned in Section 3.2.1, the nanopores basically do not exist in illite and kaolinite. In addition, considering the single mode porosity distribution for the two samples, it can be inferred that the inter-stack porosity in compacted illite is distributed mainly at 13.5 nm and in kaolinite at 170 nm.

Besides, Fig. 3.28d indicates a double porosity mode for the bentonite sample. One could argue that this double porosity distribution for bentonite is related to the presence of granulations, and for the finer fractions this level of porosity could be eliminated due to the static compaction. However, it is aimed to highlight the retention behaviour by an insight into the micropores, it was mentioned that the macropores do not play a role in the water retention behaviour of bentonite material in this range of total suctions. However, it is believed that the total elimination of the macropores of this level (1.5 mm) upon this target density would not be possible and it can be achieved under higher densities (such as in bentonite grains, Fig. 3.8) or at higher water contents (such as in a compacted bentonite sample, Fig. 3.22c).

The other point is the difference in the total suction values at which these clay minerals reach the fully saturated state. The lower total suction obtained for kaolinite which is in agreement with the higher peak modal value in plot of PSD (Fig. 3.28d), if the capillary mechanism is considered.

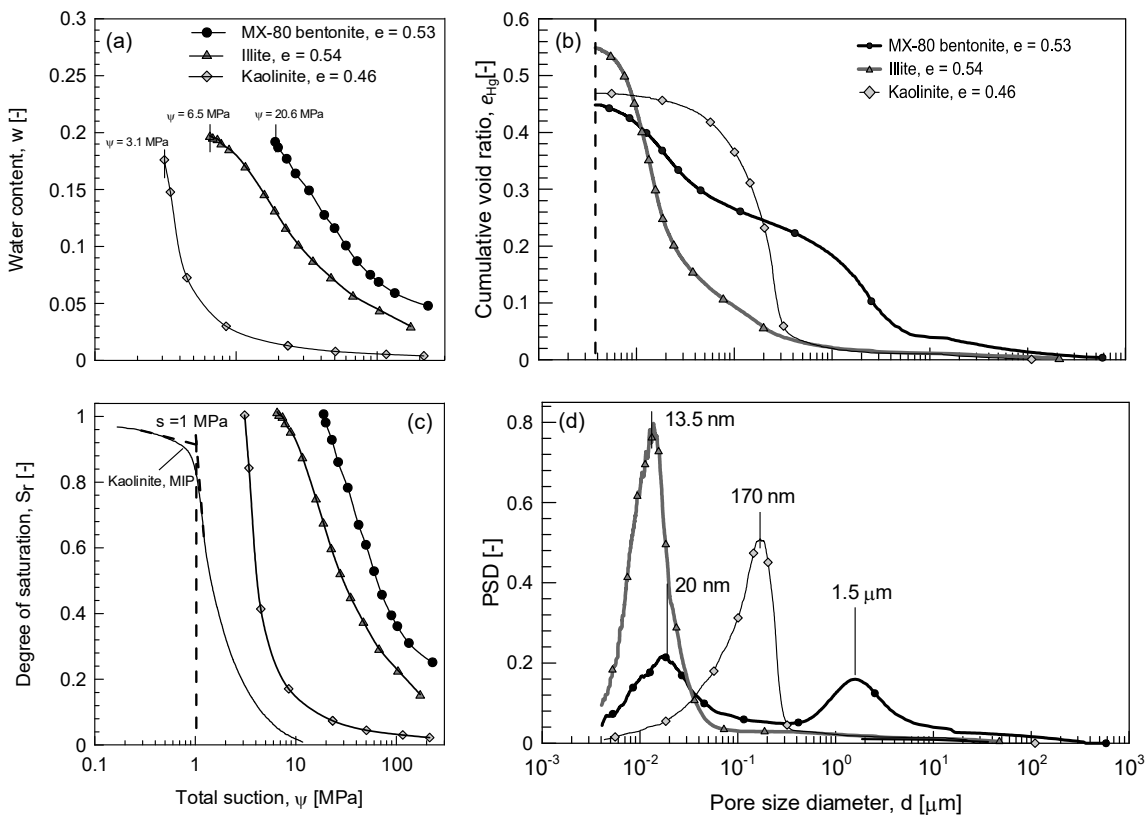


Fig. 3.28: Water retention behaviour and porosity distribution in the as compacted state for the Wyoming bentonite, illite and kaolinite samples (all compacted at a dry density of  $1.80 \text{ Mg/m}^3$ ).

Using the Laplace equation that considers equilibrium of the air – water interface in a capillary system (Eq. 2.5), the matric suction can be calculated by assuming that the contact angle  $\theta_w = 0^\circ$ , the surface tension  $T = 0.072$  N/m and the pore diameter  $d$  can be replaced by the modal pore diameter from MIP data. This equation returns a capillary suction of 1.69 MPa for  $d = 170$  nm in case of kaolinite. In Fig. 3.28c, the retention curve from the MIP data is also plotted using Eq. 3.21 and 3.27. The air-entry value at about 1 MPa was obtained from the MIP data which is close to the one obtained from the water retention curve. This equation does not return the right trend for bentonite and illite with respect to the obtained water retention curves in Fig. 3.28c. Although the bentonite sample has a modal peak at a higher value (20 nm) with respect to illite (13.5 nm), it exhibits a higher total suction at the saturated state. This shows the importance of the osmotic mechanisms in water retention response of bentonite clays.

In the next section, the microstructural evolutions of illite and bentonite samples compacted to the same dry densities are compared. The water retention behaviour in wetting and drying cycles and the structural modifications in both materials are investigated using MIP analysis.

### 3.3.7.2 Microstructural evolutions in wetting and drying cycles

Water retention behaviour of compacted illite and Wyoming bentonite samples are presented in Fig. 3.29 for different episodes during wetting and drying. The tests were carried out under constant volume conditions. The samples were compacted at the same dry density of  $1.80$  Mg/m<sup>3</sup>. The void ratios of  $e = 0.53$  and  $e = 0.54$  were obtained for Wyoming bentonite and illite, respectively. Fig. 3.29a, shows the main wetting path for both materials. A wetting path was initiated from as compacted state for both materials (A, A'). At fully saturated state, the bentonite sample reached a total suction of 20.65 MPa, while illite reached a total suction of 6.52 MPa (B, B'). The wetting path of the bentonite material for both granular and powder form (the same as illite) are plotted to show the negligible influence of granulometry in the retention behaviour of the bentonite material. It is seen that at the full saturation state, there is a difference of 14.1 MPa in the total suction values. A drying path was then initiated (Fig. 3.29b) until the samples reached a degree of saturation of 0.66 in the main drying path (C, C').

As shown in Fig. 3.29c, a scanning path was performed and then a wetting path until full saturation was continued. While the scanning path of the illite sample reached the main wetting path, the scanning path of bentonite independently reached the fully saturated condition not following the main wetting path. Fig. 3.29d depicts the second drying attempt. For both materials, the new drying path is aligned with the first drying and it was continued until a degree of saturation of 0.4 and 0.32 for bentonite and illite, respectively. The second scanning has been initiated at D and D' for illite and bentonite, respectively. Further wetting from E and E' indicates that although illite followed the main and first wetting path, the bentonite sample apparently underwent a second wetting path that already was created after fully saturated conditions.

For both materials, the new drying path is aligned with the first drying and it was continued until a degree of saturation of 40 and 32 % for bentonite and illite, respectively. The second scanning has been initiated at D and D' for illite and bentonite, respectively. Further wetting from E and E' indicates that although illite followed the main and first wetting path, the bentonite sample apparently is undertaking the second wetting path that already was created after fully saturated conditions.

The creation of a new wetting path for the compacted bentonite was discussed in detail in Section 3.4.4. This change of structure was attributed to the subdivision in the smectite particles. It was shown that the change of macropore does not influence the main wetting path, and up to a degree of saturation of 0.90 the main wetting path is recovered in all scanning attempts.

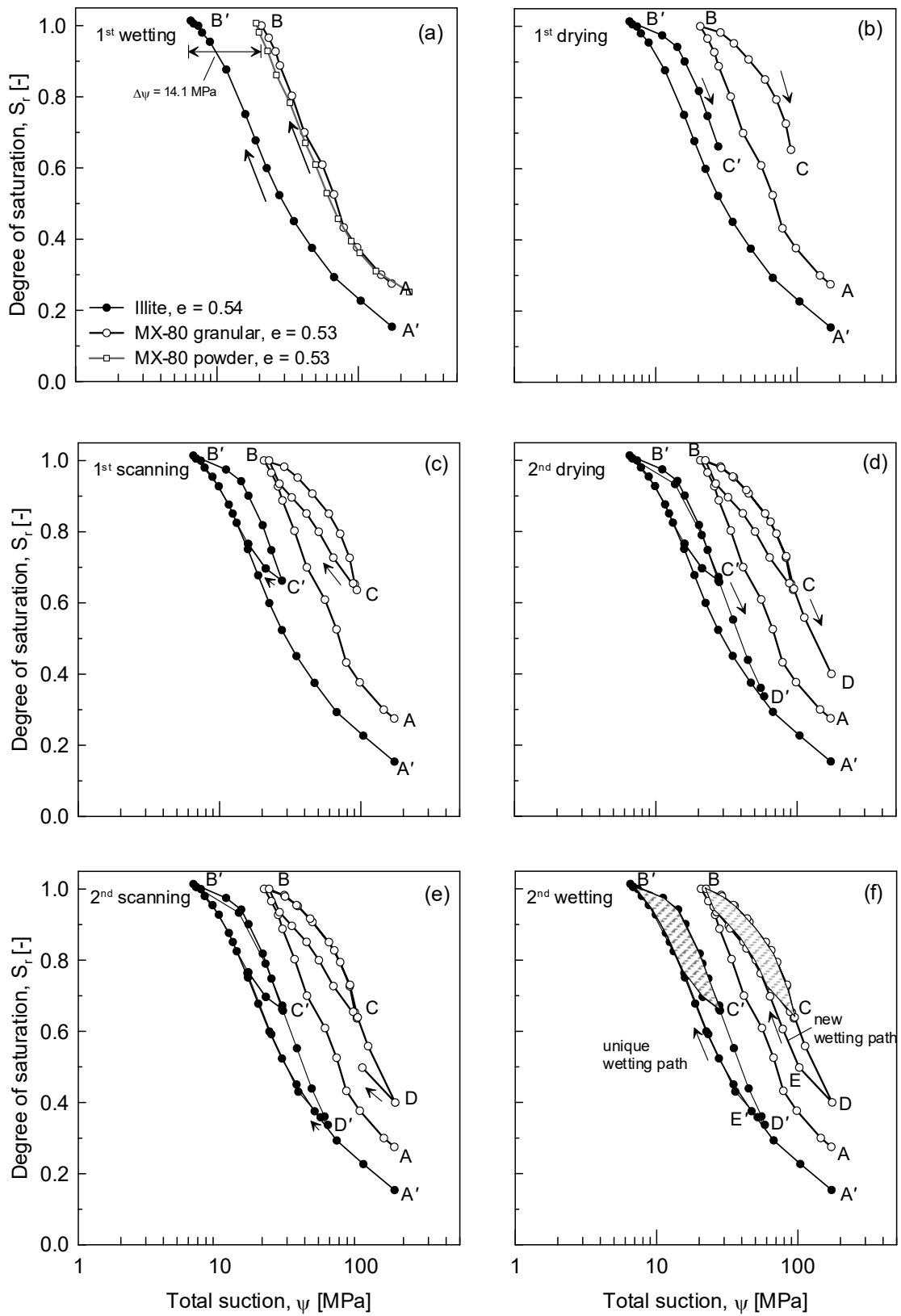


Fig. 3.29: Water retention behaviour of highly active Wyoming bentonite and non-active illite clay in constant volume condition compacted at dry density of  $1.80 \text{ Mg/m}^3$  in wetting/drying cycles.

An inspection of the macrostructure of illite and its comparison with bentonite is depicted in Fig. 3.30. The intruded void ratio (cumulative) and the *PSD* function of both materials in hydraulic state A/A' and D/D' reveal that the illite sample has a single porosity distribution in the as compacted state and the hydraulic path (wetting and drying) does not influence the porosity distribution. It is seen that for the bentonite material, in addition to the total elimination of macropores in higher saturations, the frequency of micropores is increased as a result of the subdivision process in the smectite particles. This observation indicates the main difference between active (smectite) and non-active (illite) clays. In the latter, the particles can expand due to the presence of active nano-porosities, which results in the subdivision process. This subdivision increases by a decrease in total suction.

The subdivision in particles is a function of the total suction and also the confinement. The influence of the confinement is seen in the minimum total suction that material reached under constant volume condition. This total suction corresponds to a maximum modification in the microstructure. The microstructure after this point is stabilised and remained unchanged for the next wetting and drying cycles.

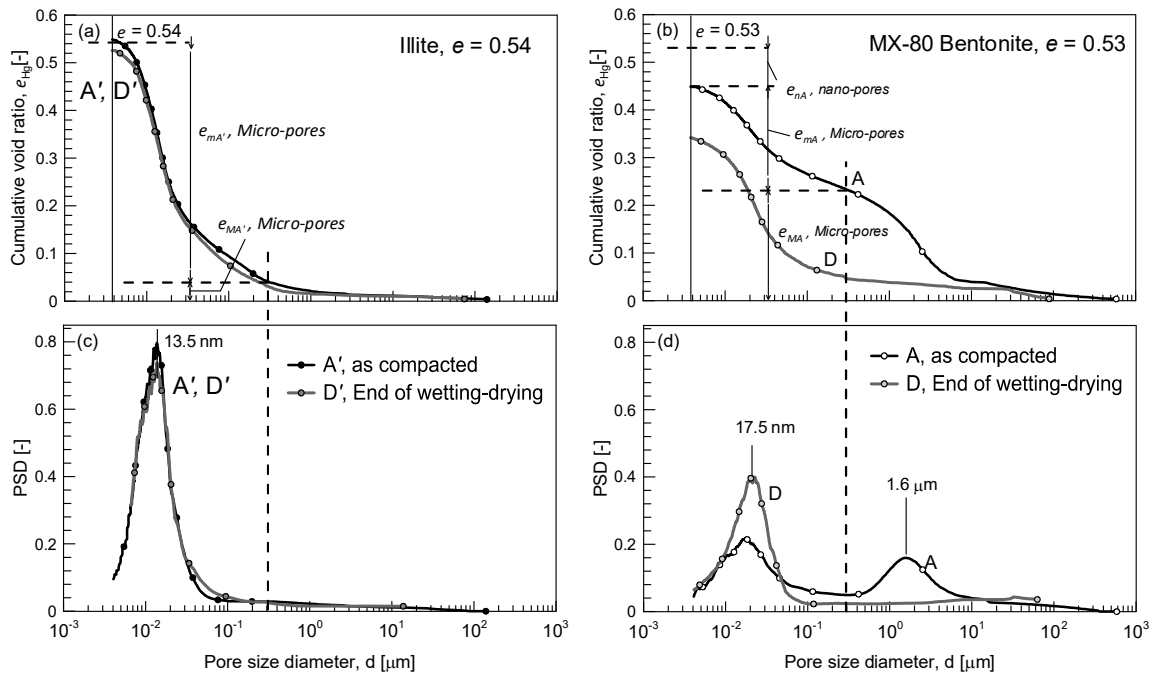


Fig. 3.30: Microstructural evolution of of highly active Wyoming bentonite and non-active illite at constant volume conditions compacted at a dry density of  $1.80 \text{ Mg/m}^3$ .

In Fig. 3.29f, the permanent hysteresis area belted between stabilised wetting and drying paths of bentonite is compared with the one of illite. This particular feature of the active bentonite material results in an enhancement of the retention capacity after the first full saturation.

In addition, considering that the total suction is defined as the sum of the matric and osmotic suctions (Eq. 2.1), the matric suction approximately has the same order of influence for both illite and bentonite (micropore peak modal values of 13.5 and 20 nm for illite and bentonite, respectively). This implies that the difference in total suction at fully saturated state corresponds to the difference in osmotic suction in both illite and bentonite.

Due to the different crystalline structure, an osmotic mechanism related to the interlayer features does not exist or is negligible for illite. Therefore, it can further be concluded that this difference in total suction values at saturation state ( $\Delta\psi = 14.1$  MPa) is exclusively due to the osmotic attraction component presented in smectite interlayers. This also could be considered as an additional suction component term for the nano-porosity of the smectite.

### 3.4 Summary and conclusions

The following conclusions are presented with regard to the content of this chapter from the microscopic characterisation analysis of the Wyoming granular bentonite:

- The water retention behaviour in bentonite is mainly influenced by two mechanisms: the hydration of the exchangeable cations (sodium) and the osmotic attraction. Although the smectite (composing mineral of Wyoming bentonite) and illite have similar structural compositions, the interlayer porosity remains active in smectite, while it is collapsed in illite due to the presence of potassium ions.
- In terms of the clay – pore water interaction, the majority of pore water remains within the interlayer of the smectite mineral and the micropores which form a relatively immobile pore water.
- The osmotic potential is the tendency of adsorption of polar water molecules due to different ion concentrations in the polar solution near the smectite particles and away from them. The tendency of cations to diffuse away and the opposing electrostatic attraction, which lead to ion distributions adjacent to a single clay particle, are together termed the *diffuse double layer*. The osmotic potential is referred to as the osmotic pressure of the pore water. This osmotic potential is responsible for the osmotic suction and the swelling pressure during the saturation process of smectite clay minerals.
- Granular bentonite is a mixture of different fractions of bentonite grains and aggregations. The grains consist of well iso-oriented clay particles and a single porosity distribution mode with a peak value at 12 nm. The as compacted granular material shows a wide distribution of pore diameters with respect to the single grain. The MIP and SEM analyses suggest that the inter-grain pore space is filled up with the bentonite aggregates. A macropore network corresponding to the inter-aggregate porosity and a micropore network associated with intra-aggregate and intra-grain porosities are detectable for the as compacted granular bentonite. A further level of porosity in bentonite materials (interlayer or intra-particle pores) to which the hydration and osmotic mechanisms are attributed cannot be detected using MIP or SEM methods. The nitrogen adsorption test determines this interlayer porosity of the material at the as compacted state.
- The microstructural observation using MIP analysis during wetting and drying cycles for compacted bentonite samples indicated an irreversible change of the microstructure which is associated with the hydration state at the smectite particle level. This evolution of the smectite particles are related to the active interlayer properties in terms of inclusion of water molecules and subdivision of smectite particles. Before the full saturation, the microstructure behaved reversible, despite the irreversible change of the macroscopic void ratio. In terms of the water retention response, the wetting path was still preserved at this domain. Further hydration beyond this limit, resulted in irreversible and permanent modifications of the microstructure. This modification of the microstructure resulted in a dramatic change of the retention behaviour due to a new hydraulic domain created by a secondary wetting path.

- Comparison of the free and confined water retention behaviour indicated a water content of 0.3 (corresponding to a total suction of 4.85 MPa) at which the curves diverge each other. This water content is corresponding to the transition from two to three layers of water in smectite particles. The microstructural observations show the formation of a mesh-like (honeycomb) structure for the clay fabric. The formation of such structure can be influenced by compaction efforts. These structures create cells containing the gel-like material which is basically the expanded and subdivided smectite particles with a stable structure even after sublimation of the water molecules.
- The main difference in microscopic and macroscopic behaviour of active and non-active clays is exclusively related to the existence of the active interlayer or nanopores. The hydration of interlayer cations and the osmotic potential originated from the presence of the cations in nanopores of smectite minerals enhance the water retention and swelling capacities. The non-active clays could basically refer to a non-active microstructure which is initially fabricated due to compaction attempt and remains stable during the applied hydraulic paths in terms of wetting and drying. Nevertheless, the microstructure of smectite material is formed by active particles at the nano-scale which evolves in an elastoplastic form. Such modification at the microscale is consequently influencing the macroscopic behaviour of the material. The change of the microstructure is adaptive and actively occurred depending on the boundary conditions of the material in terms of constraint. These particular features must be taken into account the design and performance of the Wyoming bentonite used as buffer material under the repository-like conditions. The bentonite barrier would be subjected to wetting and drying cycles due to the environmental conditions or the heat generated from the waste canisters during the life time of the repository. Modelling the water retention features of the bentonite is an essential key point to analyse and predict the long-term hydro-mechanical response of the bentonite under this condition.



## 4 A model for water retention behaviour of Wyoming granular bentonite

Following the experimental results on the water retention behaviour and the microstructural evolutions of the Wyoming granular bentonite presented in Chapter 2 and Chapter 3, a conceptual model for the water retention curves of the material is presented in this chapter. The model aims at the integration of the behavioural features of the material in terms of the water retention into a consistent mathematical formulation. The model presents the retention curves in terms of degree of saturation under a constant total void ratio. In Chapter 2 it was observed that in the plane of water content versus total suction, the retention curves at different void ratios in a wetting path were aligned up to the corresponding total suctions at which the full saturation occurred under each void ratio; higher the void ratio, lower the air-entry and the suction at saturated condition. This intrinsic trend was associated with the adsorption mechanisms that govern the water retention behaviour. Thus, the change of the void ratio is directly related to the change of the macropores without influencing the micropores. On the other hand, the exponential evolution of the air-entry (and the total suction at full saturation) with the change in void ratio was observed. Moreover, the hydraulic domain within the retention curves was found to be expanding by decreasing the void ratio. These particular features of the water retention behaviour of the granular bentonite enable to conceptualise the behaviour of the material into a modelling framework. The proposed model uses the theory of elasto-plasticity and is extended to the hysteresis model and takes into account the microstructural void ratio evolution at a given compaction state. The model requires the experimental data of the retention curves at two void ratios for the calibration. One of the data sets belongs to the granular bentonite under poured conditions and is selected as the reference retention data. To account for the microstructure and water retention interaction, data on the evolution of the microstructural void ratio with respect to the degree of saturation is required. The model is validated by using the experimental data of the retention at a given compaction state.

### 4.1 Water retention modelling

The influence of the change of the void ratio on the water retention curves has been evidenced by various works (e.g. Romero & Vaunat 2000, Miller et al. 2002, Suggi et al. 2002, Tarantino & Tombolato 2005, Salager et al. 2011, Parent et al. 2011, Salager et al. 2013).

The change of the void ratio is basically associated with the externally applied stresses that deform the soil (Salager et al. 2013). Besides, experimental observations proved that wetting or drying also influences the change in void ratio (e.g. Delage et al. 1998, Romero 1999, Fleureau et al. 2002).

In capillary dominated regions, most of the existing models associate the degree of saturation with the void ratio using a simple relationship (e.g. Kawai et al. 2000, Gallipoli et al. 2003, Mbonimpa et al. 2006, Nuth & Laloui 2008, Mašin 2010). Thus, the air-entry value is usually assumed to evolve with the void ratio (e.g. in linear form in Nuth & Laloui 2008).

Tarantino (2009) presented a void ratio dependent water retention model that converges to a single equation in high suction domains where the influence of the void ratio is no longer seen due to the governing adsorptive mechanisms in clay materials.

Salager et al. (2013) state that the coupling parameter of the air-entry value in the capillary domain may not be a representative parameter for the osmotic suction domains. Besides, the water retention behaviour of double structured geomaterials can react in different ways due to the change of the voids related to the macropores and micropores, respectively. Then, they proposed a model in which a convergence point in the water retention domain was considered where the retention curves of the material at different void ratios were found to be unique and independent of the compaction states. The conceptual representation of the model proposed by Salager et al. (2013) is shown in Fig. 4.1. The convergence point has a suction of  $s_{conv}$ , where beyond this value all water retention curves in the plane of the water content converge into a unique curve with a linear trend (in logarithmic scale) until the maximum suction  $s_{max}$ . The model was tested to simulate the retention behaviour of granular and clayey materials.

Romero et al. (2011) proposed a model for the water retention of partially swelling clays. The model associates the water retention behaviour of the material with microstructural evolutions by considering two regions corresponding to the water retention mechanisms governed in micro- and macropores. The influence of the void ratio is negligible in the former region, while the dimension of macropores is firmly correlated with the capillary mechanism. The evolution of the micropores with the water ratio  $e_w$  ( $e_w = w.G_s = e.S_r$ ), is used to account for the influence of the porosity evolution in capillary regions of the water retention domain based on the Van Genuchten model (Van Genuchten 1980). It should be noted that the model presents the water retention curves in the plane of total suction versus water ratio but not the degree of saturation.

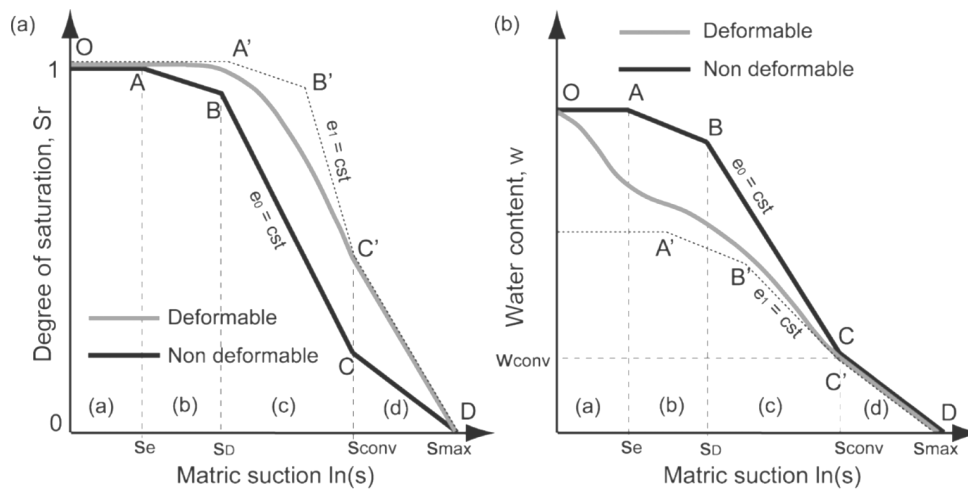


Fig. 4.1: Conceptual representations of the water retention model proposed by Salager et al. (2013): (a) degree of saturation, and (b) water content ( $s_{conv}$  and  $w_{conv}$  are the coordinates of the convergence point).

Available literature on the water retention modelling shows that there are not yet models developed for the water retention behaviour of highly swelling materials such as Wyoming bentonite where in a wide range of the total suctions, the adsorption mechanisms are governing the retention behaviour, more particularly to account for the influence of the void ratio and the microstructural evolutions. One of the reasons could be related to the shortage of data on the retention behaviour of such materials in wetting and drying cycles upon exact control of the void ratio and more important on the mutual interactions with the microstructure.

## 4.2 Water retention features of Wyoming bentonite

The water retention modelling of the bentonite barrier is an essential aspect of the analysis of the performance of the engineered barriers. Earlier in Chapter 2 the motivations for the characterisation of the water retention behaviour of bentonite in such circumstances related to the storage of HLW were presented. Although the bentonite barrier remains under confined conditions, a gradient of the void ratio would be established due to the internal interactions within the buffer. Since the saturation of the bentonite barriers will have initiated from the external boundaries at the host rock formation, a progressive swelling mechanism would harden the internal bentonite materials and could consequently influence the retention behaviour. In addition, when using bentonite in both the granular form and blocks (e.g. Swiss concept), there would be a density gradient between the blocks and the adjacent granular bentonite after the emplacement, since the blocks will be initially emplaced at void ratios ( $e = 0.53 - 0.61$ ) which are much less than the one of the granular bentonite ( $e = 0.83 - 0.95$ ). In addition, the bentonite barrier would be subjected to wetting and drying cycles due to the environmental conditions at the repositories (Section 2.4.2). It was shown in Chapter 2 that the microstructure evolves in a wetting path where the material is approaching the fully saturated state. The evolution of the microstructural void ratio with the degree of saturation for a compacted bentonite material was obtained using the MIP experiments at different points associated to the state of the material on the retention curve. The aim here is to correlate that information with the water retention response of the material. This section aims at presenting a mathematical formulation for the retention behaviour of bentonite which considers the importance of the microstructural evolutions. First, the behavioural features of the bentonite material presented in Chapter 2 are summarised and some terms and trends are defined.

The water retention behaviour of the granular bentonite at different void ratios in terms of water content and degree of saturation is presented in Fig. 4.2. Analysis of the results in terms of water content shows that the retention in this plane is an intrinsic feature that is associated with the adsorption mechanism within the material particles. The retention curves are aligned until they reach the fully saturated state corresponding to their void ratio and total suction called  $\psi_e$ . In the same plane (Fig. 4.2a), it is realised that in a wetting path, the retention curves at different void ratios undergo a change in the slope that implies a yielding mechanism. This yield behaviour occurs at a certain total suction for all compaction states and can be termed as a wetting yield total suction  $\psi_{ew}$ .

Moreover, a residual water content can be considered where the first wetting and the drying paths converge to this value. The corresponding total suction of this residual water content is called residual total suction  $\psi_{res}$ , where it can be assumed about 400 MPa as shown in Fig. 4.2a.

Analysis of the results in terms of degree of saturation (Fig. 4.2b) implies that the presentation of the curves in this plane is resulted from the mapping of the curves in terms of the water content to the degree of saturation by using the relationship  $S_r = w \cdot G_s / e$  for the corresponding void ratios. It can be realised that the hydraulic domain created within the wetting/drying cycles (the hysteresis aperture) is expanding when the void ratio decrease (Fig. 4.2b).

Fig. 4.3a presents the evolution of the total suction term at full saturation state and the air-entry value defined at  $S_r = 0.95$  versus void ratio. Besides, the total suction at which the yield behaviour in a drying path occurs is plotted in this figure. It is observed that all terms are exponentially decreasing with increasing the void ratio.

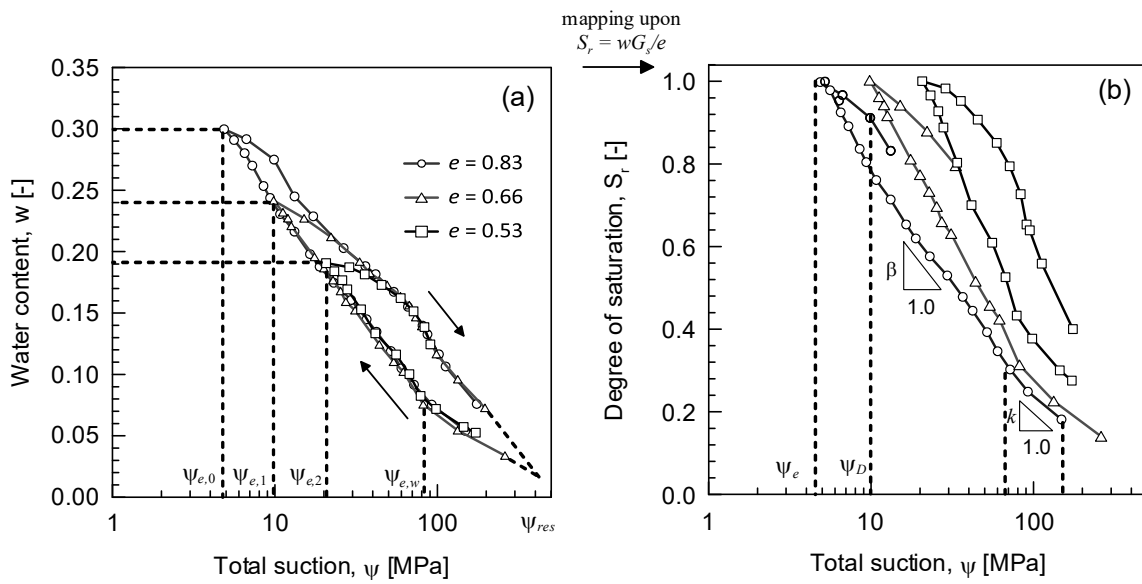


Fig. 4.2: Water retention behaviour of Wyoming granular bentonite: (a) water content vs. total suction, and (b) degree of saturation vs. total suction.

In Fig. 4.2b, it is possible to define two terms for the slope of the water retention curves in a wetting path. The slope of the first part  $k$  which implies a reversible behaviour considering an elasto-plastic framework and a wetting yield total suction  $\psi_{ew}$ .

The second slope  $\beta$  can be observed that represents the compressibility behaviour in an elasto-plastic framework. In Fig. 4.3a both slopes are plotted with respect to the void ratio. Although the parameter  $\beta$  exponentially decreases with an increase of the void ratio, the parameter  $k$  exhibits independent of the void ratio and is averaged at a value of  $k = 0.14$ .

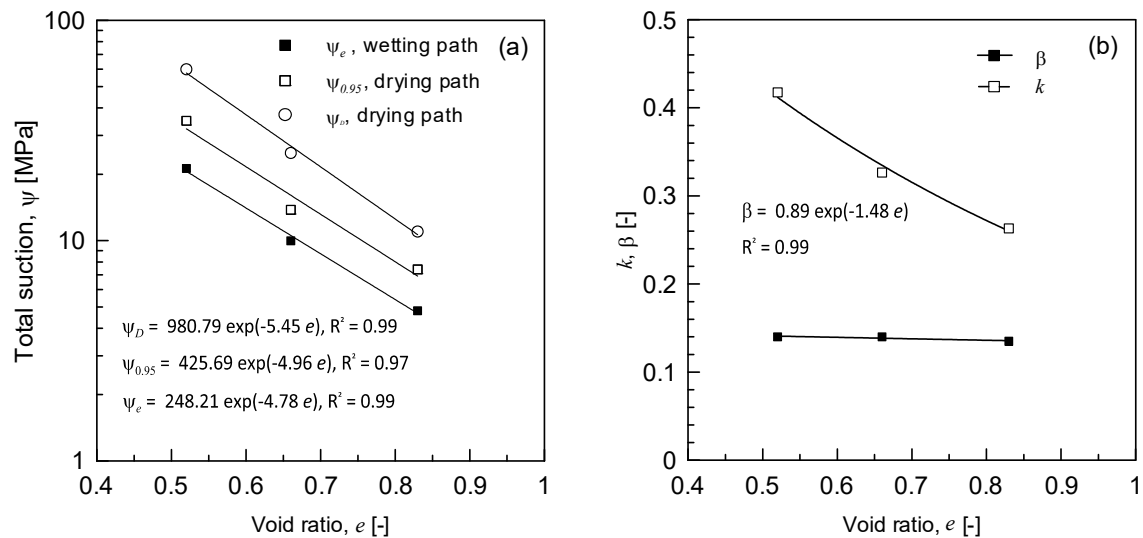


Fig. 4.3 : (a) Evolution of the air-entry value suction, total suction at saturation and drying yield total suction with void ratio, and (b) evolution of coefficients of compressibility with void ratio.

In Fig. 4.4, the retention behaviour of the compacted bentonite at  $e = 0.53$  for two performed tests is shown (see Section 2.4.3.4). As it was mentioned before, the bentonite material exhibits a totally reversible retention behaviour in path A – A' – A'' without a hysteresis cycle. In Chapter 3 it was stated that the smectite particles have only one layer of water with a maximum number of sheets per particle at this range of the total suction (from  $\psi_{res}$  to  $\psi_{ew}$ ). This initial hydration is believed to occur on the mineral surface and around the exchangeable cations ( $\text{Na}^+$  for Wyoming bentonite) in the interlayer space. This information can justify the assumption on the elastic behaviour of the retention curve before the wetting yield suction  $\psi_{ew}$ . As shown, two wetting and drying cycles have been performed at point B and C before the initiation of the drying path at full saturation state of point D. It can be observed that although the total void ratio for these tests remains constant for the entire test, the drying yield suction  $\psi_D$  is different for the drying paths B – B', C – C' and finally D – E. To interpret such behaviour, the data on microstructural evolutions during this wetting path obtained in Chapter 3 are integrated to the evolution of the yield drying suction.

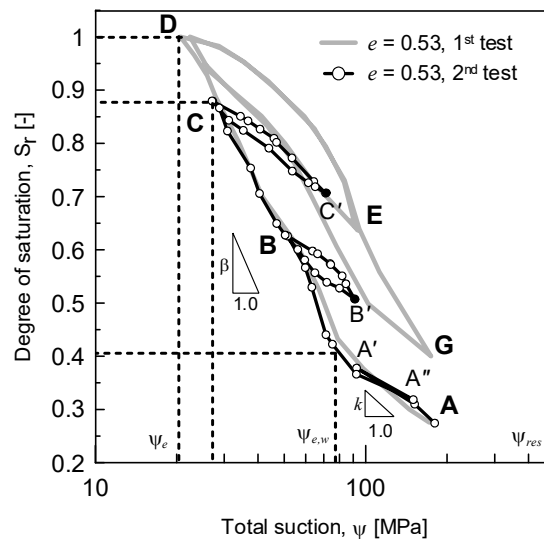


Fig. 4.4: Water retention behaviour in reversible and irreversible hydraulic domains.

The evolution of the microstructural void ratio  $e_m$  with total suction and degree of saturation using MIP data is presented in Fig. 4.5a. Accordingly, the evolution of the drying yield suction obtained from Fig. 4.4 versus microstructural void ratio  $e_m$  is plotted in Fig. 4.5b. It is seen that the drying yield suction  $\psi_D$  is exponentially increasing with an increase in microstructural void ratio  $e_m$ . This observation reveals the expansion of the hydraulic domain created by wetting/drying cycles due to the evolution of this microstructural term. These observations in terms of water retention and microstructural behaviour of the granular bentonite are integrated into a mathematical model as follows.

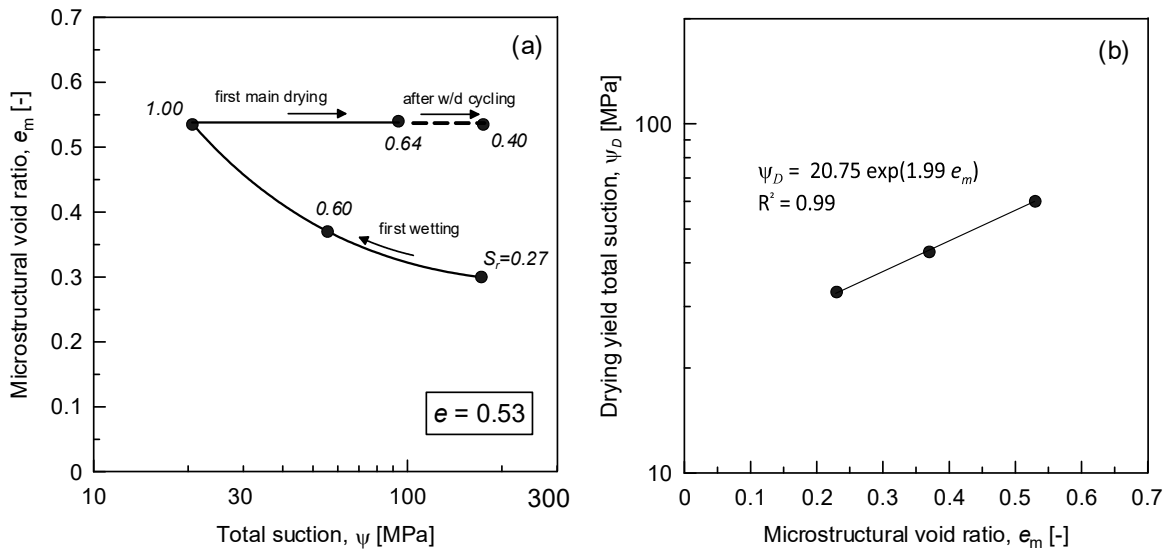


Fig. 4.5: (a) Evolution of the microstructural void ration with total suction, and (b) evolution of the drying yield total suction with microstructural void ratio.

#### 4.2.1 Mathematical formulation

With regards to the particular behavioural features of the water retention curves of bentonite and their mutual interaction with the microstructure, a retention model is presented similar to the conceptual framework developed by Nuth & Laloui (2008). Although the model proposed by Nuth & Laloui (2008) considers the capillary suction, it will be referred here in order to account for the shape rather than the water retention mechanism. Moreover, the coupling between the water retention behaviour and the void ratio is presented in a different way taking into account an exponential evolution of the drying yield and compressibility slope with the void ratio rather a linear relationship. Besides, an *anisotropic* hardening is proposed here rather than a *kinematic* hardening used by Nuth & Laloui (2008) to account for the observations on the water retention behaviour of the bentonite material.

To model the evolution of the degree of saturation with total suction, the following principles are respected:

1. An elasto-plastic approach is considered to describe the scanning paths. The decomposition of the degree of saturation is performed to describe the scanning lines that are the unloading – reloading paths during drying and wetting cycles.
2. Linear anisotropic hardening is used to describe the main wetting and main drying paths and thus the hysteresis behaviour. Analysis of the retention curves in Fig. 4.2b reveals that an anisotropic hardening is required to account for both the change in size and translation of the yield surface due to the increase of the compressibility slope and expansion of the hydraulic domain by the decrease in the void ratio, respectively. The proposed model is represented in Fig. 4.6.

3. A non-linear evolution of the slope of the compressibility  $\beta$  with the void ratio is considered to account for the shape of the retention curve. Thus, the wetting paths at the lower void ratios are obtained due to the rotation of a reference wetting path and the evolution of  $\beta$  with the void ratio. The evolution of the suction at full saturation state  $\psi_e$  takes place automatically because  $\psi_e$  is geometrically linked to the wetting yield total suction  $\psi_{ew}$  ( $\psi_{ew}$  does not change with void ratio) as follows:

$$\ln\left(\frac{\psi_{ew}}{\psi_e}\right) = (1 - S_{r,ew})\beta^{-1} \quad \text{Eq. 4.1}$$

where  $S_{r,ew}$  is the corresponding degree of saturation at  $\psi_{ew}$ .

4. The expansion of the aperture of the hysteresis with the void ratio is taken into account by considering the evolution of the drying yield suction  $\psi_D$  with the void ratio.
5. It was shown that for a given void ratio, the drying yield suction  $\psi_D$  evolves with the microstructural void ratio  $e_m$  (Fig. 4.5). This feature of the model requires informations on the microstructural evolution of the material at a given void ratio during a wetting process. The representation of the model is shown in Fig. 4.8.

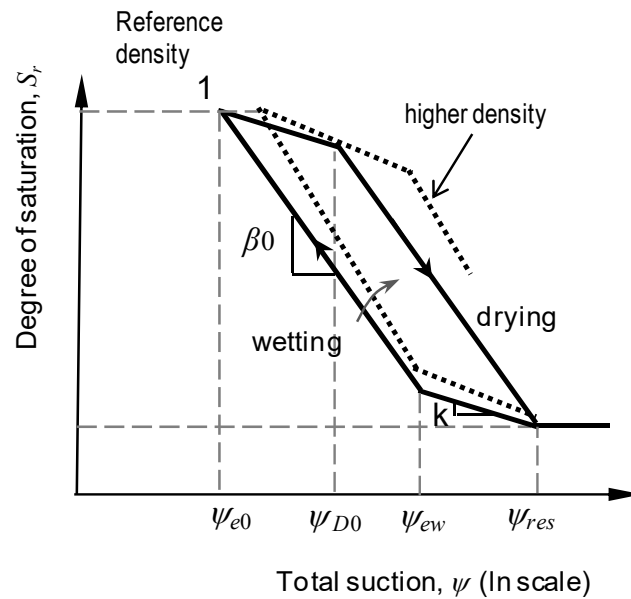


Fig. 4.6: Proposed model for the water retention behaviour of the bentonite material based on the anisotropic hardening behaviour.

Thus, the change of the degree of saturation is decomposed in reversible and dissipative with an elasto-plasticity approach:

$$dS_r = dS_r^e + S_r^p \quad \text{Eq. 4.2}$$

The elastic increment of degree of saturation can be then defined as:

$$dS_r^e = k \frac{d\psi}{\psi/\psi_e} \quad \text{Eq. 4.3}$$

As mentioned before,  $k$  is an elastic modulus represented in Fig. 4.6. It is noted that in this model corresponding to the experimental observations, the full saturation state is defined when the degree of saturation reaches 1.0 and the model is considering  $\psi < \psi_e$  as the impossible zone under constant volume conditions at a given void ratio. This assumption is in agreement with the observation on the influence of the confinement on the water retention behaviour of the bentonite material (Section 2.4.3.5). Moreover, the elastic increment remains null for the range  $\psi > \psi_{res}$ .

The yield surface to delimit the reversible domain is defined for both wetting and drying paths:

$$f = \left\| \ln(\psi) - \ln(\psi_D) + \frac{1}{2} [\ln(\psi_D) - \ln(\psi_{e,0})] \right\| - \frac{1}{2} [\ln(\psi_D) - \ln(\psi_{e,0})] \quad \text{Eq. 4.4}$$

where  $\psi_{e,0}$  is the reference total suction at full saturation and  $\psi_D$  is the actual drying yield total suction which evolves from an initial value  $\psi_{D,0}$  which is the reference yield total suction. The aperture of the hysteresis domain is defined by the term  $\frac{1}{2} [\ln(\psi_D) - \ln(\psi_e)]$ . A plastic increment for the change of the degree of saturation is defined considering the associated flow rule:

$$dS_r^p = \lambda_H^p \frac{\partial f}{\partial \psi} \quad \text{Eq. 4.5}$$

where the plastic multiplier  $\lambda_H^p$  can be written as:

$$\lambda_H^p = \beta \frac{d\psi}{\psi_D} \text{sign} \left( \ln \left( \frac{\psi}{\psi_D} \right) + \frac{1}{2} \ln \left( \frac{\psi_{D0}}{\psi_e} \right) \right) \quad \text{Eq. 4.6}$$

As mentioned before,  $\beta$  is called the coefficient of compressibility for the plastic part of the degree of saturation  $S_r^p$  (Fig. 4.6) which is the translational term of the hardening rule and formulated as a function of the void ratio as follows:

$$\beta = \beta_0 \exp[a(e - e_0)] \quad \text{Eq. 4.7}$$

where  $e_0$  is a reference void ratio selected as the void ratio of the material at the poured state, i.e.  $e = 0.83$  and  $a$  is a material parameter. In order to have the evolution of the aperture to account for the expansion of the hydraulic domain with the void ratio (change of size of the yield surface), the reference drying yield total suction is updated by the following equation:

$$\psi_D = \psi_{D,0} \exp[d(e - e_0)] \quad \text{Eq. 4.8}$$

where the reference drying yield total suction  $\psi_{D,0}$  is also considered to be associated with the poured state of the granular bentonite and  $d$  is a material parameter as well. It is noted that the evolution of  $\psi_e$  is automatically performed through the evolution of  $\beta$  with the void ratio.

For the scanning behaviour within the hydraulic domain upon a constant total void ratio, it was observed that the drying yield suction  $\psi_D$  is evolving with the microstructural void ratio. Thus, at a given void ratio,  $\psi_D$  is formulated as:

$$\psi_D = \psi_{D,0} \exp[m(e_m - e_{m,0})] \quad \text{Eq. 4.9}$$

Where  $m$  is a microstructural parameter obtained from typical representation plots (see Fig. 4.5b) and  $e_{m,0}$  is the microstructural void ratio at the as compacted state. In the following section the model is calibrated and validated by the experimental results.

The representation of the model to account for the evolution of the microstructural void ratio under constant volume conditions is shown in Fig. 4.7.

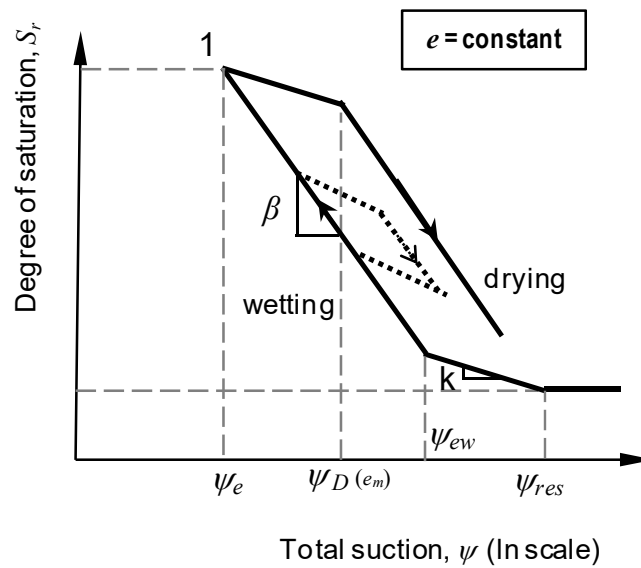


Fig. 4.7: Representation of the model to take into account the evolution of the drying yield suction with microstructural void ratio.

## 4.2.2 Model response

### 4.2.2.1 Void ratio dependency

For the calibration of the model to account for the influence of the void ratio on the entire water retention curve, there are seven parameters to determine: the reference total suction at full saturation state  $\psi_{e,0}$  (or the reference wetting yield total suction  $\psi_{ew}$ , by Eq. 4.1), the residual total suction  $\psi_{res}$  which is assumed at 400 MPa, the elastic modulus  $k$ , the reference coefficient of compressibility  $\beta_0$ , the reference drying yield total suction  $\psi_{D,0}$  and the material parameters  $a$  and  $d$ . As it was mentioned in the previous section, the reference values in the model are correspondent with the retention behaviour of the granular bentonite at poured state.

Thus, the curve fitting results for the calibration of the model based on the water retention curve at  $e = e_0 = 0.83$  is presented in Fig. 4.8a. The reference values of  $\beta_0$ ,  $\psi_{D,0}$  and the parameters  $\psi_{ew}$  and  $\psi_{res}$  are presented in this figure. Besides, the value of  $k = 0.14$  is obtained.  $k$  is assumed as a model parameter, however, analysis of the results in Fig. 4.3 shows that  $k$  can be assumed as constant for all compaction states.

In order to evaluate the other parameters  $a$  and  $d$  which update the evolution of the compressibility slope  $\beta$  and the actual drying yield total suction  $\psi_D$  (and consequently the aperture of the hysteresis), the calibration with experimental data of the retention curve at  $e = 0.53$  is selected. The results of the curve fitting and the parameters  $a$  and  $d$  are shown in Fig. 4.8b. After setting the parameters, the simulation of the water retention curve of the compacted granular bentonite at  $e = 0.66$  is presented in Fig. 4.9. It is observed that the model fits the experimental data well.

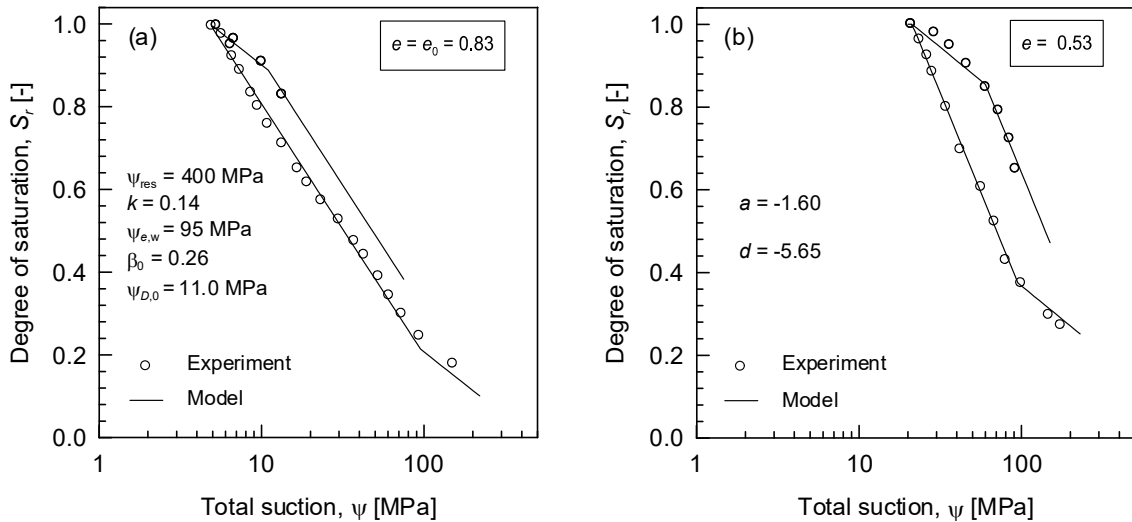


Fig. 4.8: Calibration of the water retention model with experimental results of Wyoming granular bentonite at (a) poured state ( $e = e_0 = 0.83$ ), and (b) compacted state ( $e = 0.53$ ).

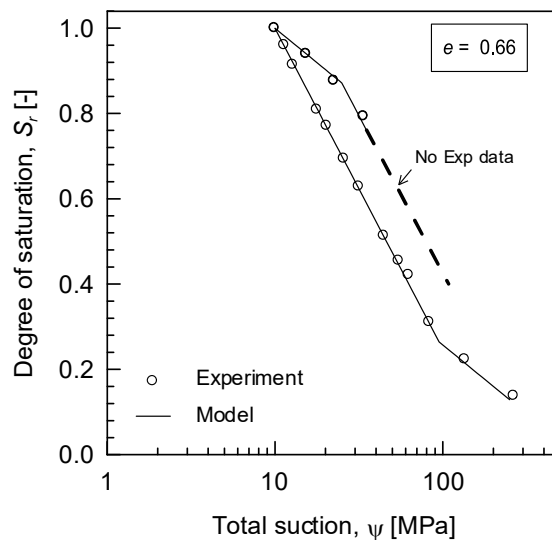


Fig. 4.9: Simulation of the retention behaviour of Wyoming granular bentonite compacted at  $e = 0.66$  corresponding to dry density of  $1.65 \text{ Mg/m}^3$ .

### 4.2.2.2 Microstructural evolution

For the scanning paths within the entire hydraulic domain, informations on the microstructural evolution at a given void ratio are required. Thus, in addition to the previously mentioned parameters, there are additional parameters  $m$  and  $e_{m,0}$  that should be determined to find the evolution of the drying yield suction  $\psi_D$  at a given void ratio. Besides, similar to the previous section that the model was formulated based on the void ratio  $e$  as the variable; the model to account for the microstructural evolution is expressed as a function of the microstructural void ratio  $e_m$ .

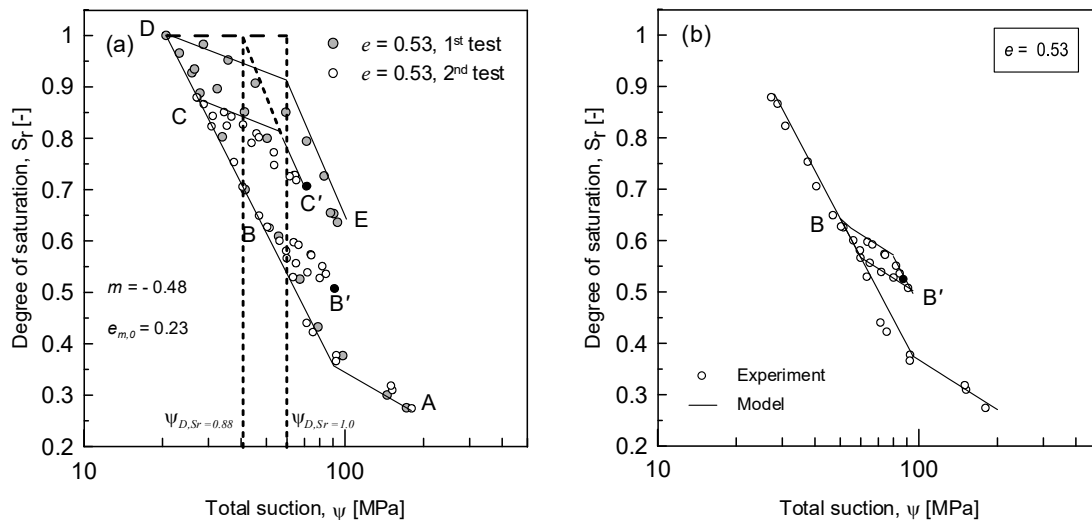


Fig. 4.10: (a) Calibration of the model for the microstructural parameters, and (b) simulations of the wetting and scanning path B – B' of Wyoming granular bentonite compacted at  $e = 0.53$  corresponding to dry density of  $1.80 \text{ Mg/m}^3$ .

For  $e = 0.53$ , in addition to the parameters that were obtained by the curve fitting on the experimental data of the first test in Fig. 4.10a (in grey colour), the evolution of the drying yield suction between path C – C' and path D – E is considered to calibrate the model for the parameter  $m$ . Thus,  $m = -0.48$  is obtained for an initial microstructural void ratio  $e_{m,0} = 0.23$ .

The model then is used to simulate the second test in Fig. 4.4 for the scanning path B – B'. The results of the simulation and the experimental data are presented in Fig. 4.10b. The simulation data and the experimental results are found in a good agreement.

## 4.3 Summary and conclusions

A mathematical model based on an elasto-plasticity framework and a linear anisotropic kinematic rule was presented for the water retention curves in terms of degree of saturation. The aim was to integrate the behavioural features of the granular bentonite into a water retention model based on the observations presented in Chapters 2 and 3. The model parameters were defined based on the physical concepts behind the water retention behaviour of the bentonite and were supported by experimental evidences from previous chapters.

The model produces the water retention curves for the entire hydraulic domain (wetting up to the full saturation state followed by a drying path) under a constant void ratio at which the granular bentonite is compacted. The model has seven parameters, and to calibrate the model, a

reference state of the granular bentonite corresponding to the poured conditions was selected. At this state the material had the maximum void ratio which was chosen as the reference void ratio. The other features of the retention curve such as the slope of the compressibility line ( $\beta$ ) and the drying yield total suction ( $\psi_{D,0}$ ) at this material state were selected as the reference values. Three material parameters of the slope of the elastic part ( $k$ ), the residual total suction ( $\psi_{res}$ ) and the wetting yield total suction ( $\psi_{e,w}$ ) were determined and found independent of the void ratio. The other material parameters of the model ( $a, d$ ) to account for the evolution of the compressibility line and the drying yield total suction were calibrated using another data set at a given compaction state. Moreover, the drying yield total suction was found to be evolving with the microstructural void ratio  $e_m$  which required the MIP data on a wetting path. Two additional parameters to consider this feature of the retention behaviour were calibrated at a given void ratio. These parameters describe the evolution of the hysteresis domain created by subsequent scanning paths within the entire retention domain at a given void ratio. Lastly, the model was validated for the evolutions of both total and microstructural void ratios for the entire hydraulic domain and for the scanning path within this domain, respectively. The model was found to fit well the available experimental data obtained in Chapter 2.

## **5 Thermo-hydro-mechanical characterisation of Wyoming granular bentonite using an advanced triaxial cell system**

This chapter is addressing the thermo-hydro-mechanical (THM) analysis of Wyoming granular bentonite in triaxial conditions. The chapter consists of two main parts: the first one which is devoted to the introduction and calibration of an innovative double-wall triaxial system for studying the behaviour of geomaterials subjected to complex THM loading conditions; and the second part dedicated to the analysis of the behaviour of Wyoming granular bentonite using the THM triaxial cell described in the first part.

In the case of the deep geological disposal of radioactive wastes, the involved geomaterials basically undergo significant changes in temperature, stress state and water content. The response of the Wyoming granular bentonite in such complex THM stress paths has to be quantified to assess the performance of the buffer material in engineered barrier systems.

The calibration process of the THM triaxial system to assess the actual response of the material is first presented. An analytical approach is used and validated to obtain the stress – strain and the volume change behaviour of the material upon mechanical and thermal loading conditions.

Based on the primary analyses of the hydro-mechanical behaviour of Wyoming granular bentonite performed in Chapter 2, particular sample preparation and testing procedures are proposed for the granular bentonite in saturated and unsaturated conditions. The total suction is controlled by the means of the vapour equilibrium technique. The influence of the total suction on the isotropic and deviatoric behaviours of the material is investigated. The influence of confining stress on the deviatoric behaviour of saturated and unsaturated samples is analysed as well. The influence of temperature is studied in terms of thermal volumetric strains and deviatoric behaviour of the material. The results provide a global picture of the general behaviour of Wyoming granular bentonite subjected to different THM conditions in a wide range of applied total suctions, mechanical loading and temperatures.

### **5.1 THM triaxial testing in geomaterials**

#### **5.1.1 Backgrounds**

The emerging technologies such as disposal of high-level waste (HLW) in deep rock/clay-rich formations (Gens et al. 1998), gas production in shales, petroleum drilling, injection and production activities (Dusseault et al. 1988) and geothermal structures (Laloui et al. 2003) require advanced experimental testing facilities. To interpret the response of such thermally active systems, an understanding of the coupled thermo-hydro-mechanical (THM) behaviour of the involved geomaterials is an essential task. In general, to analyse the coupled THM behaviour of geomaterials, the application of suction and temperature and the measurement of volume change of the sample are the most challenging subjects.

### 5.1.1.1 Application of suction and temperature

In recent years the triaxial behaviour of geomaterials in different THM paths has been investigated by various researchers. The impacts of high suction magnitude on the triaxial response of bentonite-based materials were evaluated (e.g. Graham & Blatz 2000, Blatz & Graham 2003). The influence of temperature on volume change and shear stress – strain behaviour of unsaturated bentonite-based material at triaxial conditions was evaluated by other researchers (e.g. Wiebe et al. 1998, Uchaipichat & Khalili 2009).

The vapour equilibrium technique has been mainly used in triaxial systems in several studies to control the total suction (e.g. Romero 1999, Graham & Blatz 2000, Blatz et al. 2008, Alsherif & McCartney 2013). This technique involves the use of saturated salt solutions to control the relative humidity of air within a closed system applied to the sample. The relative humidity is related to the total suction through the psychrometric law (Eq. 2.4).

In addition, the axis translation techniques have been as well used in triaxial cells (e.g. Aversa & Nicotera 2002). With this technique, the capillary suction and net stress can be controlled by applying a positive water pressure, elevating the total stress and air pressure by the same amount and preventing the occurrence of cavitations. It is worth mentioning that the application of this technique for a nearly saturation state (i.e. degree of saturation greater than 0.8 – 0.9) has been criticised by some researchers (e.g. Bocking & Fredlund 1980, Delage et al. 2008) due to the existence of the discontinuous air phase.

Triaxial cells for thermo-mechanical testing of soils have been developed for three main techniques as reported by Cekerevac et al. (2005): (i) heating by circulating fluid (e.g. Savvidou & Britto 1995, Cekerevac et al. 2005), (ii) internal heaters (e.g. Kuntiwattanakul et al. 1995, Moritz 1995, Alsherif & McCartney 2013), and (iii) lateral heaters (e.g. Baldi et al. 1985, Delage et al. 2000). For testing under unsaturated conditions, the coupled influence of high temperature and the applied suction by the vapour equilibrium technique should be considered due to the sensitivity of the method to air temperature (Alsherif & McCartney 2013).

Tang & Cui (2005) investigated a calibration test for several saturated salt solutions to account for the effect of temperature on the total suction values given by salt solutions. A high rate of 0.45 %/°C was obtained for the variation of the relative humidity with respect to the temperature increase for  $Mg(NO_3)_2$  saturated solutions used for the determination of the water retention of Wyoming bentonite.

### 5.1.1.2 Volume change measurement

For saturated conditions, the volume change of the sample is obtained based on the exchanged pore water volume by the assumption that both soil particles and water are incompressible. For unsaturated conditions, the volume change should be evaluated by more advanced techniques.

Laloui et al. (2006) categorised the volume change measurement of unsaturated soil samples into three main categories: (i) cell liquid measurement, (ii) direct air-volume and water-volume measurements, and (iii) direct measurements on the sample.

With the cell liquid measurement technique, the volume of the confining liquid moving in and out from the triaxial cell is measured. This technique is influenced by the expansion of the cell wall, the thermal volume expansion of the confining fluid and the accuracy of the volume measurement (Leong et al. 2012). These problems can be reduced by utilising a double-wall cell (e.g. Wheeler 1988, Sivakumar 1993, Yin 2003, Sivakumar et al. 2006) and minimising the

liquid volume using an inner-cylinder (e.g. Bishop & Donald 1961, Aversa & Nicotera 2002, Toyota et al. 2001). Thus, the inner-cell is totally enclosed within the outer-cell; both the inside and outside of the inner-cell are subjected to identical pressures (Laloui et al. 2006).

Direct air-volume and water-volume measurements involve separate measurements of both the volume of air and the water drained from the soil sample. The method may be successful as soon as the air phase is continuous (Laloui et al. 2006).

In direct measurements, local displacement transducers (for local measurements) are used in order to evaluate the sample volume change under triaxial stress conditions (Maatouk et al. 1995 and Blatz & Graham 2003). However, the shortcoming of this method is that measurements are not particularly reliable at large strains (Sivakumar. 1993, Sivakumar et al. 2006). Laser techniques (e.g. Romero et al. 1997), digital imaging (Gachet et al. 2003) and non-contact transducers such as proximity transducers (e.g. Fredlund & Rahardjo 1993, Leong et al. 2012) are other methods for the volume measurement of soil samples in triaxial systems.

In the following sections an advanced multipurpose triaxial system for suction-controlled testing under wide ranges of temperature and pressure is presented (Salager et al. 2010, Seiphoori et al. 2011a and 2013). First, the THM triaxial cell and its advanced features are highlighted and presented. Then, a new approach for the calibration procedure is proposed to formulate the load-displacement under high mechanical stress applications. Considering that the system is provided with a double-wall technique, the calibration of the volume change measurement under geometrical, mechanical and thermal evolutions of the inner-cell is presented.

## **5.2 THM triaxial cell system used in this study**

The triaxial system consists of five main parts: the double-wall triaxial cell, the heating system, the suction control systems and the loading system, including the data acquisition. The general view of the THM double-wall cell and its associated components is shown in Fig. 5.1.

The cell holds samples with 50 mm in diameter and 100 mm in height. Top and bottom caps are equipped with sintered steel porous plates, designed to work at high mechanical pressures.

The inner-cell cylinder is made of stainless steel. Water and air connection lines are fitted to the upper and lower caps inside the inner-cell and they are then conducted through the outer-cell in order to connect them to the relevant pressure/volume controlling systems. O-ring seals are used in the perimeter of both caps to prevent any leak of inner-cell fluid (water) into the outer-cell fluid (oil) or vice versa. While the system is under operation, the outer-cell fully encloses the inner-cell and both are pressurised to the same confining pressure using a double volume/pressure controller. Using this configuration ensures that the inner-cell does not deflect, preventing the measurement of the sample volume variation being affected by the inner-cell deformation (see also Wheeler 1988).

In this system, the cell pressure can be controlled in the range of 0 – 30 MPa. Therefore, the inner-cell volume measurements should be corrected for the evolution of the tubing systems and the pressure/volume controller with the applied cell pressure. Since the measurement of the sample volume change is calibrated to the water flow into or out of the inner-cell, the temperature variation can also affect the results.

Temperature of the system can be controlled in the range of 5 – 150 °C using a heating/cooling device which regulates the heat of the fluid in the outer-cell. There is a thermocouple attached to the sample to assess the sample temperature which is different from the temperature in the heating bath (resolution of 0.01 °C).

The mechanical axial load on the sample is applied by controlling the pressure in a hydraulic press which is applied by a pressure controller. The maximum applicable axial force is 450 kN corresponding to 230 MPa axial stress with respect to the sample area. The axial load can be measured by the means of an internal load cell and also an external load cell (Fig. 5.2). The external load cell measures the force by taking into account the pressure in the hydraulic press and an effective area. The vertical displacement is measured by two LVDTs (Linear Variable Differential Transformer) positioned outside the cell. In this system, several experimental layouts can be used depending mainly on the degree of saturation of the sample. For this reason, the apparatus can be adapted by simple modifications such as changing the positions of various components. A conventional experimental layout for tests at saturated conditions can also be applied with or without the inner-cell cylinder. In case of removal of the inner-cell, the volume change of the sample would rely on the pore volume change.

Two pressure/volume controllers are used to independently control the pore water pressure (see Fig. 5.1) and to measure the water volume exchange at each base (top and bottom). The use of independent controllers provides the measurement of the pore water pressure developed under undrained conditions and allows running permeability tests by applying a hydraulic gradient along the sample.

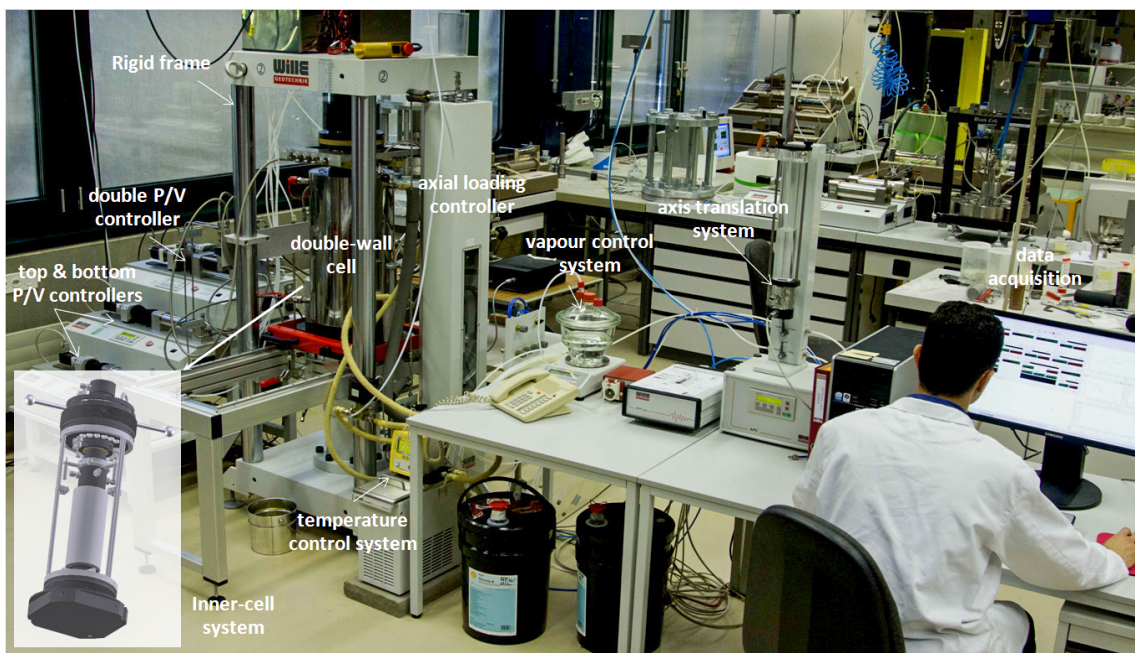


Fig. 5.1: General view of the THM triaxial system and its associated parts.

The system is provided with two systems for the suction controlled tests: the axis translation and the vapour transfer techniques. To control the capillarity pressure in the range of 0 – 1.5 MPa, air pressure and water pressure are independently regulated inside the sample to control their difference (matric suction). In Fig. 5.2, the general layout of the system is shown for testing under unsaturated conditions using the vapour transfer technique. Fig. 5.3a depicts the schematic diagrams of the axis translation system. To reduce the equalisation time to the imposed matric suction value, a double drainage system has been developed, allowing air and water pressures on the top and on the bottom bases.

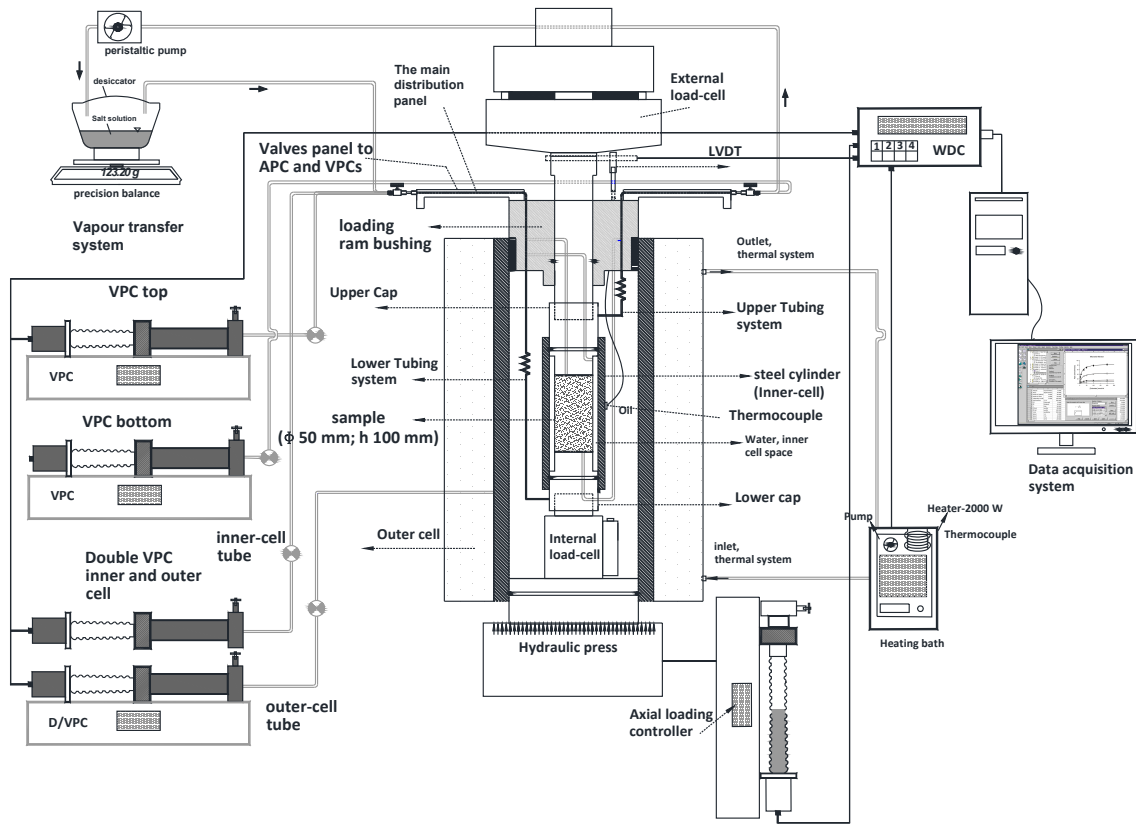


Fig. 5.2: Schematic layout of the double-wall triaxial cell for testing in unsaturated conditions.

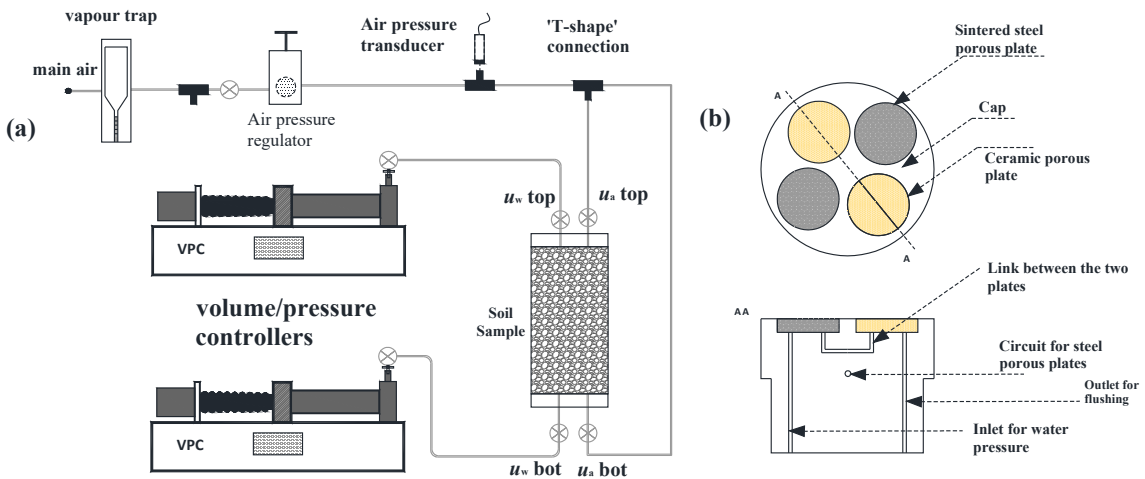


Fig. 5.3: (a) Experimental setup for application of the axis translation technique, and (b) special cap for the application of the axis translation technique.

In this regard, special 4-hole caps are developed (Fig. 5.3b): one pair for applying pore water pressure and flushing and the other pair for air pressure. The two fluids are separated by using a high air-entry value (HAEV) ceramic disc (1.5 MPa). Air pressure is provided by the laboratory system for compressed air (maximum pressure 1.5 MPa) and regulated to the target value by an electronic air pressure regulator.

Vapour equilibrium consists of controlling the relative humidity of a closed system in which the soil is immersed. The relative humidity of the reference system is controlled using salt solutions at various concentrations. In this configuration, the caps with coarse porous stones are applied. By this technique the pore water potential can be controlled in the range of 4 – 400 MPa.

### 5.2.1 Calibration procedure

When performing THM experimental tests particularly at high pressure and temperature ranges, the measured data must be adjusted in order to assess the real response of the sample. The deformation of the components of the system due to the applied mechanical loading is considered for the force – deformation response of the sample. Moreover, the expansion of the connections and the controllers due to the application of pressure and temperature must be taken into account for the calibration of the sample volume change. The calibration of the force – displacement response of the sample and the volume change behaviour at elevated temperatures and pressures are presented in the next sections.

#### 5.2.1.1 Axial load-deformation calibration

To obtain the actual force – deformation behaviour of the sample, it is necessary to calibrate the measurements recorded by transducers. This difference is related to the deformation of the components of the system and the frictional forces in the O-ring seals. In this regard, the free body diagrams (FBD) of the involved components were considered by assuming the equilibrium of the system at static conditions. First, it is assumed that the cell has moved  $\delta h$  upward due to a loading step.  $\delta h$  is recorded by the LVDT out of the cell called cell displacement. The initial and final configurations of the cell are shown in Fig. 5.4. In this mechanism, the upper component consisting of the loading piston and the upper cap remains fixed at their initial positions and the whole system moves upward. Therefore, three main resisting forces become active during the loading step: (i) upper tubing system resisting force ( $F_t$ ), (ii) frictional force in loading ram bushing ( $F_F$ ), and (iii) frictional force due to O-ring seals at the upper cap ( $F_{o,up}$ ). It has to be mentioned that the lower tubing system is inducing no resistance upon this configuration.

Fig. 5.5 shows the FBDs of the three main components in the axial direction involved in the loading mechanism.  $F_v$  is the actual force applied on the sample,  $F$  and  $F'$  are the forces recorded by the internal and external load-cells, respectively;  $F_{o,up}$  and  $F_{o,lr}$  are the frictional forces of the O-ring seals;  $\sigma_{in}$  and  $\sigma_{out}$  are the inner and outer-cell pressures,  $F_F$  is the frictional force in the loading piston bushing;  $W_u$ ,  $W_L$  and  $W_s$  are the weights of the upper part, lower part and the inner-cell cylinder, respectively.  $A_{in}$  is the internal area of the inner-cell space and  $A_o$  is the area of the sample in contact with the caps.  $F_s$  is the force applied to a supporting screw to push the inner cell steel cylinder during a loading step. By assuming the equilibrium in vertical direction for the FBD (1),  $F_v$  can be written as:

$$F_v = F' - F_t - F_F - F_{o,up} - (\sigma_{in} - \sigma_{out})A_{in} + W_u \quad \text{Eq. 5.1}$$

Referring to FBD (3) in which the internal load cell is involved, the following expression can be written:

$$F_v = F - (\sigma_{in} - \sigma_{out})A_{in} - F_s - W_L \quad \text{Eq. 5.2}$$

The equilibrium for the FBD (2) returns the following relationships:

$$F_s = F_{o,up} + W_s \quad \text{Eq. 5.3}$$

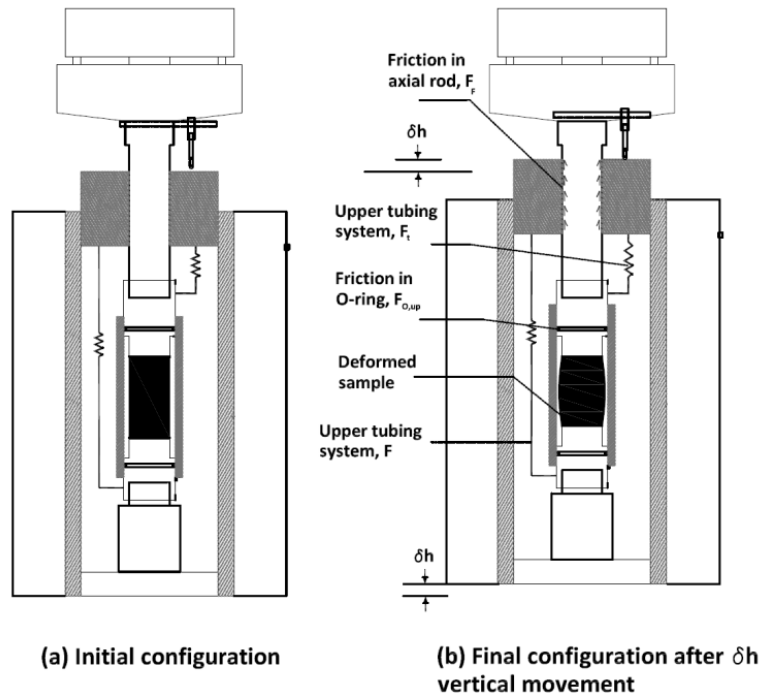


Fig. 5.4: Initial and final configurations of the cell in a loading step.

For a loading step, the friction in the lower O-ring is not applying any resistance and the steel cylinder is actually sliding around the upper cap. Then this term has not come in Eq. 5.2 and Eq. 5.3. By substituting Eq. 5.3 in Eq. 5.2, the following equation is obtained for the vertical force applied on the sample.

$$F_v = F - (\sigma_{in} - \sigma_{out})A_{in} - F_{o,up} - W_s - W_L \quad \text{Eq. 5.4}$$

Eq. 5.4 implies that the vertical force imposed to the sample is a function of both inner- and outer-cell pressures. However, when the inner- and outer-cell pressures are equalised by the means of the double volume pressure controller, this term would be cancelled from the above equation. Thus, when the pressures on both walls of the inner-cell are equal, Eq. 5.4 can be written in a simpler form:

$$F_v = F - F_{o,up} - W_s - W_L \quad \text{Eq. 5.5}$$

Loading tests on the inner-cell proved that in case of enough lubrication,  $F_{o,up}$  is negligible (< 20 N). There is a small discrepancy between  $F$  and  $F'$  records due to the frictional force in the loading piston bushing ( $F_f$ ) and the resistance of the upper tubing connections ( $F_t$ ).

By subtracting Eq. 5.1 and Eq. 5.2 and setting the inner- and outer-cell pressures equal to each other, the following relationship can be obtained:

$$F' - F = F_t + F_f - W \quad \text{Eq. 5.6}$$

where,  $W$  is the total weight of all components in Fig. 5.5. The force term of  $F_t$  is due to the stiffness of the tubing connection and  $F_f$  is a frictional force.

In order to evaluate the resistance stress due to the terms  $F_t$  and  $F_f$ , a particular configuration for the inner-cell was considered. Thus, the inner-cell was first filled with water and then an inlet flow with a rate of 0.15 ml/min was applied. The displacement of the loading piston was

allowed so that the only resistance was due to the friction in the bushing and the one of the tubing system. This test provided the determination of the resisting force in terms of pressure which is applied inside the inner-cell. The equivalent pressure resulted from the tubing connection, and the piston friction is expressed as  $(\sigma_t + \sigma_F)$  depicted in Fig. 5.6.

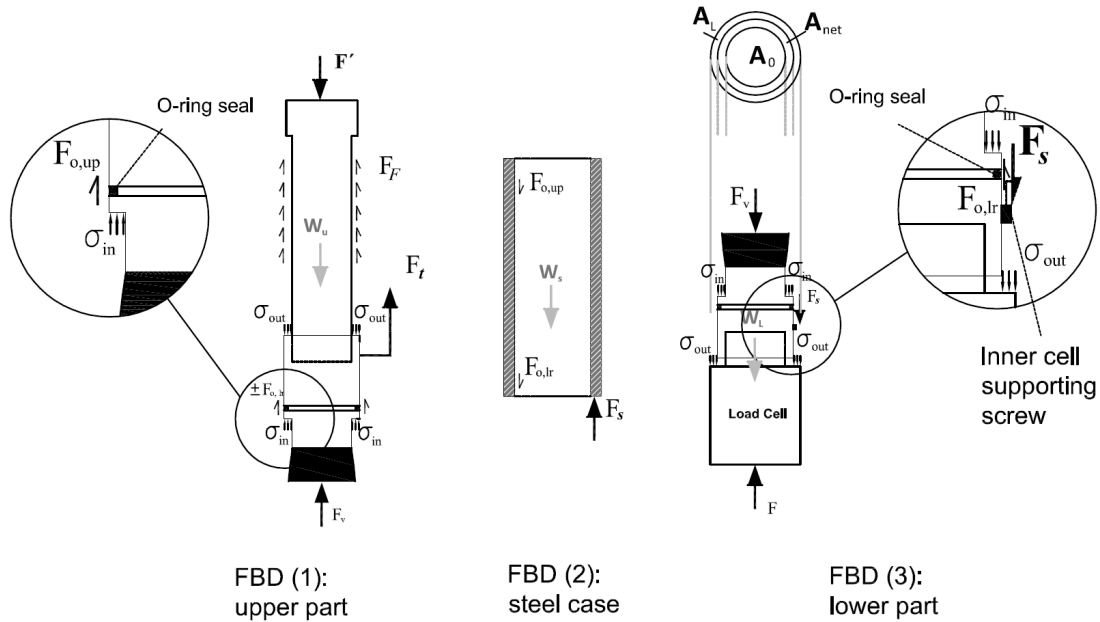


Fig. 5.5: Free body diagrams at static equilibrium for different components of the inner-cell system.

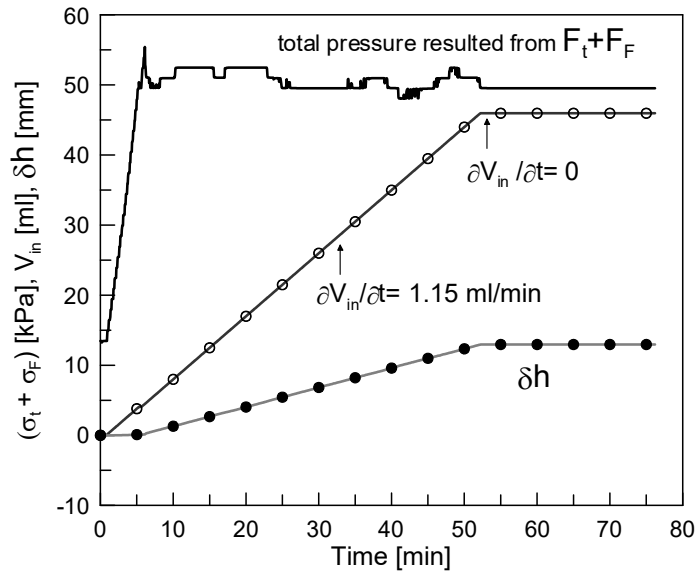


Fig. 5.6: Evaluation of the stress resulted from tubing connections and frictional force in the loading piston.

Referring to Eq. 5.6, it can be implied that the external and internal load cells yield approximately the same values and the difference between these two measurements are negligible. However, in case of using the external load cell, the correction according to Eq. 5.6 should be

considered. In this study, the measurements of the external load cell were considered and then these corrections were considered as well. On the other hand, as the cell is working under a wide range of mechanical loads (up to 450 kN), the deformations of these components (lower and upper components including the porous discs) should be quantified in order to correct the displacement recorded by the external LVDTs.

If the actual displacement of the sample is assumed as  $\delta h_s$ , the relationship between the recorded displacement and the actual one can be written by the following equation:

$$\delta h_s = \delta h - \delta h_l - \delta h_u - \delta h_d \quad \text{Eq. 5.7}$$

where,  $\delta h$  is the displacement recorded by LVDT,  $\delta h_l$  and  $\delta h_u$  are the displacement in lower and upper components and  $\delta h_d$  is the displacement of the metallic porous discs.

The porous metallic discs were already compressed to a high range of loading before being used in the triaxial cell. These deformation values can be achieved if the force – deformation response of the upper and lower components and the porous discs are available.

In this regard, a series of axial loading tests using a high capacity axial press was done to obtain the force-displacement behaviour of the involved components. The results of the loading tests are summarised in Fig. 5.7. As the difference between  $F$  and  $F'$  can be ignored with respect to the large loading values, the force applied to the upper part is assumed as  $F$ . The force-deformation curves of the upper and lower part can be interpolated by quadratic function for force less than 50 kN and then it can be assumed linear for the higher forces. Thus, for a given force  $F$  in the axial direction the corresponding deformations of both components can be obtained and consequently the actual deformation of the sample ( $\delta h_s$ ) can be computed using Eq. 5.7.

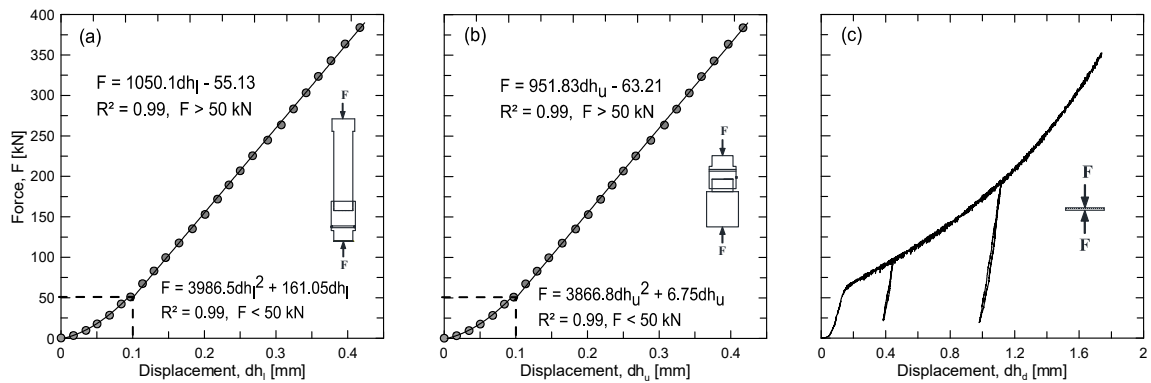


Fig. 5.7: Force-displacement behaviour of the components of the system in axial loading: (a) upper component, (b) lower component and (c) the porous metallic disc.

A solid PVC (Polyvinyl Chloride) sample manufactured with 50 mm diameter and 100 mm height was used in order to verify the calibration process of the force – displacement. PVC is a flexible isotropic material with variance of Poisson's ratio in the range from 0.37 to 0.46 (Puiša & Belevičius 2005).

The force – deformation ( $F_v - \delta h_s$ ) of the PVC sample after correction of the measurement of the system is shown in Fig. 5.8. The measured data were obtained directly from the system and the corrected data were computed using Eq. 5.7. As seen in Fig. 5.8, the maximum deformation of the sample has been corrected for about 0.33 mm (21 % of the actual displacement) using this equation. The corrected data are in very good agreement with the actual behaviour of the PVC sample.

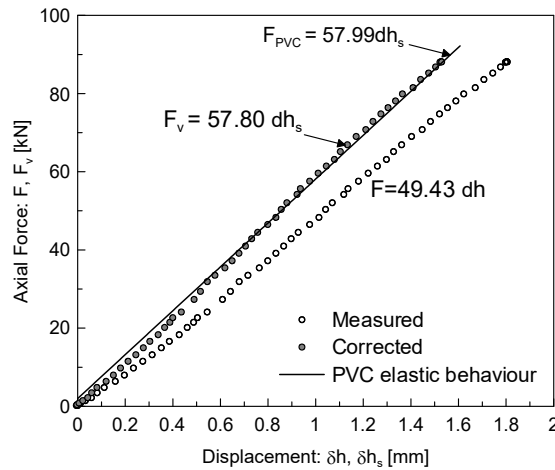


Fig. 5.8: Measured and corrected force – displacement curve of the PVC sample under axial loading.

### 5.2.1.2 Calibration of the volume change of the sample

#### a) Volume change due to geometrical evolution of the inner-cell

The measurement of the volume change is related to the water that flows into or out of the inner-cell. A calibration is then required to account for the volume of the water replaced by the movement of the upper cap into the inner-cell during shearing. This relationship can be formulated based on the geometrical changes of the inner-cell due to an axial displacement. In Fig. 5.9, the initial and final configurations of the inner-cell after a displacement of  $\delta h$  are described. The volume change of the sample can be formulated as the summation of lateral and axial volume changes:

$$\Delta V_s = \Delta V_{s,l} + \Delta V_{s,a} \quad \text{Eq. 5.8}$$

where,  $\Delta V_s$  is the volume change of the sample,  $\Delta V_{s,l}$  is the lateral volume change and  $\Delta V_{s,a}$  is the axial part of the volume change. Also, the inner-cell volume change can be expressed by the following relationship:

$$\Delta V_{in} = -\Delta V_{s,l} - \delta h_s A_{in} \quad \text{Eq. 5.9}$$

where,  $A_{in}$  is the internal area of the inner-cell as shown in Fig. 5.5,  $\Delta V_{in}$  is the inner-cell volume change. This equation can be rearranged for  $\Delta V_{s,l}$  as follows:

$$\Delta V_{s,l} = -\Delta V_{in} - \delta h_s A_{in} \quad \text{Eq. 5.10}$$

On the other hand, it is possible to write the  $\Delta V_{s,a}$  by the following relationship:

$$\Delta V_{s,a} = -A_0(\delta h - \delta h_l) \quad \text{Eq. 5.11}$$

By substituting Eq. 5.10 and Eq. 5.11 in Eq. 5.8, the following relationship is obtained for the volume change of the sample:

$$\Delta V_s = -\Delta V_{in} - \delta h_s A_{in} - A_0(\delta h - \delta h_l) \quad \text{Eq. 5.12}$$

In Eq. 5.11, it is noted that:  $\Delta V_s > 0$  when the volume increases,  $\delta h > 0$  when the height of the sample is decreasing, and  $\Delta V_{in} < 0$  when water is going out of the inner-cell.

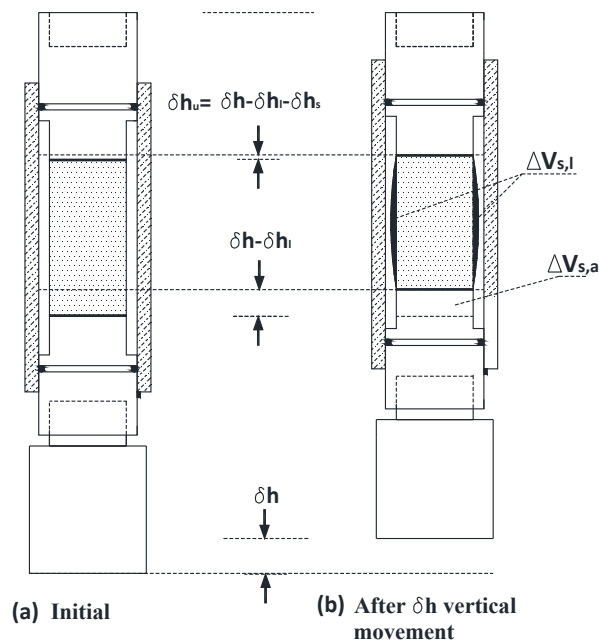


Fig. 5.9: Geometrical evolution of the inner-cell system due to the loading step and deformation of the sample.

In order to validate Eq. 5.12, a test setup was considered using a membrane filled with water (without a sample) inside the inner-cell. Using this configuration, in the absence of any axial displacement, the volume change of membrane (called pore volume) is equal to the inner-cell volume change. The results of this test are shown in Fig. 5.10a. As seen, at a flow rate of  $0.001 \text{ mm}^3/\text{sec}$ , the inner-cell volume change is plotted with respect to the pore volume change recorded with the pore water controller. This agreement confirms the validity of Eq. 5.11 where there is no axial deformation.

Another setup was considered where the axial displacement was applied at undrained conditions where the membrane was filled with water. At given inner-cell and pore volume pressures, an axial displacement with the rate of  $\delta h/\delta t = 0.0001 \text{ mm/sec}$  was applied as shown in Fig. 5.10b. In this setup, the lateral volume change (Eq. 5.10) should be compensated by the axial volume change (Eq. 5.11) to return no volume change for the sample. The sample volume change using Eq. 5.12 was computed and plotted in Fig. 5.10b. As seen, the volume change of the sample is averaged at zero which is in agreement with the assumption of undrained loading conditions.

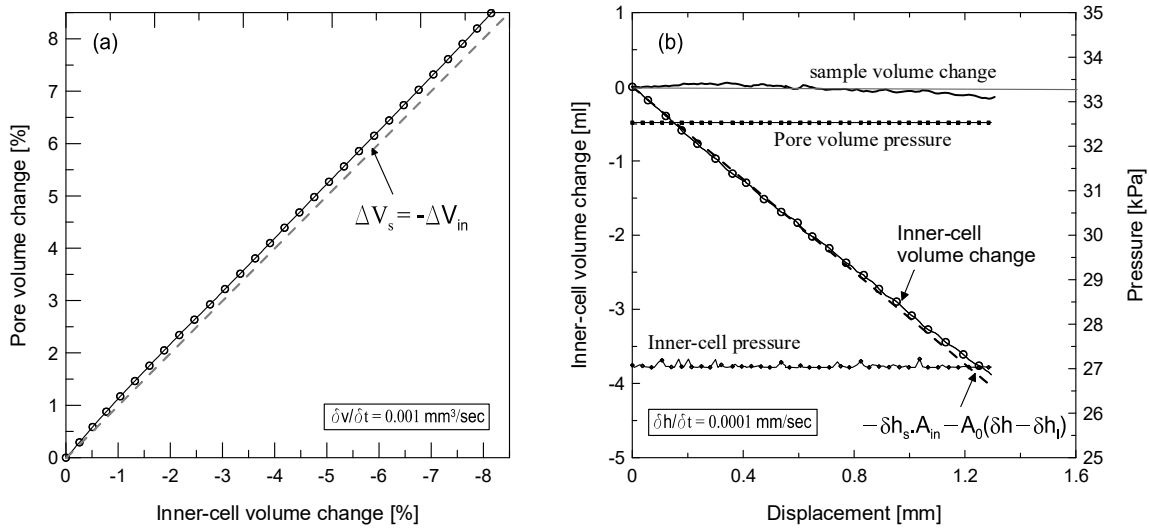


Fig. 5.10: Calibration test for the sample volume change: (a) sample volume change in the absence of axial displacement, and (b) volume change of the sample at undrained loading conditions.

**b) Inner-cell expansion due to pressure increase**

Even though the inner- and outer-cells are pressurised under identical pressures, the inner-cell volume can change due to the expansion of the fittings, connections, volume/pressure controller and compressibility of water.

For this purpose, a steel cylinder (diameter 50 mm and height 100 mm) with known bulk modulus (160 GP) was installed inside the cell. The volume change of the inner-cell versus applied pressure to the inner-cell is plotted in Fig. 5.11. The evolution of the inner-cell volume with pressure can be normalised with the sample volume as presented in this graph. The inner-cell volume can evolve up to 5 % of the sample volume due to an increase of the inner-cell pressure to 10 MPa. The isotropic volume change of the steel cylinder was calculated and subtracted from the measured volume change. The cell pressure was ramped at a rate of 10 kPa per min up to a maximum pressure of 10 MPa. As seen in this plot, the evolution of the inner-cell volume can be divided in three main domains. These domains are considered for  $\sigma_{in} < 500 \text{ kPa}$ ,  $500 \text{ kPa} < \sigma_{in} < 2000 \text{ kPa}$  and  $\sigma_{in} > 2000 \text{ kPa}$  with different interpolation functions.

The hysteresis of the volume change of the system due to the pressure reversal was examined up to 500 kPa. Thus, no hysteresis was observed and the inner-cell exhibited a totally reversible behaviour in this domain. The first two regions of the volume change were interpolated by quadratic equations. The inner-cell volume exhibits a linear trend with respect to the pressure for pressures higher than 2000 kPa.

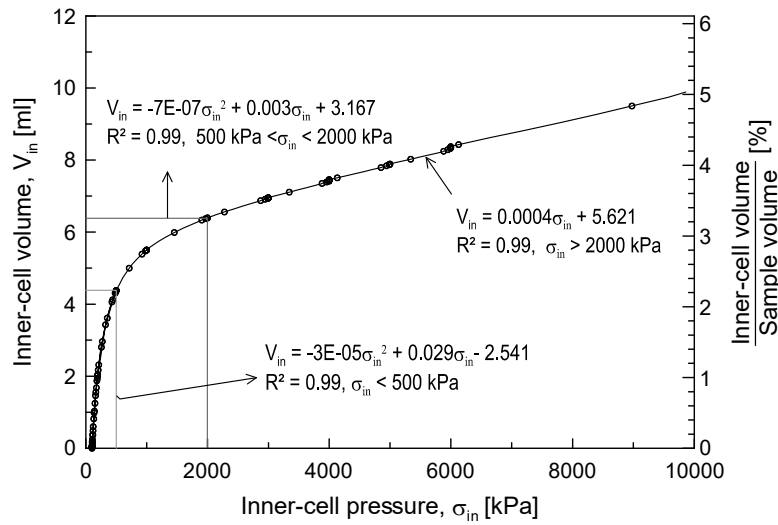


Fig. 5.11: Apparent volume change of the inner-cell with inner-cell pressure.

**c) Inner-cell expansion due to temperature increase**

For the measurement of the temperature, a thermocouple is installed at minimum distance to the inner-cell. Since the temperature is applied to the heating bath and then measured near the sample, the preliminary calibration tests are required to obtain the correlation between the temperature of the sample ( $T$ ) and the temperature of the heating bath ( $T_b$ ). A test setup using a steel sample similar to the previous section was carried out and the temperature was applied in steps of  $5\text{ }^\circ\text{C}$ . Then, the temperature of the sample was registered after it was stabilised at a given time as presented in Fig. 5.12. A linear trend was obtained between the temperature of the bath and the temperature of the sample. A second test (Trial 2) with different steps for the applied temperature was carried out and the results were found in good agreement with the first experiment (Trial 1).

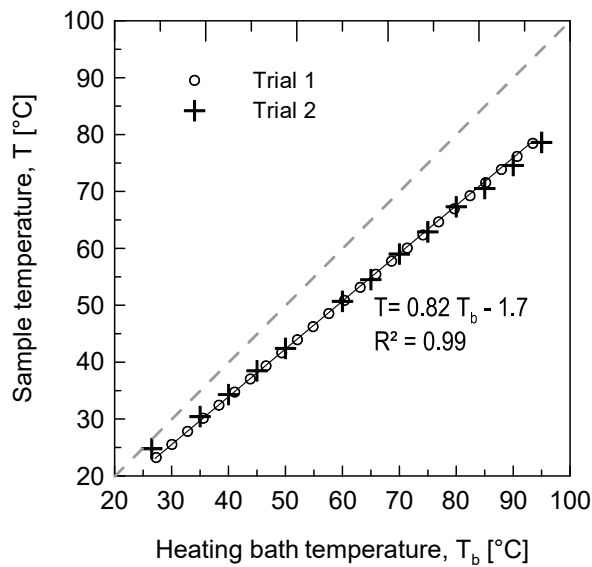


Fig. 5.12: Correlation between the applied temperature and the sample temperature.

The thermal expansion of the inner-cell volume (due to thermal expansion of the water inside the inner-cell and its associated hydraulic paths) was investigated using the same configuration for a steel sample with thermal expansion coefficient of  $28 \times 10^{-6}/^{\circ}\text{C}$ . The temperature was applied in steps and the inner-cell volume was recorded. The thermal expansion of the sample was computed and subtracted from the recorded inner-cell volume change. The remaining value represents the thermal evolution of the inner-cell volume which has to be considered for the correction of the inner-cell volume change in temperature application.

The thermal expansion of the inner-cell volume with respect to the temperature of the sample is presented in Fig. 5.13. The temperature was applied under two different cell pressures of 50 and 500 kPa. It can be observed that the temperature evolution of the inner-cell is not influenced by the applied pressure. A quadratic equation for the evolution of the inner-cell volume as a function of the temperature of the sample was obtained and will be used for the thermal corrections.

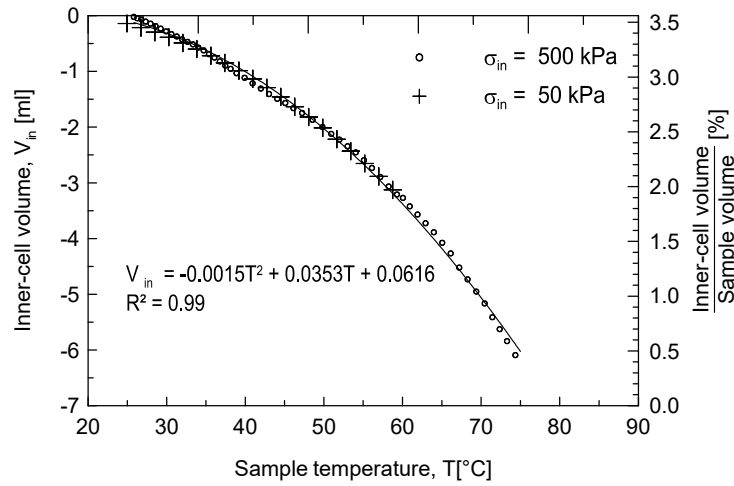


Fig. 5.13: Evolution of the inner-cell volume with temperature of the sample.

#### d) General formulation for sample volume change

It is possible to formulate the volume change of the sample based on the geometrical (Eq. 5.12), the pressure (Fig. 5.12) and the thermal (Fig. 5.13) evolutions through the following general expression:

$$\Delta V_s = -\Delta V_{in} - [\delta h_s A_{in} + A_0 (\delta h - \delta h_l)] - V_{in}^{\sigma}(\sigma_{in}) - V_{in}^T(T)$$

$$V_{in}^{\sigma}(\sigma_{in}) = \begin{cases} -3 \times 10^{-5} \sigma_{in}^2 + 0.029 \sigma_{in} - 2.5, & 0 < \sigma_{in} < 500 \text{ kPa} \\ -7 \times 10^{-7} \sigma_{in}^2 + 0.003 \sigma_{in} + 3.2, & 500 \text{ kPa} < \sigma_{in} < 2000 \text{ kPa} \\ 4 \times 10^{-4} \sigma_{in} + 5.6, & 2000 \text{ kPa} < \sigma_{in} \end{cases} \quad \text{Eq. 5.13}$$

$$V_{in}^T(T) = -0.001T^2 + 0.035T + 0.062, \quad 24^{\circ}\text{C} < T < 80^{\circ}\text{C}$$

where  $V_{in}^{\sigma}$  and  $V_{in}^T$  are the pressure and thermal evolution functions of the inner-cell volume. It is noted that the  $\Delta V_{in}$  is the total inner-cell volume change that should be corrected using the next terms in Eq. 5.13 for displacement, inner-cell pressure and temperature evolutions, respectively.

### 5.3 THM triaxial behaviour of bentonites

Although bentonite will be mostly emplaced at its hygroscopic water content, a progressive saturation of the buffer upon uptake of water from the host rock will take place. The saturation under such confined conditions will result in the development of the swelling pressure. This swelling happens in the boundaries nearby the surrounding host rock where the wetting will first take place. Furthermore, heat is generated from the canisters, whose temperature can increase up to 150 °C (Pusch 1994). In Fig. 5.14, the use of bentonite material in form of blocks to support the canister, and in granular form to fill the space between the canister and the host rock is schematically represented. The granular bentonite will be subjected to heating from the canister and wetting from the host rock. The bentonite material undergoes a complex thermo-hydro-mechanical stress path in such circumstances, that a full understanding of its behaviour is required to evaluate the performance of the engineered barrier system.

Amongst all possible stress paths and with the assumption that the granular material is initially at unsaturated conditions, the thermo-mechanics of saturated material at zone C, the unsaturated material at zones A and B are of great importance (A, B and C corresponding to Fig. 5.14).

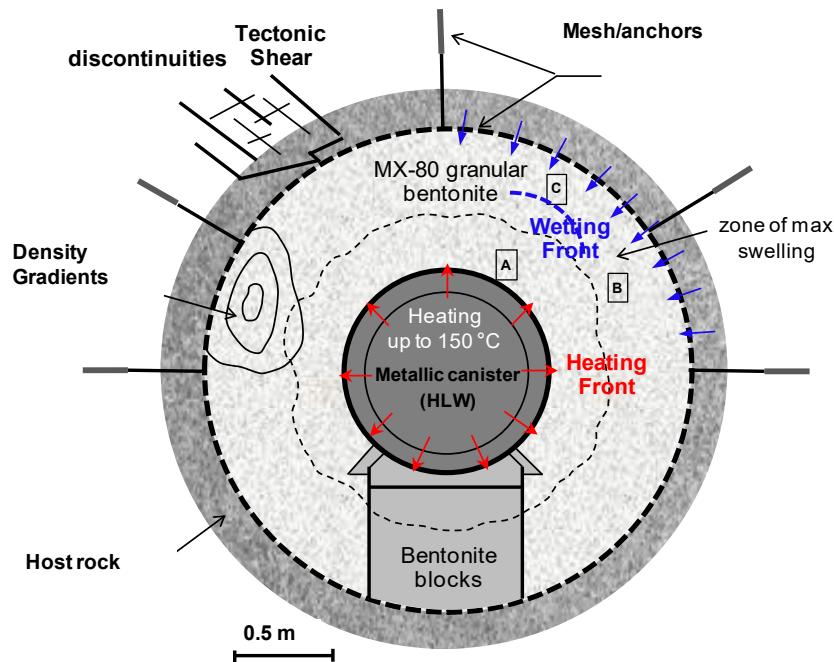


Fig. 5.14: THM loading mechanisms on bentonite barriers in high-level radioactive waste deep geological repositories.

Considering the maximum temperature of the canister, the range of swelling pressures at these densities (assuming a typical emplacement density of 1.50 Mg/m<sup>3</sup> for the granular bentonite and 1.70 Mg/m<sup>3</sup> for the blocks) and the initial suction of the emplaced material in the repository, a wide range of pressure, temperature and total suction should be considered for the bentonite material. As soon as the material in zone C is progressively saturated, a swelling pressure of a dozen of MPa (depending on the compaction state, Chapter 2, Figs. 2.9 and 2.10) will develop and harden the internal unsaturated layers at zones A and B. Considering the compaction state of the granular bentonite material in the canister near-field ( $\rho_d = 1.50 \text{ Mg/m}^3$ ), a swelling pressure up to 3 – 4 MPa can be expected. Since the bentonite blocks have higher dry densities and the granular bentonite in the vicinity of the blocks can undergo higher confinement due to the swelling of the blocks upon saturation, a maximum confinement of 5 MPa can be a realistic value.

There are few contributions available for THM triaxial testing of bentonite-based material particularly under unsaturated conditions. The THM behaviour of saturated and unsaturated sand/bentonite mixtures used as buffer in the Canadian concept of nuclear wastes (Hancox 1986) under triaxial stress paths has been reported by several researchers (e.g. Graham et al. 1989, Yin et al. 1990, Lingnau et al. 1996, Wiebe et al. 1998, Blatz et al. 2002, Blatz & Graham 2003).

Lingnau et al. (1996) performed consolidated isothermal undrained and isothermal drained constant- $p'$  (mean effective stress) triaxial tests on saturated sand/bentonite mixtures (50/50 percentage in terms of dry weight). The samples were consolidated at effective stresses up to 9.0 MPa and temperatures up to 100 °C. A decrease of the maximum deviatoric stress  $q_f$  and increase of the pore water pressure at failure were observed under higher temperatures. A curved critical state envelope was found in the  $q - p'$  plane. The effect of drained heating to 100 °C on compressibility, strength and stiffness was not noticeable.

Wiebe et al. (1998) reported the results of triaxial compression tests on unsaturated sand/bentonite mixtures (similar material analysed by Lingnau et al. 1996, but in unsaturated state). The influence of the elevated temperature and confining stresses were studied at fully undrained conditions. The air and water pressure lines during heating, isotropic and deviatoric loading were kept closed and the mass of water and air were assumed to remain constant. The degree of saturation of the samples was ranged in 0.35 – 0.98 and the samples were prepared by static compaction of the wetted mixtures. A confining stress up to 3.0 MPa and a temperature up to 100 °C were applied. Results indicated that undrained strengths increase with decreasing in degree of saturation, increasing in confining stress and decrease in temperature. The stiffness of the material was observed not responding monotonically to change in degree of saturation, stress and temperature. For instance, stiffness was observed to increase with total confining stress up to 1.0 MPa, but decreases at higher stresses.

Blatz et al. (2002) reported the results of quick undrained (UU) triaxial behaviour of unsaturated sand/bentonite mixture (50/50). The initial total suction of the samples at given water contents were determined and it was assumed that the tests are fast enough so that the total suction remained constant during the isotropic and deviatoric loadings. It was observed that samples at low confining stresses of 500 kPa show a brittle behaviour and at higher confining stresses exhibit a ductile behaviour with barrel-shaped after shearing. The strength and stiffness of the material increased non-linearly with increasing suction.

Blatz & Graham (2003) evaluated the influence of suction on the yield stress under isotropic loading and on the shear strength. The tested material was similar to the previous research and the tests were performed using a vapour equilibrium system, while the internal suction of the material was also measured by the means of a psychrometer. A reversible trend for the suction variation against volume strain was observed in wetting and drying cycles. The application of the vapour equilibrium was found to be successful to maintain suction and the change of internal suction was found to be negligible during the shearing phase.

As discussed also in Chapter 2, the analyses of the thermo-mechanical behaviour of saturated clays were presented by various researchers (e.g. Campanella & Mitchell 1968, Baldi et al. 1988, Hueckel & Baldi 1990, Del Olmo et al. 1996, Delage et al. 2000, Sultan et al. 2002, Cekerevac & Laloui 2004, Abuel-Naga et al. 2007, Tang et al. 2008). It has been generally observed that heating induces expansion for highly overconsolidated (or at low stresses) and contraction for slightly overconsolidated (or at high stresses) conditions, respectively. The influence of temperature on compressibility parameters of saturated clays were found to be negligible, while the yield stress slightly decreases with temperature increase. Besides, the overconsolidation ratio and the total suction were found important parameters that control the thermal volumetric behaviour. On the other hand, a decrease in suction resulted in an increase in

compressibility. The effect of total suction on the compressibility behaviour of Wyoming granular bentonite was analysed in Chapter 2 and similar trends were obtained as well.

The influence of temperature on the shear strength of the geomaterials was reported in the literature through conflicting results due to opposed phenomena simultaneously influencing the mechanical behaviour of the thermally induced geomaterials: The expansion of the aggregates results in a decrease in the material strength, and the thermal contraction hardens the material and increases the shear strength (Tang et al. 2008).

This section is addressing the results obtained from THM triaxial testing of the Wyoming granular samples. The tests were performed under unsaturated and saturated conditions and under different applied confining stresses. The vapour transfer technique was used for controlled-suction tests. The saturated tests were performed under drained conditions. As dealing with a high swelling material, particular sample preparation and test procedures were considered and applied for the granular material. The triaxial behaviour of the compacted Wyoming bentonite material under wide ranges of total suction, confining stress and temperature is analysed in the next section. For experimental purposes a maximum temperature of 80 °C is considered to keep the water still in the liquid phase. Higher temperatures will result in two phase flow conditions which will not be considered in this study. A total suction variation from  $\psi = 100$  MPa to the saturated conditions and confining stresses up to 5 MPa are considered for the experiments.

In the following sections the sample preparation techniques and the testing procedures at unsaturated and saturated conditions are presented based on the primary analysis of the material in Chapter 2. The results of the triaxial testing on granular Wyoming bentonite are presented and analysed as well.

## **5.4 Triaxial testing on Wyoming granular bentonite**

### **5.4.1 Sample preparation**

#### **5.4.1.1 Unsaturated conditions**

To prepare a sample for the triaxial testing, similar to the procedures for the static compaction and consolidation tests and the determination of water retention behaviour, different fractions of the granular material were mixed according to the apparent grain size distribution in Fig. 2.1. This procedure was performed for each single sample to have always the same grain size distribution. The granular material then was compacted to the target dry density. For triaxial testing, a reference dry density of 1.5 Mg/m<sup>3</sup> was always respected according to the requirements for the practical emplacement of the material in the repositories (Plötze & Weber 2007).

As it was earlier mentioned in Chapter 2, the granular bentonite in this case was found to have enough pourability under hygroscopic conditions to reach this target dry density (1.5 Mg/m<sup>3</sup>) without any compaction effort. However, the material swells as soon as it absorbs water. In a wetting path, the material exhibits an increase in void ratio due to the swelling mechanism.

The unsaturated tests were performed under total suctions of  $\psi = 100$ , 50 and 20 MPa. At a total suction of  $\psi = 100$  MPa, the material has a dry density of 1.5 Mg/m<sup>3</sup> (corresponding to  $e = 0.83$ ) under poured conditions. For lower total suctions of 50 and 20 MPa, the material swells and has lower dry densities upon poured conditions. Considering this swelling behaviour at higher water

contents, it would be practically possible to perform the unsaturated tests in two ways with respect to the fact that the initial dry density of  $1.5 \text{ Mg/m}^3$  should be respected in all tests.

A first solution is to hydrate the poured material inside the triaxial cell. The material at hygroscopic conditions has already the target dry density. The wetting process would be possible by transferring the water vapour through the sample. This could be carried out using the vapour transfer technique integrated in the triaxial cell. To prevent a volume increase due to the hydration, the inner-cell volume can be halted. Consequently, the wetting process will result in a swelling pressure developed inside the inner-cell. Preliminary tests using this method showed that the wetting of the material by the vapour transfer is a long-term procedure. The small macropores (Fig. 3.8) and the relatively long dimension of the sample make the circulation of the vapour through the material a time-consuming process.

The other approach is to hydrate the material under free volume conditions and then to compact the swollen material to the reference dry density of  $1.50 \text{ Mg/m}^3$ . To do so, the information on the water retention behaviour of the material is required.

The variation of the total void ratio versus total suction under free volume conditions and its corresponding water retention curve is presented in Fig. 5.15a and b (detailed in section 2.6.6). The wetting of the material is possible through the vapour phase up to a water content of about 0.3 under free swelling conditions. Further hydration would be possible through the liquid phase. In Fig. 5.15c, the visual observation of the same sample at different total suctions (A, B and C) corresponding to the water retention curve is presented.

To reach total suctions of 50 MPa and 20 MPa, the wetting was performed through the vapour phase. Thus, the granular material was first stored in a humid chamber ( $RH = 100\%$ ) to adsorb water in a controlled way. After reaching a certain water content and its corresponding total suction (Fig. 5.15), the material was statically compacted to the target dry density inside an ad-hoc mould. The sample was then extracted from the mould, weighted and the dimensions were measured in a short period of a few minutes prior to the installation inside the triaxial cell. A bentonite sample prepared for triaxial testing by compaction of the swollen material is shown in Fig. 5.16a.

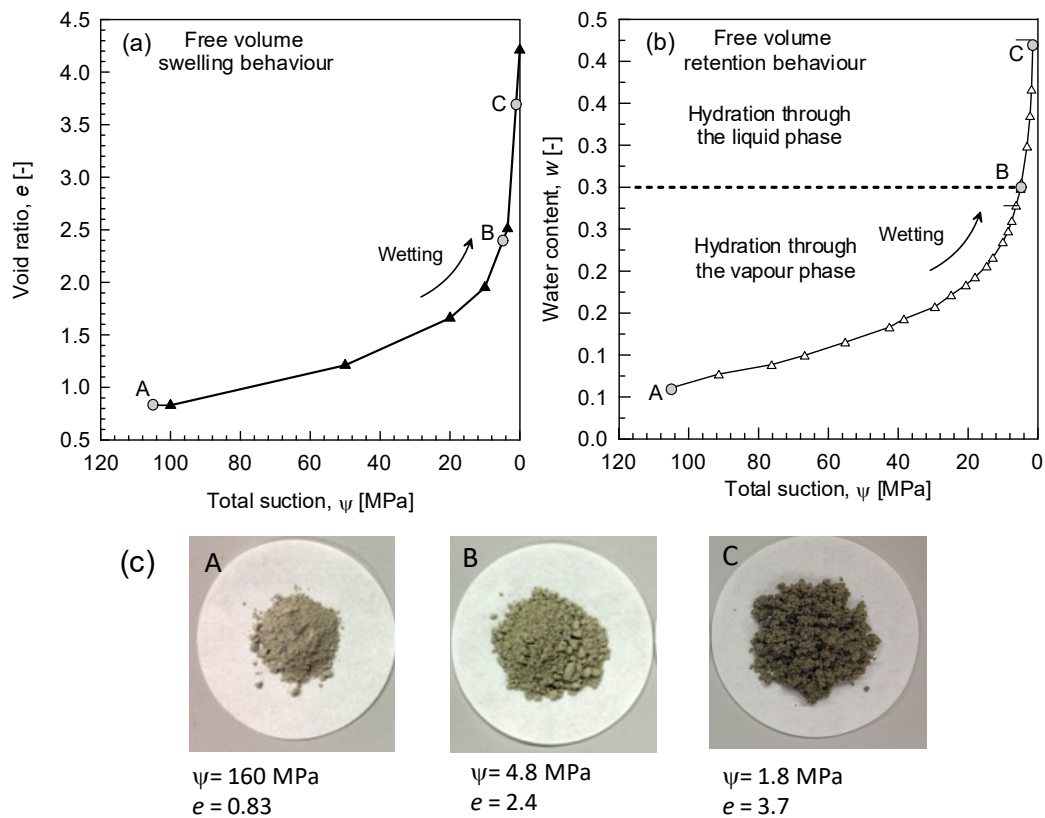


Fig. 5.15: Free volume swelling and retention behaviour of granular bentonite material: (a) evolution of the void ratio vs. suction, (b) corresponding water retention behaviour, and (c) visual observation of the swelling at different points along the retention curve.

The compaction behaviour of the sample at different total suction values is also presented in Fig. 5.16b. The material first swelled from its initial poured void ratio (path a – b) and then was compacted to the initial void ratio through path b – c. This is equivalent to the hydration of the material in path a – c at which the swelling pressure will develop under constant volume conditions. It should be also noted that the compaction of the material at given water contents does not influence the total suction due to the residence of water molecules inside the micropores. Thus, the loading mechanism influences mainly the macroporosity. Consequently, the degree of saturation will change due to macroporosity reduction at a constant micropores' water content.

These observations were detailed in Chapter 2 through introducing the iso-suction curves (Section 2.3.2.2) and linked to the microstructural characteristics of bentonite material in Chapter 3 (Section 3.4.3). This particular feature is a key point for the sample preparation under unsaturated conditions that was used in this section.

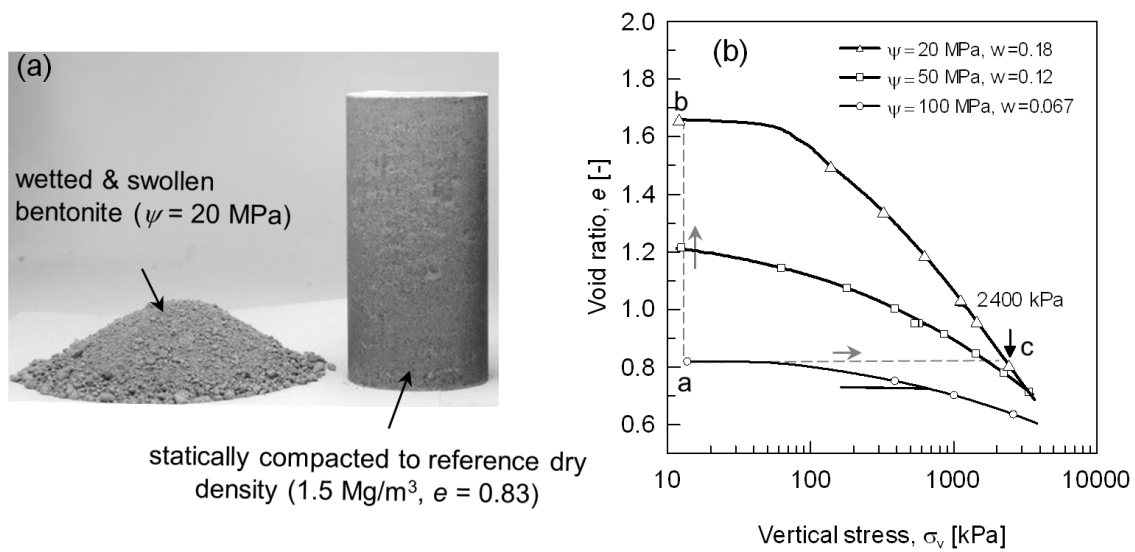


Fig. 5.16: Compaction of the swollen granular bentonite material to the target dry density of  $1.5 \text{ Mg/m}^3$ .

#### 5.4.1.2 Saturated conditions

To prepare a sample for the triaxial testing at saturated conditions, the material was first saturated outside the cell to accelerate the process of saturation. The saturation should be performed under constant volume conditions to maintain the initial void ratio  $e = 0.83$ .

The saturation could be carried out inside the triaxial test and under constant volume conditions. However, due to the very low hydraulic conductivity (less than  $10^{-12} \text{ m/sec}$ ) the saturation of the sample inside the cell takes a long time. The information on the saturated hydraulics is presented in section 5.5.6. Moreover, it is proved that under certain hydraulic gradients, no flow was obtained through the saturated bentonite material.

For this reason, another saturation process was considered in the way that the material at hygroscopic conditions was first poured in a two-piece mould with 100 mm height and 50 mm diameter. The mould provided constant volume conditions by installation in a rigid frame. A steel cap was placed on the top of the mould and a load cell was installed between the rigid frame and the top cap to measure the swelling pressure during the saturation process. Two metallic porous discs were placed on both sides of the sample. The whole sample was then flooded with water which was provided by a reservoir enclosing the mould. A net of small holes (diameter of 1 mm) was designed all around the mould to facilitate the access to water. Thus, saturation of the sample was provided from all boundaries. To prevent the migration of the bentonite particles, the internal wall of the mould was covered by filter papers. The setup for the saturation process is schematically shown in Fig. 5.17a.

The swelling pressure was recorded during the saturation. When the change in the swelling pressure is almost negligible (less than 15 kPa/day), it was assumed that the sample is saturated. As seen in Fig. 5.17b, the swelling pressure reached a maximum value of about 2 MPa after about 18 days. At this time, the water was evacuated and the mould was unloaded. The sample was extracted from the mould and the weight and dimensions were recorded prior to the installation in triaxial cell. The degree of saturation of the sample was computed from the water content and the void ratio data ( $S_r = wG_s/e$ ). An average degree of saturation of about 0.98 was obtained for the samples saturated under this configuration. In Fig. 5.17c and d, the cross

section of the sample at different points during the saturation time is shown. As seen, the sample after 5 days is not yet fully saturated and consists of an unsaturated core. The middle cross section of the sample after 18 days when the swelling pressure is stabilised, exhibits a full saturation and homogenisation. The extracted sample at this point was then installed inside the inner-cell to initiate a test procedure in saturated condition.

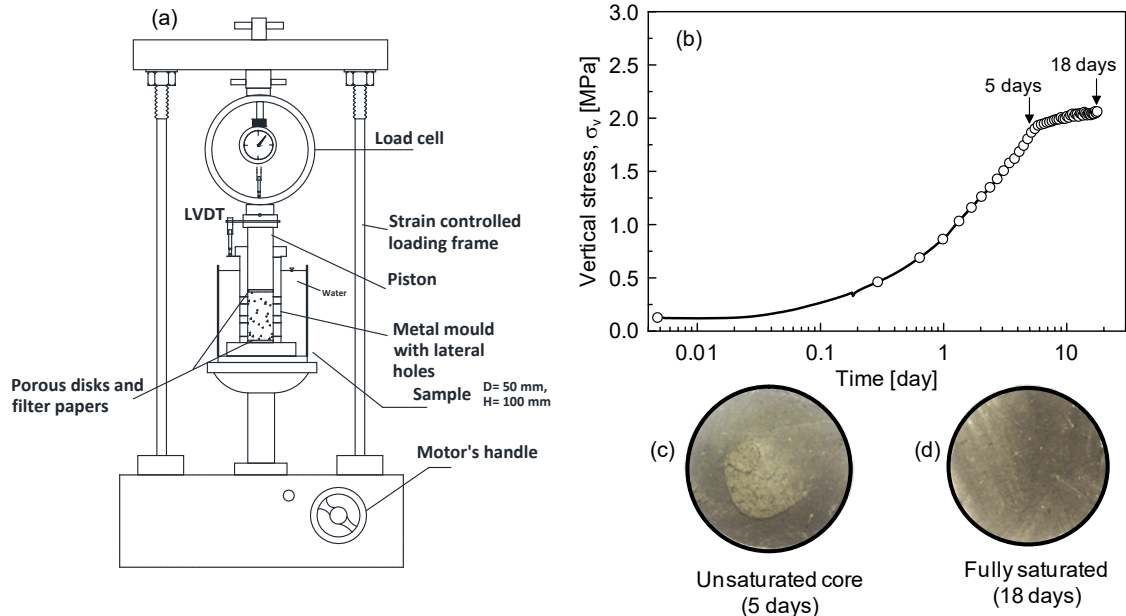


Fig. 5.17: (a) Experimental setup to saturate the bentonite sample under constant volume conditions, (b) swelling pressure developed during the saturation, (c) unsaturated core of the sample after 5 days, and (d) fully saturated sample after 18 days.

### 5.4.1.3 Homogenisation during sample preparation

The homogenisation and uniformity of water content or void ratio during sample preparation were evaluated. This control was performed to ensure that there is no remarkable variation of dry density along the height of the sample during preparation. Saturated and unsaturated samples were selected (Fig. 5.18) and cut into 5 parts of approximately 2 cm height. The variation of the water content for a sample prepared at a total suction of  $\psi = 50$  MPa (target water content of 0.12) along its height is shown in Fig. 5.19a.

Variation of the void ratio along a saturated sample is also presented in Fig. 5.19b. The calculation of the void ratio was not possible in case of the unsaturated sample due to the existence of granulations and the irregular shapes of the cut pieces. The calculation of the volume and consequently the void ratio was possible for the saturated sample with cylindrical pieces. As seen in Fig. 5.17d, the material has a homogenised structure and the bentonite grains cannot be detected anymore. As it was addressed in section 3.4.4, this modification of the structure happens due to further expansion and subdivisions of the microstructure at higher water contents.



Fig. 5.18: Samples prepared for unsaturated and saturated triaxial testing.

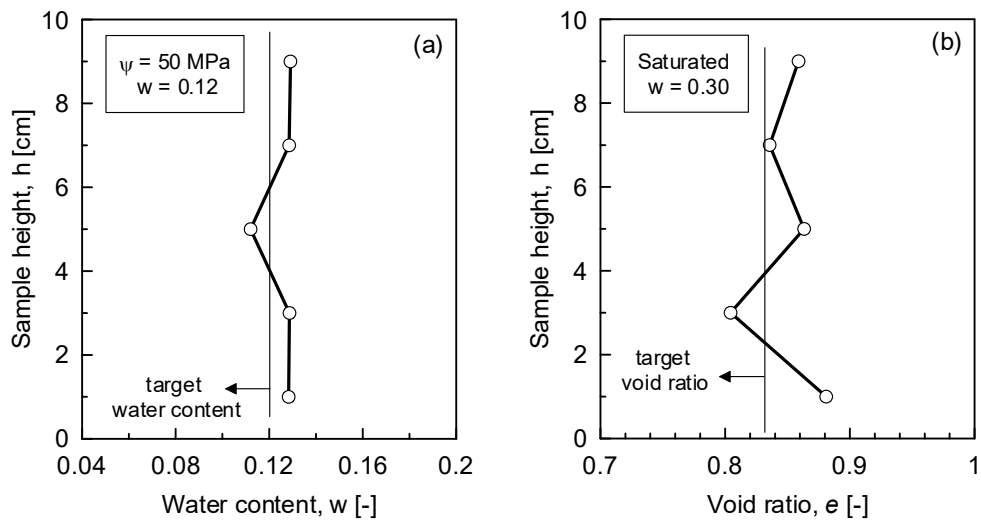


Fig. 5.19: (a) Variation of the water content along the height of the unsaturated sample, and (b) variation of the void ratio of the saturated sample along the height.

## 5.4.2 Triaxial testing procedure at ambient temperature

### 5.4.2.1 Unsaturated condition

Controlled suction isotropic and deviatoric tests were carried out on the compacted granular bentonite samples at two temperatures of 24 and 80 °C. Three different confining pressures of 500, 2000 and 5000 kPa were selected. These ranges were selected based on the discussion presented in Section 5.4 on the possible THM loading description under repository conditions.

As it was mentioned before, the total suction was controlled at  $\psi = 100, 50, 20$  MPa using the vapour transfer technique. The test at  $80\text{ }^{\circ}\text{C}$  was performed on a controlled suction of  $\psi = 20$  MPa. Samples prepared as described in section 5.5.1, were installed inside the triaxial cell. In general, the sample rested on the lower cap and two compressed porous metallic discs and filter papers were placed on the top and bottom of the sample. NBR<sup>1</sup> membranes with a thickness of 1.5 mm were used for the experiments (Section 5.5.2.3).

The membrane enclosed the sample and a layer of geotextile (Bidim Gammes, 0.3 mm) and filter paper (LS 14 Whatman, 0.12 mm) were used between the membrane and the sample. The application of the geotextile and filter paper facilitated the circulation of the vapour through the sample. Silicon grease was used between the membrane and the caps. The membrane provided enough sealing and the use of O-ring was not required. The installation of the sample at a total suction of  $\psi = 100$  MPa was done by simply pouring the material (previously conditioned at this suction value) inside the membrane and closing the ends by filter papers and the metallic discs.

The change of void ratio does influence the total suction at constant water content for granular bentonite. Thus, the total suction was basically controlled in the boundaries of the sample during the test to ensure that the water content of the sample remains constant during the experiment. The vapour was passed through the sample during all steps of the test and the water exchange was recorded using a precision balance (0.001 g).

The relative humidity of the vapour transfer system was controlled using saturated KI (corresponding to a total suction of  $\psi = 51$  MPa) and variably saturated LiCl solution (2.8 molar at  $24\text{ }^{\circ}\text{C}$  corresponding to a total suction of  $\psi = 100$  MPa) and variably saturated NaCl solution (3.8 molar at  $24\text{ }^{\circ}\text{C}$  and 3.3 molar at  $80\text{ }^{\circ}\text{C}$  for corresponding total suction of  $\psi = 20$  MPa).

The controlled-suction experiments consist of isotropic consolidation at mean total stresses of  $p = 500, 2000$  and  $5000$  kPa. The tests then were followed by deviatoric mechanical loading at  $0.6\text{ } \%/ \text{min}$  of axial strain to the maximum shearing resistance or  $15\text{ } \%$  axial strain, whichever was achieved first. However, in some cases, deviatoric loading was continued for the axial strains more than  $15\text{ } \%$ .

Axial loads, axial displacement, inner-cell pressure, inner-cell volume change, water exchange with vapour control system and the temperature were recorded during different stages of the experiment.

#### 5.4.2.2 Saturated condition

The saturated samples prepared as described in section 5.5.1.2 were enclosed with the membrane and then installed inside the inner-cell. The installation procedure was similar to the unsaturated samples, except that no lateral membrane or filter paper was used when the determination of the permeability was addressed. To ensure the saturation of the sample, a saturation procedure was considered inside the cell. This step was carried out if any desaturation could happen during the installation of the sample inside the triaxial cell. A back water pressure of  $50$  kPa was applied from top and bottom of the sample, while the volume was kept constant. This could be possible by halting the inner-cell volume. Application of the back pressure causes the air to be adsorbed into the water and the degree of saturation consequently increases.

It was observed that the sample absorbed a small amount of water and produced approximately an isotropic swelling pressure of about  $1$  MPa. The swelling pressure was measured in terms of the inner-cell pressure and the axial force independent of each other. The inner-cell pressure

---

<sup>1</sup> Nitrile butadiene rubber (manufactured by Wille Geotechnik).

(here the radial pressure) term was measured by the double volume/pressure controller and the axial stress by the external load cell. This phase of the experiment is called the swelling equilibrium phase. The results of this step are presented in Fig. 5.20a for the swelling pressure in axial and radial direction. The pore volume variation of the sample in terms of percentage of the volume is also shown in Fig. 5.20b.

As it was mentioned, a back pressure of 50 kPa was applied (top and bottom of the sample) during the saturation. This back pressure was held during the isotropic and deviatoric loadings as well. The application of such back pressure could decrease water evaporation in case of testing at higher temperatures.

Cekerevac (2003) showed that there is no important difference in the stress – strain behaviour of saturated kaolinite clay under application of different back pressures.

As seen, the saturation of the sample was controlled after the preparation and as well in the phase of the swelling pressure measurement in the triaxial cell. However, the saturation was also investigated using Skempton's  $B$  criterion. If a sample is fully saturated and no pore water drainage is allowed, an increase in the isotropic confining stress ( $\sigma_c$ ) on the sample should result in an equivalent change in pore water pressure ( $u_w$ ). Thus, the  $B$  value is expressed as follows:

$$B = \frac{\Delta u_w}{\Delta \sigma_c} \quad \text{Eq. 5.14}$$

$B$  values in the range of 0.92 – 0.95 were obtained which indicate an acceptable saturation of the sample prior to a consolidation test.

After this step the isotropic mean total stresses up to  $p = 1150, 2000$  and  $3000$  kPa were applied for drained consolidations. After consolidation was assumed to be completed, the tests were followed by a deviatoric mechanical loading at  $0.012$  %/hour of the axial strain to the maximum shearing resistance or  $15$  % axial strain, whichever was reached earlier.

A degree of dissipation of  $95$  % of the excess pore pressure was selected for the derivation of the drained strength parameters. The time required to failure ( $t_f$ ) in drained tests is equal to (Head & Epps 1980):

$$t_f = \left[ \frac{5r^2 \zeta}{\pi \eta} \right] t_{100} \quad \text{Eq. 5.15}$$

where  $r = h/D$  ( $D$  is the diameter of the sample and  $h$  the height of the sample),  $\zeta$  and  $\eta$  are constants depending on the drainage boundary conditions. For  $r = 2$  which is approximately the case for all performed tests in this study, Eq. 5.15 can be written as:

$$t_f = \left( \frac{20 \zeta}{\pi \eta} \right) t_{100} = F \cdot t_{100} \quad \text{Eq. 5.16}$$

If the drainage is applied from the radial boundary and both ends (top and bottom) during the consolidation, a value of  $F = 15.8$  is suggested by Head & Epps (1980). The variation of the volume change of the sample versus the square-root of time during a consolidation step is depicted in Fig. 5.21.

As seen, the total mean stress was increased from  $p = 1150$  kPa (at which the sample was slightly consolidated after reaching the swelling equilibrium) to  $p = 2000$  kPa to initiate a consolidation process upon the applied loading step.

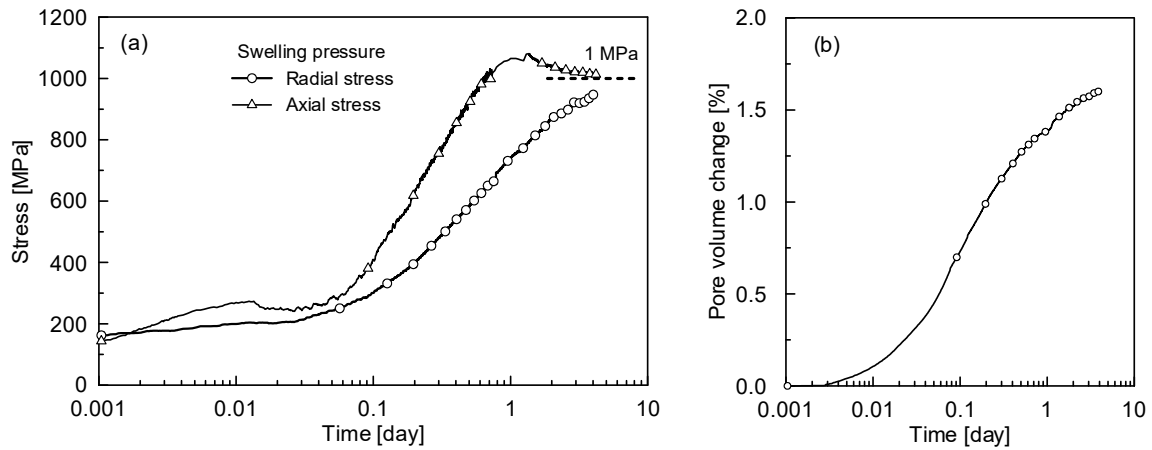


Fig. 5.20: Evolution of the radial and axial swelling stresses during the swelling phase in the triaxial cell.

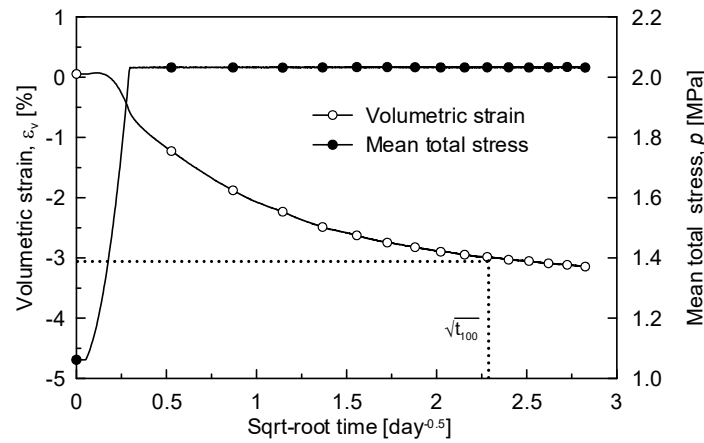


Fig. 5.21: Derivation of the theoretical failure time in drained triaxial tests from the isotropic consolidation behaviour.

### 5.4.2.3 Influence of the rubber membrane on the measured deviatoric strength

The influence of the rubber membrane whether it could impose any apparent strength on the bentonite samples was investigated based on the work of Henkel & Gilbert (1952).

If it is assumed that the membrane and the test sample deform as a unit, the rubber membrane performs as a compression shell. Thus, the following correction for the deviatoric stress was proposed:

$$\sigma_{m,q} = \frac{\pi DM \varepsilon_a (1 - \varepsilon_a)}{A_0} \quad \text{Eq. 5.17}$$

where  $\sigma_{m,q}$  ( $\text{N/m}^2$ ) is the rubber membrane correction term that should be subtracted from the measured deviatoric stress,  $D$  is the initial diameter of the sample,  $A_0$  is the initial area of the sample,  $M$  is the compression modulus of the rubber membrane ( $\text{N/m}$ ) and  $\varepsilon_a$  is the axial strain of the sample. Henkel & Gilbert (1952) stated that the compression modulus  $M$  can be replaced by the extension modulus. In order to quantitatively evaluate the extension modulus of the rubber membrane, load-extension test results are required. For this reason, circumferential strips of 1 cm width were cut from the NBR membrane used in the triaxial tests and the extension

force/strains upon applied forces were obtained (Fig. 5.22). For the used membrane a compression modulus  $M_m = 74.6 \text{ N/m}$  and consequently the maximum rubber membrane correction of  $\sigma_{m,q} = 95.4 \text{ kPa}$  were obtained. This correction on the deviatoric strength was considered through the analyses of the results of the triaxial tests.

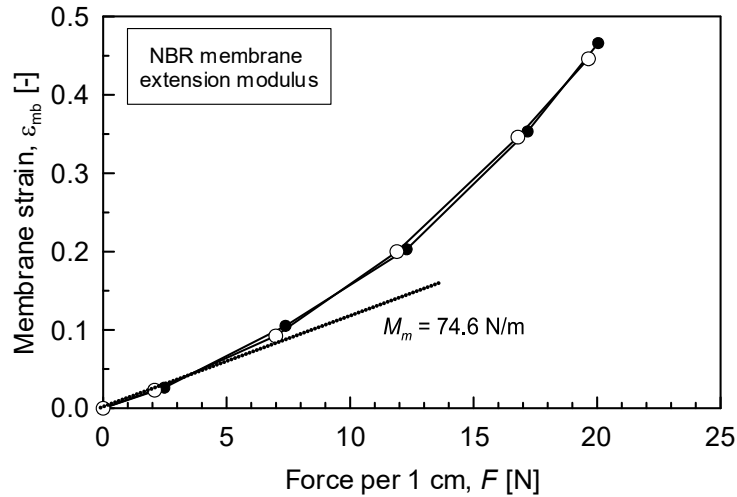


Fig. 5.22: Extension loading behaviour of the rubber membrane (NBR) used in this study.

### 5.4.3 Hydraulic conductivity analysis

Hydraulic conductivity analysis was performed on a saturated sample after consolidation at  $p = 2000 \text{ kPa}$  for a void ratio  $e = 0.81$  corresponding to a dry density of  $1.51 \text{ Mg/m}^3$ . Different hydraulic gradients ( $i$ ) were applied between the top and bottom of the sample to obtain a measurable flow through the sample. Thus, the hydraulic conductivity ( $K$  in m/s) was computed using Darcy's law for incompressible fluids and neglecting the difference in the elevation head:

$$K = \frac{Q\rho_w}{iA}, \quad i = \frac{u_{top} - u_{bot}}{h} \quad \text{Eq. 5.18}$$

where  $Q$  is the volumetric flux,  $A$  is the specimen surface,  $u_{top}$  and  $u_{bot}$  are the top and bottom pore water pressures,  $\rho_w$  is the specific weight and  $h$  is the drainage length which is here the height of the sample. The influence of the temperature on the hydraulic conductivity was investigated at given hydraulic gradients. Two steps of temperature were applied and after the thermal consolidation, the volumetric flux was computed at a given temperature under a hydraulic gradient.

### 5.4.4 Triaxial testing procedure at elevated temperature

The effect of temperature on the volumetric and deviatoric behaviours of the granular bentonite at unsaturated conditions was investigated. The tests were performed based on a combination of three loading steps: (a) isothermal isotropic loading to a given mean total stress at  $24 \text{ }^\circ\text{C}$ , (b) thermal loading, and (c) isothermal deviatoric loading. The applied thermo-mechanical testing path is summarised in Fig. 5.23.

The mechanical isotropic loadings up to  $p = 500, 2000, 5000 \text{ kPa}$  were applied under a controlled total suction of  $\psi = 20 \text{ MPa}$  (typical paths  $O \rightarrow A$  and  $O \rightarrow C$ ). Suction-controlled heating by steps of  $10 - 15 \text{ }^\circ\text{C}$  with a rate of  $5 \text{ }^\circ\text{C}$  per hour (typical paths  $A \rightarrow A'$  and  $C \rightarrow C'$ )



After installation of the samples in the triaxial cell, they were subjected to the isotropic confining stress. An over-consolidation ratio (OCR) can then be considered based on the applied isotropic stress during the consolidation phase.

Tab. 5.1: List of tests performed at ambient temperature ( $T = 24\text{ }^{\circ}\text{C}$ ).

Test name	OCR	Initial state		Consolidation		Failure state (at peak)			Hydro-mechanical test
		$e_0$ [-]	$S_r$ [-]	$P$ [kPa]	$e_c$ [-]	$e_f$ [-]	$S_r$ [-]	$q_f$ [MPa]	
$\psi_{100\_p0.5}$	NC	0.83	0.22	500	0.82	0.80	0.23	1.90	Controlled suction $\psi = 100\text{ MPa}$
$\psi_{100\_p2}$	NC	0.82	0.22	2000	0.80	0.76	0.24	5.57	
$\psi_{100\_p5}$	NC	0.83	0.22	5000	0.76	0.71	0.25	9.15	
$\psi_{100\_p5\_OCR2.5}$	2.5	0.83	0.22	2000	0.77	0.76	0.24	5.61	
$\psi_{50\_p0.5}$	4.0	0.82	0.40	500	0.81	0.80	0.41	1.98	Controlled suction $\psi = 50\text{ MPa}$ , $\sigma_s = 2000\text{ kPa}$
$\psi_{50\_p2}$	1.0	0.83	0.40	2000	0.77	0.72	0.46	4.02	
$\psi_{50\_p5}$	NC	0.83	0.40	5000	0.73	0.66	0.49	6.48	
$\psi_{20\_p0.5}$	4.9	0.83	0.60	500	0.82	0.80	0.62	2.23	Controlled suction $\psi = 20\text{ MPa}$ , $\sigma_{st} = 2430\text{ kPa}$
$\psi_{20\_p2}$	1.2	0.83	0.60	2000	0.78	0.74	0.67	3.08	
$\psi_{20\_p5}$	NC	0.83	0.60	5000	0.70	0.64	0.77	3.50	
$\psi_{20\_p0.5\_2}$	4.9	0.84	0.60	500	0.83	0.81	0.61	1.94	
$Sat\_p1.15$	1.7	0.83	0.99	1150	0.83	0.82	1.0	0.57	Saturated $\sigma_{cv,p} = 2.0\text{ MPa}$
$Sat\_p2$	1.0	0.83	0.98	2000	0.81	0.79	1.0	2.06	
$Sat\_p3$	NC	0.84	1.0	3000	0.80	0.78	1.0	2.28	

Note:  $p$  is the mean total stress which is defined as  $p = [\sigma_1 + 2\sigma_3]/3$  and  $q$  is the deviatoric stress defined as  $q = [\sigma_1 - \sigma_3]$ .

$e_0$  is the initial void ratio,  $e_c$  is void ratio after mechanical consolidation and  $e_f$  is the void ratio at failure (at peak) due to deviatoric mechanism

Calculation of the OCR for the samples compacted under static conditions and subjected to isotropic loading requires the evaluation of the  $K_0$  (coefficient of the lateral earth pressure) value. The  $K_0$  value is also a function of OCR and it can be evaluated by extended Jaky's equation (Jaky 1944) proposed by Alpan (1967) as it follows:

$$K_0 = (1 - \sin \phi')(OCR)^\alpha \quad \text{Eq. 5.19}$$

where,  $\phi'$  is the shear strength angle at drained conditions and  $\alpha$  is a coefficient that is assumed as 0.32 for plastic clays (Ladd 1977). However, here the OCR values were calculated for the vertical component of the mean total stress and is defined as  $OCR = \sigma_1/\sigma_{st}$ , which is the ratio of the vertical stress at triaxial conditions to the vertical compaction stress during sample preparation as presented in Fig. 5.16b. The OCR of the samples at a total suction of  $\psi = 20$  and 50 MPa was computed with this assumption.

The samples prepared at a total suction of  $\psi = 100\text{ MPa}$  are basically in normally consolidated state when they are loaded inside the cell. To evaluate the influence of the OCR on the deviatoric behaviour of the material at this suction, a sample was first isotropically loaded up to 5000 kPa and then was unloaded to 2000 kPa to induce an OCR of 2.5. The isotropic behaviour

of the material at different suctions including the saturated conditions is presented in Fig. 5.24. As seen in Fig. 5.24a, the compressibility of the material in unsaturated tests increases when the total suction decreases. In case of the saturated sample, no volume change was allowed until  $p_s = 1$  MPa which is basically referring to the swelling equilibrium phase where the volume of the sample is kept constant. However, it has to be mentioned that the pore volume change registered during this step (Fig. 5.20b) is associated to the uptake of water by the sample and the lateral drainage (filter paper and geotextile layer). It was mentioned that the sample could become slightly desaturated after extraction from the saturation mould and during the installation inside the triaxial cell. Thus, the saturated sample starts to be consolidated for mean total stresses higher than 1 MPa.

The change of the degree of saturation for unsaturated tests upon a constant water content is due to the reduction of the void ratio as depicted in Fig. 5.24b. In this range of total suction, the water content of the material is associated with the residence of water in micropores including the interlayer porosity.

In Fig. 5.24c, the corresponding stress path in the water retention plane is presented. For unsaturated samples, under a typical stress path like A  $\rightarrow$  B, the void ratio decreases at constant water conditions, while the total suction remains constant. Such a path was already called iso-suction path (Section 2.3.2.2). Thus, this stress path can be shown between two successive retention curves of two void ratios of 0.83 and 0.66.

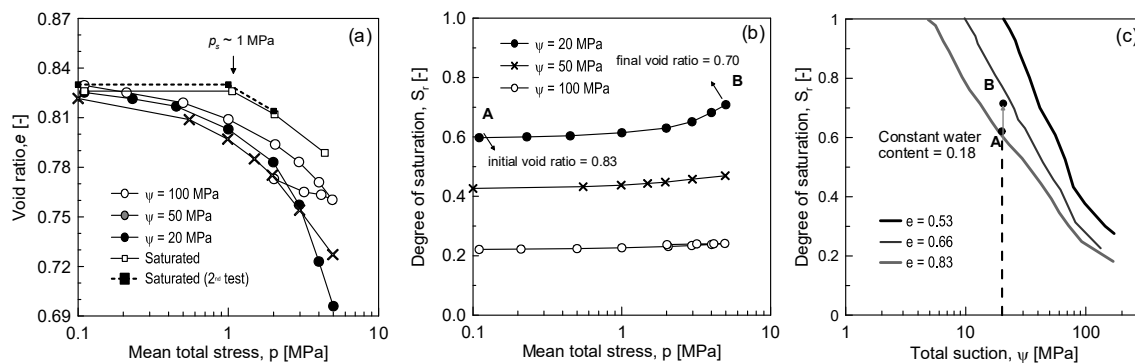


Fig. 5.24: (a) Influence of the total suction on the isotropic behaviour of Wyoming granular bentonite, (b) variation of degree of saturation in unsaturated tests, and (c) corresponding path for unsaturated tests in water retention plane.

Based on the isotropic consolidation tests, the compressibility of granular bentonite at different total suctions and under saturated conditions was calculated in terms of compression index,  $C_c$ . This parameter is defined as the slope of the normally consolidated (NC) line in the void ratio- $\log p$  plane (Fig. 5.24a).  $C_c$  is related to parameter  $\lambda$  through the following equation:

$$C_c = \frac{de}{d(\log p)}, \quad \lambda = \frac{C_c}{\ln 10} \quad \text{Eq. 5.20}$$

Compression indices of unsaturated samples were listed in Tab. 5.2. The compression indices obtained under these conditions are remarkably lower than the ones registered for the compression of the freely swollen bentonite upon a total suction (Section 2.3.2.2).

Besides, the compression index of the saturated sample was 0.04 which shows that the compressibility of the saturated samples is less than the unsaturated ones. The reason could be explained by the difference in the microstructural features of the compacted unsaturated bentonite and initially saturated bentonite. As it was discussed in Section 3.4.6.2, the FIB-*nt* analysis on the compacted unsaturated samples indicated a pore network which was related to the mesh-like structure. This structure consisted of macropores filled with partially expanded smectite particles and established a porosity of about 30 % of the volume of the sample at a dry density of about 1.47 Mg/m<sup>3</sup>. Such structures are expected to be even more developed for the granular bentonite samples that initially swelled upon a total suction (Fig. 5.15).

This implies that in a compaction attempt, the change of the void ratio is first influencing this level of porosity assumed as inter-aggregate (macro) pores. However, in an initially saturated sample, due to hydration and expansion of the particles during saturation, the macropores or inter-aggregates are already eliminated (detailed in Section 3.4.4.2). When the bentonite sample at this void ratio ( $e = 0.83$ ) is fully saturated, a maximum of 4 water molecules were already included in expanded and subdivided smectite particles (Fig. 3.15, referred to Saiyouri et al. 1998). At these circumstances, the change of void ratio due to the applied external loads is directly influencing the interlayer pores where the adsorbed water is under strong influence of the smectite layers. Similar discussions on the different mechanism of the compressibility behaviour of initially saturated and compacted saturated bentonite samples were given by Baille et al. (2010).

Tab. 5.2: Compression indices of unsaturated bentonite samples.

<b>Total suction <math>\psi</math></b>	100	50	20
<b>Compression index <math>C_c</math></b>	0.05	0.07	0.20

### 5.5.2 Deviatoric behaviour at ambient temperature

The void ratio and deviatoric stress at failure (peak shear failure) for the tested samples is presented in Tab. 5.1. The deviatoric behaviour of the material at controlled total suctions and different mean total stresses is presented in Figs. 5.25 and 5.26.

The influence of the confining stress on the deviatoric behaviour of the material at total suctions of 100 MPa and 50 MPa is presented in Figs. 5.25a and b. The decrease in the elastic domain of the overconsolidated sample at  $\psi = 100$  MPa can be observed.

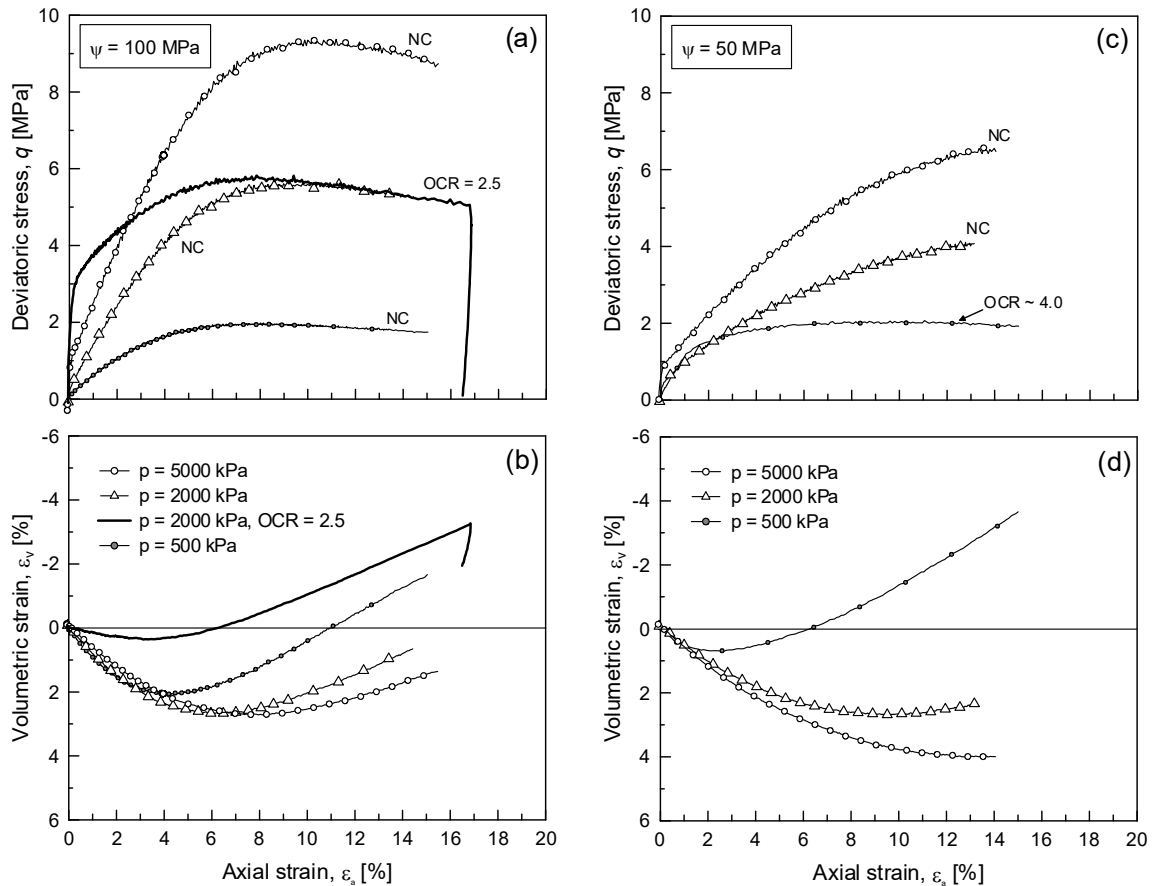


Fig. 5.25: Deviatoric behaviour of Wyoming granular bentonite: (a), (b) influence of confining stress at  $\psi = 100$  MPa, and (c), (d) influence of confining stress at  $\psi = 50$  MPa.

Fig. 5.25b presents the volumetric behaviour at the same suction, and the dilative behaviour is seen for the overconsolidated sample starting from about 6 % of the axial strain. The samples show a tendency to dilate after failure. This behaviour could be associated to the geometrical deformation of the samples after failure. Fig. 5.25c indicates that the sample at  $p = 500$  kPa exhibits ductile behaviour with deviatoric stress remaining constant after failure. Similar behaviour was reported by Graham et al. (2001) on the sand/Na-bentonite mixture (50/50 percent in terms of dry weight) at constant water content conditions and an initial total suction of 4.5 MPa.

The influence of the induced OCR (as earlier discussed) can be seen at lower confining stress of  $p = 500$  kPa. The dilative behaviour of the sample is also seen in Fig. 5.26a and b, which presents the deviatoric response of the material at 20 MPa of total suction. A visual observation of the tested samples after the failure given in Section 5.6.2.1 confirms such behaviour due to shearing at lower confining stresses. A repetitive test was also performed at a confining stress of  $p = 500$  kPa to check the reproducibility of the tests. The second test shows a good correspondence with the first test which proves the reproducibility of the results obtained from the triaxial cell.

The influence of total suction and confining stress can be explained by the theory of hardening plasticity. This concept assumes a yield surface as the locus of stress points where the irreversible strains happen. In order to define such a framework, the appropriate stress variables have to be selected. In general, any two of the three possible state variables amongst  $\sigma$ ,  $u_w$ ,  $u_a$  can be

selected to define the stress state (discussed by Nuth & Laloui 2008). The most frequently used couple of these variables are in the form of the net stress ( $\sigma_{net} = \sigma - u_a$ ) and the matric (capillary) suction ( $s = u_a - u_w$ ) for instance in Fredlund et al. (1978).

The second possible combination of stresses could be based on the saturated effective stress or Terzaghi effective stress ( $\sigma - u_w$ ) with matric suction ( $s = u_a - u_w$ ) for instance in (Geiser et al. 2006).

In the current tests on bentonite material, the total suction which is the summation of the osmotic and capillary suction terms was controlled. The use of both above-mentioned frameworks needs the determination of the capillary suction for the tested material. It is believed that the contribution of the capillary suction in smectite-based materials such as bentonite in a wide range of the total suction is negligible (Alonso et al. 2010).

Moreover, with regard to the use of the second framework, it is important to define an effective stress formulation that considers the physico-chemical forces originated from diffuse double layer in smectite clays. Various researches have been conducted to find the contribution of the physicochemical stresses in the effective stress formulation of the saturated smectite-based clay materials (e.g. Sridharan & Rao 1979, Hueckel 1992, Graham et al. 1992). A lack of a well-defined framework for the effective stress concept in smectite-based material with high water activity can be realised based on the literature.

For the sake of the generality and comparison with literature, the results of this chapter have been presented in terms of mean total stress ( $p$ ) and total suction ( $\psi$ ). Thus, the hardening plasticity is also defined with these two parameters not necessarily taking total suction as an independent stress variable.

Analyses of the results presented in Figs. 5.25 and 5.26 imply a yield curve representing the locus of yield point in the ( $p$ ,  $\psi$ ) space. The effect of confining stress on the deviatoric behaviour of the saturated granular bentonite is presented in Fig. 5.26c and d. The tests were carried out at  $p = 1150, 2000$  and  $3000$  kPa. The lowest confining stress corresponds to the swelling pressure of the sample at constant volume conditions as described in Section 5.5.2.2. When the sample reached about 1 MPa of the swelling pressure, the mean total stress was increased to 1150 kPa (while the back pressure of 50 kPa was still applied). After a given time for the equilibrium at these conditions, the deviatoric loading was applied. It is seen that the material exhibits negligible volume change behaviour together with a small shear strength.

It should be mentioned that the data on the volumetric strain of the saturated samples were obtained from the pore volume data with the assumption that the solid part of the saturated material is incompressible. However, for the case of  $p = 1150$ , the volume strain computed from the inner-cell data (as performed for unsaturated tests) is also presented. This good agreement between the records of the inner-cell and the ones of the pore volume confirms the accuracy of the inner-cell volume measurements. It is observed that the increase in confining stress from 2000 kPa and 3000 kPa has a negligible influence on the shear strength of the saturated material. Similar behaviour was already observed in Fig. 5.26a for the total suction of 20 MPa. This implies that the influence of the confining stress on the shear resistance is more notable at higher suctions.

The influence of the total suction on the deviatoric behaviour is presented in Fig. 5.27 at the mean total stress of  $p = 2000$  kPa. The decrease in the shear strength of the material with suction decrease can be observed.

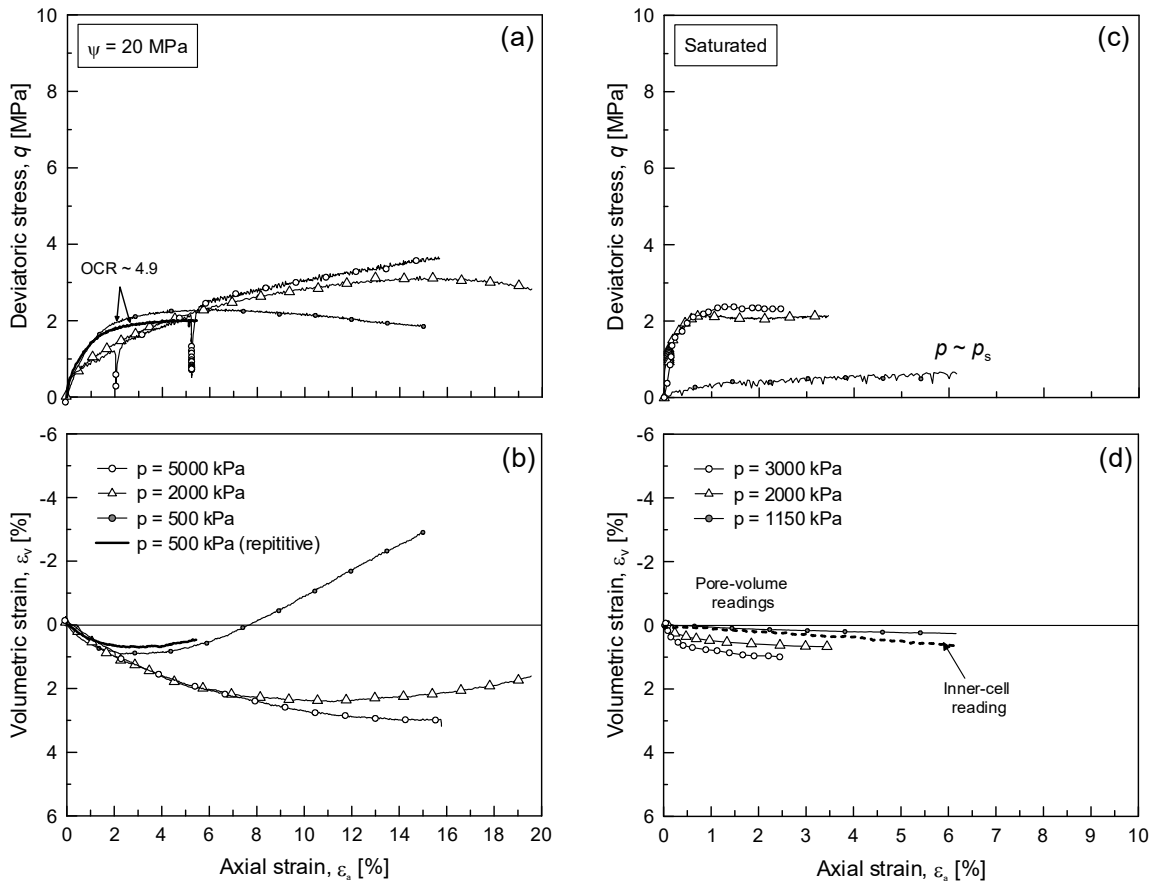


Fig. 5.26: Deviatoric behaviour of Wyoming granular bentonite: (a), (b) influence of confining stress at  $\psi = 20$  MPa, and (c), (d) influence of confining stress at saturated conditions.

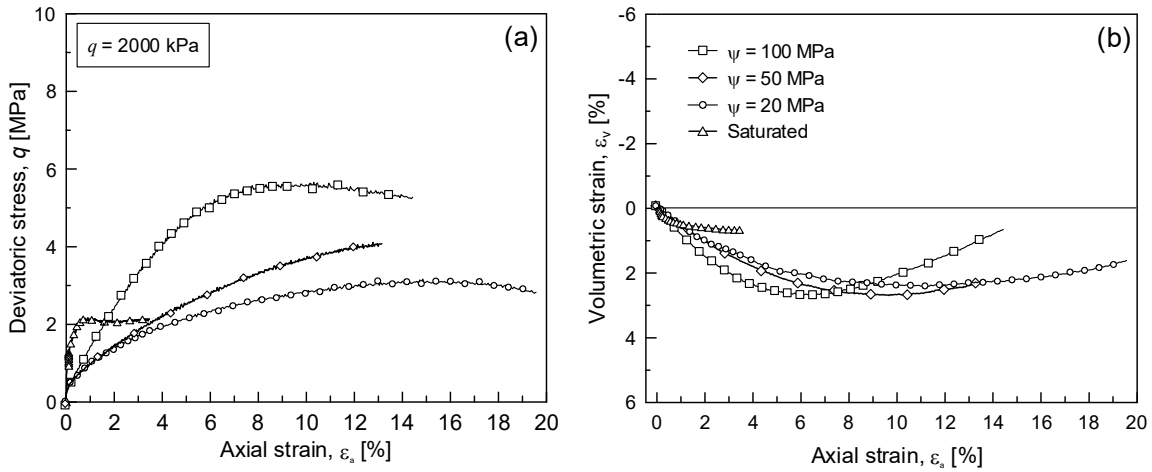


Fig. 5.27: Influence of total suction on the deviatoric behaviour of Wyoming granular bentonite.

The material exhibits a ductile behaviour under saturated conditions. The deviatoric stress at the failure with respect to the mean total stress and total suction is presented in Fig. 5.28. The Critical State Line (CSL) at different suction values is presented in Fig. 5.28a, and the slope of the CSL is assumed to be constant. This is valid with the assumption that the shear strength angle of the material remains constant at different total mean stress values.

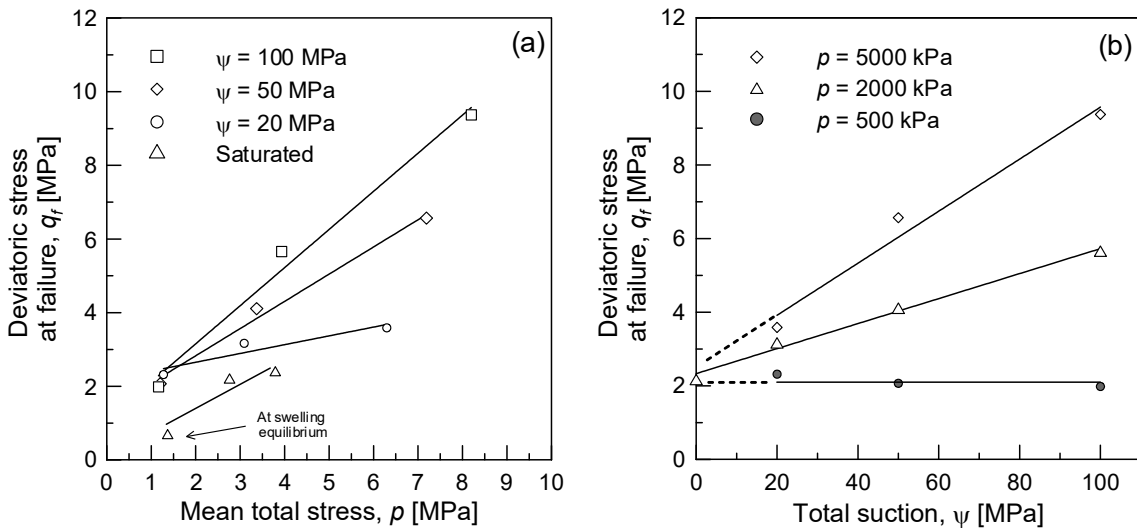


Fig. 5.28: Influence of the suction and mean total stress on the deviatoric stress at failure of Wyoming granular bentonite.

In unsaturated samples, an increase in internal friction resistance can be seen with an increase in total suction. Regardless the deviatoric response of the saturated sample at swelling equilibrium, this trend can include the saturated samples as well. Fig. 5.28b shows that the evolution of the peak strength of the material with a total suction increase is negligible under lower confining stress. However, the hardening due to the increase in total mean stress and total suction is observable in the performed tests. As it was mentioned, the influence of the total suction and confining stress can be explained by the hardening plasticity. The hardening associated to the movement of the yield surface is assumed to depend on the plastic volumetric strains. In the triaxial stress space, by considering deviatoric stress  $q$ , the yield surface can be represented by, for instance, the elliptic form of the modified Cam-clay model as shown in Fig. 5.29a, b.

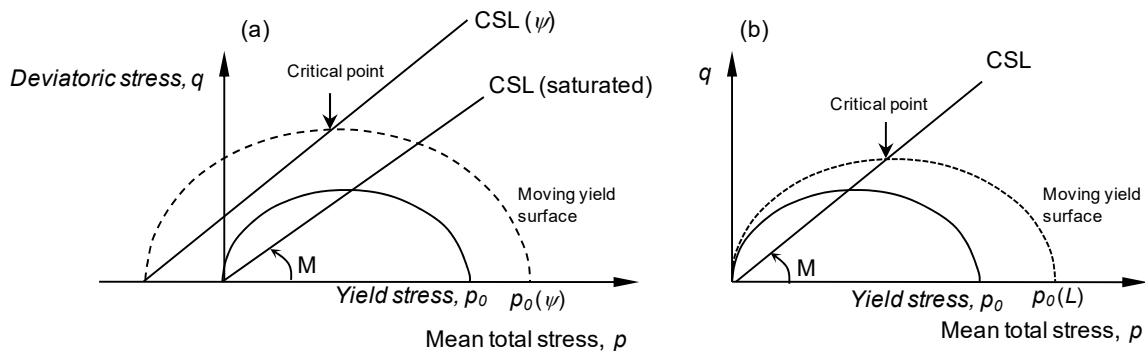


Fig. 5.29: Evolution of the yield surface and Critical State Line (CSL) in the hardening plasticity approach: (a) suction hardening, and (b) strain hardening.

The yield stress  $p_0$  varies in the  $(p, \psi)$  plane. The increase of the strength of the material is then related to the evolution of the CSL with the total suction values. Such behaviour in terms of the influence of the total suction on the yield surface and the CSL can be observed by comparing the behaviour of the saturated sample with the unsaturated samples as presented in Fig. 5.27a.

The strain hardening associated with the behaviour of the material in Fig. 5.28b is presented in Fig. 5.29a where at a given suction, the yield surface evolves due to the generation of the volumetric plastic strain. It should be noted that the Cam-clay model does not provide an accurate evaluation of the soil behaviour, and more sophisticated models to describe the behaviour of unsaturated geomaterials have been developed. Amongst them, the BBM model developed by Alonso et al. (1990) which incorporates the net stress and matric suction and the ACMEG-TS model developed by François & Laloui (2008) which uses the effective stress and matric suction, can be mentioned.

### 5.5.2.1 Visual observation of the tested samples

The images of the unsaturated samples after failure due to the deviatoric loading are presented in Fig. 5.30. At total suction of  $\psi = 100$  MPa (Fig. 5.30a), the material was poured inside the membrane. The failed sample at a confining stress of 5000 kPa is compared with a steel sample representing the initial dimensions of the poured sample. The failure modes at different confining stresses at  $\psi = 50$  MPa are shown in Fig. 5.30b.

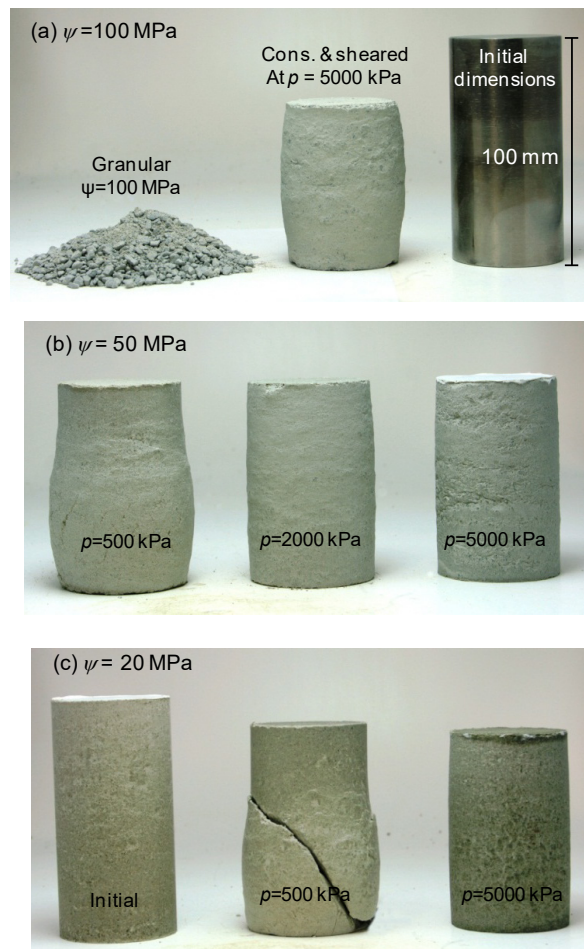


Fig. 5.30: Failure modes under deviatoric loading at different controlled suction tests.

Finally, the failed samples at  $\psi = 20$  MPa are presented in Fig. 5.30c. It is seen that a clear shear surface followed by a dilative response and brittle failure is obtained at a lower confining stress of 500 kPa, while the material exhibits a ductile behaviour under a high confining stress of 5000 kPa. The extraction of the saturated samples was not successful, and the image of the saturated samples after failure is not available.

### 5.5.3 Influence of temperature

#### 5.5.3.1 Influence of temperature on unsaturated volumetric and deviatoric behaviours

This session is addressing the influence of the temperature on the thermal volumetric strains and deviatoric behaviour of unsaturated granular bentonite samples (at total suction  $\psi = 20$  MPa). According to the testing procedure outlined in section 5.5.4, heating paths were applied after samples were isotropically loaded to a given confining stress. The paths were then followed by deviatoric loading. The non-isothermal isotropic behaviour of the material was not investigated in these thermal analyses. However, as discussed in section 5.4, a negligible influence of temperature on the compressibility behaviour of Wyoming bentonite material is anticipated (Tang et al. 2008). The results of the performed tests are listed in Tab. 5.3. The initial and final void ratio of the material after mechanical and thermal consolidation and the deviatoric loading are presented in this table. The variation of thermal volumetric strains with respect to temperature of the sample at different mean total stresses of  $p = 500$ , 2000 and 5000 kPa is presented in Fig. 5.31. The sample at  $p = 500$  kPa exhibits dilative behaviour. On the other side, the sample tested under mean total stress of  $p = 2000$  kPa shows contractive behaviour. The dilation behaviour of bentonite material for high values of OCR and the contraction for slightly overconsolidated condition have been reported in oedometric behaviour of Wyoming bentonite (Tang et al. 2008).

Tab. 5.3: List of the tests performed at elevated temperature ( $T = 80$  °C).

		Initial state		Consolidation (mechanical/thermal)		Failure state		
Test name	OCR	$e_0$ [-]	$P$ [kPa]	$e_c$ [-]	$e_T$ [-]	$e_f$ [-]	$q_f$ [MPa]	Hydro-mechanical test
$\psi_{20\_p0.5}$	4.9	0.84	500	0.83	0.82	0.78	1.61	Controlled suction $\psi = 20$ MPa
$\psi_{20\_p2}$	1.2	0.83	2000	0.78	0.80	0.76	2.51	
$\psi_{20\_p5}$	NC	0.83	5000	0.69	0.70	†	†	

Note:  $e_0$  The initial void ratio  $e_c$  is the void ratio after mechanical consolidation,  $e_T$  is the void ratio after thermal consolidation and  $e_f$  is the void ratio at failure due to deviatoric mechanism.

† This test was stopped at 5.6 % of the axial strain due to technical problems during the test. A deviatoric stress of 1.7 MPa was registered at this strain. The dimensions of the sample were measured after the test and extraction of the sample from the cell. A dry density of  $1.70 \text{ Mg/m}^3$  ( $e = 0.61$ ) was registered for the sample at this stage.

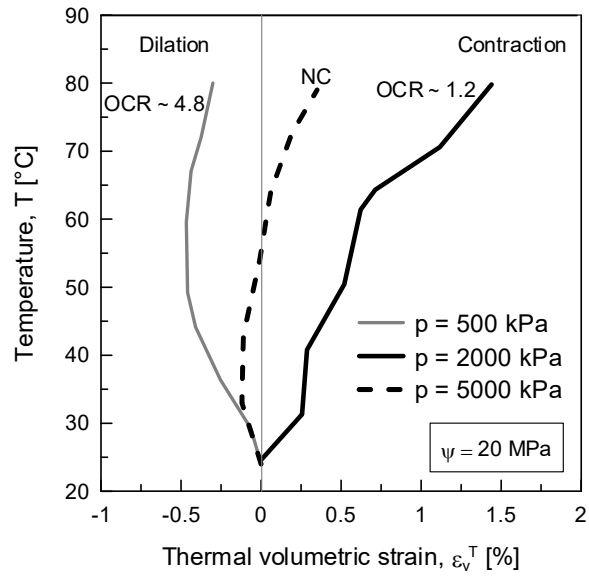


Fig. 5.31: Influence of temperature on the controlled suction volumetric strain behaviour of granular bentonite.

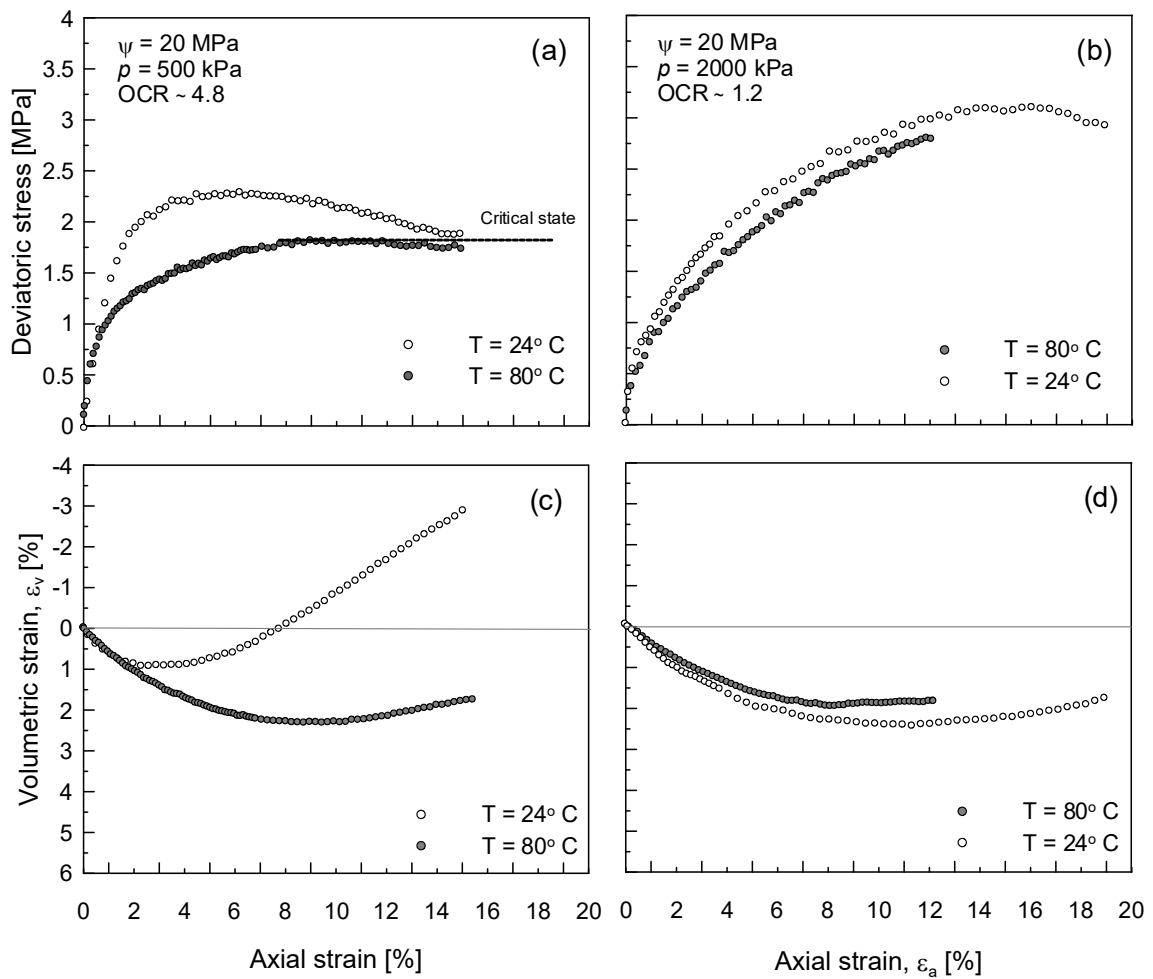


Fig. 5.32: Influence of temperature on the controlled suction deviatoric behaviour of compacted granular bentonite.

However, it is observed that the material exhibits small thermal volumetric strains at a higher confining stress of  $p = 5000$  kPa. This could be associated to the reduction in the voids during the mechanical loading, which does resist the further change of the void ratio due to the temperature increase. It seems that at this confining stress, the material exhibits an initial expansion followed by a small contraction behaviour.

The deviatoric behaviour of the samples consolidated at  $p = 500$  and  $2000$  kPa at two temperatures of  $24$  and  $80$  °C are presented in Fig. 5.32. It is observed that at lower confining stress  $p = 500$  kPa (Fig. 5.32a, c) where the material is overconsolidated, a dilative behaviour is exhibited. At higher temperatures the material shows a contractive response. The yield locus also seems to be diminished at higher temperatures. On the contrary, the change in deviatoric behaviour under different temperatures is negligible at  $p = 2000$  kPa. These phenomena can be explained by simultaneous influence of thermal softening and strain hardening as shown in Fig. 5.33. The normally consolidated or slightly overconsolidated samples undergo path A – B – C before initiation of the deviatoric loading, while the overconsolidated samples follow path A – B – D before shear.

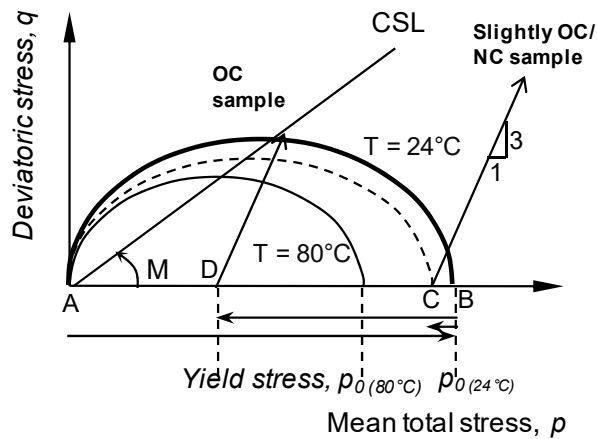


Fig. 5.33: Simultaneous influence of thermal softening and strain hardening on the yield surface.

### 5.5.3.2 Visual observation of the temperature effect on unsaturated samples

The images of the samples before and after failure due to the deviatoric loading are presented in Fig. 5.34 corresponding to the results presented in Fig. 5.33. The dilative behaviour of the material at  $p = 500$  kPa at the lower temperature can be observed in Fig. 5.34a. A clear shear zone was created under these conditions. On the other side, the image in Fig. 5.34b indicates a contractive behaviour of the material for both temperatures at  $p = 2000$  kPa.

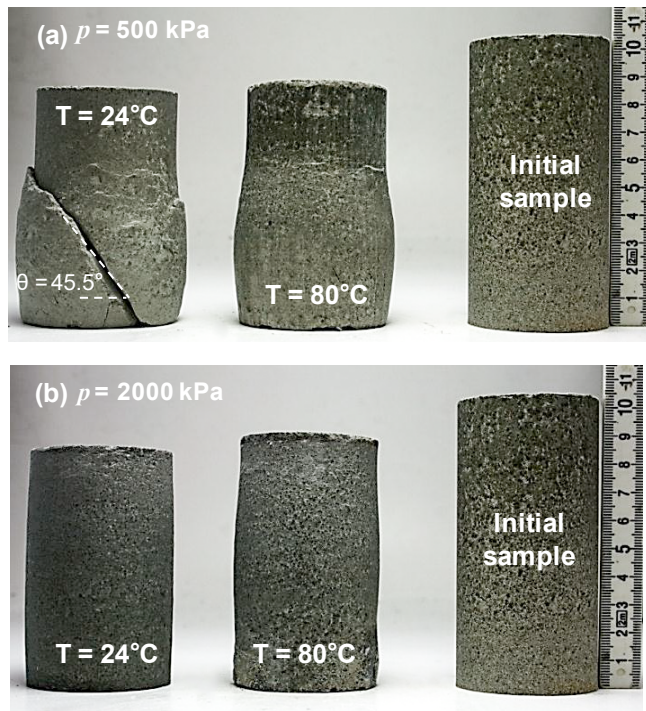


Fig. 5.34: Deviatoric failure modes of compacted Wyoming granular bentonite samples under a total suction of  $\psi = 20 \text{ MPa}$  and at different temperatures: (a) under  $p = 500 \text{ kPa}$ , and (b) under  $p = 2000 \text{ kPa}$ .

### 5.5.3.3 Influence of temperature on saturated bentonites

The calculation of the thermal volumetric strains of saturated samples was performed as suggested by Baldi et al. (1988). Accordingly, the volumetric strains,  $\varepsilon_v^T$  during heating were calculated by subtracting the estimated volume of thermal expansion of the pore water from the net volume of the expelled water. The variation of the computed thermal volume strain  $\varepsilon_v^T$  versus temperature is presented in Figs. 5.35 and 5.36.

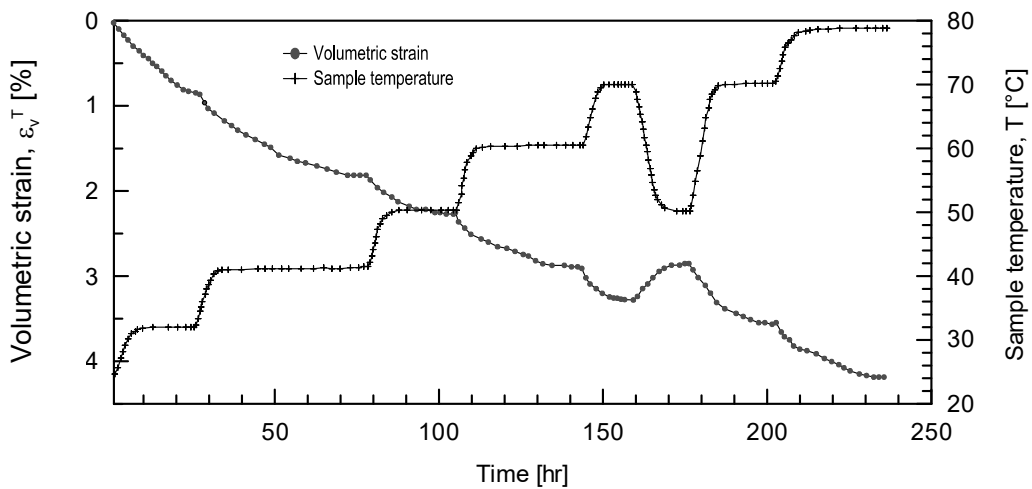


Fig. 5.35: Evolution of thermal volumetric strains of the saturated sample at applied temperatures.

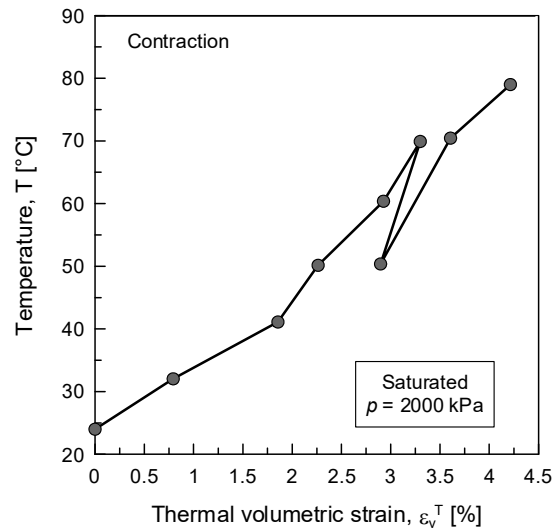


Fig. 5.36: Influence of temperature on the volumetric strain behaviour of granular bentonite at saturated conditions.

A cooling/heating cycle with negligible accumulation of the volumetric strain was registered for the material as presented in Fig. 5.35. By a comparison with the behaviour of unsaturated bentonite (Fig. 5.31), it can be observed that the volumetric strains obtained for the saturated material are almost twice of the one in case of unsaturated material under the same confining stress for a given temperature increase.

### 5.5.4 Hydraulic conductivity of saturated bentonite

Analysis of the application of different hydraulic gradients on the hydraulic conductivity of saturated bentonite samples revealed that below a certain gradient ( $i < 300$ ), no flow was obtained through the material. Villar et al. (2010) reported similar observations for the hydraulic analysis of FEBEX bentonite samples. The temperature and dry density were mentioned as the important parameters to control this threshold value for the hydraulic gradient. The slight increase of the hydraulic conductivity of the saturated samples with hydraulic gradients is shown in Fig. 5.37a. After application of a gradient of  $i = 713$ , the temperature was increased in two steps from 24 °C to 40 °C and 60 °C by maintaining the same hydraulic gradient.

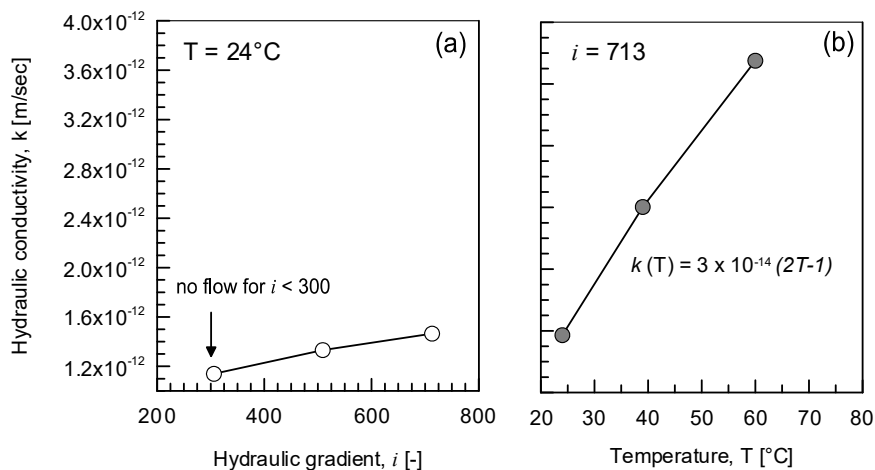


Fig. 5.37: Influence of hydraulic gradient and temperature on the hydraulic conductivity.

A more remarkable change of the hydraulic conductivity values were obtained due to the temperature increase. Temperature affects the hydraulic conductivity of the bentonite due to the change in viscosity of water (Section 3.3.2) and change in interaction mechanisms between bentonite particles and water. Ma & Hueckel (1993) mentioned the mechanism of transfer of water from the interlayer pores to the macropores due to the temperature application and consequently increasing the hydraulic conductivity. Due to this mechanism a part of the immobile water within the structure is transferred to the mobile water which increases the hydraulic conductivity of the material.

## 5.6 Summary and conclusions

This chapter was dedicated to the presentation of the thermo-hydro-mechanical behaviour of Wyoming granular bentonite using an advanced and multi-purpose triaxial cell. The following points are concluded with regard to the content of this chapter:

- Progressive saturation of the buffer upon water saturation from the host rock, the tectonically induced stresses from the overburden formation, swelling pressures due to saturation and heat generated from the canisters imposed complex THM conditions to the bentonite material used as buffer in the engineered barriers for the disposal of HLW. In order to assess the complex THM actions in bentonite, application of suction, stress and temperature in a wide range are the most challenging subjects. The advanced triaxial cell used in this research provides implementation of different stress paths according to the application of the material in HLW repositories.
- The calibration process of the THM triaxial cell was carried out in analytical form to obtain the actual force – deformation and volume change of the tested samples. Provided with the inner-cell technique to measure the volume change of the sample, the correlation to the actual volume change and the thermal and pressure evolution of the system related to the inner-cell was required to be taken into account for the calibration of the volume change. The calibration approach was found to be successful and was verified using particular testing procedures.
- THM analysis of Wyoming granular bentonite at saturated and unsaturated conditions was carried out using the introduced triaxial system. The tests were performed at unsaturated and saturated conditions under different applied confining stresses ( $p = 500, 2000$  and  $5000$  kPa for unsaturated and  $p = 1150, 2000$  and  $3000$  for saturated conditions). The vapour transfer technique was used for controlled suction tests and a wide range of total suction ( $\psi = 100, 50$  and  $20$  MPa) was considered. The saturated tests were performed under drained conditions. The influence of the total suction on the isotropic behaviour of the material indicated that the compressibility index of the material increases with decreasing total suction. However, the saturated material exhibited less compressibility in the range of the applied stresses. The induced overconsolidation condition during sample preparation of the unsaturated material was seen in terms of dilation and contraction with regard to the applied stress before shearing. The OC samples exhibit dilation and the slightly OC or NC samples showed contraction during application of the deviatoric stress. The influence of the confining stress was better observed under lower confining stresses. The observed results could be associated with the evolution of the yield surface of the material upon strain hardening and suction hardening mechanisms.

- The influence of temperature on the volumetric strain and deviatoric response of the material was investigated at different confining stresses under a total suction of  $\psi = 20$  MPa. It was observed that the overconsolidated material expanded during the heating process, while the slightly overconsolidated material exhibited a contractive behaviour. However, the consolidated sample at high confining stress of 5 MPa showed negligible thermal volume strains. This observation could be associated with reduction in the pore structure before application of the temperature. In terms of deviatoric loading two simultaneous mechanisms were observed influencing the material response: the strain hardening and the thermal softening mechanisms. Thus, the overconsolidated material at higher temperatures showed a decrease in the size of the yield surface which resulted in decreasing of the elastic domain. The dilative behaviour and the stress softening result in less shear strength for the overconsolidated material at higher temperatures. On the other side, at a higher confining stress the thermal softening seems to be compensated with the strain hardening (contractive behaviour of the sample). Thus, the influence of temperature on the deviatoric behaviour of the material was found to be negligible.

## 6 Assessment of the hydro-mechanical behaviour of shot-clay Wyoming bentonite

This chapter presents the results of an experimental study carried out to characterise the hydro-mechanical behaviour of shot-clay Wyoming bentonite (Ferrari et al. 2014). In the shot-clay process, granular bentonite was mixed continuously with water and shot on the walls of a tunnel section at the Grimsel Test Site (GTS) in Switzerland. The shot-clay was placed to create a layer of bentonite in direct contact with the host rock to avoid preferential water and/or gas flow along the tunnel wall. Samples for an experimental programme were collected during the shooting. The index properties, microstructural features, swelling potential and water retention properties of the shot-clay were analysed. An experiment was then conducted under controlled total suction to analyse the hydro-mechanical behaviour of the material along a predefined stress path involving suction and confining stress variations. Based on the results of this test, the expected behaviour of the shot-clay bentonite, when subjected to the environmental conditions in the repository, was determined. The test results were compared with data on the observed behaviour of compacted Wyoming granular bentonite to assess the effects of the shot-clay emplacement technique on the behaviour of shot-clay Wyoming bentonite. The results highlight the role of the emplacement dry density on the behaviour of bentonite.

### 6.1 Shot-clay Wyoming bentonite and technological gaps

"Shot-claying" of Wyoming bentonite has been selected as a candidate for the filling material to amend the performance of the Engineered Gas Transport System (EGTS) due to the creation of the technological voids or gaps. EGTS is used to limit gas overpressures in the backfilled underground structures of radioactive waste repositories to acceptable levels without compromising the radionuclide retention capacity of the engineered barrier system (EBS) (Nagra 2008). The main design elements of an EGTS are: (i) specially designed backfill materials for the emplacement caverns, characterised by high porosity and high compressive strength and (ii) gas-permeable tunnel seals consisting of sand/bentonite (S/B) mixtures with bentonite contents of 20 to 30 %.

The Gas-Permeable Seal Test (GAST) was initiated in 2010 and conducted at the Grimsel Test Site (GTS, Switzerland) in 2011 and 2012. An S/B seal with a length of 8 m and a diameter of 3 m was emplaced to demonstrate the effective functioning of gas-permeable seals at realistic scales and under realistic hydraulic boundary conditions ('proof of concept').

Technological gaps may generate preferential flow paths within the swollen S/B mixture (Wang et al. 2013). To avoid preferential water and/or gas flow along the tunnel wall, a bentonite ring with a target hydraulic conductivity of at least  $1 \times 10^{-12}$  m/s, corresponding to a dry density of the bentonite of approximately  $1.4 \text{ Mg/m}^3$ , had to be emplaced around the S/B seal. The first emplacement option assessed was shot-claying, which involved mixing Wyoming granular bentonite with water (at a volumetric water-to-bentonite ratio of 3 to 11.7), feeding the mixture into a hydraulic pump and shooting the mixture onto the tunnel wall (Fig. 6.1). A shot-clay test was performed at the GTS as part of the pre-testing for the final experimental setup (Teodori et al. 2013).

Dixon et al. (2011) presented a comprehensive summary of granular and bentonite pellet installations to fill technological gaps in high-level waste repositories. This summary highlighted the difficulties related to the low repose angle of dry pellets when poured and the pellet damage that occurs when the material is blown under dry conditions.



Fig. 6.1: Shot-clay experiment carried out at the GTS.

Wyoming granular bentonite was mixed with water, pumped and shot on the wall of the tunnel.

In the experiment described in the present study, after the layer of emplacing the bentonite on a tunnel wall, the layer was subjected to several hydro-mechanical processes, some of which resulted from the experimental emplacement and others were tested in the lab to assess their potential to optimise the final dry density of the bentonite ring after full saturation. The laboratory tests primarily assessed the impact of a ventilation phase immediately following shot-claying and the compaction due to the emplacement of the S/B seal inside the bentonite ring. The sampling procedure at the GTS is described in the first section. The material was characterised in terms of its index properties, microstructural features, swelling potential and water retention capacity. A comprehensive stress path was designed and a controlled suction test was carried out to assess the probable hydro-mechanical response of the material during the various expected phases of environmental conditions in the repository. The results of the experiments were compared with other data on the behaviour of compacted Wyoming granular bentonite to assess the effects of the shot-clay emplacement technique on the behaviour of Wyoming bentonite.

## 6.2 Tested material

### 6.2.1 Sampling procedure

Laboratory tests were carried out on material samples collected on-site during the emplacement of the shot-clay. After the emplacement of the first bentonite layer, the shooting was suspended to allow the installation of several cylindrical steel tubes (with a diameter of 9.5 cm and a height of 12 cm), that were pushed approximately 1 cm into the bentonite layer (Fig. 6.2a).

The mixture of bentonite and water was then shot directly into the sampling tubes (Fig. 6.2b) and eventually, the cylinders were extracted, trimmed (Fig. 6.2c), sealed and transported to the laboratory. Visual inspection of the shot-clay front on the tunnel surface suggested that good homogenisation of water and bentonite was obtained during the shooting. Examination of the trimmed core (Fig. 6.2c) suggested that the bentonite grains were dry in their interiors and that water was absorbed by the finer particles and on the surfaces of the grains only.



Fig. 6.2: Sampling of the shot-clay Wyoming bentonite: (a) installation of the steel sampling tubes on the tunnel wall, (b) shooting of the mixture of water and bentonite into the tubes, and (c) extracted tube containing the sample.

### 6.2.2 Index properties

Wyoming granular bentonite was used for the shot-clay experiment. The index properties of the shot-clay Wyoming bentonite were determined in the laboratory. A specific gravity  $G_s = 2.74$  was measured. A liquid limit  $w_l = 4.30$  and a plastic limit  $w_p = 0.65$  were defined similar to the methods used in Chapter 2 to determine the Atterberg limits of granular Wyoming bentonite. The average water content was 0.39 for the samples that were extracted immediately from the shot layer and sealed, and 0.32 for the samples that were exposed to the site conditions for approximately 30 minutes before the tubes were sealed. Determination of the grain size distribution of the granular bentonite (apparent grain size distribution) was performed by sieving the bentonite grains at their hygroscopic water content; the analysis revealed a sand-sized fraction of 60 % and a gravel-sized fraction of 30 %.

The bulk density and the dry density were in the ranges of  $1.58 - 1.63 \text{ Mg/m}^3$  and  $1.14 - 1.17 \text{ Mg/m}^3$ , respectively. The average void ratio was 1.4. Complementary density measurements were performed on samples cored from the bentonite layer after the shot-clay was completed. The density values of these samples were in the same range of those obtained for the samples collected in the tubes installed before the shooting.

The initial total suction was measured using WP4C (Decagon Device Inc. 2002). Initial total suction values of 4 and 6 MPa were measured for the samples at water contents of 0.38 and 0.32, respectively.

### 6.2.3 Microstructural features

MIP tests were used to determine the pore size density (*PSD*) function of the shot-clay. The MIP test and the concepts were detailed in Chapter 3. To perform the tests, a cubic specimen approximately 5 mm in size was taken from one of the collected samples and freeze-dried prior to the MIP test.

Fig. 6.3 shows the cumulative intruded void ratio and the *PSD* versus entrance pore diameter (*d*). The difference between the cumulative void ratio and the void ratio measured on samples (0.45) is associated with the interlayer porosity that cannot be accessed by mercury, the so-called nanopores as described in Chapter 3. A multimodal pore size density function was obtained and is shown in Fig. 6.3b. A peak with a modal value of approximately 20 nm is observed. Similar to the various observations presented in Chapter 3, this level of porosity is associated with the intra-aggregate or intra-assemblage porosity. Pore sizes in the range of 0.04 to 10  $\mu\text{m}$  correspond to inter-aggregates. Pore sizes larger than 10  $\mu\text{m}$  seems to correspond to the inter-bentonite assemblage pores and represent the macropores in the shot-clay bentonite.

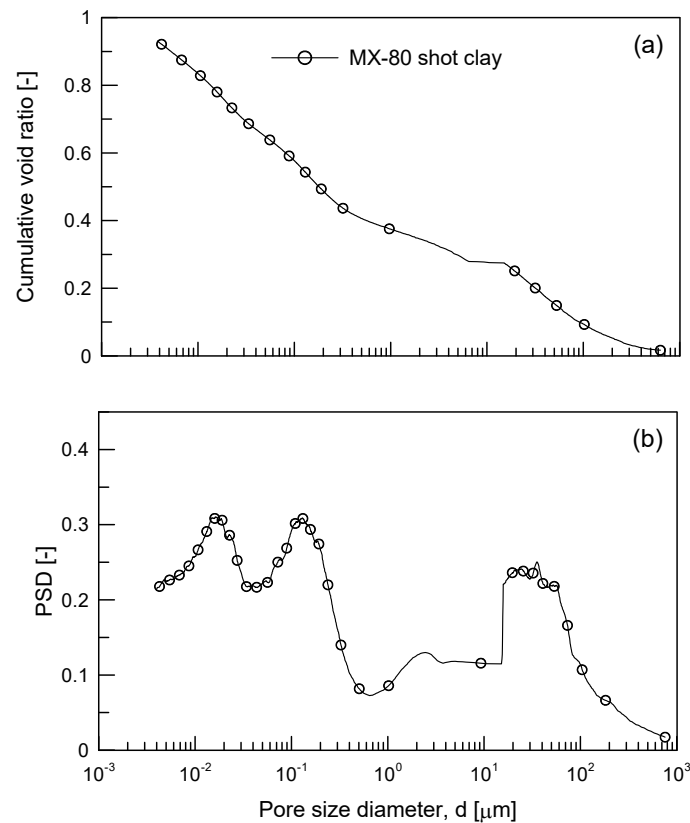


Fig. 6.3: Results of the MIP test on a sample of Wyoming shot-clay bentonite: (a) cumulative void ratio, and (b) pore size density function (*PSD*) vs. pore size diameter.

### 6.3 Experimental programme

The behaviour of the shot-clay Wyoming bentonite was assessed through a comprehensive laboratory campaign. The aim of the tests was to analyse the response of the material to the environmental conditions expected in the repository from emplacement through full saturation. The material's swelling potential, retention behaviour and volumetric response under hydro-mechanical loading were analysed. All tests were performed on specimens cored out from the tube samples collected on-site. The initial characteristics of the tested specimens in the various experiments are listed in Tab. 6.1. Distilled water was used in all experiments. All of the tests were run under temperature-controlled laboratory conditions ( $22 \pm 0.5$   $^{\circ}\text{C}$ ). Details of the testing procedures are given in the following sections.

Tab. 6.1: Initial characteristics of the tested specimens in the experimental activities.

Test	Water content	Void ratio	Degree of saturation
Constant volume swelling	0.380	1.38	0.75
Free swelling	0.319	1.38	0.63
Water retention	0.390	1.43	0.75
Controlled suction hydro-mechanical test	0.320	1.38	0.63

### 6.3.1 Swelling behaviour

To evaluate the swelling potential of the shot-clay Wyoming bentonite, constrained and free swelling tests were performed on specimens 1.88 cm in height and 7.53 cm in diameter. Each specimen was placed in a rigid steel cell, resting on a porous disc connected to a water inlet. The upper part of the specimen was in contact with a coarse porous stone, and a flushing line was connected to the upper part of the cell.

The swelling pressure was measured by inserting the cell containing the specimen into a rigid frame to ensure constant-volume conditions. To capture any swelling associated with the homogenisation of the water content in the material after the shooting, the specimen was taken to the laboratory and placed in the test apparatus as soon as possible (approximately 2.5 hours after the shooting time). In this phase, no access to water was provided. A load cell (with an accuracy of 10 kPa with respect to the area of the specimen) was placed between the top cap and the frame to measure the swelling pressure. An initial total vertical stress of 80 kPa was applied to ensure good contact of the various parts of the apparatus. The specimen was then inundated with water, and the swelling pressure was continuously monitored until it stabilised.

A free swelling test was carried out by saturating the specimen and measuring the vertical heave with an LVDT system. A constant pore water pressure of 10 kPa was applied to the lower base of the specimen and the flushing line on the top was opened periodically. This configuration ensured the evacuation of air from the top of the cell during rising of the wetting front.

### 6.3.2 Water retention behaviour

The retention curve for the main drying path was analysed using a controlled air-drying process in which the total suction was measured with a chilled-mirror dew-point psychrometer. Several specimens were cored from one sample using a special holder that could be positioned directly in the device for the suction measurement. After determination of the initial water content and total suction of the sample, a drying path was initiated in each specimen by controlled air-drying at ambient laboratory conditions ( $T = 22\text{ }^{\circ}\text{C}$ ,  $RH = 40\%$ ). The evolution of the water content was monitored for each specimen by continuously weighing the sample holder. The air-drying process was stopped once each specimen reached its target water content value. The sample holder was then sealed and the sample was cured for 2 days to ensure a good distribution of the water within the specimen. The total suction of the specimen was then measured using the WP4C device. After the suction was measured, the volume of the specimen and the water content were determined, the latter by oven-drying.

### 6.3.3 Controlled suction hydro-mechanical test

#### 6.3.3.1 Experimental setup

A controlled suction hydro-mechanical test was carried out to measure the volume change and water content variation in the material over the range of environmental conditions expected in the repository. A schematic diagram of the experimental arrangement is shown in Fig. 6.4. The cell holds a sample with a diameter of 7.53 cm and a height of 1.88 cm. The vertical load is controlled by a level arm system. The applied vertical stress is assumed to be representative for the radial stress of the shot-clay layer in the tunnel. The vertical displacement is measured by a LVDT installed on top of the cell. The computed vertical strains are proportional to the radial strains of the shot-clay in the tunnel. The total suction is controlled using the vapour equilibrium technique. The pore water potential of the material is represented by the migration of water molecules through the vapour phase, relative to a reference system of a known water potential, until equilibrium is achieved (Romero 2001). At the end of the equalisation phase, the pore water and the vapour phase have the same potential.

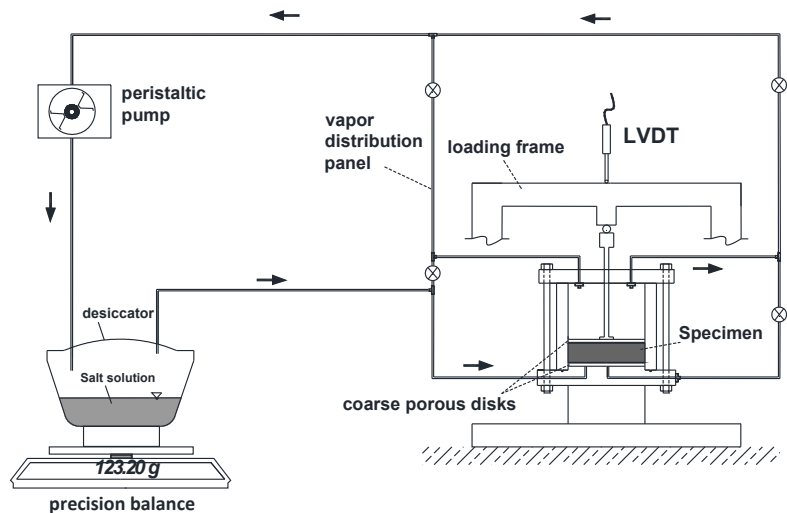


Fig. 6.4: Schematic layout of the experimental setup for the controlled hydro-mechanical test.

Through this equality and by assuming that the water vapour obeys the ideal gas law, it is possible to express the total suction of the material as a function of the relative humidity of the closed system in which the specimen is placed, according to the psychrometric law. The relative humidity ( $RH$ ) and the absolute temperature ( $T$ ) are related to the total suction ( $\psi$ ) through the psychrometric equation (Eq. 2.1).

Variably saturated NaCl solutions and a saturated  $Mg(NO_3)_2$  solution were used to control the relative humidity and hence the total suction of the reference system. Romero (2001) and Witteveen et al. (2013) provided the relationship between the solution concentration and the applied suction. A pump was used to force a humid air flow through the pores of the specimen to reduce the time required to reach equilibrium (Pintado et al. 2009).

### 6.3.3.2 Hydro-mechanical stress path

To consider the different environmental conditions which the shot-clay layer will be subjected to, a schematic diagram is shown in Fig. 6.5. An applied stress path is considered based on the range of environmental conditions that the shot-clay material is expected to experience in the evolution of the repository with regard to the simple representation in Fig. 6.5. Although the shot-claying was proposed for the EGTS system, here it is assumed that the process can be applied to fill the technological gaps in HLW repositories as well. The following steps were then considered and applied as depicted in Fig. 6.6:

1. In the initial state (point A), the specimen was placed in the cell and equalised to a total suction of 6 MPa using a 1.3 M NaCl solution (corresponding to  $RH = 94\%$ ). This suction was the value measured in the sample immediately following the shooting. A vertical stress of 8 kPa was applied to ensure a good contact between the specimen and the loading system. This step is representing the emplacement of the shot-clay on the walls of the repository tunnel (Fig. 6.5a).
2. The vertical load was increased to 67 kPa to simulate an initial compaction of the material (path A – B) to reproduce the emplacement of the buffer material (such as bentonite blocks, concrete bed and canister in case of HLW repositories) in the system. For a canister with a weight of 26.2 t and length of 5 m and considering that the bentonite blocks are emplaced at a bulk density of about  $2 \text{ Mg/m}^3$  (data from Senger & Ewing 2008, García-Siñeriz et al. 2008) a total vertical stress of about 70 – 80 kPa can be expected (Fig. 6.5b).
3. A drying path (B – C) was then applied to reflect the ventilation phase of the repository, during which the material will be exposed to the relative humidity of the tunnel. A suction of 87 MPa was applied using a saturated  $\text{Mg}(\text{NO}_3)_2$  solution, corresponding to a relative humidity of 50 % at the laboratory temperature, which was the average relative humidity at the Grimsel Test Site. It should be mentioned that this step is concurrent with the other stages of the construction of the barriers, such as filling the upper gap between the canister and the host rock with granular bentonite or blocks (Fig. 6.5b).
4. A loading path (C – D) was then applied increasing the vertical stress to 249 kPa at a constant total suction of 87 MPa. This phase is intended to reproduce the development of the swelling pressure in the buffer material when it is wetted through the vapour phase (Fig. 6.5c). This adsorption is justified when considering that the buffer material is usually emplaced at its hygroscopic water content (e.g. 5 % for the granular Wyoming bentonite at  $RH = 34\%$ ) and exposed to the relative humidity in the tunnel.
5. Path D – E reflected the wetting of the material upon water vapour uptake from the surrounding host rock (Fig. 6.5d). The wetting was performed using a saturated NaCl solution, resulting in a total suction of 37 MPa (corresponding to a relative humidity of 75 %). During this phase, the volume was kept constant to reflect the presence of the buffer material. The axial strain was limited to the range of  $\pm 0.25\%$  by increasing the vertical stress in small steps, to prevent swelling of the material. This process was repeated until the specimen did not exhibit any further tendency to swell.
6. Lastly, the specimen was flooded with distilled water (path E – F) to measure the maximum swelling potential associated with the full saturation of the material. To accomplish this operation, the cell was removed from the loading system and installed in a highly rigid frame equipped with a load cell. An initial vertical stress equal to the swelling pressure obtained at the end of path D – E was applied.

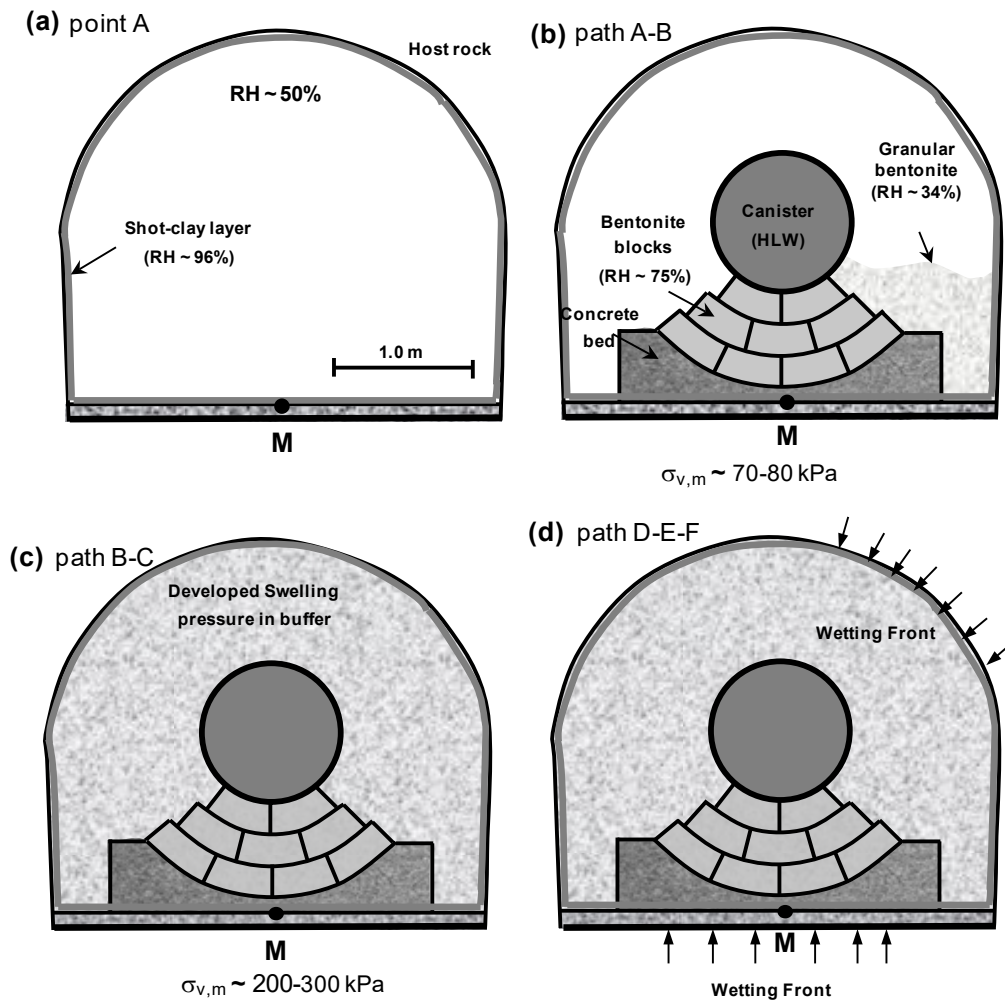


Fig. 6.5: Shot-clay emplaced before different stages of the construction of the engineered barrier systems.

To better observe the material behaviour during the application of the stress path described above, the cell was opened for visual observation at the ends of steps B – C, D – E and E – F. This operation was performed quickly to minimise disturbance of the test. After each inspection, the conditions of suction and vertical stress at the end of the imposed step were re-stabilised before the following step was applied. No vertical strain or water content change was observed during this equalisation phase, confirming that the opening of the cell did not cause disturbance of the test procedure.

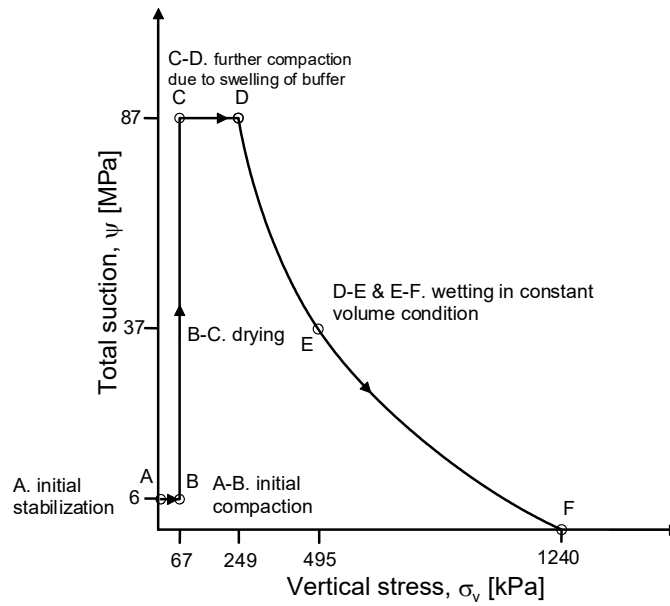


Fig. 6.6: Stress path implemented for the investigation of the hydro-mechanical behaviour of the shot-clay Wyoming bentonite.

## 6.4 Test results

### 6.4.1 Swelling potential of the as-shot material

The results of the constrained swelling test are shown in Fig. 6.7a, in which the measured swelling pressure is plotted with respect to time. The initial homogenisation of the water content after the shooting did not produce any appreciable swelling pressure. A maximum swelling pressure of 990 kPa was observed 10 days after the cell was flooded under constant-volume conditions.

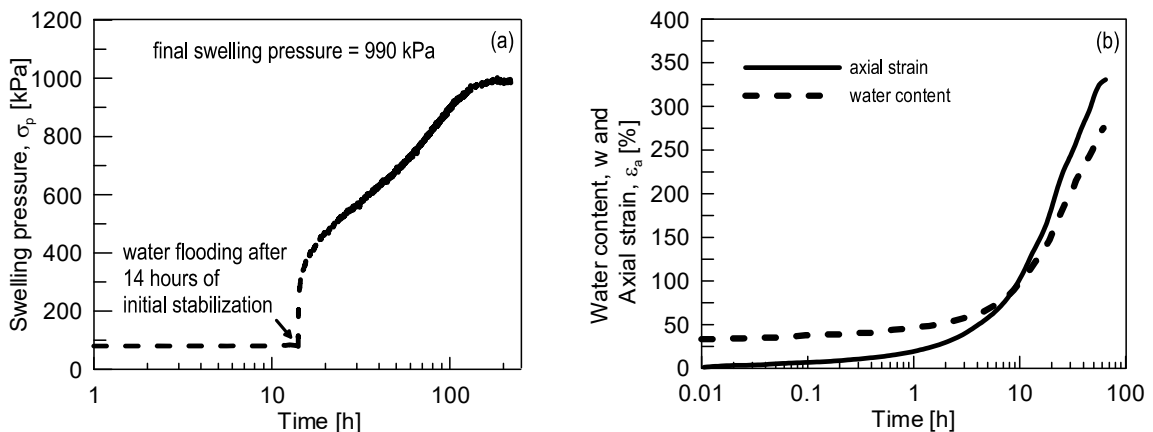


Fig. 6.7: Results of the swelling tests: (a) swelling pressure evolution vs. time under constant volume conditions, and (b) swelling heave and water content evolution under free swelling conditions.

The results of the free swelling test, in terms of axial strain and water content evolution over time, are shown in Fig. 6.7b. A final swelling strain of 324 % and a final water content of 280 % (corresponding to a calculated degree of saturation of 99 %) were reached after approximately 64 days.

### 6.4.2 Water Retention behaviour

The retention behaviour of shot-clay Wyoming bentonite along a drying path is depicted in Fig. 6.8 in terms of void ratio, water content and degree of saturation versus total suction. The initial conditions measured on the whole sample, from which the specimens were extracted, are also reported. The measured void ratio of the specimens was initially higher than the sample void ratio. This difference is attributable to the rebound of the material during the specimen extraction. This observation seems to be confirmed by the change in slope in Fig. 6.8a once the void ratio of the sample was reached during the drying process. A residual degree of saturation of approximately 40 % was obtained.

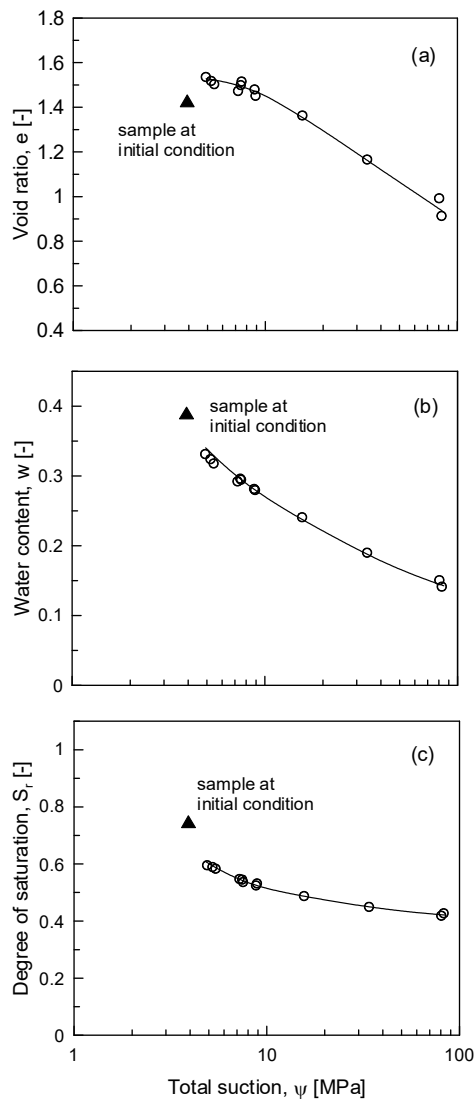


Fig. 6.8: (a) Void ratio vs. suction for drying path in shot-clay Wyoming bentonite material, (b) retention behaviour of shot-clay Wyoming bentonite in terms of water content, and (c) degree of saturation.

### 6.4.3 Controlled suction hydro-mechanical behaviour

The initial characteristics of the tested specimens are reported in Tab. 6.1. The evolution of the water content and axial strain over time for the different steps of the imposed stress path are shown in Figs. 6.9 and 6.10 where the equilibrium states in the planes of total suction versus vertical stress, axial strain versus vertical stress, total suction versus water content and axial strain versus water content are depicted. During the initial equalisation phase (A), no significant deformation of the specimen was recorded and only limited wetting was observed. This wetting is attributed to initial drying of the specimen during cell installation. The water content reached (34 %) is consistent with the retention curve shown in Fig. 6.8b. The loading path (A – B) at constant total suction caused an axial strain of approximately 1 % without any expulsion of water.

The following drying step (B – C) took 33 days to reach equilibrium and resulted in a significant shrinkage of the material (9 %) and a reduction of the water content to 14.2 %, consistent with the retention curve shown in Fig. 6.8b. At this stage, the cell was opened to assess the loss of lateral contact with the oedometric ring and the formation of drying cracks. Lateral shrinkage of approximately 4 % in radial strain was calculated by analysing the collected images (Fig. 6.11a). Interestingly, the creation of drying cracks was also observed on-site, three to four days after the shooting. A loading path was applied by increasing the vertical stress to 249 kPa (C – D) while maintaining a constant total suction. As a result, the axial strain increased up to 11 % while the water content increased only slightly. The wetting path D – E, which was applied using an unsaturated NaCl solution in the vapour phase, resulted in an increase of the water content to approximately 20 %, while the variation in the axial strain was maintained in the range of  $\pm 0.25$  %. A swelling pressure of 495 kPa was measured during that intermediate saturation step (Fig. 6.12a). The cell was also opened for visual observation after this path. As Fig. 6.11b shows, the specimen swelled due to water vapour uptake, reversing the lateral shrinkage around the perimeter that occurred during the drying procedure along path B – C. The cracks observed earlier in the centre of the sample were only partially healed and could still clearly be observed.

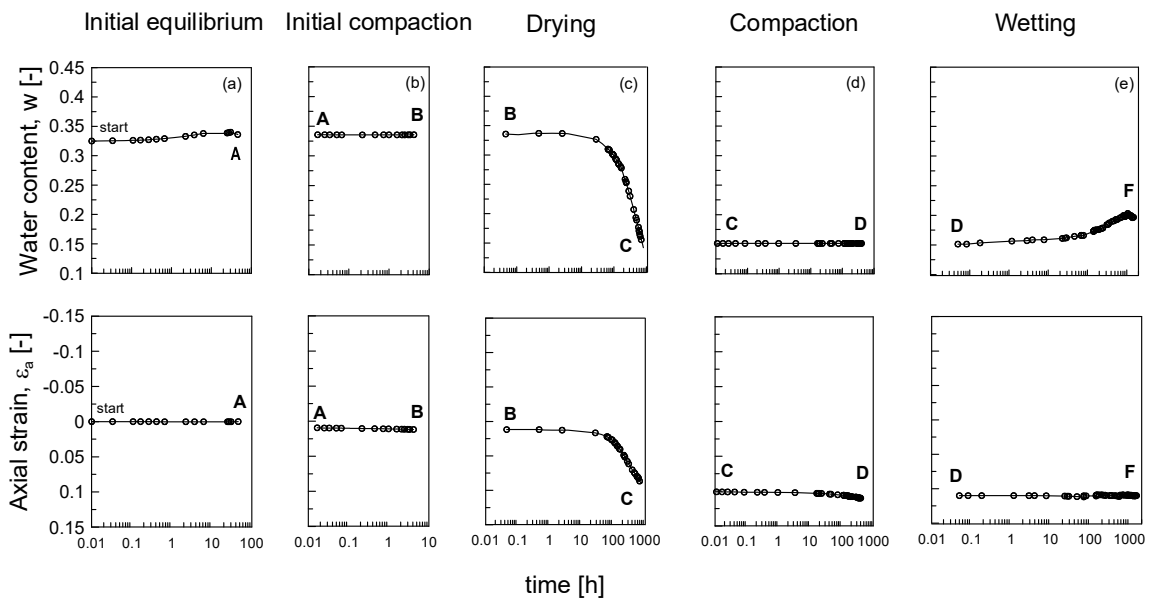


Fig. 6.9: Variation of the water content and axial strain of the specimen during the different steps of the applied stress path shown in Fig. 6.6.

The flooding of the specimen (path E – F) at a constant volume led to the development of a final swelling pressure of 1250 kPa after approximately 6 days (Fig. 6.12b). The cell was finally dismantled and the full homogenisation of the specimen was observed due to saturation (Fig. 6.10c). A final water content of 0.41 (corresponding to a computed final degree of saturation of 99 %) was measured.

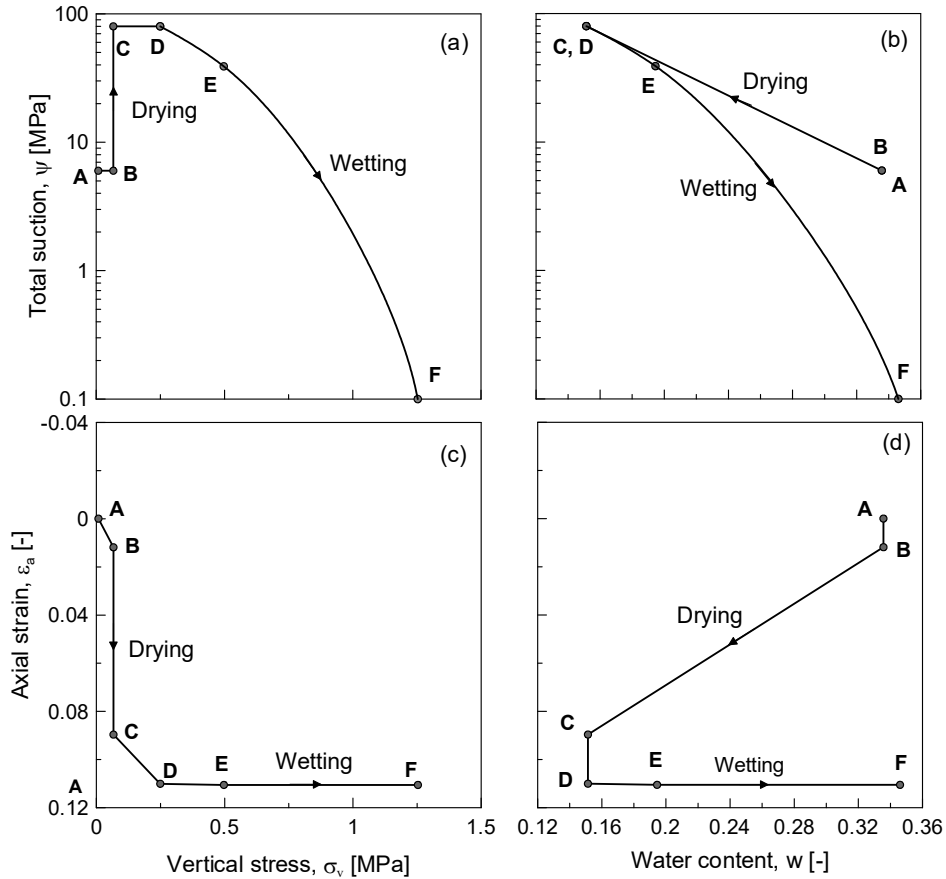


Fig. 6.10: Results of the controlled suction hydro-mechanical test.

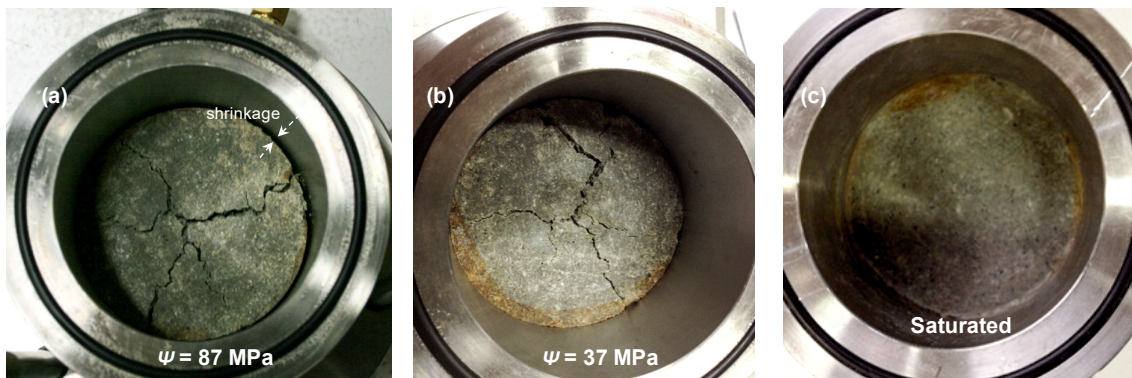


Fig. 6.11: Observation of the specimen after opening the cell at the end of different steps: (a) drying due to step B – C, (b) wetting due to step D – E, and (c) full saturation due to step E – F.

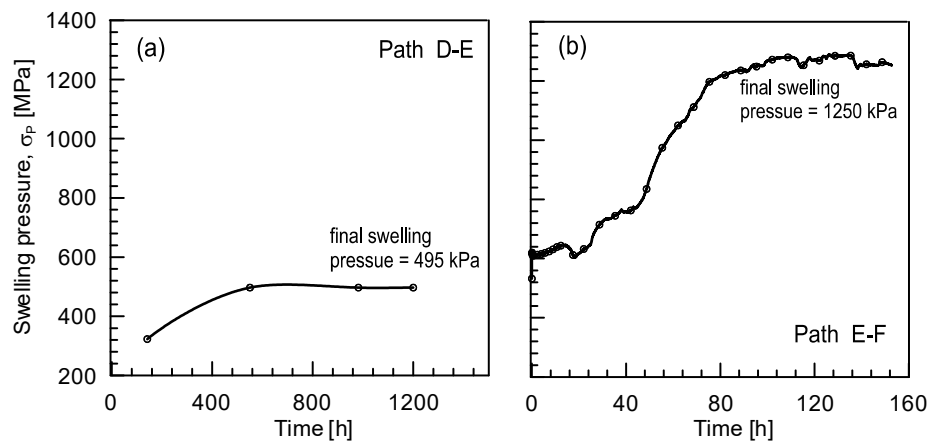


Fig. 6.12: Swelling pressure development during the wetting phase: (a) step D – E, and (b) step E – F in Fig. 6.6.

## 6.5 Summary and conclusions

The summary of this chapter is presented by comparison of the experimental results obtained for shot-clay bentonite with the results of tests performed on poured/compacted samples of granular Wyoming bentonite with a similar apparent grain size distribution, prepared at various dry densities as presented in Chapters 2 and 3.

The dry density achieved by the shot-claying procedure (approximately  $1.15 \text{ Mg/m}^3$ ) was similar to the density that would be obtained if granular bentonite were simply poured on the ground (approximately  $1.2 \text{ Mg/m}^3$ ) but lower than the one that would be obtained using a granular material optimised to a Fuller distribution ( $1.5 \text{ Mg/m}^3$ ), as is foreseen for the use of granular bentonite as buffer material in accordance with the Swiss concept of high-level waste disposal (Plötze & Weber 2007). The lower dry density achieved by the shot-claying procedure is attributed to the fast swelling of the bentonite grains during mixing with water in the pump system, and it is strongly depending on the initial properties of the material and the amount of water added during shot-claying.

To compare the microstructural features associated with the different emplacement techniques, the results of an MIP test (in terms of *PSD*) on a poured granular bentonite sample (with a dry density of  $1.5 \text{ Mg/m}^3$ ) was compared to the *PSD* of the as-shot bentonite (Fig. 6.13). The comparison confirmed that the bentonite grains swell during mixing with water. Earlier in Chapter 3 (Section 3.4.4), it was mentioned that a maximum subdivision at the suction range would happen that bentonite achieved after mixing with water before shooting. This subdivision in smectite particles will result in an expansion of the aggregates and creation of a new level of porosity as seen in Fig. 6.13.

This swelling resulted in the creation of larger void spaces particularly in the pore size range attributed to inter-bentonite grain pores. This structure also resulted in a lower dry density for the shot-clay. Evolution with time for the microstructural features of the shot-clay bentonite may be expected as a result of ageing effects (Delage et al. 2006).

The initial low dry density and high water content after shooting were also responsible for the reduced swelling potential of the bentonite of approximately 1 MPa. In Fig. 6.14, the swelling pressure measured in this study is compared with the results of swelling pressure tests carried out on granular bentonite compacted at various dry densities (Chapter 2). Interestingly, the

swelling pressure for the shot-clay bentonite fits the general exponential trend for the compacted material well. The outcome of this comparison suggests that the result of the emplacement technique on the behaviour of the material could be assessed directly by considering the dry density achieved in the shooting.

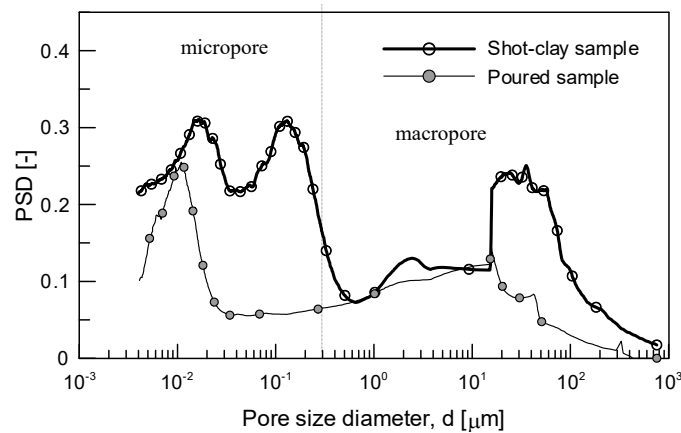


Fig. 6.13: Comparison between the results of the MIP test on a sample of shot-clay Wyoming bentonite and a sample of compacted granular Wyoming bentonite.

This tendency also seems to be confirmed by the results of the analysis of the retention properties of the materials. The retention behaviour of the shot-clay and the compacted Wyoming bentonite at different initial dry densities along drying paths are compared in Fig. 6.15. The retention behaviour observed in the controlled suction oedometric test (point C) is also represented in this plot. The retention properties of the samples prepared by different emplacement techniques follow a unique trend for a wide range of total suction values, despite their different initial dry densities. This unique trend between the total suction and the water content was obtained for the domain governed by the adsorptive storage mechanism, according to which water is retained in the intra-aggregate pores (Salager et al. 2013). The effect of the emplacement technique can be observed in the reduced air-entry value for the shot-clay bentonite. This is a direct consequence of the lower initial dry density.

The controlled suction test provided informations on the hydro-mechanical behaviour of the material under various loading conditions. The most severe changes in strain and water content were associated with drying during the ventilation phase. The test also highlighted the tendency of the material to crack during the drying step at a relative humidity of 50 %, which is typical for GTS in the winter. The shot-clay bentonite showed, however, good self-sealing properties once full saturation was attained. The formation of drying cracks at the imposed relative humidity could be a consequence of the low emplacement dry density (Kleppe & Olson 1985, Péron et al. 2009).

Based on the above discussion, it can be concluded that the shot-clay emplacement technique does not change the overall behaviour of the granular Wyoming bentonite, except that the low initial dry density leads to a reduced swelling capacity, a reduced air-entry value and an increasing tendency to form drying cracks compared to the compacted Wyoming bentonite. The dry density achieved with the shot-clay technique can be improved by optimising the original granular bentonite material and reducing the amount of water added during shot-claying (Koch 2002). The laboratory test results show that the final density (after full saturation under constrained conditions) can be improved considerably by ventilating the tunnel at  $RH = 50\%$ , but the results also show that post-compaction of the material has little impact on the final density.

Overall, the shot-clay technique has a high potential to achieve the final dry density of 1.4 g/cm<sup>3</sup> for Wyoming bentonite, which was the target density in this experiment. However, the shot-clay application of the bentonite on the tunnel surface, which permits free swelling, may be more limited than the application into a closed volume, as performed by Dixon et al. (2011), because in that case, the early swelling of the material is limited by the confined volume of the back-filled void space.

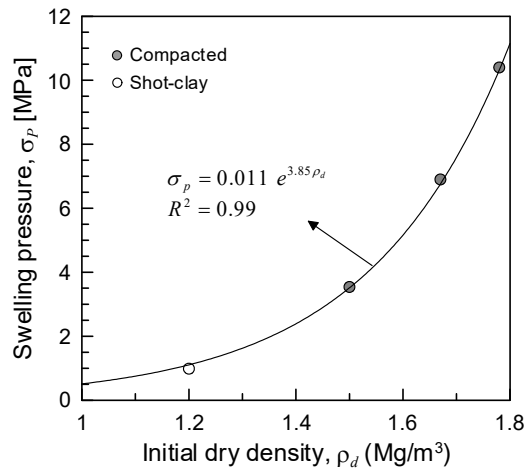


Fig. 6.14: Swelling pressure vs. initial dry density under constant volume conditions for compacted and shot-clay Wyoming bentonite samples.

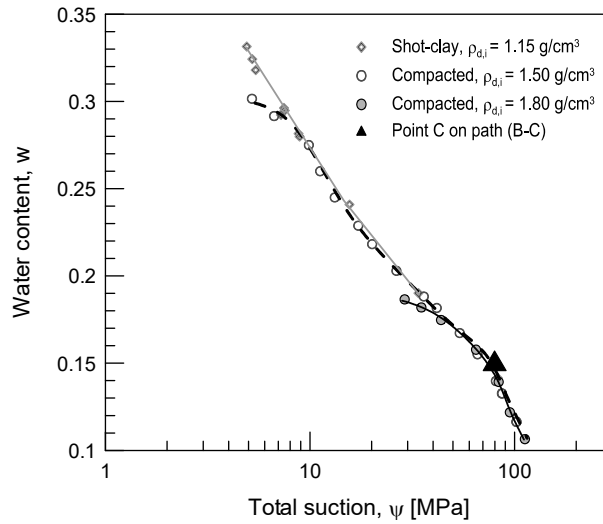


Fig. 6.15: Comparison of the retention behaviour of shot-clay and the compacted Wyoming bentonite compacted at different initial dry densities.

Point C recorded during the hydro-mechanical stress path is also shown;  $\rho_{d, i}$  is the initial dry density.



## 7 Conclusions and perspective

### 7.1 Conclusions

The present study was aimed at understanding and characterising the behaviour of Wyoming granular bentonite subjected to thermo-hydro-mechanical loading conditions with an application to the disposal of high-level radioactive waste in Switzerland. To achieve this goal, comprehensive multi-scale experimental activities and theoretical developments were combined. The present research was conducted in three main directions related to the macroscopic behaviour, microstructural observations and constitutive modelling. The following section presents these directions and their contributions towards understanding and analysing the behaviour of granular bentonite in high-level radioactive waste repositories.

#### (i) Characterisation of the macroscopic behaviour

Due to the lack of experimental data on the macroscopic behaviour of Wyoming granular bentonite, a systematic method was used to assess the thermo-hydro-mechanical behaviour of the material under different stress paths. A reference grain size distribution for the granular material was selected and the influence of hydro-mechanical loading conditions on the grain size distribution was evaluated. After determination of the index properties, the swelling pressure behaviour was evaluated at different compact states and under constant volume conditions. The swelling potential of the material in terms of void ratio variations versus total suction was investigated. The compressibility behaviour of the material was assessed under saturated and unsaturated conditions.

A comprehensive analysis of the water retention behaviour of the material was conducted by developing the 'Micro-cell' technique. The influence of the void ratio, confinement and wetting and drying cycles was analysed using a systematic protocol. The technique involved an accurate control of the degree of saturation under constant volume conditions and the measurement of the total suction after equalisation upon hydration/dehydration in a hydraulic path. In this manner, the evolution of the buffer material was determined in relation to swelling mechanisms, density redistribution and wetting/drying cycles. These primary analyses provided a sound basis for developing new methodologies for further investigation using a triaxial testing system. After developing/calibrating an advanced double-wall triaxial testing system, the THM triaxial behaviour of compacted granular bentonite was investigated. The isothermal isotropic and thermally induced strain – stress responses of the saturated and unsaturated buffer material were analysed. Deviatoric behaviour was evaluated under wide ranges of total suction, confining stresses and temperatures according to the repository conditions. The influence of the hydraulic gradient and temperature on the hydraulic conductivity of the saturated buffer materials was determined. These experimental activities provided a global picture of the thermo-hydro-mechanical evolution of Wyoming granular bentonite under repository-like conditions.

#### (ii) Characterisation of the microscopic behaviour

In the light of the microstructural investigation techniques (MIP, SEM and FIB-*nt*), the evolution of the microstructure of compacted granular bentonites was determined. The Micro-cell technique allowed representative samples to be collected for microstructural investigation at different stages of the imposed hydraulic stress paths. In this way, it enabled the evolution of the retention behaviour to be associated with the microstructural modifications during wetting and drying cycles. Further work was carried out to integrate the information on the hydration mechanisms of smectite clay, by comparing results of the macroscopic behaviour of the material

at a particle level with the physical phenomena at a microscopic level. Further investigation has been carried out concerning the interaction between the microstructure and water retention behaviour by analysing the behaviour of bentonite and illite clays. The integration of the hydration mechanisms of smectite particles into the macroscopic response of bentonite material exhibits an important aspect of the hydro-mechanical analysis of the buffer barriers.

### **(iii) Constitutive Modelling**

Following the experimental characterisation of the granular bentonite, a conceptual water retention model was developed to account for the change of void ratio and the microstructural evolutions during the hydration of the bentonite material. The model was established based on an elasto-plasticity approach that uses a linear anisotropic hardening rule. The exponential evolution of the air-entry value with the void ratio is taken into account for the mathematical formulations. The model produces the water retention curves for the entire hydraulic domain under a constant void ratio. The scanning behaviour at a given compaction state is analysed by considering the microstructural void ratio at different saturation stages. This process is an essential contribution to the constitutive modelling of high-swelling geomaterials.

## **7.2 Outlook for future works**

Particular emphasis is placed on the applications of the Micro-cell where there is still room for the further development to assess the behavioural features of high-swelling geomaterials.

Important improvements to the Micro-cell technique can be made by the installation of internal thin pressure transducers inside the cell to measure the swelling pressures that develop in a hydration path. In this way, the simultaneous measurement of the swelling pressure along with the total suction and degree of saturation would be possible using the procedure described in Chapter 2. It is thus possible to produce characteristic curves of swelling pressure versus total suction for a given compaction state. Application of such pressure transducers would also identify the points along a drying path at which the material at lower compaction densities will lose the contact with the cell walls due to the shrinkage process.

An increase in the capacity of the dew-point potentiometer system for higher temperatures provides an application for the Micro-cell technique for the determination of water retention curves at temperatures higher than the current limit (up to 40 °C). This application would result in the fast and precise determination of the water retention capacity compared to the controlled total suction techniques. The assessment of the hydro-mechanical coupling features in the swelling bentonite materials would be possible by application of mechanical loads at different hydraulic stages along the water retention domain. This would be practically possible by designing adaptive lids for the Micro-cell to maintain constant volume conditions and initiate a hydraulic path after the application of mechanical loadings at a certain point along the water retention domain.

Concerning the investigation of the fabric of the bentonite material using MIP and SEM data, further observations concerning the influence of the initial water content on the microstructure and its mutual interaction with the water retention behaviour could be performed. Such observations would be required to assess the water retention capacity of the buffer material where it is emplaced at a higher degree of saturation than those upon the hygroscopic water content. Estimation of the microstructural evolution of the bentonite material at unconfined conditions and its connection to hydration at the particle level would be a matter of interest where the bentonite material is subjected to free swelling conditions. In addition, continuous particle evolution

during the hydration of the material under the application of techniques such as ESEM observations at varying levels of relative humidity would provide informations on the evolution of the particle arrangement and porosity distribution at different hydraulic states in which the water is still preserved within the material during the observations.

Improvement of the water retention model for the hydro-mechanical coupling provided by additional experimental data using the Micro-cell technique would be feasible. In addition, the influence of temperature on the water retention model could be assessed. To this end, more experimental data concerning the influence of temperature on water retention and the microstructural void ratio are required. The water retention model can be further developed by introducing a new hardening yield surface to account for the cyclical behaviour of the material after first wetting and drying.

The impact of high temperatures on the water retention behaviour of Wyoming bentonite could be further analysed in order to consider the application of the material in the near field. This influence was already mentioned due to the illitisation process, which may have a significant impact on the hydro-mechanical response of the material in terms of water retention and swelling behaviour.

In terms of triaxial testing, in addition to the application of further stress paths such as undrained deviatoric testing on saturated samples or other stress paths, rather the triaxial compression, the influence of the mineralogical alterations on the shearing strength parameters could be analysed at high temperatures of up to 150 °C using the triaxial cell introduced in this study.

Finally, the water retention model developed in this study could be introduced into an elastoplastic framework. Such models can be further implemented into a finite element code for the solution of boundary value issues related to the application of the bentonite material in barriers of waste disposal.



## 8 Referenzverzeichnis

- Abuel-Naga, H.M., Bergado, D.T., Bouazza, A. & Ramana, G.V. (2007): Volume change behaviour of saturated clays under drained heating conditions: experimental results and constitutive modeling. *Canadian Geotechnical Journal* 44/8, 942-956.
- Airò Farulla, C., Ferrari, A. & Romero, E. (2010): Volume change behaviour of a compacted scaly clay during cyclic suction changes. *Canadian Geotechnical Journal* 47/6, 688-703.
- Aitchison, G.D., Russam, K. & Richards, B.G. (1965): Engineering concepts of moisture equilibrium and moisture changes in soils. *In: Moisture Equilibrium and Moisture Changes in Soils Beneath Covered Areas*. Butterworth, Sydney, Australia, 7-21.
- Alonso, E.E., Gens, A. & Josa, A. (1990): A constitutive model for partially saturated soils. *Géotechnique* 40/3, 405-430.
- Alonso, E.E. Vaunat, J. & Gens, A. (1999): Modelling the mechanical behaviour of expansive clays. *Engineering Geology* 54/1, 173-183.
- Alonso, E.E., Pereira, J.M., Vaunat, J. & Olivella, S. (2010): A microstructurally based effective stress for unsaturated soils. *Géotechnique* 60/12, 913-925.
- Alpan, I. (1967): The empirical evaluation of the coefficient  $k_o$  and  $k_{or}$ . *Soil and foundation* 7/1, 31-40.
- Alsherif, N. A., & McCartney, J. S. (2013): Triaxial cell for nonisothermal shear strength of compacted silt under high suction magnitudes. *Pan-Am Unsaturated Soils*, 147.
- Al-Mukhtar, M., Qi, Y., Alcover, J.F. & Bergaya, F. (1999): Oedometric and water-retention behaviour of highly compacted unsaturated smectites. *Canadian Geotechnical Journal* 36/4, 675-684.
- Arifin, Y.F. (2008): Thermo-hydro-mechanical behavior of compacted bentonite sand mixtures: an experimental study. PhD thesis. Bauhaus-University Weimar.
- Arifin, Y.F. & Schanz, T. (2009): Osmotic suction of highly plastic clays. *Acta Geotechnica* 4/3, 177-191.
- ASTM D4318-10 (2010): Standard test methods for liquid limit, plastic limit and plasticity index of soils.
- ASTM D5298-94 (1994): Standard test method for measurement of soil potential (suction) using filter paper.
- ASTM D698-07 (2007): Standard test methods for laboratory compaction characteristics of soil using standard effort ( $600 \text{ kN}\cdot\text{m}/\text{m}^3$ ).
- Aversa, S. & Nicotera, M.V. (2002): A triaxial and oedometer apparatus for testing unsaturated soils. *ASTM Spec. Technical Publication* 25/1, 3-15.
- Baille, W., Tripathy, S. & Schanz, T. (2010): Swelling pressures and one-dimensional compressibility behaviour of bentonite at large pressures. *Applied Clay Science* 48/3, 324-333.

- Baldi, G., Borsetto, M., Hueckel, T. & Tassoni, E. (1985): Thermally induced strains and pore pressure in clays. Proceedings of International Symposium on Environmental Geotechnology, Allentown, PA, 391-402.
- Baldi, G., Hueckel, T. & Pellegrini, R. (1988): Thermal volume change of the mineral-water system in low-porosity clay soils. Canadian Geotechnical Journal 25/4, 807-825.
- Barbour, S.L. & Fredlund, D.G. (1989): Mechanisms of osmotic flow and volume change in clay soils. Canadian Geotechnical Journal 26, 551-562.
- Barden, L. & Sides, G.R. (1970): Engineering behaviour and structure of compacted clay. Journal of Soil Mechanics & Foundations Division 96/SM4, 1171-1197.
- Bestel, M. (2014): Water-montmorillonite systems: Neutron scattering and tracer through diffusion studies. PhD Thesis Paul Scherrer Institute, Villigen, Switzerland.
- Bishop, A.W. & Donald, I.B. (1961): The experimental study of partly saturated soil in the triaxial apparatus. Proceedings of the 5th International Conference on Soil Mechanics and Foundation Engineering, Paris 1, 13-21.
- Blatz, J. & Graham, J. (2003): Elasto-plastic modelling of unsaturated soils using the results from a new triaxial test with controlled suction. Géotechnique 53/1, 113-122.
- Blatz, J.A., Graham, J. & Chandler, N.A. (2002): Influence of suction on the strength and stiffness of compacted sand bentonite. Canadian Geotechnical Journal 39/5, 1005-1015.
- Blatz, A.J., Cui, Y.J. & Oldecop, L.A. (2008): Vapour equilibrium and osmotic technique for suction control. Geotech. Geol. Eng. 26/6, 661-673.
- Bocking, K.A. & Fredlund, D.G. (1980): Limitations of the axis translation technique. Expansive Soils, 117-135. ASCE.
- Bolt, G.H. (1955): Analysis of the validity of the Gouy–Chapman theory of the electric double layer. Journal of Colloidal Science 10, 206.
- Bolt, G.H. (1956): Physico-chemical analysis of the compressibility of pure clays. Géotechnique 6/2, 86-93.
- BSI (1990): Methods of test for soils for civil engineering purposes: Classification tests (Atterberg Limit). British Standard Institution (BSI), BS 1377-2.
- Bucher, F. & Mayor, P.A. (1989): Medium-scale experiments on highly compacted bentonites. Proc. 12<sup>th</sup> Int. Conf. Soil. Mech. Found. Engng, Rio de Janeiro 1, 583-585.
- Bucher, F. & Müller-Vonmoos, M. (1989): Bentonite as a containment barrier for the disposal of highly radioactive waste. Applied Clay Science 4/2, 157-177.
- Campanella, R.G. & Mitchell, J.K. (1968): Influence of temperature variations on soil behavior. J. Soil Mech. Found. Div. 94/3, 709-734.
- Cardoso, R., Romero, E., Lima, A. & Ferrari, A. (2007): A comparative study of soil suction measurement using two different high-range psychrometers. In: Schanz, T. (ed.): 2<sup>nd</sup> Int. Conf. on Mech. of Unsat. Soils, Weimar, Germany, 79-93. Springer, Berlin.

- Cekerevac, C. (2003): Thermal effects on the mechanical behaviour of saturated clays: an experimental and constitutive study. Doctoral dissertation, Thèse de doctorat, Ecole Polytechnique Fédérale de Lausanne.
- Cekerevac, C. & Laloui, L. (2004): Experimental study of thermal effects on the mechanical behaviour of a clay. *International Journal for Numerical and Analytical Methods in Geomechanics* 28/3, 209-228.
- Cekerevac, C. & Laloui, L. (2010): Experimental analysis of the cyclic behaviour of kaolin at high temperature. *Géotechnique* 60/8, 651-655.
- Cekerevac, C., Laloui, L. & Vulliet, L. (2005): A novel triaxial apparatus for thermo-mechanical testing of soils. *ASTM Geotechnical Testing Journal* 28/2, 161-170.
- Chapman, D.L. (1913): A contribution to the theory of electrocapillarity. *Philosophical Magazine* 25, 475-481.
- Collins, K.T. & McGown, A. (1974): The form and function of microfabric features in a variety of natural soils. *Géotechnique* 24/2, 223-254.
- Cui, Y. J., Sultan, N. & Delage, P. (2000): A thermomechanical model for saturated clays. *Canadian Geotechnical Journal* 37/3, 607-620.
- Cuisinier, O. & Masrouri, F. (2005): Hydromechanical behaviour of a compacted swelling soil over a wide suction range. *Engineering Geology* 81/3, 204-212.
- De la Fuente, S., Cuadros, J., Fiore, S. & Linares, J. (2000): Electron microscopy study of volcanic tuff alteration to illite-smectite under hydrothermal conditions. *Clays and Clay Minerals* 48/3, 339-350.
- De Las Cuevas, C. (1997): Pore structure characterization in rock salt. *Engineering Geology* 47/1, 17-30.
- Decagon Device Inc. (2002): Dewpoint PotentialMeter: Operators Manual Version 2.1.
- Del Olmo, C., Fioravante, V., Gera, F., Hueckel, T., Mayor, J.C. & Pellegrini, R. (1996): Thermomechanical properties of deep argillaceous formations. *Engineering Geology* 41/1-4, 87-101.
- Delage, P. (2007): Microstructure features in the behaviour of engineered barriers for nuclear waste disposal. *In: Experimental Unsaturated Soil Mechanics* (pp. 11-32). Springer Berlin Heidelberg.
- Delage, P., Howat, M.D. & Cui, Y.J. (1998): The relationship between suction and swelling properties in a heavily compacted unsaturated clay. *Engineering Geology* 50/1, 31-48.
- Delage, P., Sultan, N. & Cui, Y.J. (2000): On the thermal consolidation of Boom clay. *Canadian Geotechnical Journal* 37/2, 343-354.
- Delage, P., Marcial, D., Cui, Y.J. & Ruiz, X. (2006): Ageing effects in a compacted bentonite: a microstructure approach. *Géotechnique* 56/5, 291-304.

- Delage, P., Schroeder, C. & Cui, Y.J. (2008): Subsidence and capillary effects in chalks. arXiv preprint arXiv:0803.1308.
- Dixon, D., Sandén, T., Jonsson, E. & Hansen, J. (2011): Backfilling of deposition tunnels: Use of bentonite pellets. Clay Technology AB, Swedish Nuclear Fuel and Waste Management Co. P-11-44.
- Dueck, A. (2004): Hydro-mechanical properties of a water unsaturated sodium bentonite. Laboratory study and theoretical interpretation. PhD Thesis, Lund Institute of Technology, Sweden.
- Dusseault, M.B., Wang, Y. & Simmons, J.V. (1988): Induced stresses near a fireflood front. AOSTRa Journal of Research 4/2, 153-70.
- ENRESA (2000): Full-scale engineered barriers experiment for a deep geological repository for high level radioactive waste in crystalline host rock, FEBEX Project. ENRESA, Madrid.
- Ferrari, A. & Laloui, L. (2012): Advances in the Testing of the Hydro-mechanical Behaviour of Shales. *In: Multiphysical Testing of Soils and Shales*, 57-68. Springer Berlin Heidelberg.
- Ferrari, A., Seiphoori, A., Rüedi, J. & Laloui, L. (2014): Shot-clay MX-80 bentonite: an assessment of the hydro-mechanical behaviour. *Engineering Geology* 173, 10-18.
- Fleureau, J.-M., Verbrugge, J.-C., Huergo, P.J., Gomes Correia, A. & Kheirbek-Saoud, S. (2002): Aspects of the behaviour of compacted clayey soils on drying and wetting paths. *Canadian Geotechnical Journal* 39/6, 1341-1357.
- François, B. & Laloui, L. (2008): ACMEG-TS: A constitutive model for unsaturated soils under non-isothermal conditions. *International Journal for Numerical and Analytical Methods in Geomechanics* 32/16, 1955-1988.
- Fredlund, D.G., Morgenstern, N.R. & Widger, R.A. (1978): The shear strength of unsaturated soils. *Canadian Geotechnical Journal* 15/3, 313-321.
- Fredlund, D.G. & Rahardjo, H. (1993): *Soil mechanics for unsaturated soils*. John Wiley & Sons.
- Gachet, P., Klubertanz, G., Vulliet, L. & Laloui, L. (2003): Interfacial behavior of unsaturated soil with small-scale models and use of image processing techniques. *Geotechnical Testing Journal* 26/1, 12-21.
- Gallipoli, D., Wheeler, S. & Karstunen, M. (2003): Modelling the variation of degree of saturation in a deformable unsaturated soil. *Géotechnique* 53/1, 105-112.
- Garcia-Sineriz, J.L., Rey, M. & Mayor, J.C. (2008): The Engineered Barrier Experiment at Mont Terri Rock Laboratory. *Science & Technology* n° 334. Andra, Châtenay-Malabry.
- Gee, G., Campbell, M., Campbell, G. & Campbell, J. (1992): Rapid measurement of low soil potentials using a water activity meter. *Soil Science Society of America Journal* 56, 1068-1070.
- Geiser, F., Laloui, L. & Vulliet, L. (2006): Elasto-plasticity of unsaturated soils: laboratory test results on a remoulded silt. *Soils and foundations* 46/5, 545-556.

- Gens, A. (2010): Soil – environment interactions in geotechnical engineering. *Géotechnique* 60/1, 3-74.
- Gens, A. & Alonso, E.E. (1992): A framework for the behaviour of unsaturated expansive clays. *Canadian Geotechnical Journal* 29/6, 1013-1032.
- Gens, A., Garcia-Molina, A.J., Olivella, S., Alonso, E.E. & Huertas, F. (1998): Analysis of a full scale in situ test simulating repository conditions. *International Journal for Numerical and Analytical Methods in Geomechanics* 22, 515-548.
- Goldstein, J., Newbury, D.E., Joy, D.C., Lyman, C.E., Echlin, P., Lifshin, E., Sawyer, L. & Michael, J.R. (2003): *Scanning electron microscopy and X-ray microanalysis*. Springer.
- Gouy, G. (1910): Electric charge on the surface of an electrolyte. *Journal of Physics* 4/9, 457.
- Graham, J. & Blatz, J. (2000): A system for controlled suction in triaxial tests. *Géotechnique* 50/4, 465-470.
- Graham, J., Oswell, J.M. & Gray, M.N. (1992): The effective stress concept in saturated sand-clay buffer. *Canadian Geotechnical Journal* 29/6, 1033-1043.
- Graham, J., Saadat, F., Gray, M.N., Dixon, D.A. & Zhang, Q.Y. (1989): Strength and volume change behaviour of a sand-bentonite mixture. *Canadian Geotechnical Journal* 26/2, 292-305.
- Graham, J., Tanaka, N., Crilly, T. & Alfaro, M. (2001): Modified Cam-Clay modelling of temperature effects in clays. *Canadian Geotechnical Journal* 38/3, 608-621.
- Güven, N. (1990): Longevity of bentonite as buffer material in a nuclear-waste repository. *Engineering Geology* 28/3, 233-247.
- Hancox, W.T. (1986): Progress in the Canadian nuclear fuel waste management program. *Proceedings 2<sup>nd</sup> International Conference on Radioactive Waste Management*, Winnipeg, Man., 1-9.
- Head, K.H. & Epps, R. (1980): *Manual of soil laboratory testing* 1, 291-298. Pentech Press, London.
- Henkel, D.J. & Gilbert, G.D. (1952): The effect measured of the rubber membrane on the triaxial compression strength of clay samples. *Geotechnique* 3/1, 20-29.
- Hoffmann, C., Alonso, E.E. & Romero, E. (2007): Hydro-mechanical behaviour of bentonite pellet mixtures. *Physics and Chemistry of the Earth* 32/8, 832-849.
- Holzer, L., Münch, B., Rizzi, M., Wepf, R., Marschall, P. & Graule, T. (2010): 3D-microstructure analysis of hydrated bentonite with cryo-stabilized pore water. *Applied Clay Science* 47, 330-342.
- Hueckel, T. (1992): On effective stress concepts and deformation in clays subjected to environmental loads: Discussion. *Canadian Geotechnical Journal* 29/6, 1120-1125.
- Houston, S.L., Houston, W.N. & Wagner, A. (1994): Laboratory filter paper suction measurements. *Geotechnical Testing Journal* 17/2, 185-194.

- Hudson, J.A. & Harrison, J.P. (1997): Engineering rock mechanics: an introduction to the principles. Pergamon, Oxford.
- Hueckel, T. (1992): On effective stress concepts and deformation in clays subjected to environmental loads: Discussion. Canadian Geotechnical Journal 29/6, 1120-1125.
- Hueckel, T. & Baldi, G. (1990): Thermoplasticity of saturated clays: experimental constitutive study. Journal of Geotechnical Engineering 116/12, 1778-1796.
- Hueckel, T., Francois, B. & Laloui, L. (2009): Explaining thermal failure in saturated clays. Géotechnique 59/3, 197.
- Jaky, J. (1944): The coefficient of earth pressure at rest. Journal of the Society of Hungarian Architects and Engineers 78/22, 355-358.
- Juang, C.H. & Holtz, R.D. (1986): A probabilistic permeability model and the pore size density function. International Journal for Numerical and Analytical Methods in Geomechanics 10/5, 543-553.
- Karland, O., Nilsson, U., Weber, H. & Wersin, P. (2008): Sealing ability of Wyoming bentonite pellets foreseen as buffer material – laboratory results. Physics and Chemistry of the Earth, Parts A/B/C, 33, S472-S475.
- Kassiff, G. & Shalom, A.B. (1971): Experimental relationship between swell pressure and suction. Géotechnique 21/3, 245-255.
- Kaufhold, S., Plötze, M., Klinkenberg, M. & Dohrmann, R. (2013): Density and porosity of bentonites. Journal of Porous Materials 20/1, 191-208.
- Kawai, K., Kato, S., Karube, D., Rahardjo, H., Toll, D.G. & Leong, E.C. (2000): The model of water retention curve considering effects of void ratio. *In*: Unsaturated soils for Asia. Proceedings of the Asian Conference on Unsaturated Soils, UNSAT-Asia 2000, Singapore, 18-19 May, 2000, 329-334. AA Balkema.
- Keller, L.M., Seiphoori, A., Gasser, P., Lucas, F., Holzer, L. & Ferrari, A. (2014): The pore structure of compacted and partly saturated MX-80 bentonite at different dry densities. Clays and Clay Minerals 62/3, 174-187.
- Kleppe, J.H. & Olson, R.E. (1985): Desiccation cracking of soil barriers. Hydraulic barriers in soil and rock, ASTM STP 874, 263-275.
- Koch, D. (2002): Bentonites as a basic material for technical base liners and site encapsulation cut-off walls. Applied Clay Science 21/1, 1-11.
- Komine, H. & Ogata, N. (1994): Experimental study on swelling characteristics of compacted bentonite. Canadian Geotechnical Journal 31/4, 478-490.
- Komine, H. & Ogata, N. (1996): Prediction for swelling characteristics of compacted bentonite. Canadian Geotechnical Journal 33, 11-22.
- Kuntiwattanukul, P., Towhata, I., Ohishi, K. & Seko, I. (1995): Temperature effects on undrained shear characteristics of clay. Soils and foundations 35/1, 147-162.

- Ladd, C.C. (1977): Stress-deformation and strength characteristics, state of the art report. Proceedings of 9<sup>th</sup> ISFMFE 4, 421-494.
- Laloui, L., Moreni, M. & Vulliet, L. (2003): Behaviour of a dual-purpose pile as foundation and heat exchanger. Canadian Geotechnical Journal 40/2, 388-402.
- Laloui, L., Peron, H., Geiser, F., Rifa'i, A. & Vulliet, L. (2006): Advances in volume measurement in unsaturated soil triaxial tests. Soils and Foundations 46/3, 341-349.
- Lambe, T.W. & Whitman, R.V. (1979): Soil mechanics. Wiley & Sons, New York, 29-39.
- Lawrence, G.P. (1977): Measurement of pore sizes in fine-textured soils: a review of existing techniques. Journal of Soil Science 28/4, 527-540.
- Leong, E.-C., Tripathy, S. & Rahardjo, H. (2003): Total suction measurement of unsaturated soils with a device using the chilled-mirror dew point technique. Géotechnique 53/2, 173-182.
- Leong, E.C., Nyunt, T.T. & Rahardjo, H. (2012): Triaxial testing of unsaturated soils. Multi-physical Testing of Soils and Shales, 33-44. Springer Berlin Heidelberg.
- Leupin, O.X. (ed.), Birgersson, M., Karnland, O., Korkeakoski, P., Sellin, P., Mäder U.K. & Wersin, P. (2014): Montmorillonite stability under nearfield conditions. Nagra Tech. Report NTB 14-12. Nagra, Wettingen.
- Leupin, O.X., Smith, P., Marschall, P., Johnson, L., Savage, D., Cloet, V., Schneider, J. (2016): High-level waste repository-induced effects. Nagra Tech. Report NTB 14-13. Nagra, Wettingen.
- Lide, D.R. (ed.) (2004): CRC Handbook of Chemistry and Physics 2004-2005: A Ready-Reference Book of Chemical and Physical Data. CRC press.
- Lingnau, B.E., Graham, J., Yarechewski, D., Tanaka, N. & Gray, M.N. (1996): Effects of temperature on strength and compressibility of sand-bentonite buffer. Engineering Geology 41/1, 103-115.
- Lloret, A., Villar, M.V., Sánchez, M., Gens, A., Pintado, X. & Alonso, E.E. (2003): Mechanical behaviour of heavily compacted bentonite under high suction changes. Géotechnique 53/1, 27-40.
- Lu, N. & Likos, W.J. (2004): Unsaturated soil mechanics. J. Wiley.
- Ma, C. & Hueckel, T. (1993): Thermomechanical effects on adsorbed water in clays around a heat source. International Journal for Numerical and Analytical Methods in Geomechanics 17/3, 175-196.
- Maatouk, A., Leroueil, S. & Rochelle, P.L. (1995): Yielding and critical state of collapsible unsaturated silty soil. Géotechnique 45/3, 465-477.
- Madsen, F.T. & Müller-Vonmoos, M. (1985): Swelling pressure calculated from mineralogical properties of a Jurassic Opalinus shale, Switzerland. Clays and Clay Minerals 33, 501-509.

- Marcial, D., Delage, P. & Cui, Y.J. (2002): On the high stress compression of bentonites. Canadian Geotechnical Journal 39/4, 812-820.
- Mašin, D. (2010): Predicting the dependency of a degree of saturation on void ratio and suction using effective stress principle for unsaturated soils. International Journal for Numerical and Analytical Methods in Geomechanics 34, 73-90.
- Mbonimpa, M., Aubertin, M., Maqsood, A. & Bussière, B. (2006): Predictive model for the water retention curve of deformable clayey soils. Journal of Geotechnical and Geoenvironmental Engineering 132, 1121-1132.
- Miller, C.J., Yesiller, N., Yaldo, K. & Merayyan, S. (2002): Impact of soil type and compaction conditions on soil water characteristic. Journal of Geotechnical and Geoenvironmental Engineering 128, 733-742.
- Minon, S. (2009): Microstructural studies in geomaterials. EPFL Master thesis.
- Mitchell, J.K. (1993): Fundamentals of soil behaviour. Second Edition, John Wiley and Sons, Inc. New York.
- Mitchell, J.K. & Soga, K. (2005): Fundamentals of soil behaviour. Third edition, Wiley.
- Montanez, J.E.C. (2002): Suction and volume changes of compacted sand-bentonite mixtures. Ph.D Thesis, Univ. of London (Imperial College of Science).
- Moritz, L. (1995): Geotechnical properties of clay at elevated temperatures. Report 47. Swedish Geotechnical Institute, Linköping.
- Müller-Vonmoos, M. & Kahr, G. (1983): Mineralogische Untersuchungen von Wyoming Bentonit MX-80 und Montigel. Nagra Tech. Report NTB 83-12. Nagra, Wettingen.
- Nagra (2002): Project Opalinus Clay: Safety report: Demonstration of disposal feasibility for spent fuel, vitrified high-level waste and long-lived intermediate-level waste (Entsorgungsnachweis). Nagra Tech. Report NTB 02-05. Nagra, Wettingen.
- Nagra (2003): Engineered barrier emplacement experiment in Opalinus Clay (EB). Granular Material Emplacement QA Report with Emplacement Description. Deliverable D12 of the EB Project.
- Nagra (2004): Effects of Post-disposal Gas Generation in a Repository for Spent Fuel, High-level Waste and Long-lived Intermediate Level Waste Sited in Opalinus Clay. Nagra Tech. Report NTB 04-06. Nagra, Wettingen.
- Nagra (2008): Effects of post-disposal gas generation in a repository for low- and intermediate-level waste sited in the Opalinus Clay of Northern Switzerland. Nagra Tech. Report NTB 08-07. Nagra, Wettingen.
- Nagra (2009): The Nagra Research, Development and Demonstration (RD&D) Plan for the Disposal of Radioactive Waste in Switzerland. Nagra Tech. Report NTB 09-06. Nagra, Wettingen.

- Nagra (2014): SGT Etappe 2: Vorschlag weiter zu untersuchender geologischer Standortgebiete mit zugehörigen Standortarealen für die Oberflächenanlage – Geologische Grundlagen. Nagra Tech. Rep. NTB 14-02. Nagra, Wettingen.
- Norrish, K. (1954): The swelling of montmorillonite. *Discussions of the Faraday society* 18, 120-134.
- Nowamooz, H. & Masrouri, F. (2009): Density-dependent hydromechanical behaviour of a compacted expansive soil. *Engineering Geology* 106/3, 105-115.
- Nowamooz, H., Jahangir, E. & Masrouri, F. (2012): Volume change behaviour of a swelling soil compacted at different initial states. *Engineering Geology* 153, 25-34.
- Nuth, M. & Laloui, L. (2008): Advances in modelling hysteretic water retention curve in deformable soils. *Computers and Geotechnics* 35/6, 835-844.
- Olson, K.R. (1985): Characterization of pore size distributions within soils by mercury intrusion and water-release methods. *Soil Science* 139/ 5, 400-404.
- Parent, S.E., Abdolazadeh, A.M., Nuth, M. & Cabral, A.R. (2011): Hydraulic conductivity and water retention curve of highly compressible materials. *In: Dikinya, O. (ed.): Developments in hydraulic conductivity research. In-Tech.*, 71-110.
- Péron, H., Hueckel, T. & Laloui, L. (2007): An improved volume measurement for determining soil water retention curves. *Geotechnical Testing Journal* 30/1, 1-7.
- Péron, H., Hueckel, T., Laloui, L. & Hu, L. (2009): Fundamentals of desiccation cracking of fine-grained soils: experimental characterisation and mechanisms identification. *Canadian Geotechnical Journal* 46/10, 1177-1201.
- Pintado, X., Lloret, A. & Romero, E. (2009): Assessment of the use of the vapour equilibrium technique in controlled-suction tests. *Canadian Geotechnical Journal* 46/4, 411-423.
- Plötze, M. & Weber, H.P. (2007): ESDRED: Emplacement tests with granular bentonite Wyoming. Laboratory results from ETH Zürich. Nagra Arbeitsber. NAB 07-24. Nagra, Wettingen.
- Puiša, R. & Belevičius, R. (2005): Grading the PVC material by solving a static inverse problem with genetic algorithm. *Mechanika* 2/52.
- Pusch, R. (1992): Use of bentonite for isolation of radioactive waste products. *Clay Minerals* 27, 353-361.
- Pusch, R. (1994): Waste disposal in rock. *Developments in Geotechnical Engineering* 76. Elsevier Publ. Co. ISBN: 0:444-89449-7.
- Pusch, R. (2000): On the effect of hot water vapor on MX-80 clay. SKB TR-00-16. Swedish Nuclear Fuel and Waste Management Co., Stockholm.
- Pusch, R. & Güven, N. (1990): Electron microscopic examination of hydrothermally treated bentonite clay. *Engineering Geology* 28/3, 303-314.

- Pusch, R. & Karnland, O. (1996): Physicochemical stability of smectite clays. *Engineering Geology* 41/1, 73-85.
- Pusch, R. & Schomburg, J. (1999): Impact of microstructure on the hydraulic conductivity of undisturbed and artificially prepared smectitic clay. *Engineering Geology* 54/1, 167-172.
- Pusch, R. & Yong, R.N. (2006): *Microstructure of smectite clays and engineering performance*. Taylor & Francis, London and New York. ISBN10: 0-415-36863-4.1.
- Pusch, R., Karnland, O. & Hokmark, H. (1990): GMM – a general microstructural model for qualitative and quantitative studies of smectite clays. SKB Technical Report 90-43. Swedish Nuclear Fuel and Waste Management Co., Stockholm.
- Pusch, R., Bluemling, P. & Johnson, L. (2003): Performance of strongly compressed MX-80 pellets under repository-like conditions. *Applied Clay Science* 23, 239-244.
- Reeves, G.M., Sims, I. & Cripps, J.C. (2006): Clay materials used in construction. Geological Society, London, *Engineering Geology Special Publication* 21, 15.
- Richards, L.A. (1941): A pressure-membrane extraction apparatus for soil solution. *Soil Science* 51/5, 377-386.
- Ridley, A.M. (1993): The measurement of soil moisture suction. PhD Thesis. Univ. of London.
- Romero, E. (1999): Characterisation and thermo-hydro-mechanical behaviour of unsaturated boom clay: experimental study. Ph.D. Thesis, Universitat Politècnica de Catalunya, Barcelona, 405 pp.
- Romero, E. (2001): Controlled-suction techniques. *In: Gehling, W.Y.Y. & Schnaid, F. (eds.): 4º Simpósio Brasileiro de Solos Não Saturados*. Porto Alegre, Brazil, 533-542.
- Romero, E. (2013): A microstructural insight into compacted clayey soils and their hydraulic properties. *Engineering Geology* 165, 3-19.
- Romero, E. & Li, X.L. (2005): Thermo-hydro-mechanical tests using vapour and liquid transfer on a clay-based mixture. *In: Tarantino, A., Romero, E. & Cui, Y.J. (eds.): Advanced Experimental Unsaturated Soil Mechanics*, 483-488. Taylor and Francis Group, London.
- Romero, E. & Simms, P.H. (2008): Microstructure investigation in unsaturated soils: a review with special attention to contribution of mercury intrusion porosimetry and environmental scanning electron microscopy. *Geotechnical and Geological Engineering* 26/6, 705-727.
- Romero, E. & Vaunat, J. (2000): Retention curves of deformable clays. *In: Tarantino, A. & Mancuso, C. (eds.): Experimental evidence and theoretical approaches in unsaturated soils*. Proceedings of an international workshop on unsaturated soils, Trento, Italy, 91-106. A.A. Balkema, Rotterdam.
- Romero, E., Facio, J.A., Lloret, A., Gens, A. & Alonso, E.E. (1997): A new suction and temperature controlled triaxial apparatus. Proceedings of the International Conference on Soil Mechanics and Foundation Engineering – International Society for Soil Mechanics and Foundation Engineering 1, 185-188.

- Romero, E., DellaVecchia, G. & Jommi, C. (2011): An insight into the water retention properties of compacted clayey soils. *Géotechnique* 61/4, 313-328.
- Romero, E.E., Musso, G. & Jommi, C. (2012): Experimental techniques for multi-scale description of soil fabric and its dual pore network. ALERT Doctoral School, 125-150.
- Rometsch, R., Issler, H., McCombie, C. & Thury, M. (1985): Project Gewähr 1985: Nuclear waste management in Switzerland: Feasibility studies and safety analyses. Nagra Project Report NGB 85-09. Nagra, Wettingen.
- Saiyouri, N., Hicher, P.Y. & Tessier, D. (1998): Microstructural analysis of highly compacted clay swelling. Proceedings of the 2<sup>nd</sup> International Conference on Unsaturated Soils, Beijing 1, 119-124.
- Saiyouri, N., Hicher, P.Y. & Tessier, D. (2004): Experimental study of swelling in unsaturated compacted clays. *Clay Minerals* 39/4, 469-479.
- Salager, S., Ferrari, A. & Laloui, L. (2010): New experimental tools for the characterization of highly overconsolidated clayey materials in unsaturated conditions. *In*: Laloui, L. (ed.): Mechanics of unsaturated geomaterials, 29-51, John Wiley & Sons.
- Salager, S., Rizzi, M., & Laloui, L. (2011): An innovative device for determining the soil water retention curve under high suction at different temperatures. *Acta Geotechnica* 6/3, 135-142.
- Salager, S., Nuth, M., Ferrari, A. & Laloui, L. (2013): Investigation into water retention behaviour of deformable soils. *Canadian Geotechnical Journal* 50/2, 200-208.
- Santamarina, J.C., Klein, K.A., Wang, Y.H. & Prencke, E. (2002): Specific surface: determination and relevance. *Canadian Geotechnical Journal* 39, 233-241. DOI: 10.1139/T01-077.
- Savvidou, C. & Britto, A.M. (1995): Numerical and experimental investigation of thermally induced effects in saturated clay. *Soils and Foundation* 35/1, 37-44.
- Schanz, T., Arifin, Y.F., Khan, M.I. & Agus, S.S. (2010): Time effects on total suction of bentonites. *Soils and foundations* 50/2, 195-202.
- Seiphoori, A. (2014): Thermo-hydro-mechanical characterisation and modelling of MX-80 granular bentonite. Thèse EPFL, No. 6159. Ecole Polytechnique Fédérale de Lausanne.
- Seiphoori, A., Ferrari, A. & Laloui, L. (2011a): An advanced calibration process for a thermo-hydro-mechanical triaxial system. Proceedings International Symposium on Deformation Characteristics of Geomaterials, Séoul, South Korea, 396-403.
- Seiphoori A., Ferrari, A. & Laloui, L. (2013): Characterization of THM behaviour of compacted MX-80 granular bentonite using an advanced double-wall triaxial cell. International Workshop on Geomechanics and Energy, Lausanne, Switzerland.
- Seiphoori, A., Ferrari, A. & Laloui, L. (2014): Water retention behaviour and microstructural evolutions of MX-80 granular bentonite during wetting and drying episodes. *Géotechnique* 64/9, 721-734.

- Senger, R. & Ewing, J. (2008): Evolution of temperature and water content in the bentonite buffer: Detailed modelling of two-phase flow processes associated with the early closure period. Nagra Arbeitsber. NAB 08-32. Nagra, Wettingen.
- Sivakumar, V. (1993): A critical state framework for unsaturated soil. Doctoral dissertation, University of Sheffield.
- Sivakumar, R., Sivakumar, V., Blatz, J. & Vimalan, J. (2006): Twin-cell stress path apparatus for testing unsaturated soils, technical note. *Geotechnical Testing Journal* 29/2.
- Spanner, D.C. (1951): The Peltier effect and its use in the measurement of suction pressure. *Journal of Experimental Botany* 11, 145-168.
- Sposito, G. & Prost, R. (1982): Structure of water adsorbed on smectites. *Chemical Reviews* 82/6, 553-573.
- Sridharan, A. & Jayadeva, M.S. (1982): Double layer theory and compressibility of clays. *Géotechnique* 32/2, 133-144.
- Sridharan, A. & Rao, G.V. (1979): Shear strength behaviour of saturated clays and the role of the effective stress concept. *Géotechnique* 29/2, 177-193.
- Sugii, T., Yamada, K. & Kondou, T. (2002): Relationship between soil-water characteristic curve and void ratio. *In: Juca, J.F.T., de Campos, T.M.P. & Marinho, F.A.M. (eds.): Proceedings of the 3<sup>rd</sup> International Conference on Unsaturated Soils. Swets and Zeitlinger, Lisse 1, 209-214.*
- Sultan, N., Delage, P. & Cui, Y.J. (2002): Temperature effects on the volume change behaviour of Boom Clay. *Engineering Geology* 64/2-3, 135-145.
- Tang, A.M. & Cui, Y.J. (2005): Controlling suction by the vapour equilibrium technique at different temperatures and its application in determining the water retention properties of MX80 clay. *Canadian Geotechnical Journal* 42/1, 287-296.
- Tang, A.M., Cui, Y.J. & Barnel, N. (2008): Thermo-mechanical behaviour of a compacted swelling clay. *Canadian Geotechnical Journal* 44/3, 942-956.
- Tarantino, A. (2009): A water retention model for deformable soils. *Géotechnique* 59/9, 751-762.
- Tarantino, A. (2010): Basic concepts in the mechanics and hydraulics of unsaturated geomaterials. *In: Laloui, L. (ed.): Mechanics of unsaturated geomaterials, 3-28. Wiley, Hoboken, NJ.*
- Tarantino, A. & Tombolato, S. (2005): Coupling of hydraulic and mechanical behaviour in unsaturated compacted clay. *Géotechnique* 55/4, 307-317.
- Teodori, S.-P. (ed.), Gaus, I. (ed.), Köhler, S., Weber, H.-P., Rösli, U., Steiner, P., Trick, T., García Siñeriz, J.-L., Nussbaum, C., Wiczorek, K., Schuster, K. & Mayor, J.C. (2011): Long term performance of engineered barrier systems (PEBS). Mont Terri HG-E experiment: as-built report. Nagra Arbeitsber. NAB 11-25. Nagra, Wettingen.

- Teodori, S.-P., Rüedi, J., Spillmann, T., Reinhold, M., Trick, T., Keller, M., Steiner, P., Isler, S., Gräfe, K., García-Siñeriz, J.L., Palacios Jimenez, B., Jacobs, F., Maurer, H.R., Tisato, N., Marelli, S., Ferrari, A., Manca, D. & Seiphooori, A. (2013): GAST (Gas-Permeable Seal Test) pre-testing report. Nagra Arbeitsber. NAB 12-58. Nagra, Wettingen.
- Tessier, D., Lajudie, A. & Petit, J.C. (1992): Relation between the macroscopic behavior of clays and their microstructural properties. *Applied Geochemistry* 7, 151-161.
- Toyota, H., Sakai, N. & Nishimura, T. (2001): Effects of stress history due to unsaturation and drainage condition on shear properties of unsaturated cohesive soil. *Soils and Foundations* 41/1, 13-24.
- Tripathy, S., Schanz, T. (2007): Compressibility behaviour of clays at large pressures. *Canadian Geotechnical Journal* 44/3, 355-362.
- Tripathy, S., Sridharan, A. & Schanz, T. (2004): Swelling pressures of compacted bentonites from diffuse double layer theory. *Canadian Geotechnical Journal* 41, 437-450.
- Tsang, C.F., Bernier, F. & Davies, C. (2005): Geohydromechanical processes in the Excavation Damaged Zone in crystalline rock, rock salt and indurated and plastic clays in the context of radioactive waste disposal. *Internat. J. Rock Mech. & Min. Sci* 42/1, 109-125.
- Uchaipichat, A. & Khalili, N. (2009): Experimental investigation of thermo-hydro-mechanical behaviour of an unsaturated silt. *Géotechnique* 59/4, 339-353.
- Vali, H. & Hesse, R. (1992): The microstructure of dilute clay and humic acid suspensions revealed by freeze-fracture electron microscopy: discussion. *Clays and Clay Minerals* 40, 620-623.
- Van Genuchten, M.T. (1980): A closed-form equation for predicting the hydraulic conductivity of unsaturated soils. *Soil Science Society of America Journal* 44/5, 892-898.
- van Olphen, H. (1963): *An introduction to clay colloid chemistry: for clay technologists, geologists and soil scientists.* Interscience, New York.
- Villar, M.V. (1999): Investigation of the behaviour of bentonite by means of suction-controlled oedometer tests. *Engineering Geology* 54/1, 67-73.
- Villar, M.V. (2007): Water retention of two natural compacted bentonites. *Clays and Clay Minerals* 55/3, 311-322.
- Villar, M.V. & Lloret, A. (2004): Influence of temperature on the hydro-mechanical behaviour of a compacted bentonite. *Applied Clay Science* 26/1, 337-350.
- Villar, M., & Lloret, A. (2008): Influence of dry density and water content on the swelling of a compacted bentonite. *Applied Clay Science* 39/1, 38-49.
- Villar, M.V., García-Siñeriz, J.L., Bárcena, I. & Lloret, A. (2005): State of the bentonite barrier after five years operation of an in situ test simulating a high level radioactive waste repository. *Engineering Geology* 80/3, 175-198.

- Villar, M.V., Gómez-Espina, R. & Lloret Morancho, A. (2010): Experimental investigation into temperature effect on hydro-mechanical behaviours of bentonite. *Journal of Rock Mechanics and Geotechnical Engineering* 2/1, 71-78.
- Villar, M.V., Gómez-Espina, R. & Gutiérrez-Nebot, L. (2012): Basal spacings of smectite in compacted bentonite. *Applied Clay Science* 65, 95-105.
- Wang, Q., Minh Tang, A., Cui, Y.J., Delage, P. & Gatmiri, B. (2012): Experimental study on the swelling behaviour of bentonite/claystone mixture. *Engineering Geology* 124, 59-66.
- Wang, Q., Minh Tang, A., Cui, Y.J., Delage, P., Barnichon, J.D. & Ye, W.M. (2013): The effects of technological voids on the hydro-mechanical behaviour of compacted bentonite-sand mixture. *Soils and Foundations* 53/2, 232-245.
- Washburn, E.W. (1921): The dynamics of capillary flow. *Physical Review* 17/3, 273.
- Wheeler, S.J. (1988): The undrained shear strength of soils containing large gas bubbles. *Géotechnique* 28/3, 399-413.
- Wiebe, B., Graham, J., Tang, G.X. & Dixon, D. (1998): Influence of pressure, saturation, and temperature on the behaviour of unsaturated sand-bentonite. *Canadian Geotechnical Journal* 35/2, 194-205.
- Wille Geotechnik: <http://www.wille-geotechnik.com/>. Accessed on 29<sup>th</sup> February 2016.
- Witteveen, P., Ferrari, A. & Laloui, L. (2013): An experimental and constitutive investigation on the chemo-mechanical behaviour of a clay. *Géotechnique* 63/3, 244-255.
- Wood, D.M. (1985): Some fall-cone tests. *Géotechnique* 35/1, 64-68.
- Ye, W.M., Zhang, Y.W., Chen, B., Zhang, Z.J., Chen, Y.G. & Cui, Y.J. (2012): Investigation on compression behaviour of highly compacted GMZ01 bentonite with suction and temperature control. *Nuclear Engineering and Design* 252, 11-188.
- Yin, J. (2003): A Double cell triaxial system for continuous measurement of volume changes of an unsaturated soil sample in triaxial testing, technical note. *Geotechnical Testing Journal* 26/3.
- Yin, J.H., Saadat, F. & Graham, J. (1990): Constitutive modelling of a compacted sand-bentonite mixture using three-modulus hypoelasticity. *Canadian Geotechnical Journal* 27/3, 365-372.

## Appendix A

### A.1 List of symbols and abbreviations

#### List of symbols

$A_0$	initial area of the sample
$A_{in}$	internal area of the inner-cell
$A_{net}$	area of the triaxial caps
$a$	material parameter for evolution of the coefficient of compressibility ( $\beta$ )
$B$	Skempton's B coefficient
$\beta, \beta_0$	plastic compressibility modulus, plastic compressibility modulus at reference void ratio $e_0$
$\beta_w$	soil – liquid contact angle
$C_c$	compression index, defined as the slope of NC line in <i>void ratio – log <math>\sigma</math></i> plane
$C_s$	swelling index, defined as the slope of unloading-reloading line in <i>void ratio – log <math>\sigma</math></i> plane
$d$	pore diameter in Chapter 3; material parameter to account the evolution of the drying yield suction with void ratio in Chapter 4
$dS_r^e, dS_r^p$	elastic and plastic increments of the degree of saturation
$D$	diameter of the sample in triaxial test
$e$	void ratio
$e_c$	void ratio after isotropic consolidation
$e_0$	initial void ratio
$e_f$	void ratio at critical state
$e_m, e_{m0}$	microstructural void ratio, microstructural void ratio at the as compacted state
$e_M$	macrostructural void ratio
$e_m^*$	intruded microstructural void ratio
$e_n$	nonstructural void ratio
$e_{Hg}, e_{rnm}$	intruded void ratio by mercury
$E$	Young's modulus
$\varepsilon_v, \varepsilon_v^T, \varepsilon_a$	volumetric strain, thermal volumetric strain, axial strain, respectively
$F$	internal axial force in triaxial cell
$F'$	external axial force in triaxial cell
$F_F$	frictional force in loading ram bushing of triaxial cell

$F_t$	upper tubing system resistance force of triaxial cell
$F_{o,up}, F_{o,lr}$	frictional force due to O-ring systems in triaxial cell
$F_v$	actual force applied on the sample in triaxial cell
$F_s$	applied force to steel cylinder system in triaxial cell
$f_x(x)$	probability function of encountering pore diameters between $x$ and $x+dx$
$F_X(x)$	complimentary cumulative distribution function
$f_{v,x}(x)$	pore diameter probability density function
$f(\log x_i)$	pore size distribution function
$G_s$	specific gravity
$h$	height of the sample in triaxial test
$\delta h, \delta h_s, \delta h_w$	displacement recorded by external LVDT, actual deformation of the sample, deformation of the upper component, lower component and the porous discs in triaxial tests, respectively
$\delta h_b, \delta h_d$	
$k$	elastic compressibility modulus
$k_b$	Boltzmann's constant
$K_0$	coefficient of the lateral earth pressure at rest
$\lambda_H^p$	plastic multiplier
$\lambda$	compression index (Cam-clay)
$M_m$	compression/extension modulus of the rubber membrane
$M$	slope of the critical state line in $p'$ - $q$ plane
$M_w$	molecular mass of water
$\Delta M_w^i$	incremental water mass transferred in vapour form
$n$	molar concentration of ions in pore fluid
$v$	valency
$OCR$	overconsolidation ratio
$p_0$	atmospheric pressure (101.325 kPa)
$P_{Hg}$	capillary pressure for the mercury system
$\theta_w, \theta_{nw}$	air – water contact angle, non-wetting fluid contact angle and the vacuum
$\pi$	osmotic suction

$\psi, \psi_{res}, \psi_{ew}$	total suction, residual suction, wetting yield suction, suction at full saturation,
$\psi_e, \psi_{e0}$	suction at full saturation at reference $e_0$ , drying yield suction, drying yield
$\psi_D, \psi_{D0}$	suction at reference $e_0$ , respectively
$q$	deviatoric stress
$R$	universal gas constant
$\rho$	bulk density
$\rho_w$	density of water
$\rho_d$	dry density
$r$	pore radius
$S_r$	degree of saturation
$S_{rm}$	complementary degree of saturation intruded by mercury
$s$	matric (capillary) suction
$S_{rw}$	degree of saturation intruded by mercury
$S_{r,ew}$	degree of saturation at wetting yield point
$s(x)$	volumetric shape function
$\sigma_{Hg}$	interfacial tension of mercury
$\sigma_w$	interfacial tension of the wetting fluid
$\sigma_p$	swelling pressure
$\sigma_{in}$	inner-cell pressure of triaxial cell
$\sigma_{out}$	outer-cell pressure of triaxial cell
$\sigma_c$	isotropic confining stress in triaxial testing condition
$\sigma_a$	axial stress in triaxial testing condition
$\sigma_i + \sigma_f$	summation of the tubing and friction stress in triaxial cell
$\sigma_{m,q}$	rubber membrane correction stress term
$t$	time
$t_{100}$	time required for 100 % of primary consolidation
$t_f$	time to failure under deviatoric loading in triaxial test
$T$	temperature/absolute temperature
$T_s$	temperature of the sample in triaxial test

$T_b$	temperature of the heating bath
$u_a, u_w$	pore air pressure, pore water pressure
$u_v, u_{v0}$	vapour pressure, saturated vapour pressure
$V$	intruded pore volume with mercury
$V_{in}$	inner-cell volume
$V_s$	sample volume in triaxial test
$V_t$	total pore volume
$\Delta V_s, \Delta V_{s,b}$	volume change of the sample, lateral volume change of the sample, axial
$\Delta V_{s,a}$	volume change of the sample, respectively
$W, W_u, W_L, W_s$	total weight of the components as well as the weights of upper, lower and the inner-cell cylinder components in triaxial cell
$w$	water content
$w_l, w_p$	liquid limit, plastic limit
$w_{sat}, w_r$	water content at saturation, residual water content
$x$	modal pore diameter

**Abbreviations**

<i>AEV</i>	air-entry value
<i>BSE</i>	back scattered electron
<i>CSL</i>	critical state line
<i>EBS</i>	engineered barrier system
<i>EGTS</i>	engineered gas transport system
<i>FBD</i>	free body diagram
<i>FIB-nt</i>	focused ion beam nanotomography
<i>GAST</i>	gas-permeable seal test
<i>GTS</i>	Grimsel test site
<i>HAEV</i>	high air-entry value
<i>HLW</i>	high-level radioactive waste
<i>LVDT</i>	linear variable differential transformer
<i>MIP</i>	mercury intrusion porosimetry
<i>MU</i>	microstructural units
<i>NBR</i>	nitrile butadiene rubber
<i>OCR</i>	over-consolidation ratio
<i>PSD</i>	pore size density
<i>RH</i>	relative humidity
<i>S/B</i>	sand/bentonite
<i>SEM</i>	scanning electron microscopy
<i>TEM</i>	transmission electron microscopy
<i>THM</i>	thermo-hydro-mechanical
<i>URL</i>	underground research laboratory
<i>WP4C</i>	dew-point chilled-mirror psychrometer
<i>XRD</i>	X-ray diffraction

*Nota Bene:* Throughout this report, the sign convention is the usual convention of soil mechanics which is that compression is positive. However, a positive statics sign convention is chosen for the formulation presented in Chapter 5.